UNIVERSITÀ DEGLI STUDI DI PALERMO
Dottorato in Scienze Fisiche
Dipartimento di Fisica e Chimica – Emilio Segrè
Settore Astronomia ed Astrofisica (FIS/05)

IMPERFECT ACCRETION
Ejecting matter in X-ray Binaries

IL DOTTORE
ALESSIO MARINO

IL COORDINATORE
Prof. GIOACCHINO MASSIMO PALMA

IL TUTOR
Prof.ssa TIZIANA DI SALVO

EVENTUALE CO TUTOR
Dr. JULIEN MALZAC
Dr.ssa MELANIA DEL SANTO

CICLO XXXIII
ANNO CONSEGUIMENTO TITOLO - 2021

Université Fédérale
Toulouse Midi-Pyrénées

THÈSE

En vue de l'obtention du
DOCTORAT DE L'UNIVERSITÉ DE TOULOUSE

Délivré par l'Université Toulouse 3 - Paul Sabatier

Cotutelle internationale : Université de Palerme

Présentée et soutenue par

Alessio MARINO

Le 17 mars 2021

l'accrétion imparfaite: l'éjection de matière dans les binaires X

Ecole doctorale : **SDU2E - Sciences de l'Univers, de l'Environnement et de l'Espace**

Spécialité : **Astrophysique, Sciences de l'Espace, Planétologie**

Unité de recherche :
IRAP - Institut de Recherche en Astrophysique et Planetologie

Thèse dirigée par
Julien MALZAC, Tiziana Di Salvo et Melania Del Santo

Jury

M. Sergio CAMPANA, Rapporteur
M. Guillaume DUBUS, Rapporteur
M. Peter VON BALLMOOS, Examinateur
M. Julien MALZAC, Directeur de thèse
Mme Tiziana DI SALVO, Co-directrice de thèse
Mme Melania DEL SANTO, Co-directrice de thèse

Abstract

X-ray binaries are binary stars composed of a compact object (a black hole, a neutron star) accreting matter from a companion star. These sources can be considered perfect astrophysical laboratories to test our knowledge of, e.g., General Relativity and Magneto-Hydrodynamics. Accretion is the key phenomenon characterizing these systems, but it is not always completely efficient. In many systems, ejections of matter are also observed, e.g. in the form of jets and winds, or also suggested, e.g. to explain the observed strong orbital expansion of a number of systems. Furthermore accretion and ejection seems to be somehow interconnected but the nature of this correlation is not completely clear. The purpose of this thesis is the study of a number of cases where the accretion is imperfect and mass losses have to be taken into account to correctly model the physical properties of the binaries.

In the first of the featured projects, I focus on the spectral study of the accretion flow in the Neutron Star (NS) Low Mass X-ray Binary (LMXB) 1RXS J180408.9-342058, an intriguing system which in the past exhibited "very faint" phases of activity. I performed a spectral analysis of data collected by different X-ray telescopes, i.e. *INTEGRAL*, *Swift* and *NuSTAR*, The study led to several interesting results, in particular the observation of the intermediate spectral state, hard to catch in NS LMXBs because very short-lived, and new constraints on the nature of the companion star, which exclude the hypothesis of a helium dwarf companion as suggested in the past.

The second project presents a systematic study of (almost) all known Accreting Millisecond X-ray Pulsars (AMXPs), i.e. LMXBs hosting an X-ray pulsar spinning at millisecond periods, with the aim of looking for indications of non-conservative mass-transfer in this class. Comparing this observed luminosity averaged over twenty years with the one expected from the theory in a conservative scenario, I found that over a sample of 19 sources, around one half of it shows indications for mass losses.

The third project in this thesis is dedicated to jets, the most known form of mass ejection in X-ray binaries. Jets are characterized by flat radio-to-mid-IR spectra, which have been modelled in the last few decades using the Internal Shocks model ISHEM. The basic idea of this model consists in using the observed X-ray variability as a proxy for the fluctuations of the Lorentz factor in the ejected shells along the jet. I applied the model on the multi-wavelength data set of the NS LMXB 4U 0614+091. I found that ISHEM describes satisfactorily the data only in two cases: using the X-ray variability but in non-conical geometry or either in conical geometry but using flicker noise instead of the X-ray variability.

The final project of my thesis aims at testing a unified accretion-ejection model to the Black Hole LMXB MAXI J1820+070. The model considers the accretion flow in X-ray binaries as two-fold, comprising a truncated geometrically thin disk far from the Black Hole and a so-called jet emitting disk serving as the base of the jet close to the Black Hole. Interestingly, the model allows not only to

describe the X-rays data, but also to predict the radio power emitted by the jet. In order to test the model, I used X-rays data from *Swift* and *NuSTAR*. The preliminary results of the spectral fitting suggest that the model is indeed effective in describing the observed X-ray spectra. Furthermore, the analysis reveals the need for describing the reflection spectrum with two reflection components instead of one: the origin of such intriguing component, if confirmed, will be object of future investigations.

Résumé

Les binaires X sont étoiles binaires composées d'un objet compact (un trou noir ou une étoile à neutrons) accumulant la matière d'une étoile partenaire à travers le processus d'accrétion. On peut considérer ces sources comme de parfaits laboratoires astrophysiques pour tester notre compréhension des processus physiques à l'œuvre au voisinage d'un objet compact. L'accrétion joue un rôle essentiel pour la caractérisation des ces sources, mais elle n'est pas toujours entièrement efficace. En fait, dans de nombreux systèmes on observe aussi des éjections de matière. De plus, l'éjection de matière pourrait expliquer la forte expansion orbitale observée dans un certain nombre de ces systèmes. Accrétion et éjection semblent être en quelque sorte interconnectées mais la nature de cette liaison n'est pas claire. L'objectif de cette thèse est l'étude d'un nombre de cas où l'accrétion est « imparfaite » et où la prise en compte des pertes de masse est nécessaire à la modéliser les propriétés physiques des binaires X.

Dans le premier projet, je me suis concentré sur l'étude spectrale du flot d'accrétion dans la binaire X de faible masse avec une étoile à neutrons (NS LMXB) 1RXS J180408.9-342058. J'ai effectué une analyse spectrale utilisant des données recueillies par les télescopes à rayons X *INTEGRAL*, *Swift* et *NuSTAR*. L'étude a permis d'obtenir des résultats intéressants, en particulier l'observation d'un état spectral « intermédiaire », particulièrement difficile à observer dans les NS LMXBs car très éphémère, et de nouvelles contraintes sur la nature de l'étoile compagne.

Le deuxième projet présente une étude systématique de presque toutes les sources appartenant à la classe des « Accreting Millisecond X-ray Pulsars » (AMXPs), i.e. des NS LMXBs où l'étoile primaire est un pulsar X avec une période de rotation de l'ordre de la milliseconde. L'objectif était de chercher des indications de transfert de masse non-conservatif dans ces sources. À partir de la comparaison entre la luminosité X moyenne observée au cours des vingt dernières années et la luminosité prévue par la théorie dans le cas conservatif, j'ai trouvé que presque la moitié des sources analysées montre des signes d'éjection de matière.

Le projet suivant est plutôt focalisé sur l'étude des jets, la forme la plus connue des éjections de masse dans les binaires X. Les jets sont caractérisés par des spectres plats entre les fréquences radio et l'infra-rouge, modélisées dans la dernière décade avec le modèle des chocs internes ISHEM. L'idée à la base du modèle est d'utiliser la variabilité observée dans les courbes de lumière X comme traceur des fluctuations du factor de Lorentz du jet. J'ai utilisé le même modèle sur un ensemble de données allant de la radio aux rayons X relatifs à une binaire X à étoile à neutrons, i.e. la LMXB 4U 0614+091. Le modèle décrit de manière satisfaisante les données seulement dans deux cas: soit en utilisant la variabilité X comme traceur des variations de vitesse du jet mais en supposant une géométrie non-conique, soit avec une géométrie conique mais en utilisant un bruit de scintillation pour décrire les fluctuations de vitesse du jet.

Avec le projet final de ma thèse, j'ai essayé d'appliquer le modèle JED-SAD, unifiant accrétion et

éjection, à la source à trou noir MAXI J1820+070. Selon ce modèle, le flot d'accrétion dans les binaires est composés des deux disques : un disque externe optiquement épais (SAD) et un disque interne optiquement fin d'où est lancé le jet (JED). Le modèle prédit non seulement les spectres X du le flot d'accrétion mais également la puissance émise aux fréquences radio par le jet. Les résultats préliminaires des ajustements spectraux indiquent que le modèle reproduit bien les observations X. De plus, l'étude révèle la nécessité de considérer deux composantes de réflexion distinctes pour bien reproduire les observations. L'origine de cette double réflexion sera objet de futures investigations.

Contents

Introduction

> Now it's full night, clear, moonless and filled with stars, which are not eternal as was once thought, which are not where we think they are. If they were sounds, they would be echoes, of something that happened millions of years ago: a word made of numbers. Echoes of light, shining out of the midst of nothing. It's old light, and there's not much of it. But it's enough to see by.
>
> *Cat's Eye*, Margaret Atwood

In *Interstellar* (2014) the protagonist, Dr. Cooper, ventures in proximity of *Gargantua*, a gigantic black hole, in order to give humanity a new hope. The image of the scientist staring at the supermassive black hole is likely one of the most epic scenes in contemporary science fiction and provides viewers, whatever their scientific background, a glimpse in how fascinating and complex studying compact objects is. However there are things that films do not tell. In real life scientists do not directly *stare* at black holes, firstly because interstellar travels are so far limited to science fiction and secondly because you really do *not* want to find yourself close to a black hole - unless of course the fate of humanity depends on it. What astronomers do, instead, is studying the radiation emitted by celestial bodies all over the electromagnetic spectrum. As much as less thrilling of exploring the cosmos onboard a spaceship, analyzing data gives the community the unique opportunity to obtain insights on these extreme environments.

Black holes (BHs) and neutron stars (NSs) are the final stages of the stellar evolution of massive stars. They are enormously dense objects which challenge our understanding of both General Relativity and Quantum Mechanics. Catching these objects when isolated is very challenging (I will go back on this topic in Chapter 1), but luckily in many cases these objects like company. It is known from the early '60s, when X-ray astronomy was born, that among the most common X-ray sources in the Galaxy there were X-ray binaries (XRBs), binary systems composed of Black Holes or Neutron Stars accreting matter from a companion star. Matter accretion is the mechanism by which the gravitational energy of the mass transferred from the partner star is converted into (mostly) X-rays. Accreting compact objects are found also beyond the Milky Way. Very likely at the center of each galaxy lies a supermassive black hole (like the aforementioned fictional *Gargantua*) which accretes matter from the surroundings and shines in X-rays as an Active Galactic Nucleus (AGN), and X-ray binaries have been also observed in other galaxies (see, for a review, Fabbiano 2006).

Since the discovery of Sco X-1 in 1962, i.e. the first X-ray binary, X-ray astronomy progressed

enormously. Today scientists can exploit data with high spectral and angular resolution over wide energy ranges in X-rays. Furthermore, working in combination with observatories at other wavelengths, astronomers gained a more general picture of the different physical phenomena at play in X-ray binaries.

X-rays spectra of XRBs usually reveal the presence of a quasi-blackbody component at soft X-rays, i.e. below 10 keV. It arises from an accretion disk orbiting around the compact object. Indeed accreted matter does not fall straight onto the BH (or NS) since it has its own specific angular momentum and it instead moves along circular orbits. As angular momentum is lost, matter moves towards progressively smaller orbits towards the compact object, moving in spiral and building this way a disk-like structure. Disks are however not the only ingredient of X-rays spectra from these sources: in most cases also a power-law-like spectral component extending to hard (even beyond 100 keV) X-rays is observed. This feature is considered the spectral signature of an accretion *corona*, i.e. a hotter, less dense and optically thin region of the accretion flow. Depending on whether spectra are dominated by the disk or by the corona, scientists classify observations of XRBs in two states, labelled soft and hard respectively. The geometry and properties of the accretion flow in both states have been object of decades of investigations. According to the general and most universally accepted scenario, the disk is truncated far away from the compact object in the hard state while it reaches the Innermost Stable Circular Orbit or ISCO (or the NS surface if the accretor is a NS) in soft states. However in a number of cases the observations have been proven inconsistent with this model and yet many questions on the geometry and the physics of the accretion flow across spectral states lie unanswered. Furthermore in almost all BH XRBs and a vast majority of NS binaries, the level of emitted flux varies largely over short time scales. These systems, dubbed transient X-ray binaries, spend indeed most of their existence in a so-called quiescence state, where accretion is almost entirely shut off, and display only episodical (usually of the order of months) periods of X-ray activity, called outbursts. During an outburst, systems usually follow a well established script according to which they start in hard state, transition to soft state, go back to the hard state but at lower luminosity (*hysteresis*) and finally end up in quiescence again.

In a very simplified way, it could be said that variations in the mass accretion rate level determine the dichotomy between outbursts and quiescence, while variations in the geometry and physical properties of the accretion flow determine the spectral states. However accretion is not the end of the story. As mentioned earlier, multi-wavelength observations allow scientists to obtain a more comprehensive description of the physics in accreting compact objects. Indeed, these objects are also observed in radio to mid-IR frequencies and the origin of such emission is ascribed to a jet, a collimated relativistic outflow of plasma expelled along an axis perpendicular to the orbital plane. Jets are observed in outburst but, at least for systems hosting BHs, only in hard state, while they are quenched in the transition to the soft state. This link seems to imply some level of correlation between the ejection and the evolving accretion flow, which is also demonstrated by a direct correlation between the radio and the X-ray luminosity of both XRBs and AGNs (see, e.g. Gallo et al. 2003; Coriat et al. 2011). Furthermore, the spectra emitted from jets can be modelled under the assumption that the variability in the accretion flow is transmitted to the jet (Malzac 2013), showing that the accretion flow might determine not only the onset of the jet, but also its emission properties. And if so, it may be true also the opposite, i.e. the launch of the jet modifies the structure of the accretion flow, as proposed in the Jet Emitting Disks model by e.g. Ferreira et al. (2006). The examples enlisted here are however sparse clues; a global model of the accretion/ejection interconnection able to explain the geometry of the accretion flow, the quenching of the jet, the hysteretical cycles and all the spectro-temporal signatures related to these phenomena is still missing. Ejection is present also

during the soft spectral states, under the form of disk winds. Accretion is therefore almost never *perfect*, it is almost anytime accompanied to some level of outflows.
In systems hosting pulsating NSs as accretor, outflows can be caused also by the direct interaction between the accretion stream and the NS magnetic field (propeller effect) or even the pulsar wind (*radio -ejection*, Burderi et al. 2001). The net effect is a reduction of the amount of mass accreted with respect to the mass transferred from the companion, i.e. a non-conservative mass-transfer (NCMT). The loss of at least a fraction of the transferred mass can directly impact the orbital evolution of some systems, as proposed by e.g. Di Salvo et al. (2008). This could be related to the existence of an entire class of XRBs (likely all hosting NS) which has been observed persistently in *very faint* outbursts, at levels intermediate between the typical bright outbursts and quiescence (the so-called Very Faint X-ray Transients Wijnands et al. 2006).
The last argument sheds light on another crucial point in studying NS and BH XRBs: the role, if any, of the nature of the compact object. For many aspects it is tempting to assume that we can describe accretion and ejection with similar models in both cases. This is however not always true if we consider e.g. that jets are often not quenched in NS systems during the soft state. Moreover transitions between hard and soft states are somehow faster in NS systems compared to BH systems. Finally also spectral and timing characteristics are slightly different in the two classes, i.e. BH XRBs display spectra usually harder than NS XRBs while the latters are characterized by having Power Density Spectra with more power at high frequencies.
My thesis is aimed at investigating on some of the topics and open problems introduced above, mainly via spectral analysis of X-rays data. In particular, the goal of my research is to study several cases where accretion is somehow *imperfect* and taking into account the impact of the ejection is unavoidable. The main questions I am trying to answer are therefore:

- What are the geometry and the physical properties of the accretion flow in XRBs?
- How do the geometry and the physical properties evolve across different spectral states?
- How can we describe the emission from jets in XRBs?
- What type of connection exists between accretion flows and jets in XRBs?
- What is the impact of the outflows on the secular evolution of these systems?
- Do the answers to the questions above depend on the nature of the compact object (BH or NS)?

My thesis is structured as follows. A first part, Chapters 1 and 2, introduces the theoretical background of the thesis, focusing on compact objects and accretion/ejection in X-ray binaries, respectively. Chapter 3 focuses instead on the multi-wavelength instrumentation used in the thesis and presents the general X-rays data reduction procedures I adopted. In Chapter 4, I report on the broadband X-ray spectral study performed on the NS Low Mass X-ray Binary (LMXB) 1RXS J180408.9-342058, which exhibited in the past a VFXT behaviour, during its bright outburst. The focus of the thesis start to shift to outflows in Chapter 5, where I illustrate a method to check if systems could have undergone NCMT over the last two decades and apply it to (almost) all the Accreting Millisecond X-ray Pulsars discovered so far. Chapter 6 gives a brief overview on jets and their properties and reports on the multi-wavelength spectral analysis of the jet/accretion flow of the NS LMXB 4U 0614+091. In this Chapter, I am applying for the first time the Internal

Shocks Emission Model to the jet of a NS XRB. An attempt of giving a global accretion/ejection paradigm is presented in Chapter 7, where I present a recently developed model aiming at describing both accretion and ejection in BH XRBs and apply it to the BH binary MAXI J1820+070. In the Conclusions, I am going to illustrate the main results of this thesis, the open questions and how future missions could contribute in addressing them.

1. Neutron stars and black holes

SUMMARY

When the fuel in the cores of stars, the nature of which depends on the initial mass of the stars, is exhausted, they reach their final evolutionary stage as compact objects. Three different types of compact objects exist: white dwarfs, neutron stars and black holes. They correspond to increasingly more extreme states of matter and for many aspects they defy our understanding of Nature. White dwarfs and neutron stars are held together by degeneracy pressure due to electrons and neutrons respectively, while virtually nothing stops the contraction of black holes. In this chapter, I outline the main properties of each of these compact objects, with emphasis on neutron stars and black holes, as they are the focus of this thesis.

1.1 The destiny of a star

More than 2000 years ago, the greek philosopher Aristotle wrote in his *On the heavens* (350 B.C.) that stars and celestial bodies are eternal and not subject to change or even death. While we are way over the cosmological view by Aristotle, the idea of stars as *eternal things* is likely at some level still present in our minds and in a way, it is true that the sky did not change much during the history of humanity; astrologists write the daily horoscope using the very same constellations the ancient Greek astronomers observed thousands of years ago and the Sun is not expected to change much at least for the next 5 billion years. Stars are therefore *stable* over at least the time-scale of our species. Indeed, a star exists as the result of an ongoing tension between its own self-gravity, which helds it together and gives it a spherical shape, and some other *force* that prevents gravity to collapse the star. In main sequence stars, this force is provided by the immense radiation pressure that the photons

emitted in the core as a result of the ongoing stellar nucleosynthesis exert on the upper layers of the star. However, stellar nucleosynthesis does not last forever: when the hydrogen storage in the core is exhausted, the mechanism which prevents the star to collapse on itself is off and the star contracts. Stars generally have a way out of it: contraction increases the temperature and pressure of the core, eventually triggering the thermonuclear fusion of heavier elements than hydrogen and re-establishing the temporarily lost thermodynamic equilibrium of the star. For the most massive stars, this process can be repeated again and again, burning progressively heavier elements, but not for elements with higher atomic numbers than iron[1]. All stars eventually undergo a phase where the inward pull of gravity is unsupported, shrinking them in size and leading them to the last chapter of their existence in the form of **compact objects**.
The type of compact object a star will become depends on the mass of its core M_c at the moment of the collapse (see Fig. 1.1 for a summary sketch of stellar evolution):

- Stars with M_c below the **Chandrasekhar limit** $1.4 M_\odot$, become **White Dwarfs** (WDs), which are stars of the size of the Earth made of an extremely dense ($\rho \sim 10^{18}$ g cm^{-3}) mixture of electrons and protons. At such densities, a quantum-mechanical effect prevents the white dwarf to collapse any further: indeed, since two electrons cannot occupy the same quantum-mechanical state, at such densities they tend to repel each other as if there was some kind of repulsive force, i.e. an **exchange interaction**[2], between them. This phenomenon can be explained in terms of a **degeneracy pressure** inside of the white dwarf, which counterbalances gravity. This pressure, however, is not thermal and it does not involve the motion of the particles, which, in simple models for WDs and NSs, can be considered as frozen at a temperature of 0 K (see, e.g. Longair 2011).

- If the leftover core is less massive than about 3 $M_\odot$[3], the collapse of the star squeezes together protons and electrons, until they reach the point where they interact with a **capture process**:

$$p^+ + e^- \rightarrow n + \nu_e \tag{1.1}$$

  and neutrons are produced. The final object is a **Neutron Star** (NS), an extreme object of $\sim$ 10 km in radius and mass of 1-2 times the mass of our Sun. The process which helds together neutron stars is the same as WDs, with the crucial difference that the electron degeneracy pressure dominates in WDs while the degeneracy pressure exerted by neutrons dominates in NSs..

- Finally, for cores at the moment of collapse even more massive than $\sim 3\ M_\odot$, *nothing*, not even degeneracy pressure, can prevent the star to undergo a catastrophic and unstopped collapse. What is left behind is a **Black Hole** (BH).

In this thesis I will focus on NSs and BHs. In the rest of this chapter some more details on the two, most extreme, classes of compact objects will be given, without claiming to be exhaustive on such complex and wide area. I refer instead to the dedicated chapters of Longair (2011), or the recent reviews by, e.g., Rezzolla et al. (2018) and Fabian and Lasenby (2015).

[1] Indeed, nucleosynthesis for elements with higher atomic number than iron is endoergonic instead of exoergonic and it does not occur spontaneously, but it can be triggered when enormous amounts of energy are released, e.g. during *supernova* explosions.

[2] I caution the reader that the label *interaction* could be misleading: I am not talking about a traditional force, e.g. it lacks any force carriers, but rather of a quantum-mechanical phenomenon whose net effect resembles the existence of a repulsive interaction.

[3] The exact number is the so-called **Tolman-Oppenheimer-Volkoff** limit, which is comprised in the range 2.2-2.9 $M_\odot$ (Kalogera and Baym 1996), depending on the Equation of State of ultra-dense matter (see next Section).

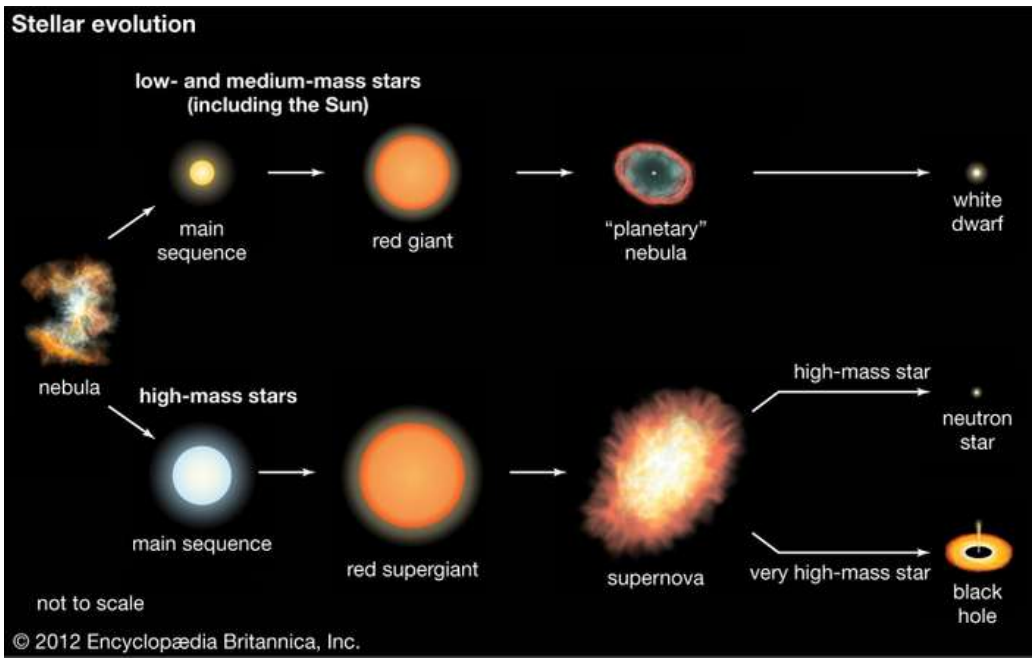

FIGURE 1.1: Sketch representing the main evolutionary stages of the stars and their final form as compact objects.

1.2 Neutron stars

The existence of neutron stars was hypothesized by Baade and Zwicky (1934) only two years after the discovery of the neutron (Chadwick 1932). These authors speculated (correctly) that NSs would be what is left of the cores of massive stars after a supernova explosion would have blown out its outer layers. However, these objects were considered too small and faint to be ever detected. Thirty years later, Pacini (1967) suggested that rapidly spinning NSs with strong enough magnetic fields could be observed as an intermittent radio signal in the sky, i.e. a **pulsar**. Unbeknown to Pacini, in Cambridge, between 1965 and 1967 two bizarre sequences of short and repetitive pulses were detected by graduate student Jocelyn Bell and her supervisor, Prof. Anthony Hewish, and originally labelled as "Little Green Men", as if they were some sort of communication from an alien civilization. The later identification of this signal as coming from the first pulsar ever observed, i.e. PSR B1919+21, opened the way to pulsars astronomy and was awarded with the Nobel Prize in Physics in 1974[4].
Although the composition and inner structure of NSs is not completely established, it is quite certain that these exotic objects are not *only* made of neutrons. Indeed, NSs structure, from outside inwards, can be roughly outlined as in the following (e.g. Longair 2011):

- a thin, i.e. of a few μm, atmosphere made mostly of H or He;
- a *surface* of atomic polymers of ^{56}Fe;
- an *outer crust* which somehow resembles WD interiors, with a Coulomb lattice of heavy nuclei embedded in a gas of relativistic degenerate electrons;

[4]Only Hewish, however, was awarded while Bell, despite being the one who actually recognized the anomalous signal as something natural and not a man-made interference, was excluded.

- an *inner crust* where matter is still organised in neutron-rich nuclei lattice but is surrounded by free degenerate neutrons and degenerate relativistic electron gas. Going deeper, density increases and matter starts losing its order, with the dissolving of nuclei and the arising a neutron fluid;

- the *core*, with such a high density, i.e. 10^{27} g cm^{-3}, that neutrons are expected to geometrically overlap;

The deeper we dig inside of a NS, the less we understand. In particular, the composition and the structure of the core is basically unknown. The behaviour of matter in such extreme conditions of density and pressure is ruled by the so-called **Equation of State of ultra-dense matter** (EoS), which is a relation between pressure and energy density (see, for a review, Özel and Freire 2016). Dozens of possible EoS have been proposed in the past, but establishing which one is the correct answer is extremely hard. It is indeed impossible to reach the required extreme densities and, at same time, the low temperatures relevant for NSs in any laboratory on Earth. Astrophysical observations can however help in the search for the EoS in NSs cores: the EoS can be directly mapped in relations $M(R)$ between the mass and the radius of the NSs. Therefore, obtaining constraints on M or R or both is at the moment one of the main goals of NSs astrophysics. Of the main techniques developed in the past for this purpose, many involve the X-ray spectral analysis of NS LMXBs (see, e.g. Degenaar and Suleimanov 2018, and references therein), which are one of the main topics of this thesis.

1.2.1 Pulsars

The most basic definition of a pulsar is that of a rapidly spinning NS endowed with a magnetic field (see Fig. 1.2, *left*). Indeed NSs have the strongest magnetic fields in the Universe, as expected by the simple following argument: imagine a star, like the Sun, with typical magnetic field of order ~ 1 G and radius $\sim 7\times10^5$ km. If this star collapses isotropically into a compact star of only 10 km, we would expect the magnetic flux over the surface, i.e. proportional to BR^2, to be conserved[5] and therefore the magnetic field to be enhanced of a factor $\sim10^{10}$. NSs display magnetic field intensities B in a range which goes from 10^8 to 10^{15} G, and beyond for *magnetars*. A similar argument for the conservation of angular momentum would also prove that NSs spin quite rapidly at birth, with periods even below 1 ms, in principle.
In pulsars, the magnetic axis is misaligned with respect to the rotation axis. Approximating then the NS as a spinning magnetic dipole, its dipole momentum varies over time and induces an electric field on the NS surface. Charged particles are then accelerated and migrate to the poles, where they can radiate away the energy gained as γ-rays by, e.g., Inverse Compton scattering of ambient thermal photons (see, e.g. Bussard et al. 1986; Sturner and Dermer 1994). In turn, these γ-ray photons are susceptible of pair production and therefore populate the polar caps of the pulsar of electrons and positrons, which in turn would produce more γ-rays and give rise to a cascade. The created leptons move on almost one-dimensional trajectories, since they lose via synchrotron radiation their orbital energy and decay rapidly to the lowest Laundau level (see, e.g. Luo and Melrose 1992). The emission mechanisms at this point of the story are not perfectly established (see Melrose et al. 2020, for a recent review on the debate over such topic): among the proposed mechanisms, likely the favored one is the coherent curvature emission, i.e. emission from relativistic particles moving along a curved magnetic field (Radhakrishnan and Cooke 1969). What it is known for certain is that very

[5] This is true, indeed, if the magnetic flux is frozen in the plasma or, equivalently, if the diffusion time for the magnetic field is much higher than the time of collapse, a condition which is actually satisfied (see, e.g. Longair 2011).

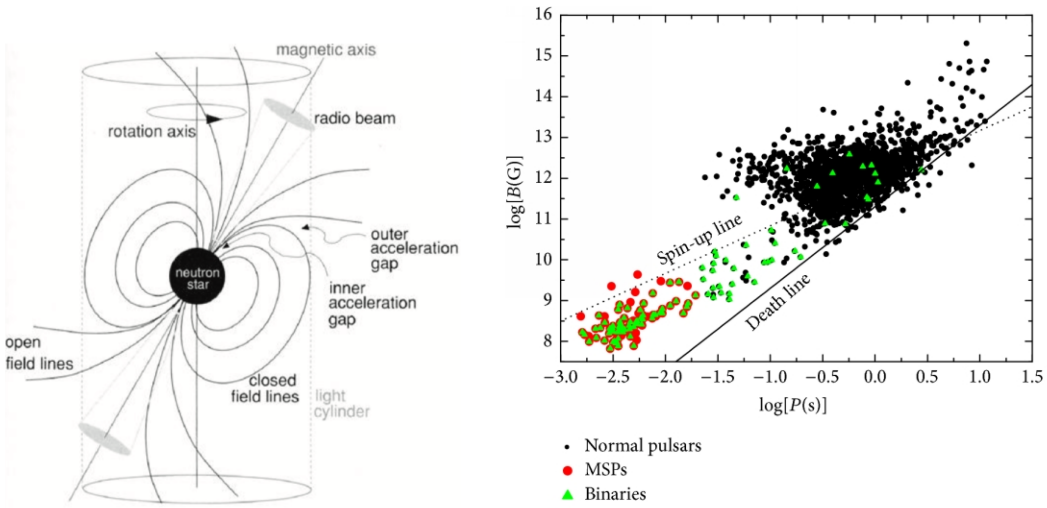

FIGURE 1.2: (*Left*) sketch representing a radio pulsar (Longair 2011) and (*Right*) typical *B*-*P* diagram for pulsars, showing the distribution of radio pulsars over period and magnetic field (adapted by Wang et al. 2011).

beamed radiation is emitted mostly in the radio band from the polar caps. Such configuration explains the periodic sequence of pulses which basically defines pulsars through the so-called **lighthouse effect**. Since the magnetic axis is tilted with respect to the rotation axis, every time the spinning NS directs each of the radio beams towards us, crossing our line of sight, we observe a sudden rise in the radio signal coming from the pulsar. Consequently, the periodicity of the pulses corresponds to the spin period of the NS.

As rapidly spinning magnetic dipoles, pulsars radiate away part of their rotational energy and tend therefore to brake, increasing their spin period P over time. Furthermore, also their magnetic field tend to decay, likely for ohmic dissipation of the magnetospheric currents which produce it (Ostriker and Gunn 1969). With decreasing spin periods and magnetic fields, pulsars at some point, in about 10^7 years, reach a condition where the voltage in the polar caps, responsible for the onset of the particles cascade and therefore of the radio beamed emission, drops below a critical value (Bhattacharya and van den Heuvel 1991) and the pulsar activity stops. In a *B*-*P* diagram (see Fig. 1.2, *right*), pulsars which reach this terminal condition would pass through the so-called **death line** and place in the *pulsar graveyard*. Non-pulsating NSs are indeed "dead" pulsars.

According to this picture, young pulsars are expected to distribute above the death line, with high magnetic fields and relatively long (longer than few tens of millisecond) spin periods, i.e. in the upper right region of the *B*-*P* diagram. However, almost 3% of the known pulsars inhabit the lower left part of the diagram, with B around 10^8-10^9 G and millisecond spin periods. **Millisecond pulsars** represent actually an anomaly in the depicted evolutionary model for pulsars. In order to have their weak magnetic field they have to be "old" systems[6], older than ex-pulsars in the graveyard, but their extreme rotation periods (which allow the voltage in the polar cap to be high enough for maintaining the pulsar emission mechanisms) is hard to reconcile with their old age. How can these systems be so old and yet so rapidly spinning? We will come back to this enigma with a satisfactory solution in Chapter 5.

[6]Furthermore, many of them have been found in Globular Clusters, which are arguably the "oldest" objects in the Galaxy (see, e.g. Chaboyer 2001)

1.3 Black Holes

The idea of a black hole arose in the XVIII century, as a star so massive for which the escape velocity would have been higher than the speed of light, so that radiation could not escape from it (Michell, 1784 and a few years later also the French mathematician Pierre-Simon Laplace). Two centuries later, it was understood that for stars more compact than neutron stars such condition on the escape velocity would have been satisfied. Furthermore, in such objects no force would have impeded the collapse of the star, leaving behind nothing but a space-time singularity. These extremely exotic stars were dubbed black - as radiation could not escape from them - and holes - as they draw a rift in space into which matter can fall but from which it cannot emerge (Wheeler 1968). The region of space surrounding the black holes from which no escape is possible it is delimited by an **event horizon**. No information can travel through it and, indeed, only three parameters can be associated to a black hole, as stated by the **no-hair theorem** (Misner et al. 1973): the mass, the electric charge and the spin. Black holes are the simplest macroscopic objects in nature.
Black holes masses span an extremely large range: at the extremes of this range[7] sit on the one hand the so-called *stellar* black holes, with masses of 3-100 $M_\odot$ and on the other the *super-massive* black holes, with masses of the order 10^{6-9} $M_\odot$, whose origin is still an open field of research (see, e.g. Volonteri 2010, and references therein). *Intermediate* mass black holes (IMBH) would inhabit the gap between these two extremal classes, but their existence is still object of debate, with many observed candidates (e.g. Irwin et al. 2010; Baldassare et al. 2015), but only one reliable detection (Lin et al. 2018).
The radius defining the event horizon is critically dependent on the spin of the black hole. For simple non-rotating black holes, the event horizon is given by the **Schwarzschild radius** $r_S = \frac{2GM}{c^2}$, which can be easily found by setting the escape velocity at distance r to c. In rotating black holes, called **Kerr black holes**, the radius can shrink down to $r_K = \frac{GM}{c^2}$ for maximally[8] rotating black holes.
But how can black holes be observed? Indeed they are by definition singularities from which no signal can escape. However, this is not completely true as some form of radiation is expected to arise from a black hole considering quantum electrodynamics, the so-called **Hawking radiation**; when a virtual pair is created from vacuum in the proximity of the event horizon of a black hole, there is a small but finite probability that one of the particles falls into the black hole carrying negative energy and then reducing the black hole energy and the other one escapes, carrying the exact energy which the black hole lost (Hawking 1975). However, the black body temperature associated to such radiation would be of the order $10^{-7}(M/M_\odot)$K, which makes it impossible to detect. Indeed, there is no way of directly observing a black hole, except for the case of two merging black holes detected from the emitted gravitational waves (Abbott et al. 2016), which recently opened the field of gravitational astronomy.
It is however possible to observe the effects black holes operate on radiation and matter surrounding them: if light from a background source travels close to an isolated black hole, its trajectory is bent by the immense gravity of the compact object, which acts as a lense (**gravitational microlensing**). The increase of the apparent brightness, the shift in position of the background source and its splitting in multiple images are signatures of the presence of a black hole between the source and the observer (see, e.g. Walker 1995).

On the other hand, black holes in binary systems with a companion star can exert a gravitational

[7] The range would be even wider including the hypothetical microscopic black holes which might have inhabited the early Universe with masses of the order of the Planck mass, i.e. 22 μg (see, e.g. Hawking 1971)

[8] Indeed, for higher angular momenta no black holes could be formed (Longair 2011).

pull on the matter of the partner star and *accrete* part of its mass. As we will discuss extensively in the next Chapters, the accreted mass emits X-rays that make these systems among the brightest objects in the X-ray sky: these systems are the so-called **X-ray binaries** (XRBs).

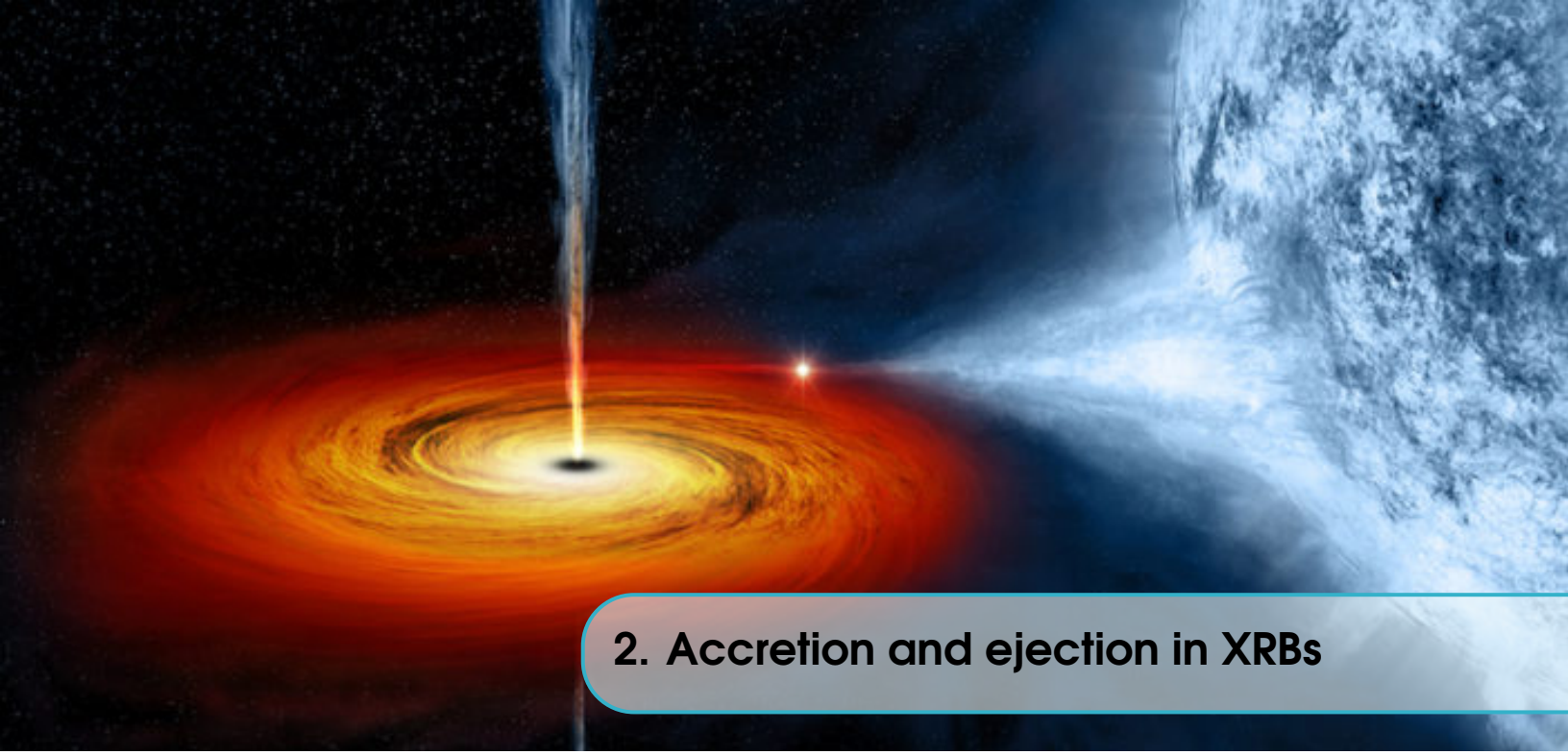

2. Accretion and ejection in XRBs

SUMMARY

All around the Galaxy, compact objects are observed in binary systems accreting material from a companion star, called X-ray binaries since they emit mostly in X-rays. According to the mass of the partner star, a subdivision exists between High Mass X-ray Binaries and Low Mass X-ray Binaries. Mainly in the second category, matter outflows from the Roche lobe of the companion star and moves on Keplerian orbits around the compact object, forming an accretion disk and, sometimes, a hot corona. According to the contribution of the disk and the corona, the X-ray spectrum emitted by the system changes shape and it is possible to distinguish between hard, intermediate and soft spectral states. These spectral states are characterized also by ejection of matter, in the form of jets in hard/intermediate states and winds mainly in soft states. In transient X-ray binaries, i.e. systems which are only sporadically observed in X-ray activity episodes called outbursts, spectral states and their related ejection properties are always observed in a well-defined sequence, forming an hysteresis cycle. The observed correlation between accretion flow configurations and outflows suggests some kind of link between accretion and ejection in X-ray Binaries.

2.1 The zoo of X-ray binaries

X-ray astronomy is a relatively young branch of astronomy, being *only* 60 years old. X-rays are unable to penetrate the Earth atmosphere, therefore only the use of rockets, balloons or satellites makes the study of the X-ray sky possible. The team led by the Nobel Prize Riccardo Giacconi pioneered the field with the first rocket observations in X-rays, originally finalized to study the Sun. However, since their first publication in the field, the group recognized that, alongside the Sun, the

X-ray sky was populated by other, unknown, sources (Giacconi et al. 1962). More than ten years later, one of these sources, i.e. Scorpius X-1, was identified as a **X-ray binary** (Giacconi 1974), a binary star composed of a compact object, in this case a neutron star, called **primary star**, *accreting* matter from a companion star, defined **secondary star**. Nowadays, the scientific community knows that analogous binaries are among the most common source of X-rays in the Galaxy and form a very diverse and heterogeneous "*zoo*" of celestial bodies.

A first distinction exists according to the nature of the primary star, i.e. white dwarf (WD), neutron star (NS) or black hole (BH). Systems hosting WDs as primary stars are dubbed **Cataclysmic Variables** (CVs), since they exhibit irregular and dramatic changes in brightness. On the other hand, systems hosting a BH or a NS are called X-ray Binaries (XRBs). The main difference between CVs and XRBs hosting BHs or NSs is the range of X-ray luminosity: CVs are less luminous, with X-ray luminosity around 10^{29}-10^{33} erg s^{-1}, while NS and BH XRBs have almost overlapping luminosity ranges, from 10^{30} to 10^{39} erg s^{-1}.

The second criterion to classify XRBs consists in the mass of the companion. Systems with massive secondary stars of spectral class O or B are defined **High Mass X-ray Binaries** (HMXBs), while systems having solar or sub-solar companion stars are called **Low Mass X-ray Binaries** (LMXBs). HMXBs are younger systems, usually 10^7 years old, with respect to LMXBs, which host Population II stars, around 10^9-10^{10} years old. Indeed, in *old* Galactic realms like Globular Clusters, only LMXBs are observed, while HMXBs populate the Galactic Disk. LMXBs are usually more compact, i.e. have shorter orbital periods, than HMXBs. Furthermore, NSs in LMXBs have weaker magnetic fields with respect to NSs in HMXBs[1], with values of B around respectively 10^8-10^9 G and 10^{12} G, respectively. Indeed, NS HMXBs usually display coherent pulsations in X-rays, while in NS LMXBs only a minority of sources are X-ray pulsators, a group of them form the class of the so-called **Accreting Millisecond X-ray Pulsars** (AMXPs). A further subdivision exists in the class of NS LMXBs between **atolls** and **Z** sources, named after the particular tracks they follow cyclically in a color-color diagram (see Fig. 2.1), i.e. a diagram where the flux in a hard energy band or color is plotted versus the flux in a soft color. Furthermore atolls are intrinsically less luminous than Z sources.

As mentioned before, X-ray luminosity is usually not a good criterion to distinguish between BH and NS XRBs. Astronomers rely often on some phenomena which are typical signatures of the presence of a NS as primary, in particular coherent pulsations and the occurrence of **Type-I X-ray bursts** (see Section 4.6). Otherwise the most useful argument to identify the nature of the primary is obviously the mass. It can be inferred by the orbital parameters of the system, in particular from the **mass function** f:

$$f(M) = \frac{P_{\rm orb} K_2^3}{2\pi G} = \frac{M_2^3 \sin^3 i}{(M_1 + M_2)^2} \tag{2.1}$$

with $P_{\rm orb}$ the orbital period of the system, K_2 the half-amplitude of the velocity curve, M_1 (M_2) mass of the primary (secondary) star and i the inclination of the system with respect to our line of sight. If $M_1 > 3 M_\odot$, the system is hosting a BH. Aside from these evidences, BH and NS XRBs show some specific differences in spectral and timing behaviours which could contribute in identifying the nature of the compact object. They will be discussed later in the thesis.

[1] With a few exception, (see, e.g. D'Aì et al. 2014)

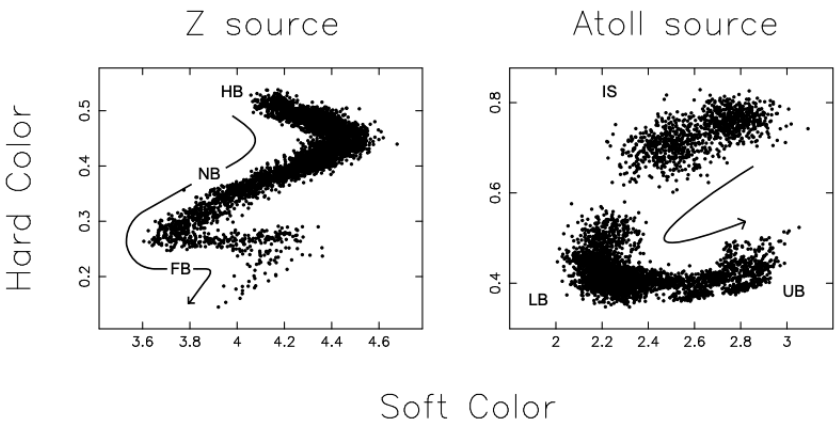

FIGURE 2.1: Typical X-ray color-color diagram for systems identifed as atolls (*right*) and Z-sources (*left*). Arrows are drawn to illustrate the evolution of these systems with increasing $\dot{M}$ (Wijnands 2001).

2.2 Accretion

As diverse as it is, the whole family of XRBs has at least one common, obvious, characteristic: they are bright in X-rays. The physical mechanism invoked in order to explain the origin of such radiation is **accretion** of matter, an efficient mechanism that allows these systems to convert gravitational energy into radiation. Indeed, in XRBs a fraction of the mass of the secondary star is transferred to the primary star and falls into the gravitational well created by the compact object. As matter falls towards progressively smaller circular orbits towards the compact object, its gravitational potential energy is liberated in the form of electromagnetic radiation mostly in the X-ray band because of the high temperature reached in such proximity to the accretor. Studying accretion flows has a key-role in many branches of physics and allows scientists to perform tests of Einstein's gravity or to investigate the exotic state of matter inside of neutron stars. Furthermore it is nowadays understood that accretion and its feedback on cosmic structure have been playing a fundamental role in the growth of structures of the Universe (see, e.g. Fender 2010).
Imagine a star of mass M and radius[2] R which accretes a mass-test m, initially at infinity; the amount of energy accreted and released in the form of radiation equals the variation of gravitational energy of the test-mass in moving from infinity to R:

$$\Delta E_{\rm acc} = \frac{GMm}{R} \tag{2.2}$$

with G the gravitational constant. In order to understand how powerful accretion can be for compact object, I introduce the **efficiency of accretion** η, which can be expressed as:

$$\eta = \frac{GM}{Rc^2} \tag{2.3}$$

and using this I can simply rewrite $\Delta E_{\rm acc} = \eta mc^2$. Using the standard values for M and R of a NS, i.e. 1.4 $M_\odot$ and 10 km, I obtain $\eta \sim 0.15$. In the case of a WD, with similar masses but 1000 times

[2]In the case of a BH accretor, consider the radius as the event horizon.

higher radii, η is much smaller and, indeed, CVs are usually sensibly fainter than NS XRBs. An analogous calculation for BHs gives values of η comprised between 0.1 and 0.5, depending on their spins (see, e.g. Frank et al. 2002). Interestingly, the conversion efficiency for thermonuclear fusion of H nuclei in the cores of stars, i.e. $\eta_{\rm fusion} \sim 0.007$ is significantly lower than η for NSs and BHs. Derivating over time $\Delta E_{\rm acc}$ **accretion luminosity** can be obtained:

$$L_{\rm acc} = \frac{GM\dot{m}}{R} \quad , \tag{2.4}$$

with $\dot{m}$ the mass-accretion rate. In a simplified picture, i.e., where gravity is the only force acting, variations in the X-ray luminosity could be interpreted as simply variations in $\dot{m}$. In reality, the X-ray luminosity is only a (non-linear) tracer of $\dot{m}$ as mass losses, advection of energy and magnetic effects have to be taken into account as well (Agol and Krolik 2000).

2.2.1 The Eddington limit

As mentioned in the previous Subsection, X-ray luminosity in BH and NS XRBs usually does not overcome 10^{38}-10^{39} erg s^{-1}. Indeed, the accretion luminosity that XRBs can achieve has an upper threshold, corresponding to the point where the radiation produced through accretion has enough energy to prevent matter to be accreted any further: this threshold luminosity is called the **Eddington luminosity**. In order to derive the standard analytical expression for such limit, a few approximations must be made:

- Mass accretion is stationary and isotropic;
- Matter is considered as composed of pure, completely ionised hydrogen, i.e. a neutral mixture of protons and electrons;
- Matter and radiation interact only through Thomson scattering.

I note that, since Thomson scattering has the lowest cross-section among the other typical matter-radiation interaction processes, the last approximation guarantees that the Eddington limit is indeed an upper limit. In this scenario accretion stability is bound to the delicate competition between gravity and radiation pressure. Gravity acts mainly on protons, as they are ≈2000 times more massive than electrons, and pulls matter onto the compact object. On the other hand, radiation pressure acts mainly on electrons, since Thomson cross-section depends on m^{-2} (with m mass of the interacting particle), and pushes matter away. However, even if acting on different particles, the effects of gravity and radiation impact both electrons and protons as they are bound together by Coulomb forces. When radiation pressure and gravity counterbalance each other perfectly, the Eddington limit is reached. More in detail, the radiation pressure can be expressed as: $p_{\rm rad} = U/c$, where U is the energy flux transported by the photons. Flux can be simply written as the luminosity divided by the surface area that is crossed by radiation at a given distance r:

$$p_{\rm rad} = \frac{L}{4\pi r^2 c} \quad . \tag{2.5}$$

The force exerted on the electrons by this pressure is obtained by multiplying $p_{\rm rad}$ by the Thomson cross-section $\sigma_{\rm T}$. Putting into equation this force with the gravitational force exerted on protons (of mass $m_{\rm p}$), I obtain the following expression for the Eddington Luminosity $L_{\rm Edd}$:

$$L_{\rm Edd} = \frac{4\pi GMm_{\rm p}c}{\sigma_{\rm T}} = 1.3 \times 10^{38} \frac{M}{M_\odot} \text{ erg s}^{-1} \quad . \tag{2.6}$$

Considering the typical range of masses for NS and stellar-mass BHs, the observational limit of about 10^{38}-10^{39} erg s^{-1} is therefore explained.
It is worth noticing that Eq. 2.6 should be considered as a crude estimate of the real limit, as the assumptions made, i.e. the pure hydrogen composition, stationary emission or spherical symmetry, are not always satisfied in the accretion flow. In NS LMXBs accreting matter from hydrogen poor highly evolved stars the observed limit is higher, i.e. estimated around 3.79×10^{38} erg s^{-1} (Kuulkers et al. 2003). Furthermore several sources have proven to be able to overcome a few times the Eddington limit at their peak luminosity, e.g. the BH binary GRS 1915+105 (Fender and Belloni 2004) or the Z source Cir X-1, which reached even luminosities of 10 $L_{\rm Edd}$ (Done and Gierliński 2003). However, some sources are known to be extremely Super-Eddington, shining at X-ray luminosities in the range 10^{39}-10^{42} erg s^{-1}: these systems form the class of the **Ultra-Luminous X-ray sources** (see, for an observational review, Kaaret et al. 2017). In the past, their existence was explained in terms of Intermediate Mass Black Holes accreting at Eddington or sub-Eddington rates. However the discovery of coherent pulsations in a number of ULXs (e.g. Bachetti et al. 2014; Israel et al. 2017; Sathyaprakash et al. 2019) made this interpretation clearly not suitable for all the systems in the class. Explaining how systems hosting neutron stars could reach luminosity several orders of magnitude beyond the Eddington limit probably requires the existence of some beaming mechanisms and it is currently one of the most challenging topics in High Energy Astrophysics.

2.3 Mass-transfer, geometry and binary evolution

In order for matter to be accreted onto the compact object and to observe it in the X-rays band, the companion star has to transfer mass. In XRBs, **mass transfer** can occur through the emission of stellar wind (1) and the so-called **Roche lobes overflow** (2), where the gravitational pull of the primary removes the outer layers of the companion star. Mechanism (1) is relevant only in HMXBs, as low mass stars eject only scarce amounts of wind, if any. Mechanism (2) can occur in both LMXBs and HMXBs, but it is of course crucial in the former class. In the following I will focus on such mechanism, as LMXBs are the topic of this thesis.

2.3.1 Roche lobes overflow

Roche lobes overflow occurs when the outer part of the companion star is close enough to the primary star, e.g. if the secondary star during its evolution inflates or if the orbital separation between the partner stars shrinks[3]. The formalism employed to describe such phenomenon introduces a so-called **Roche potential** $\Phi_{\rm R}$ which encloses the gravitational and centrifugal effects that a test-mass would experience if posed in proximity of the binary system. The expression for $\Phi_{\rm R}$ is:

$$\Phi_{\rm R}(\vec{r}) = -\frac{GM_1}{|\vec{r}-\vec{r}_1|} - \frac{GM_2}{|\vec{r}-\vec{r}_2|} - \frac{1}{2}\left(\vec{\omega}\times\vec{r}\right)^2 \quad , \tag{2.7}$$

with $\vec{r}_1$ ($\vec{r}_2$) the position of the primary (secondary) star and $\vec{\omega}$ the angular velocity of the binary in terms of the unit vector $\vec{e}$, perpendicular to the orbital plane of the system. In order to understand qualitatively the shape of $\Phi_{\rm R}$, imagine to probe the space surrounding the stars with a unit "test" mass. As apparent from Eq. 2.7, $\Phi_{\rm R}$ can be approximated to the gravitational potential of the single

[3] As discussed in Subsection 2.3.2, angular momentum losses via magnetic braking or gravitational waves tend to reduce the size of the Roche Lobe of the companion star after the increase caused by the mass transfer.

star if the test mass gets close enough to $\vec{r}_1$ ($\vec{r}_2$). Quite intuitively, the closer one gets to one star of the binary, the more the gravitational effects of the companion fade away. If instead the test mass is put far enough from both the stars, the object would be unable to resolve the two stars and would simply experience the gravitational potential of a big star with mass equal to $M_1 + M_2$. Somewhere in between these two extremes, it is possible to individuate an *8-shaped* equipotential surface composed of two lobes, each containing one star, the **Roche lobes**. The contact point between the lobes is a saddle point of the Roche potential and is called the **first Lagrange point**[4] L_1. See Fig. 2.2 for a 3-D representation of the Roche potential surrounding a binary system. If one star fills up its Roche lobe, again because the star swells or even the Roche lobe itself shrinks around the star, the system becomes *semi-detached*, matter flows freely through L_1 and it is poured onto the Roche lobe of the compact object: this mechanism is the so-called Roche lobes overflow.
The lobes are more '*pear*'-shaped than spherical, therefore in the following I will refer to the Roche lobe indicating an imaginary sphere which occupies its exact same volume. For sufficiently low-massive secondary star, i.e. for which the ratio $q = \frac{M_2}{M_1}$ is comprised between 0.1 and 0.8, the Roche lobe radius $R_{L,2}$ of the secondary star can be expressed as a fraction of the orbital separation a using the so-called **Paczynski approximation**[5]:

$$R_{L,2} = 0.462 q^{\frac{1}{3}} \left(1 + \frac{1}{q}\right)^{\frac{1}{3}} a \quad . \tag{2.8}$$

The equivalent expression for the primary star is obtained substituting the pedix '2' with '1' and using 'q^{-1}' instead of q. An interesting consequence of such formula is that, for a lobe-filling star, it is possible to find that the orbital period P of the system is inversely proportional to the mean density $\overline{\rho}$ of the star, so that for a compact system the Roche lobe can only accomodate relatively dense stars.

2.3.2 Orbital evolution of binaries

Equation 2.8 states clearly that the size of each Roche lobe depends on q and a; mass-transfer tends to affect both of these quantities. As the secondary star cedes mass to the primary, M_2 (and thereby q) decreases but at the same time, as the transferred mass carries angular momentum away from the donor, it originates a redistribution of the angular momentum which alters a. It is not obvious however how the combined effect of a and q will affect $R_{L,2}$. In order to answer this question I need to include the **orbital angular momentum** J:

$$J = M_1 M_2 \left(\frac{Ga}{M_1 + M_2}\right)^{1/2} \quad , \tag{2.9}$$

(for a derivation of such formula, see e.g. Frank et al. 2002). In the following I will consider the **conservative mass-transfer case**, where all the mass-trasferred by the secondary is accreted on the primary, while the **non-conservative mass-transfer case** will be extensively treated in Chapter 5. If no mass losses occur in the system then $\dot{M}_1 + \dot{M}_2 = 0$, with $\dot{M}_2 < 0$. It is therefore possible to differentiate logarithmically Eq. 2.9 with respect to time to easily see how the temporal evolution of a, J and M_2 will affect each other, i.e.:

$$\frac{\dot{a}}{a} = \frac{2\dot{J}}{J} + \frac{2\left(-\dot{M}_2\right)}{M_2}(1 - q) \quad . \tag{2.10}$$

[4] Lagrange points are five and are saddle points of the Roche potential.
[5] This expression is indeed a simplified expression of the original formula by Eggleton (1983) for the low-mass case.

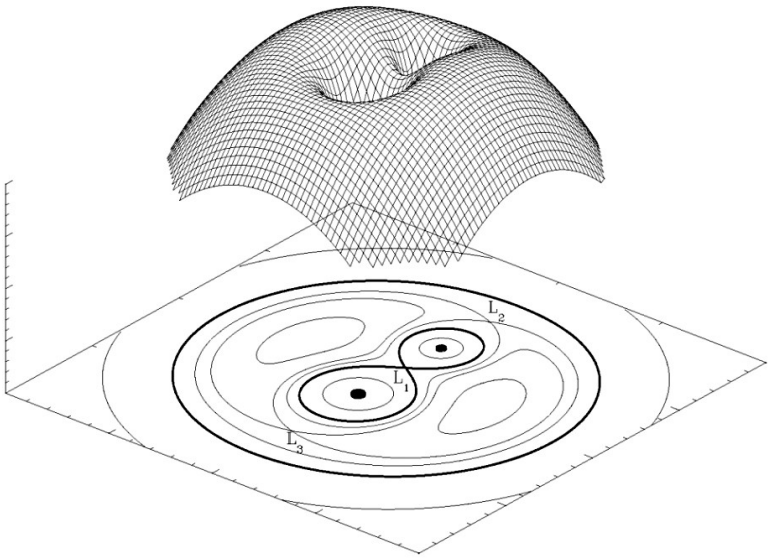

FIGURE 2.2: 3-D representation of the Roche potential in presence of a binary system. Three of the five Lagrange points are highlighted here with L_1, L_2, L_3, (*Credits:*) https:www.heaven.waarnemen.com).

For the moment I will also consider the case where the overall angular momentum is conserved, i.e. $\dot{J} = 0$. In this case, the expansion or contraction of a depends all on the ratio q: for $q < 1$ (low-mass binaries) mass-transfer implies an increase in the separation between the stars, while for $q > 1$, a tends to shrink. Quite intuitively, e.g. in the low-mass case, matter, in order to move through progressively smaller orbits towards the compact object, has to transfer back angular momentum to the donor and the orbital separation between the stars increases. What is then the effect on $R_{\mathrm{L},2}$? Differentiating logarithmically Eq. 2.8 and combining it with Eq. 2.10, I find:

$$\frac{\dot{R}_{2,\mathrm{L}}}{R_{2,\mathrm{L}}} = \frac{2\dot{J}}{J} + \frac{2\left(-\dot{M}_2\right)}{M_2}\left(\frac{5}{6} - q\right) \quad . \tag{2.11}$$

Yet again, under the hypothesis of angular momentum conservation, it all depends on q: for companion stars not sufficiently massive, i.e. $q < \frac{5}{6}$, mass-transfer swells the Roche lobe radius and eventually prevents any further mass loss for the donor, so that mass-transfer tends to stop.
Two mechanisms could reactivate the whole process: the secondary star could increase in size as a consequence of its own evolution (i) or angular momentum losses $\dot{J}$ (ii), so far willingly ignored, could drive $R_{\mathrm{L},2}$ to contraction (see Eq. 2.11). However, usually mechanism (i) is not suitable for LMXBs, as the secondary star is already evolved or it evolves over extremely long time-scales, while mechanism (ii) is always active.
In a conservative mass-transfer scenario, angular momentum is lost mainly via two different channels:

- **Gravitational Radiation** (GR), i.e. the emission of gravitational waves from the binary system takes away a fraction of the orbital angular momentum at a rate (Kraft et al. 1962; Landau and Lifshitz 1975):

$$-\left(\frac{\dot{J}}{J}\right)_{(\mathrm{GR})} = \frac{32G^3}{5c^5}\frac{M_1 M_2 (M_1 + M_2)}{a^4} \quad , \tag{2.12}$$

which quite intuitively depends strongly on the orbital separation, i.e. the more compact the system, the higher the fraction of angular momentum lost via GR.

- **Magnetic Braking** (MB), where the angular momentum lost is taken away by the stellar wind ejected from the (magnetic) secondary star (Eggleton 1976). Indeed the stellar wind is forced by the star's magnetic field to corotate with it, even at large distances from it, taking away angular momentum from stellar spin. This mechanism would brake the star, i.e. it happens for single main-sequence star, but if the star belongs to a binary system tidal forces would prevent the star from rotating slower. It follows that this angular momentum debt will be paid at the expense of the orbital angular momentum J, at a rate (Verbunt and Zwaan 1981):

$$\left(\frac{\dot{J}}{J}\right)_{(\mathrm{MB})} = \frac{-3.8\times10^{-30}R_{\odot}^{4-\gamma}(M_1+M_2)R_2^{\gamma}\omega^2}{M_1 a} \quad , \tag{2.13}$$

with R_2 radius of the secondary star, $R_{\odot}$ the Sun radius and γ a parameter depending on the type of secondary star.

In LMXBs, especially if compact or ultra-compact, the GR contribution is stronger than MB, since the amount of angular momentum removed by the stellar wind, and the amount of stellar wind itself, is negligible [6] (Nelson and Rappaport 2003). On the other hand, the more massive the companion and/or the higher the orbital separation, the more negligible becomes GR with respect to MB.
In the non-conservative case, the scenario depicted here changes dramatically, since the matter ejected by the system subtracts its own specific angular momentum to the system. The consequences of these losses on the overall orbital evolution will be explored in Chapter 5.

2.4 Accretion disks and accretion flows

In the previous sections, I focused on the Roche lobes geometry and the conditions for the lobe of the secondary to be filled, so that matter accretion can start. When matter is poured onto the Roche lobe of the accretor, matter can not free fall in straight line onto the compact object since it still has its specific (orbital) angular momentum. Once matter leaves L_1, it starts orbiting the center of mass of the system (which for a LMXB is placed inside of the primary Roche lobe and likely even inside of the compact object) to the orbit at the lowest energy for a given angular momentum, i.e. a circular orbit. The radius of this orbit is called **circularization radius** R_{circ} and, for typical values of q, is 2-3 times smaller than the Roche lobe of the primary (Frank et al. 2002). The inflowing stream of transferred matter is accumulated therefore onto a ring of matter orbiting at R_{circ}, inside of which dissipation processes (such as gas collisions, internal stresses and shocks) convert gravitational potential energy into internal energy and, eventually, radiation. As it loses energy, matter sinks deeper into the gravitational potential but, in order to do that, it has to get rid of the angular momentum in excess: the extra angular momentum is transferred back to the remaining ring at R_{circ}, which extends a little farther away from the center of mass. This delicate balance between energy and angular momentum leads the ring to spread in both directions, giving birth eventually to an **accretion disk**. In building-up such structure, mass loses energy in the form of radiation, which accounts for half of the whole accretion luminosity[7].

[6] However, MB contribution has been proven non-negligible in some cases, (see, e.g. Wang et al. 2013; Tailo et al. 2018).

[7] This result is easy to demonstrate considering matter from infinity to the inner radius of the disk and applying then the Virial Theorem (e.g. Frank et al. 2002).

In an accretion disk each ring of matter rotates with differential **Keplerian velocity** Ω_K, i.e. $\Omega_K = \left(GM_1/R^3\right)^{1/2}$. Particles orbiting in neighboring rings have also thermal "chaotic" motions, which drive them to interact with other particles and viscous stresses arise. As radiation is a direct consequence of viscous dissipation in the disk, this ignorance could appear to be fatal for our understanding or modelling of disks: actually it is not. Indeed, the viscous dissipation rate $D(R)$ of energy in a steady disk per unit area can be expressed as:

$$D(R) = \frac{3GM\dot{M}}{8\pi R^3}\left[1 - \left(\frac{R_*}{R}\right)^{1/2}\right] \tag{2.14}$$

with R_* the radius of the compact object (or its Innermost Stable Circular Orbit (ISCO) in the case of a BH). In a steady disc, i.e. where the local mass-transfer rate is constant over time at each ring, the density will adjust itself to guarantee the conservation of mass and angular momentum through each ring and will therefore not appear in Equation 2.14. In the standard disk model by Shakura and Sunyaev (1973), viscosity is simply expressed as $\nu = \alpha c_s H$, with c_s speed of sound in the disk and H the scale height of the disk, i.e. the magnitude of viscosity is parametrized in the dimensionless parameter α (the so-called **α-prescription**). The same authors show that α enters in the equations to describe the local structure of the disk only with small powers, making possible to develop a fully consistent theory of discs even ignoring its magnitude or the nature of viscosity itself. More recently, some steps away from this simple phenomenological picture have been made: the origin of viscosity has been attributed to the **magnetic rotational instability** (MRI) (see, e.g. Balbus 2005; Martin et al. 2019, for a review), while the value of α is known to be around 0.2-0.3 for fully ionized disks, some orders of magnitude lower for not fully ionized disks (King et al. 2007; Martin et al. 2019).

2.4.1 Disk spectra

In steady disks, each ring emits as a blackbody, so that at a certain radius R the equation: $\sigma T^4(R) = D(R)$ holds. The following equation for the temperature profile in the disk can be obtained:

$$T(R) = \left\{\frac{3GM\dot{M}}{8\pi R^3\sigma}\left[1 - \left(\frac{R}{R_*}\right)^2\right]\right\}^{1/4} \quad . \tag{2.15}$$

A simple phenomenological consequence of Equation 2.15 is that, for $R \gg R_*$, $T(R) \propto R^{-3/4}$. Approximately the spectrum emitted from an accretion disk can be considered as the superposition of blackbody spectra at different temperatures, dominated by the spectrum emitted at the inner radius of the disk. Indeed, the flux at frequency ν from the disc is obtained integrating the contribution from the blackbody emission at each radius:

$$F_\nu \propto \nu^3 \int_{R_*}^{R_{\rm out}} \frac{R\mathrm{d}R}{e^{h\nu/kT(R)} - 1} \quad , \tag{2.16}$$

with $R_{\rm out}$ the outer radius of the disk. In the low frequencies limit, i.e. $\nu \ll kT(R_{\rm out}/h)$, the spectrum follows approximately the Rayleigh-Jeans law, i.e. $F_\nu \propto \nu^2$, while at high energies, i.e. $\nu \gg kT(R_*)/h$, it decays exponentially (following indeed the Wien law). Interestingly, in an intermediate range of energies $kT(R_{\rm out}) \ll h\nu \ll kT(R_*)$, $F_\nu \propto \nu^{1/3}$, i.e. the disk spectrum has an almost flat top. The overall spectrum is the so-called **multi-color disk blackbody** and has a quasi-blackbody shape, except for the "flat" region. The extension of such region is directly proportional

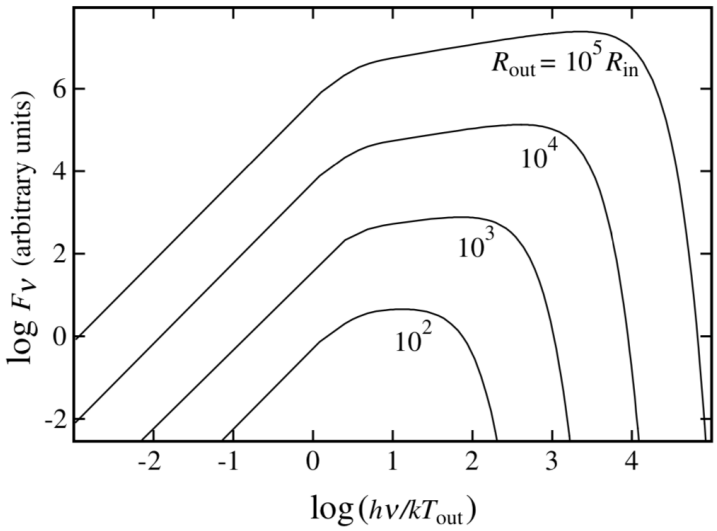

FIGURE 2.3: Multi-color disk blackbody spectra for several disk extensions, showing how the "flat" top becomes more and more significant with increasing R_{out} and it is basically absent for disks with $R_{out} = 10^2 R_{in}$, i.e. typical of CVs. *Credits*: Frank et al. (2002).

to the size of the disk, and indeed it is almost absent in CVs, that have disks smaller by two-three orders of magnitude with respect to disks in BH/NS systems (see Fig. 2.3).
This result neglects the effect of irradiation from the central source and/or the inner regions of the disk, which changes the temperature profile heating a range of intermediate radii in the disk, where $kT(R) \propto R^{-1/2}$. Using this result on Eq. 2.16, one finds that for intermediate frequency, the flux is not proportional to $\nu^{1/3}$, but to ν^{-1}. This effect is again more pronounced in LMXBs with large enough disks, i.e. with NS/BH accretors. However, this "flat" top is observable only in UV-optical wavelengths in systems where the contribution from the secondary star in this realm is negligible, i.e. such as evolved degenerate stars, white dwarfs and very low-mass stars. Indeed, spectral models which do not include irradiation effects (e.g. Mitsuda et al. 1984) are perfectly suitable for X-ray spectra, while irradiated disk models are essential to describe the disk contribution to multi-wavelength optical-to-X-rays spectra for LMXBs. (Gierliński et al. 2008).

2.4.2 Beyond the disk: boundary layers and hot electron coronae

The landscape around an accreting compact object is not composed only of the accretion disk; indeed the accretion flow assumes other forms, which leave their undebatable signature on XRBs spectra.
In accreting NSs (and WDs) with low magnetic fields the existence of a hot accretion belt connecting the inner disk radius and the surface of the star is expected, the so-called **boundary layer**. In the previous section was implicitly assumed that the disk reached the surface of the star. This is true only if two options are simultaneously satisfied: (i) the magnetic field is weak enough for the ram pressure of the accreting matter to be lower than the magnetospheric pressure everywhere around the star and (ii) the rotation velocity of the compact object is equal to the Keplerian velocity at its radius R_*. Condition (ii) is in practice never satisfied as such a rapidly rotating would be unstable and furthermore the record holder for the lowest spin period among the known NSs, e.g. PSR J1748-2446,

has a spin frequency, i.e. 716 Hz (Hessels et al. 2006), well below the Keplerian frequency of a 1.4 $M_\odot$ with a 10 km radius (around 2 kHz). Very often the inner disk radius spins faster than the surface of the NS and the region between the star and the edge of the disk hosts a boundary layer of matter rotating at angular velocity which decreases towards the compact object. As discs emit only half of the accretion luminosity, the other half is liberated from this, usually tiny, layer of accreting material (the splitting between disc and boundary layer is even more unbalanced in favor of the latter when GR effects are taken into account, Sibgatullin and Sunyaev 2000).
Accretion flows can assume other forms, as witnessed by the spectra of both NS and BH LMXBs. Indeed, in many cases these systems show a power-law like component extending up to hundreds of keV, which can not be attributed to the disc. These spectral components are modelled as Comptonization spectra from hot optically thin plasma, the **corona**. Indeed the existence of the disk as an optically thick but geometrically thin structure depends on the assumption of multiple collisions between protons and electrons and, in turn, between electrons and photons. This condition is not always fulfilled, especially at low mass-accretion rates, if so the accretion flow would not be dense enough to guarantee the energy balance between protons and electrons. Thereafter the gravitational energy acquired by the protons (again, electrons are less affected by gravity than protons, which are way more massive) is not shared sufficiently with the electrons, which gain only a small amount of energy via Coulomb collisions and lose most of it by interacting with photons, mainly via Inverse Compton scattering. This process creates a **two-temperature plasma** (Shapiro et al. 1976). In such a plasma, gravitational energy is transported inwards by advection of protons, which would eventually cross the event horizon without exchanging their energy with the electrons and making the whole accretion flow *radiatively inefficient*, as it is not able to convert entirely its gravitational energy into radiation. The structure of such optically thin flows where advection plays a crucial role is called Advection Dominated Accretion Flow or **ADAF** (Narayan and Yi 1995; Yuan 2001). A step further in the modelling of accretion flows in XRBs was made by Esin et al. (1997), which introduces the idea of a *transition radius* between a Shakura-Sunyaev disk and an advection-dominated hot electron corona closer to the Black Hole; the resulting spectrum would be a Comptonization spectrum which uses the soft X-ray photons emitted by the inner region of the disk as seed photons. The following decade saw a proliferation of models of the hot inner accretion flow, to such an extent that the all-inclusive term "?DAF" was sometimes adopted. For example some authors suggested to replace the role of advection as a cooling mechanism with convection (convection dominated accretion flows or CDAF, Blandford and Begelman 1999; Abramowicz and Igumenshchev 2001) or included the role of magnetic fields (magnetically dominated accretion flows or MDAFs Meier 2005) or of the jet (Falcke et al. 2004). I refer to Chapter 6 for a recent model which updates the original model by Esin et al. (1997) but including magnetic fields and jet launching properties.

2.5 Reflection spectra

Although the geometry of the accretion flow is still a vivaciously debated point, it is anyway expected that at least a fraction of the photons emitted by the corona is intercepted by the disk. Since the accretion disk is optically thick, the radiation hitting its surface is here entrapped and reprocessed in the form of a new spectral component, the **reflection spectrum**. The typical reflection spectrum for an incident power-law spectrum hitting an almost neutral disk is shown in Figure 2.4: soft X-rays are absorbed by the material and a jungle of fluorescence lines appear, the most prominent at around 6.4 keV and associated to neutral Fe, while at higher energies a bulge arises due to photons Compton-scattered to energies of around 20-30 keV (the so-called **Compton hump**). Part of the

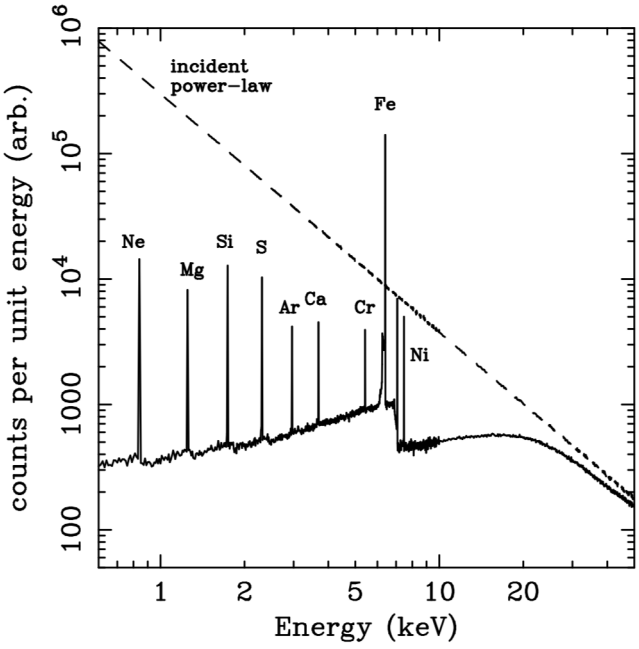

FIGURE 2.4: Simulated reflection spectrum obtained with an incident power-law spectrum (dashed line) which is reflected by a cold gas with cosmic abundances. Some of the most important spectral features are shown (Reynolds 1996).

absorbed energy is then reprocessed and emitted at even softer X-rays as a quasi-thermal spectrum (Zdziarski and De Marco 2020), usually not observed.
The intensity of such component R is related to the solid angle Ω subtended by the reflector, i.e. the disk, as seen from the emitter (the corona) and it is usually expressed as $R = \Omega/2\pi$. A crucial role in the reflection component is played by the ionisation of the disk, enclosed in the parameter $\xi(r)$ which corresponds to the ratio of the photoionization rate to the recombination rate and is described by the following equation:

$$\xi(r) = \frac{L_{\rm X}(r)}{n_{\rm e} r^2} \quad , \tag{2.17}$$

where $L_{\rm X}$ is the bolometric luminosity at radius r and $n_{\rm e}$ the electron number density at distance r from the illuminating source. At low values of ξ, i.e. $\xi < 100$ erg cm s^{-1}, the disk is cold and almost neutral and the reflection component is similar to what shown in Figure 2.4. Increasing ξ, the chemical species in the disk become more and more ionised and Auger effect becomes relevant, making the lines weaker. Finally, at full ionization regimes, i.e. $\xi > 5000$ erg cm s^{-1}, any atomic signature disappears.

2.5.1 The iron line as a diagnostics tool for the inner region of the disk

The most relevant feature of the reflection spectrum is the appearance of the Fe Kα fluorescence line at $\sim$ 6.4 keV, the intensity of which is due to the combination of a high fluorescence yield ($\omega_{K,Fe} \approx 34\%$) of iron and of its relatively high cosmic abundance (Kaastra 1999). It arises when

an electron at level $n = 2$ in the Fe atom descends to level $n = 1$ to fill the vacancy created by photoionization and radiates the excess energy as a fluorescence line at 6.4 keV. First observed in Active Galactic Nuclei (see, for a review, Fabian et al. 2000), the study of its shape represents a useful diagnostic tool to infer properties of the system as, e.g., the inner radius R_{in} of the accretion disk.

The profile of the emitted fluorescence lines is indeed shaped by several relativistic distortion effects, namely Doppler effect, relativistic aberration and gravitational red-shift, which are in turn connected to e.g. the geometry of the accretion flow close to the compact object and the inclination of the system. Since the iron line is usually the most intense reflection line, the study of its profile is used as a powerful diagnostics tool to infer some properties of the system (see, for a review, Reynolds and Nowak 2003).

Doppler effect affects the line profile in two ways: it gives the line its characteristic double-horned shape and it broadens the lines emitted close to the compact object. As material is orbiting around the compact object, a spectral line will be blue or red shifted whether matter is moving towards or away from the observer. The frequency of the emitted lines will be then Doppler scattered in a range $d\nu$, with a major contribution coming from the portion of the material which moves in the direction of the line of sight, corresponding to the receding and approaching part of each matter annulus. As a consequence of relativistic aberration, the horns are asymmetric and the blue horn is usually more pronounced (see Fig. 2.5).

The faster the Keplerian motion of the annulus, the broader the range $d\nu$ over which the line is spread over. In addition, since the disk luminosity reaches its maximum in proximity of the compact object, the broadness of the line profile can be used to estimate the rotation velocity of the material at the inner edge of the disk and, since the velocity is Keplerian, its radius. The estimation of the inner disk radius is extremely useful to e.g. constrain the spin of the black hole, establish the geometry of the accretion flow and the truncation of the disk and, in the case of a LMXB with neutron star as primary, to put an upper limit on the NS radius (see, e.g. Egron et al. 2011; Sanna et al. 2014; Di Salvo et al. 2015; Degenaar et al. 2015b; Ludlam et al. 2017) which is of primary interest to find constraints on the Equation of State of ultra-dense matter.

Finally, the full line profile is affected by the extension of the disk, i.e. its inner and outer radius $R_{\rm in}$ and $R_{\rm out}$, the emissivity profile in the disk ε, the Fe abundance and, most of all, by the inclination of the system. The effect of some of these parameters on the overall line shape can be observed in Figure 2.5 .

2.6 Spectral states

In the last few sections, I introduced the main physical processes ongoing in the accretion plasma and their spectral signature. The disc thermal emission and the Comptonization spectrum from the hot accretion flow are in fact the building blocks of XRBs spectra. As mentioned above, XRBs display a colorful variety of spectral shapes, indicating that these building blocks can be assembled in different ways to reproduce the observed **spectral states**. The first evidence for this came early, with the first X-ray observations of the very well studied BH binary Cyg X-1 showing two markedly different spectral states, the *high* state, characterized by higher X-ray flux and the *low* state, where the flux was found systematically lower. High and soft spectra had also different spectral shape; indeed, while the former displayed the expected disc-blackbody shape, the latter was rather described by a power-law spectrum. A better understanding of such spectral duality was limited by the relatively small energy range, i.e. 2-10 keV, over which the early X-ray telescopes were sensitive. It was

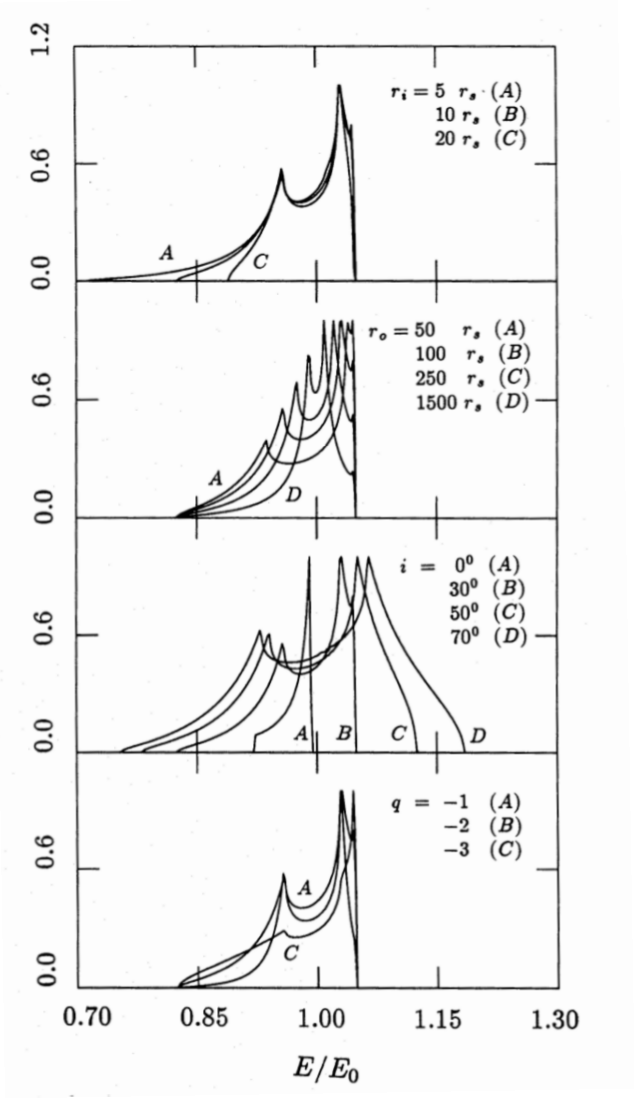

FIGURE 2.5: Iron line profiles for different values of (from top to bottom) inner and outer radius, inclination and emissivity index (here defined as q, but in this thesis I prefer the label ε to avoid any confusion with the binary mass ratio). When not specified, the profiles are computed for $R_{\rm in} = 10R_{\rm G}$, $R_{\rm out} = 100R_{\rm G}$, i=30° and $q = -2$ (Fabian et al. 1989).

not until the nineties, with the launch of new hard X-rays, as *BeppoSAX* or *RXTE*, and soft-γ, such as *CGRO*, observatories, that it was understood the real nature of "low" states. Spectra in such states indeed extend well beyond 10 keV, peaking around $\sim$ 100 keV and beyond, with a bolometric luminosity which for Cyg X-1 is almost the same in high and soft state (see, e.g. Nowak 1995; Zhang et al. 1997). The old (misleading) nomenclature was therefore replaced by the terms **soft** state (for the high state) and **hard** state (for the low state). Intuitively, the dichotomy between high/soft and hard/low state can be explained invoking the same number of components in the accretion flow, which, as discussed in Section 2.4, can be identified as an accretion disk *a la* Shakura-Sunyaev and a hot corona.
Hard and soft states were originally observed in BH XRBs, but NS LMXBs in the *atolls* class (see Section 2.1) have their own version of the same two states, identified as respectively *island* and *banana* state[8] (Hasinger and van der Klis 1989). In the following I will not use unless necessary the island-banana nomenclature, but I will instead refer to them simply as hard and soft states as in BH XRBs. The rest of the paragraph is dedicated to illustrate the observational properties of each state, the proposed physical scenarios to explain them and the transitions between soft and hard state, with an eye on the differences, if any, between systems with BH and NS accretors.

Soft state Soft states in BH LMXBs are disc-dominated spectral states, which can be modelled almost entirely with multi-color disk blackbody models in the soft, i.e. 0.1-10 keV, X-ray band. The physical description is less debated here and it invokes the presence of an optically thick accretion disk extending all the way to the ISCO (for BH XRBs). Indeed several authors observed that in this state the bolometric luminosity $L_{\rm bol}$ is proportional to T^4 (Kubota et al. 2001; Kubota and Done 2004; Davis et al. 2005), which, assuming the spectrum to be dominated by a disc blackbody so that $L_{\rm bol} = 4\pi R_{\rm in}\sigma T^4$, implies that the radius is stable, as predicted by general relativity for a disc reaching the ISCO (Done et al. 2007). NS LMXBs in soft states show sometimes the superposition of two saturated Comptonization spectra, again one for the disk and one for the boundary layer/NS (Lin et al. 2007; Armas Padilla et al. 2017).

The advent of γ-ray telescopes such as *CGRO* and *INTEGRAL* allowed to discover that XRBs spectra in soft state also extend to hard X-rays and soft γ-rays, with a power-law like component extending at least to hundreds of keV and power-law index Γ around 2 (Gierliński et al. 1999). While its nature is still not completely established, it is usually ascribed to Comptonization from a non-thermal population of electrons. Indeed, a hybrid thermal/non-thermal population of electrons probably co-exist in the Comptonizing corona (not only in the soft state) observed at higher energy (Poutanen and Coppi 1998; Coppi 1999).
Another additional power-law component has been used also to describe the hard X-rays of a number of systems and also interpreted as signature of non-thermal Comptonization (see, e.g. Fiocchi et al. 2006; Paizis et al. 2006; Tarana et al. 2011; Bouchet et al. 2009; Del Santo et al. 2013). This component has been sometimes dubbed *hard tail*. Hard tails have been observed in Z-sources (Di Salvo et al. 2006, and reference therein), in the bright Atoll-sources (Paizis et al. 2006) and in BH LMXBs (see, e.g. Malzac et al. 2006; Del Santo et al. 2008), not only in soft state (Fiocchi et al. 2006; Paizis et al. 2006; Tarana et al. 2011; Bouchet et al. 2009; Del Santo et al. 2013).

[8]The peculiar nomenclature originates from the regions spanned by atolls in a color-color diagram during spectral evolution, which appear as isolated "islands" in the hard state and as a long C-shaped "banana" region in soft state (I refer again to Fig. 2.1).

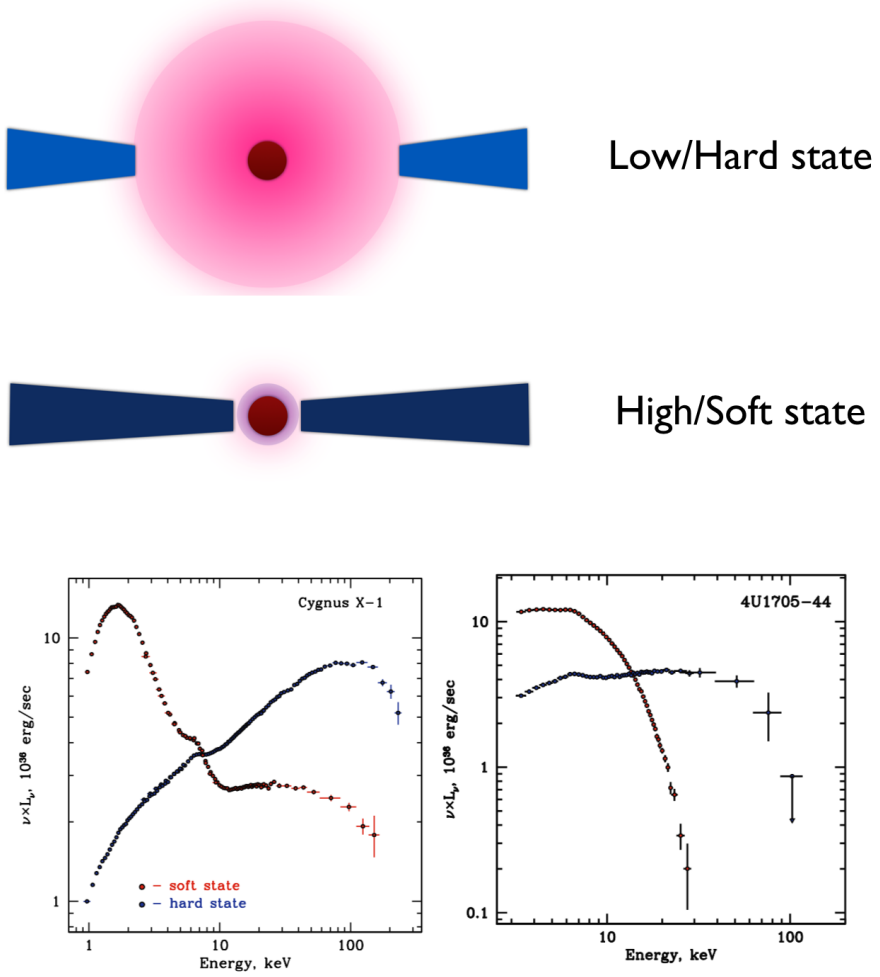

FIGURE 2.6: (*Top*) Schematic representation of the geometry of the accretion flow in XRBs according to the *truncated disk model*. (*Bottom*) Examples of hard and soft state spectra for a BH XRB (Left, Gilfanov et al. 2000) and a NS LMXB (Right, Gilfanov 2010).

Hard state Hard state spectra are usually modeled with power-law models with $\Gamma \sim 1.5-2.0$ with cutoffs beyond 10 keV. These spectral shapes are interpreted using thermal Comptonization models with electron temperatures kT_e around 70-120 keV for BH XRBs (see, e.g. Done et al. 2007, and references therein), while in NS LMXBs usually the corona appears colder (see, e.g. Done and Gierliński 2003; D'Aì et al. 2010; Di Salvo et al. 2019). The seed photons of these Comptonization spectra can be provided by synchrotron emission inside the corona[9] or thermal emission from the disk or (for NS LMXBs) also from the boundary layer or the NS surface.

Indeed, the nature of the seed photons for the Comptonization spectrum and the geometry of the corona were the subject of a tension between two different visions (and modellings) of the accretion geometry in NS LMXBs: according to the *Eastern* model, the corona is relatively small and it surrounds the NS which provides, together with the boundary layer, the seed photons population for the Comptonization (Mitsuda et al. 1989), while on the other hand the *Western* model considers the corona geometrically extended all over the inner regions of the disk (White et al. 1988), which serve in this case as the source of seed photons (see also Church and Bałucińska-Church 2004, for a modified version of the Western model which includes also the emission from the NS surface). The rapid X-ray variability usually observed in these systems, however, would favor the Eastern model to the Western (Churazov et al. 2001). Indeed, the contribution of the hot surface of the NS in this class of system, working as an additional cooling mechanism with respect to BH XRBs, would account for the NS LMXB spectra being usually softer compared those of BHs[10]. For some NS LMXBs double Comptonization models with seed photons coming from both the NS surface/boundary layer and the inner disk radius have been also used (see, e.g. Cocchi et al. 2011; Zhang et al. 2016), which are somehow a compromise between the two visions listed above.
In soft X-rays, spectra show sometimes a blackbody-like component, which is interpreted as thermal disk emission with temperature kT_{disk} below 0.5 keV (see, e.g. Di Salvo et al. 2001; Miller et al. 2006; Buisson et al. 2019) or, in the case of NS LMXBs, to the boundary layer and/or the surface of the NS (see, e.g. Lin et al. 2007; Armas Padilla et al. 2017; Mazzola et al. 2019). The ensemble of these observational evidences is traditionally explained, at least for BH LMXBs, in the framework of the so-called **truncated disk model**, which simply states that in hard states disks are truncated far enough from the compact object to contribute only indirectly, i.e. emitting the seed photons population for the observed Comptonization spectrum, to the overall spectral shape in the X-ray band. The inner region would be then filled with a hot optically thin plasma (Esin et al. 1997), as shown in Figure 2.6. The truncated disc model seems to provide not only solid ground for spectral modelling (see, e.g. Gilfanov et al. 1999; Basak et al. 2017), but it is also confirmed by other evidences, as e.g. the results based on time lags (De Marco et al. 2015), the interpretation of type C Quasi-Periodic Oscillations (see, e.g. Ingram et al. 2016) and calculations of the energy balance of these systems (Poutanen et al. 2018). However, the *consensum* on the truncated disk model is not global and a number of counterproofs have been given as well. The most used argument is that, especially in the last few years, spectral modelling of seemingly broad Fe K lines in BH LMXBs led in many cases to estimated quite small inner disk radii, close to or even equal to the ISCO (examples of these can be found in Miller et al. 2006; Tomsick et al. 2008; García et al. 2015; Parker et al. 2015; Kara et al. 2019). According to these results, even in hard state, the disk would reach the ISCO while somehow

[9] Which is especially true at low luminosities, where the disk is most likely truncated far away from the compact object (but see also Malzac et al. 2009)

[10] While this is usually true, a showy exception would be represented by the so-called *very hard* NS LMXBs (Wijnands et al. 2015; Parikh et al. 2017; Wijnands et al. 2017b), which show very flat power-law spectra ($\Gamma \lesssim 1.5$) for which a clear physical explanation is still missing.

co-habiting with a corona which could be above the disk, i.e. as a "lamppost" (e.g. Matt et al. 1991), or formed by clumps close to the surface of the disk, i.e. a "patchy corona" (e.g. Haardt et al. 1994; Nayakshin 2000).

Intermediate state Transitioning from hard to soft or from soft to hard state, LMXBs could be found in an intermediate state, which shows mixed ingredients between the two states, i.e. thermal Comptonization but from a colder corona with respect to the hard state or a disk component not as dominant as in the soft state (see, e.g. Belloni et al. 1996). The characteristics of this state find a simple explanation within the truncated disk model: when the, initially truncated disk (hard state), approaches the inner regions of the system, it overlaps more and more with the corona, forcing it to cool down gradually (intermediate state), until the optically thin regions becomes cold and optically thick and the disk reaches the ISCO (soft state). Although NS LMXBs are believed to follow the same pattern, intermediate states have been rarely observed. While transitions in BH LMXBs usually takes from weeks to months, in NS LMXBs it probably takes time-scales of days (Muñoz-Darias et al. 2014). The reason for this difference is not yet fully understood.

2.7 Ejection in LMXBs

X-rays and accretion are not the end of the story. Another main aspect of the life cycle of these systems is indeed **ejection** of matter, mainly in the form of **winds** and **jets**. Ejecta influence the evolution of the whole system and, in some cases, modify also the surrounding environment. Moreover, some form of ejection seems to be always present at each stage of the spectral evolution, in a way that accretion and ejection could be considered as *two faces of the same medal*.
High inclination XRBs at luminosities $L_X \gtrsim 0.5 L_{\rm Edd}$, typically in soft state, show sometimes absorption lines from highly ionised elements[11], most often He and H-like Fe (Done et al. 2007), which are outflowing at velocity of hundreds of km s^{-1} as witnessed by their blue shifts. The presence of these lines is considered a signature of disk winds and they have been reported in a rich variety of XRBs, both high- and low- mass, hosting both NSs or BHs (see, e.g. Ueda et al. 1998; Díaz Trigo et al. 2006; D'Aì et al. 2014; Ponti et al. 2014; Pinto et al. 2020). Their occurrence at high luminosities in spectra which show a strong disc component indicates that they are connected with accretion disks, while their physical origin could be thermal (Begelman et al. 1983) or magnetic (e.g. Proga 2003).
The other main form of matter ejection consists in jets, which dominate the emission of XRBs at radio-IR frequencies. Indeed, the wavelength domain of these systems emission extends beyond the optical-to-X-rays realm and goes way down until radio; the origin of this emission cannot be ascribed to the disk or the NS, in the case of NS LMXBs. Indeed, the main actor in the radio-to-IR emission from X-ray binaries is now established to be synchrotron emission from relativistic particles ejected from the system in the form of a collimated outflow, which was called jet (Baade and Minkowski 1954), (usually) along the axis of rotation of the system. The "jet interpretation" is based on the non-thermal nature of this spectral component and on its related high brightness temperature, which is a signature of the emission coming from "big regions" (for X-ray binaries, bigger than the size of the binary itself). Observations have confirmed the jet interpretation for X-ray binaries in several cases: e.g. high spatial resolution radio maps of BH binaries such as Cyg X-1 (Stirling et al. 2001) and GRS 1915+105 (Dhawan et al. 2000; Fuchs et al. 2003) and NS XRBs such as Sco

[11] With ξ even well above 100 (Kallman et al. 2004).

X-1 (Fomalont et al. 2001), have in fact revealed the presence of highly collimated and elongated structures, extending for tens of AU.

2.7.1 Traces of jets: the radio–X-ray correlation

Even if jets and accretion flows reign over different and almost separated regions of the electromagnetic spectrum, they are expected to have some level of correlation. Indeed jets in BH XRBs (and some NS, e.g. Gusinskaia et al. 2017) seem to be present only in hard and intermediate state, while the radio emission is suppressed or *quenched* in the soft state (Fender et al. 1999; Corbel et al. 2000), suggesting that the jet is not launched in these states (or, alternatively, the jet becomes "dark", see Drappeau et al. 2017). In BHs only a few systems represent an exception on jet quenching (e.g. Gallo et al. 2004; Brocksopp et al. 2005), while in NSs the situation seems to be reversed, as almost all of these systems show jet-related radio emission even in soft state (see, e.g. Migliari et al. 2004). However, the general picture seems to indicate that for a large portion of LMXBs some kind of correlation between the disk and the jet does exist. Furthermore, jets are likely launched within hundreds of gravitational radii from the compact object (Gandhi et al. 2017), which is the same region where X-ray originates. One of best ways to explore this connection is investigating whether the radio (jet dominated) and X-ray (accretion dominated) luminosity of these systems are somehow correlated creating **radio-X-ray $L_R - L_X$ luminosity** diagrams. In the last two decades, multi-wavelength monitoring campaigns on primarily BHs provided a wealth of data and the $L_R - L_X$ is updated constantly[12] for BH-only (the most recently publication, to my knowledge, in Bassi et al. 2019, Fig. 7) or including also NS LMXBs (Gallo et al. 2018). In such diagrams, BH XRBs tend to populate two branches $L_R \propto L_X^{\beta}$ spanning at least three orders of magnitude in X-ray luminosity: with $\beta \sim 0.6$ for the "radio loud" systems and $\beta \sim 1.4$ for the "radio quiet" systems (see, e.g. Corbel et al. 2013). Such behaviour has been proposed to originate in different physical properties in the accretion flow (Coriat et al. 2011) or in the jet (Espinasse and Fender 2018) over the two branches. A similar dichotomy can be found in NS XRBs, but the distribution appears more scattered and harder to interpret (Tetarenko et al. 2016). Alternatively, Gallo et al. (2018) proposed a single-track population for both BH and NS XRBs but with different values of β, i.e. the formers with $\beta \sim 0.7$ and the latters with $\beta \sim 0.4$. Generally jets in NSs seem to be less radio-loud than in BHs, i.e. of a factor of ~ 30 at similar X-ray flux levels (Fender and Kuulkers 2001; Migliari et al. 2003; Tudor et al. 2017; Gallo et al. 2018). It is unclear whether this observational evidence implies that the jet power is simply lower in NS than in BH systems or rather that the mass of the compact object, the spin (see, e.g. Migliari et al. 2011) or the radiative efficiency, e.g., play some role (Körding et al. 2006). An attempt of connecting the "radio loudness" with the spin has been made by Migliari et al. (2011).
The accretion-ejection coupling, as well as the physical properties of jets, will be further explored in Chapters 5 and 6.

2.7.2 Transient sources and the q-diagram

As discussed in Section 2.6, XRBs display different spectral states where the accretion flow behaves differently in terms of optical and geometrical depth as well as spectral shape and X-ray luminosity. In this section I also defined the main form of outflows characterizing each state, i.e. winds in the soft state and jets in hard and intermediate state. Having at this point an accretion/ejection

[12]The largest publicly available database of X-ray binary X-ray/radio observations is consultable at https://github.com/bersavosh/XRB-LrLx_pub

identikit for each spectral state the next step is to illustrate how systems evolve through them. First of all, as far as I know most XRBs are not always *active* but they usually spend most of their lifetime in a state of faint X-ray luminosity, called **quiescence**, i.e. $L_X \lesssim 10^{34}$ erg s^{-1} for NS LMXBs and $L_X \lesssim 10^{33}$ erg s^{-1} for BH XRBs, during which accretion is likely not active, with only sporadic episodes of variable duration of X-ray activity, called **outbursts**. Systems which switch between quiescence and outbursts are called **transients**. The origin of such behaviour is explained by the theory of the so-called **Disk Instability Model** or DIM (see, for a review, Lasota 2001). According to the DIM, steady mass-transfer from the companion builds up a cold, neutral and quiescent disk, where however even a small rise in temperature in an annulus can increase the opacity and the ionization to such an extent that a heating wave propagates through the disk, triggering the outburst. Unless the outer radius is kept sufficiently hot, i.e. if the mass-accretion rate is higher than the mass-transfer rate, the disk would tend to cool down again and decay to the original quiescent state. All BH XRBs are transients (Remillard and McClintock 2006) while NS LMXBs can be transients or persistents without an evident trend[13].

When transients rise from their long quiescence sleep, their spectral evolution follows (almost always) a specific path: the system will move from quiescence to hard state (i) in a rise of luminosity of several orders of magnitude to go then to an intermediate state (ii) and then to a soft state (iii) at almost the same bolometric luminosity. Luminosity will then decrease and the source will do the same transition backwards, then through intermediate (iv) and hard state (v) again but at a lower luminosity. This typical behaviour of LMXBs of transition from hard-to-soft and from-soft-to-hard at different luminosity is called **hysteresis** (Miyamoto et al. 1995; Zdziarski et al. 2004). In a hardness-intensity diagram (HID), i.e. where the count-rate or flux is plotted vs. the ratio between a hard and a soft X-rays energy band, the outburst cycle would indeed form the so-called **q-diagram** (see, e.g. Homan et al. 2001; Belloni et al. 2006), which is always run anti-clockwise. While the accretion flow and their spectral shape change over the cycle, its ejection properties change as well: hard and intermediate state are associated to a radio-emitting jet, which disappears in the soft state and then reappears in the backwards transition, when the system crosses the so-called "jet line" (Homan and Belloni 2005; Fender et al. 2005).

A similar hysteretical loop is found studying the relation of the intensity with the X-ray aperiodic variability in root-mean-square (rms)-intensity diagram (RID) (Muñoz-Darias et al. 2011). Indeed, hardness and variability are proportional, as most of the variability is likely originating in the hot electron corona (see, e.g. Done et al. 2007). Furthermore, the observation of **Quasi-Periodic Oscillations** (QPOs) plays a crucial role in identifying spectral states in the loop. I will go back to this topic in the following Section.

Hysteretical loops are observed in most atolls as well, for both transient and persistent LMXBs, which run the q-diagram in loop. However, as highlighted by Muñoz-Darias et al. (2014), some differences are found (see Fig. 2.7-2.8), e.g. diagonal instaed than horizontal transitions, hard states not as variable as the analogous states in BH binaries and faster transitions. Interestingly, all of them could be related to the emission from the hot NS surface as an additional cooling mechanism for the corona.

While the pattern described above is followed by the majority of XRBs, some BH XRBs displayed an incomplete cycle, being never able to reach the soft state or even the hard-intermediate state (see, e.g. Ferrigno et al. 2012; Del Santo et al. 2016; Bassi et al. 2019). These broken outbursts have been called **failed outbursts**. The physical origin of such variety of outburst behaviour, as well as

[13] Usually, NS LMXBs have smaller orbital periods than BH XRBs and therefore smaller disks, which are easier to keep in outburst for long periods (Done et al. 2007).

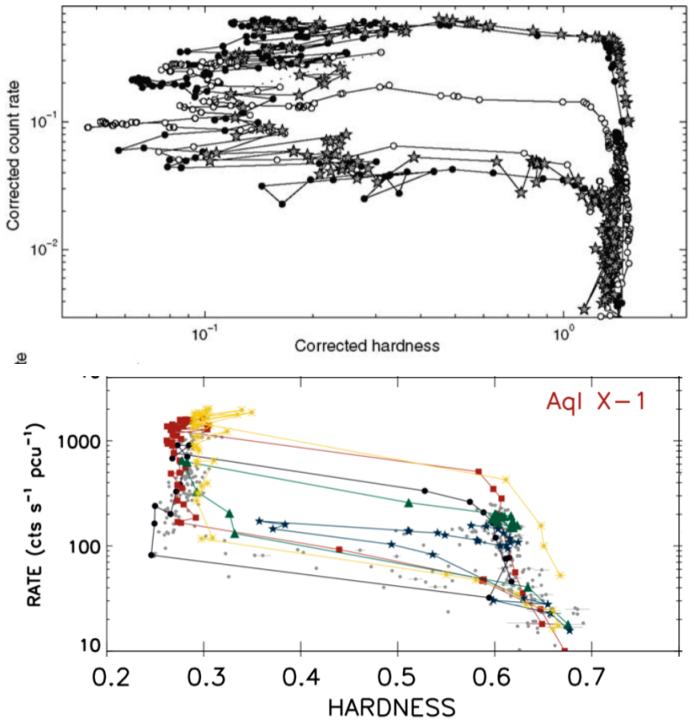

FIGURE 2.7: Example of HID showing a hysteretical loop for the BH LMXB GX 339-4 (top, Belloni 2010) and the NS LMXB Aql X-1 (bottom, Muñoz-Darias et al. 2014).

the origin for the *canonical* outbursts, is still unclear. I will return to the topic in Chapter 7.

2.8 Timing properties

As apparent in the RID diagram, spectral hardness and variability are usually interconnected and the combined study of both can give a clearer picture of the extreme physics in the accretion flow. The study of periodic and aperiodic variability is usually referred to as **timing analysis** (see, for a review, e.g. Gilfanov 2010) and it is based on the analysis of **Power Density Spectra** (PDS). In a PDS the power, i.e. meant as amplitude of variability, received from a system over a certain (short) time-scale is decomposed for Fourier frequency, in a way that allows us to individuate any periodicity in the signal and also the main noise phenomena. More in detail, if a source is observed for a time interval Δt, divided into N time segments, the **Fast Fourier Transform** can be defined as (van der Klis 1989):

$$X_j = \sum_{k=0}^{N-1} x_k e^{2\pi jk/N}, j = [-(N/2), ..., (N/2)-1] \tag{2.18}$$

with x_i the number of counts in the i-th interval and X_j is the Fourier coefficient corresponding to the frequency $\omega_j = 2\pi j/(N\Delta t)$. The squared values of X_j define the PSD, i.e. $P_j = A|X_j|^2$, with A scaling factor.

Each spectral state has its own, codified timing properties (see, e.g. van der Klis 2004). Hard state PDS for BH LMXBs are usually "flat" in $\nu P(\nu)$, exhibiting a band limited noise, with a low

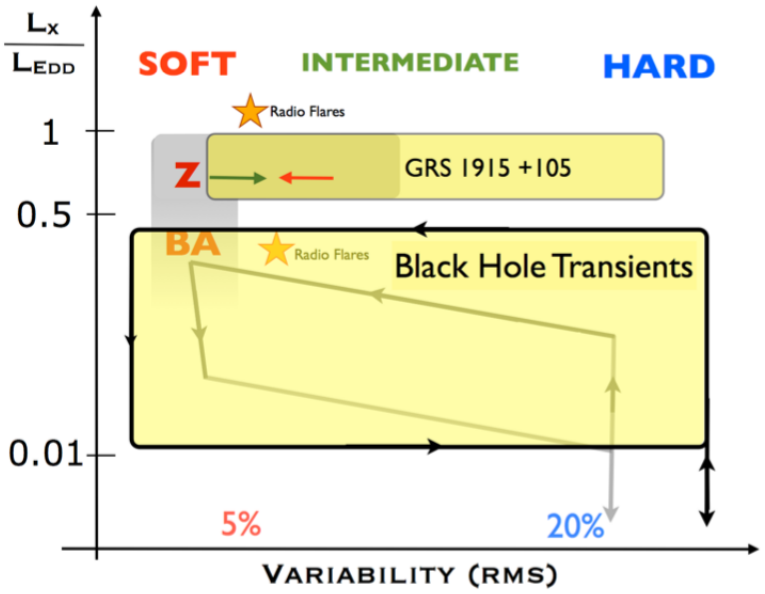

FIGURE 2.8: Sketch describing the qualitative behaviour of atolls (labelled as A), bright atolls (BA), Z sources (Z) and BH transients in RID (Muñoz-Darias et al. 2014).

frequency and a high frequency breaks. These PDS can be described as a superposition of (usually) 4-5 Lorentzians (Psaltis et al. 1999). Some atolls show very similar PDS (Belloni et al. 2002; Reig et al. 2004; van Straaten et al. 2005), in particular at low luminosity, while at higher luminosity the flat-topped noise sometimes disappear (see, e.g van Straaten et al. 2002, 2003), as shown in Figure 2.9. The systems which display flatter, BH-like PDS tend to populate a horizontal extension of the island state region in a color-color diagram, displaying thereby harder spectra with respect to sources in the usual Island State. This spectral-timing state has been sometimes classified as Extreme Island State (EIS) (Méndez and van der Klis 1997; van Straaten et al. 2003).

As both NS and BH LMXB transition from hard to soft state, the range of frequency spanned by the flat noise decreases as the Lorentzians shift to higher frequencies and eventually, i.e. around 5 Hz, they drop in amplitude and width (see, e.g. Pottschmidt et al. 2003; Kalemci et al. 2006). A series of PDS from the main spectral-timing states for an atoll is shown in Fig. 2.9.

PDS display also peaks, occurring at different frequencies and with varying widths (van der Klis 1989): these features are the aforementioned QPOs and they have been identified in both BH and NS XRBs (see, for a recent review, Ingram and Motta 2020). In BH systems QPOs are usually classified in High Frequency (with centroid frequency above 60 Hz) and Low Frequency (usually found below 30 Hz). A further distinction exists for Low Frequency QPOs in three main "species", labeled as type-A, B and C QPO (Casella et al. 2005). The main differences between these types are the range where their frequency can be found, their shape and most importantly, the spectral state they are found in: type A QPOs are found in the soft side of hard-to-soft transitions, type B QPOs are typical of soft-intermediate states while type C QPOs, the most common and studied, occur in hard or hard-intermediate state. A similar phenomenology is observed in NS systems, with the addition of the so-called *hectohertz* QPO and other very high frequency QPOs at kHz frequencies, which have never been observed in BH XRBs (van der Klis 2006). The physical origin of these features is

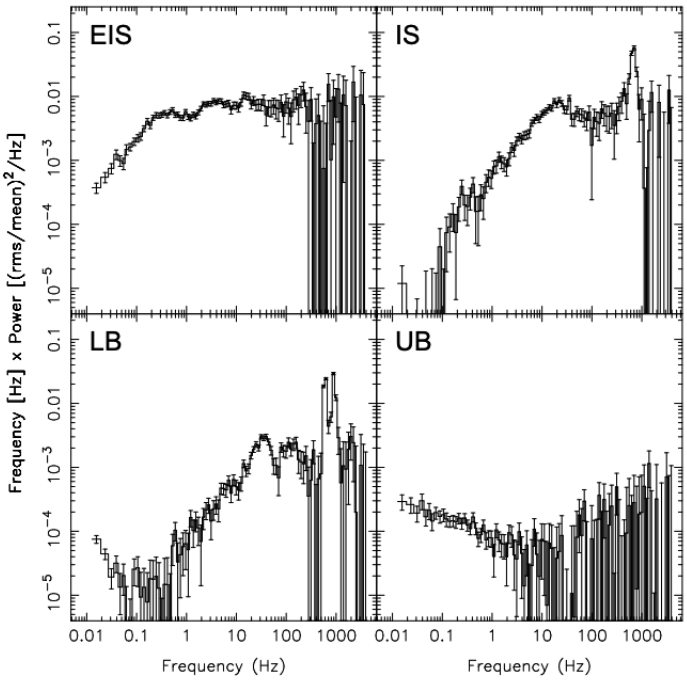

FIGURE 2.9: Power density spectrum of the atoll 4U 1608-52 in Extreme Island State (EIS), Island State (IS), Upper Banana (UB) and Lower Banana (LB) state, which could be associated to soft-intermediate and soft state (Wijnands et al. 2017b). For details on the methods of extraction of such PDS see Altamirano et al. (2008b).

still object of debate and each of them would deserve a separate Chapter; I refer again to Ingram and Motta (2020) for a discussion on the state-of-the-art theory of QPOs physics. An extensive discussion of variability in X-ray binaries is beyond the scopes of this thesis, but it is noteworthy that such an evolution of the timing properties can be explained in the framework of the disk truncation model: if the characteristic frequencies of the Lorentzians are used to describe the PDS are assumed to be linked to some specific radius in the accretion disk, the evolution of such frequencies during spectral transitions towards higher frequencies indicates roughly that also these radii are moving inwards, i.e. the whole accretion disk is approaching towards the ISCO.

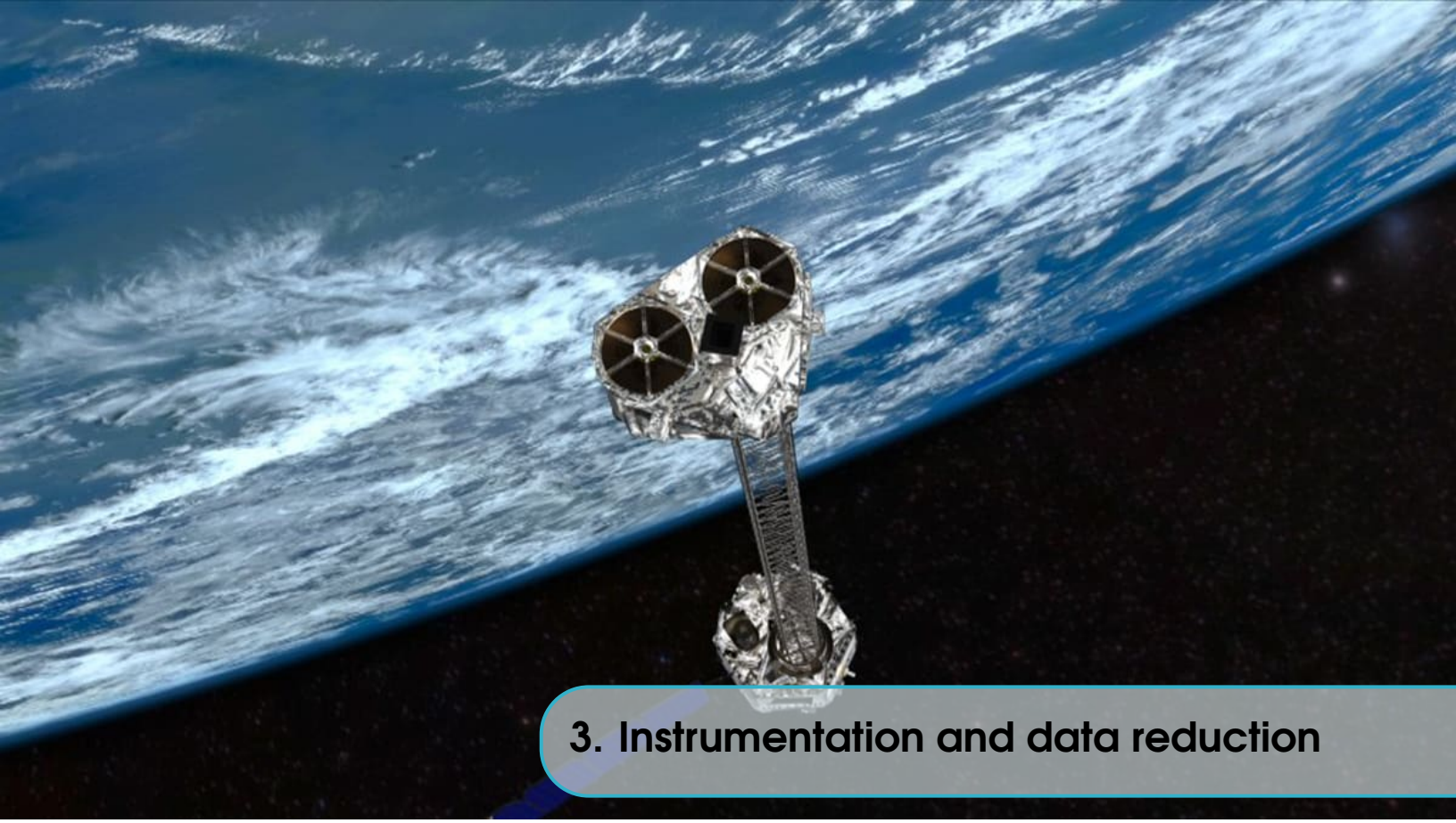

3. Instrumentation and data reduction

SUMMARY

In this thesis, I used data over a wide range of wavelengths, from radio to hard X-rays. In the first part of this chapter, I am giving first some basic information on the instruments which collected these data. Since I personally reduced the X-rays data collected by some of the listed telescopes, I am dedicating the second part of the chapter to the data reduction and analysis procedure followed for each instrument, with emphasis on strategies to avoid pile-up related issues and data oversampling.

3.1 High energy astrophysics instruments

The work carried out during my PhD and presented here exploits astronomical data over a wide range of wavelengths, i.e. from radio to hard X-rays. In Chapter 4, I take advantage of broadband X-ray spectra with data collected by *NuSTAR*, the Neil Gehrels *Swift* and by *INTEGRAL*. Data from the first two mentioned telescopes are also employed for the data analysis in Chapter 7. In Chapter 5, *Rossi X-ray Timing Explorer* (RXTE) data are used for some outbursts of the sources in the sample which were never reported in literature. Finally, Chapter 6 exploits a large multi-wavelength data set with observations collected in radio by the *Very Large Array*, in infrared by the *Spitzer* Space Telescope, in optical by *SMARTS* and in X-rays by *Swift* and *RXTE*. Details on these instruments will be given in the following two sections.

3.1.1 The Neils Gehrels Swift Observatory

The **Neil Gehrels Swift Observatory** (Gehrels et al. 2004), hereafter *Swift*, is a high energy telescope launched in 2004 and still in orbit, designed for hunting γ-ray bursts in the sky (see Fig. 3.1). By using three main instrument, the observatory is sensitive in a range of energies spanning from optical to soft γ-rays. The mission was developed from an international partnership led by USA, UK and Italy. Unlike other space mission, the name of this observatory is not an acronym, but it is instead due to the ability of the instrument to rapidly change its orientation or to *slew* in order to point towards a certain source in the sky. The telescope is placed on a low earth circular orbit, at an average altitude of about 600 km. Besides of γ-ray bursts, the unique design of *swift* makes it suitable to study all kind of transient phenomena in the high energy sky. The observatory is composed of three main instruments, which are presented in more detail in the following.

BAT The **Burst Alert Telescope** (BAT, Barthelmy et al. 2005) is a hard X-rays - soft γ-rays monitor, able to cover up to 80% of the whole sky every day. The energy range of the instrument spans from 15 up to 190 keV. Its characteristics make the telescope ideal to catch explosions in the sky and identify the source with an accuracy of 1-4 arcseconds. The instrument has also moderate spectral capabilities, i.e. with a $\sim$ 7 keV spectral resolution. BAT is a **coded mask** telescope. Indeed, hard X-ray telescopes cannot use mirrors to focus the radiation onto a detector as the typical soft X-rays telescope for the high energies involved. They instead use indirect imaging methods, e.g. through a mask made of opaque and transparent elements according to a specific pattern, which when hit by radiation casts a shadow onto the detector plane, where a *shadowgram* is produced. The shadowgram is then converted into a specific image of the sky.

XRT The **X-ray Telescope** ((XRT), Burrows et al. 2005) onboard *Swift* is an imaging spectrometer sensitive in the 0.2-10 keV energy range. It is designed to make prompt observations of transient sources individuated by the BAT monitor. The instrument is characterized by an effective area of 110 cm^2, a Field of View of 23.6$\times$23.6 arcmin and Full Width at Half Maximum (FMHM) energy resolution of about 0.3 keV at 5.9 keV. The XRT is extremely useful in determining with accuracy and rapidity the position of a source in the sky. It can operates in three different modes: Imaging Mode (IM), Windowed Timing mode (WT) and Photon Counting mode (PC). In WT mode the time resolution of the instrument is high, i.e. about 1.8 ms, and it is ideal for bright sources, i.e. fluxes up to 600 mCrab[1], while PC mode has a lower time resolution ($\sim$ 2.5 s) and is therefore preferred for fainter objects.

UVOT The **UV/Optical Telescope** (UVOT, Roming et al. 2005) is a 30 cm diameter modified Ritchey Chrétien telescope co-aligned with XRT, which provides optical/UV counterparts in the range 2-7 eV. The absence of atmospheric extinction, diffraction and background with respect to other optical telescopes make the UVOT particularly powerful. Seven broadband filters can be used, i.e. *v, b, u, uvw1, uvm2, uvw2* and *white*, with central wavelengths between 544 to 188 nm. The instrument is essential in following the optical/UV afterglow of γ-ray bursts.

3.1.2 NuSTAR

The **Nuclear Spectroscopic Telescope Array**, hereafter *NuSTAR* (Harrison et al. 2013), is a space-based X-ray telescope launched in 2012 and operating ever since. Its energy range is comprised

[1] 1 Crab is equivalent to 2.4×10^{-8} erg cm^{-2} s^{-1} in the 2-10 keV energy band.

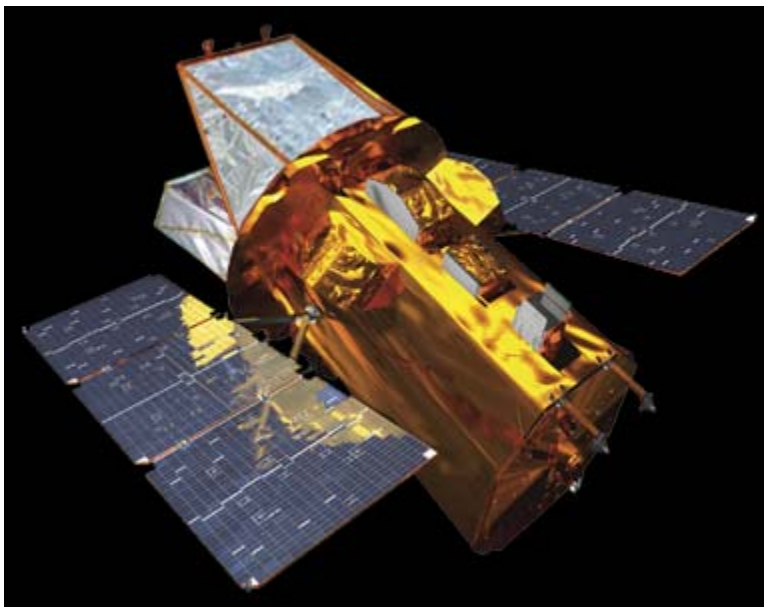

FIGURE 3.1: Sketch showing the design of the *Swift* observatory.

between 3 and 79 keV. It consists of two co-aligned X-ray optic units and two shielded detectors, connected by a 10 meters long mast deployed in space. The optic units are labelled **Focal Plane Mirror** (FPM) A and B. The telescope has a high (almost 1000 cm^2 at $\sim$10 keV) effective area, especially in the region beyond 10 keV, where most of the other operating X-ray telescopes are weakly or not sensitive at all. The energy resolution is moderate, i.e. between 0.4 keV (at 6 keV) and 0.9 keV (at 60 keV).

3.1.3 INTEGRAL

The **International Gamma-Ray Astrophysics Laboratory** (*INTEGRAL*, Winkler et al. 2003) is a X-rays-γ-rays ESA telescope launched in 2002 and operating ever since. The observatory moves on a very eccentric orbit in 72 hours, at an altitude comprised between 9000 and 155000 km from Earth. The energy range the instrument is sensitive to goes from 3 keV to about 10 MeV. The instrument carries onboard four instrument, each characterized by different capabilities and aims. Two of them are the main X-rays/γ-rays instruments and two monitors operating over different wavelength domains. The former instruments are **SPectrometer on INTEGRAL** or SPI (Vedrenne et al. 2003) and the **Imager onboard INTEGRAL Satellite** or IBIS (Ubertini et al. 2003). SPI enables high resolution spectroscopy over a wide energy range, i.e. from 20 keV to 8 MeV, with a spectral resolution of 2.5 keV (FWHM) at 1.33 MeV. While SPI has poor imaging capabilities, i.e. spatial resolution of about 2.5°, IBIS is designed to perform fine imaging, with spatial resolution about 1'-2'. The instrument is sensitive between 15 keV and 10 MeV and has a spectral resolution of 10 keV at about 1 MeV. The cooperation between the two main instruments guarantees fine imaging and spectroscopy of γ-ray sources in an energy domain crucial to e.g. locate exactly the cut-off energy of Comptonization spectra in XRBs. One X-ray and one optical monitor onboard INTEGRAL support SPI and IBIS with complementary observations at lower energies. The monitors are the **Joint European X-ray Monitor** (JEM-X, Lund et al. 2003), sensitive between 3 and 35 keV, and the **Optical Monitoring Camera** (OMC, Mas-Hesse et al. 2003), operating in the energy range

500-600 nm. Both monitors play a central role in detecting and identifying γ-ray sources. JEM-X is in turn composed of two identical instruments, JEM-X1 and JEM-X2, and is characterized by a spectral resolution of 1.3 keV at 10 keV. All of the instruments onboard INTEGRAL are coded mask telescopes (see Subsection 3.1.1).

3.1.4 Rossi X-ray Timing Explorer

The **Rossi X-ray Timing Explorer** (Bradt et al. 1993), *RXTE* hereafter, was an X-ray satellite which operated for 16 years, i.e. from 1995 to 2012. It flied on a low Earth orbit at about 500 km altitude. Exploiting three different instruments, the mission allowed data in the range 2-200 keV. These instruments were the **All-Sky Monitor** (ASM, energy range: 2-12 keV), the **Proportional Counter Array** (PCA, energy range: 2-60 keV) and the **High Energy X-ray Timing Experiment** (HEXTE, energy range: 15-250 keV). The ASM provided the first monitoring of the whole X-ray sky, completing a whole covering of the 80% of the sky in 90 min. The instrument paved the way to the study of transient phenomena like, e.g. the onset of outbursts or type-I X-ray bursts from XRBs and served as a precursor of modern all-sky monitors like BAT (Subsection 3.1.1) and the Monitor of All-Sky X-ray Image, MAXI. PCA was an array of five proportional counters, characterized by the second[2] highest time resolution ever achieved, i.e. 1 μs and a spectral resolution of about 18% at 6 keV. Finally HEXTE was characterized by a 15% energy resolution and a 8 μs time resolution. The advent of RXTE made, together with *BeppoSAX*, a deeper understanding of X-ray binaries possible and allowed proper timing studies of these sources for the first time in the history of X-ray astronomy.

3.2 Instruments for multi-wavelength studies

3.2.1 Very Large Array

The **Karl G. Jansky Very Large Array** (*VLA*, see Fig. 3.2) is a radio astronomy observatory. It consists of a complex of 27 parabolic antennas, 25-m diameter, functioning as a radio interferometer. The observatory was built between 1973 and 1980 on the Plains of San Agustin in south-western New Mexico (USA), 2124 m above the sea level. The observatory covers a quite wide range of frequencies, comprised between 74 MHz and 50 GHz. The angular resolution that can be reached is between 0.2 and 0.04 arcseconds. The key science goals include the study of jets from galactic and extra-galactic black holes, supernova remnants, γ-ray burst, the mapping of the gas and molecular clouds in the interstellar medium and even the search for communication signals coming from advanced extra-terrestrial civilizations[3].

3.2.2 Spitzer

The **Spitzer Space Telescope**, formerly the Space Infrared Telescope Facility (SIRTF), was an infrared space telescope, active between 2003 and 2020, moving on a heliocentric orbit. The telescope was composed of a 85 cm diameter primary mirror and three main instruments onboard: the **Infrared Array Camera** (IRAC), the **Infrared Spectrograph** (IRS) and the **Multiband Imaging Photometer for Spitzer** (MIPS). IRAC was an infrared camera which is sensitive at four wavelengths: 3.6 μm, 4.5 μm, 5.8 μm and 8 μm. IRS was employed for spectroscopy in the ranges 5.3-13 μm, 10-19.5μ, 14-40 μm and 19-37 μm. Finally MIPS is a photometer made also of channels

[2]The record was held by PCA before the launching of *NICER* in 2017, which has a time resolution of 300 ns.

[3]The *VLA* is indeed quite famous in pop culture as it was featured, among other movies, in the 1997 sci-fi film *Contact*.

FIGURE 3.2: A close view of the antennas forming the *VLA*, *Credits: Wikipedia*

operating at selected wavelengths, but reaching lower energies, i.e. down to 160 μm. The mission was designed to study a wide variety of targets, from young stellar objects to solar and extra-solar planets, from nebulae to other galaxies. The instrument recently enabled the discovery of five out of the seven exoplanets forming the planetary systems of rocky Earth-like planets orbiting around the star *TRAPPIST-1* (Gillon et al. 2016).

3.2.3 SMARTS

The **Small & Moderate Aperture Research Telescope System** (*SMARTS*, see Fig. 3.3) is a system of four optical telescopes led by an international open consortium and located at Cerro-Tololo, Chile. The four small telescopes operated by the consortium have different apertures, i.e. 0.9 m, 1.0 m, 1.3 m and 1.5 m. These telescopes are equipped with other instruments, e.g. the 1.3m telescope uses indeed a dual-channel optical/IR camera which enables simultaneous observations in optical and infrared selected bands, i.e. covering a wavelength region from 2 μm down to 360 nm. The 1.5m telescope is instead equipped with *CHIRON*, a high resolution spectrometer covering 410-870 nm.

3.3 Data reduction procedure

In this thesis I used data from the telescopes enlisted in the previous two sections and I personally reduced X-rays data from XRT, *NuSTAR* and JEM-X onboard *INTEGRAL*. In the following I report on the recipe used for these data. I am also including the procedure used for BAT data, even if the analysis was led by my collaborator in IASF Palermo A. Segreto.

XRT data reduction recipe The raw telemetry data are first handled and converted into FITS (Flexible Image Transport System) by the *Swift Data Center*. These data are then publicly available

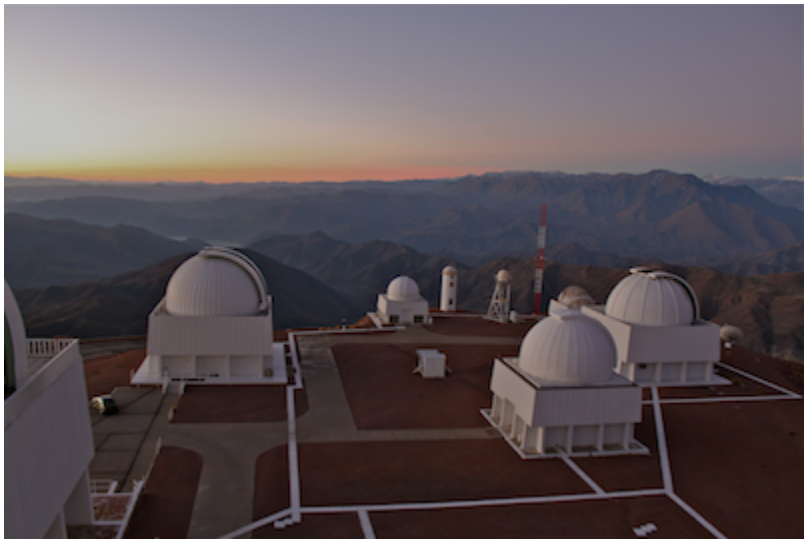

FIGURE 3.3: Panoramic view of the site of *SMARTS* at sunset. *Credits: SMARTS consortium*

in the High Energy Astrophysics Science Archive Research Center (HEASARC) public web archive[4]. Data retrieved from the archive have to be reprocessed using the task XRTPIPELINE, which is included in the software package HEASOFT. For the analysis performed in this thesis I used the v. 6.25 of HEASOFT in Chapter 4, while I used v. 6.26.1 in Chapter 7. The task is aimed at cleaning the data, i.e. removing all the bad events which are not attributed to source detection, reconstructing the true events and converting the recorded pulse heights into physical units. In XRTPIPELINE it is possible to add a further filtering for the *grade* of the data. Data with a low grade, i.e. 0, have been already corrected for spectral distortions and, partially, for pile-up (see subsection 3.3.1). I chose indeed grade '0', as also recommended by the *Swift* team to perform fine spectral analysis of data taken in WT mode. At this stage one can also selects the time interval(s) of the observation which have to be analyzed by specifying the so-called **Good Time Intervals** (GTIs). This step is particularly important if the user desires to remove a flare or a type-I X-ray burst or otherwise the user wants *only* the type-I X-ray burst. The output files are finally recalibrated according to the employed CALDB files, also publicly retrievable[5]. In the work carried on I have always kept the CALDB updated to the latest available version.

The next step consists in building science products, such as spectra and light curves, by means of the XRTPRODUCTS task. The task acts on the output files produced in the previous file but it needs a source and a background region to filter the event files. In order to do that, I used the SAOIMAGEDS9 software to read the event files and create these regions. The choice for the source region depends critically on evaluating the impact of pile-up on the data. If the event file is not affected by a critical level of pile-up[6], I chose a circular region of radius 20 pixels ($\sim 47''$), otherwise I chose an annular region instead with inner radius depending on the estimated pile-up level. The background region was instead taken using the same size and shape of the source region, but on a location sufficiently far away from the Point Spread Function (PSF) of the source.

Once a source and background region have been created, I launch XRTPRODUCTS which builds

[4] https://heasarc.gsfc.nasa.gov/docs/archive.html

[5] https://heasarc.gsfc.nasa.gov/docs/heasarc/caldb/caldb_intro.html

[6] This issue is addressed specifically in Subsection 3.3.1, where I give further details on the choice for the source region.

spectra, light curves and the corresponding **Auxiliary Response Files** (ARF), a file which contains the combined information on the effective area and quantum efficiency per energy of the detector. In order to build the observed spectrum a **Redistribution Matrix File** (RMF) is also required, to associate to each instrumental channel an energy bin and simulate the response of the detector. In this work I used the RMF value included in the CALDB folder.
The final step consists in grouping the spectra. This procedure is discussed in Subsection 3.3.2.

BAT data reduction recipe The BAT survey data were also retrieved from the HEASARC public archive. The downloaded data were processed using `BAT-IMAGER` software (Segreto et al. 2010). This code, dedicated to the processing of coded mask instrument data, computes all-sky maps and, for each detected source, produces light curves and spectra. Spectra were extracted with logarithmic binning and official BAT spectral redistribution matrix was used as well.

NuSTAR data reduction recipe The procedure described here is very similar to the one followed for XRT. Raw data from FPMA were reduced using the standard NUPIPELINE task, incorporated in HEASOFT. The main product of this step consists in event files. These files are analyzed with DS9 in order to isolate the source and the background region. *NuSTAR* data are, unlike XRT data, unaffected by pile-up, which interests X-ray data taken below 2 keV. I therefore used for both Chapter 4 and 7 a circular area of 110" centered at the coordinates of the sources. In order to take into account any background non-uniformity on the detector, I extracted the background spectra using four circles of 50" radii in different positions with negligible contamination from the source. Spectra, light curves, ARF and RMF files are then built by the routine NUPRODUCTS. The same procedure is applied to the data taken by FPMB. However, I did not sum the two final spectra but rather fitted them together by leaving a floating cross-normalization constant as suggested by the *NuSTAR* team for bright sources[7].

JEM-X data reduction recipe *INTEGRAL* data are publicly available in the Integral Science Data Center (ISDC) archive[8]. Data are grouped by *Science Windows* (SW), which are bits of activity, i.e. pointings or slews, of the observatory. Each SW consists in raw science data and housekeeping data, which contain information relative to the instruments. An observation is usually made of a number of SWs. The rest of the analysis is then performed launching the *INTEGRAL* data analysis software, i.e. the Off-line Scientific Analysis Software (`OSA`) v11. The software performs a series of tasks going through several steps, called *Analysis levels*, up to a final step defined by the user. In my work, I need to create spectra and lightcurves, so that I run `OSA` up to the light curve creation level. Setting this as the final step the software proceeds first in a correction of the raw data from instrumental effects, a filtering of the GTIs (if any), a computation of the dead time[9] and finally a setting up of the energy bins. At this point sky images are created and the software searches for significant sources by comparison with (usually) an ISDC reference catalogue. At this point the source positions and fluxes are derived and used to build a spectrum, a lightcurve and a response file.

[7] On the FAQ page, issue 19: `https://heasarc.gsfc.nasa.gov/docs/nustar/nustar_faq.html`
[8] `https://www.isdc.unige.ch/integral/archive`
[9] The time during which the instrument was not capable to register the incoming photons.

3.3.1 Pile-up issues

One of the main issues in using XRT and other sensitive X-ray detectors is the possibility that the collected data are affected by the phenomenon of **pile-up**, that results when the simultaneous, i.e. within the read-out time, arrival of two or more photons in a pixel, or two nearby pixels, is registered as a single event, a photon with energy equal to the sum of the energies of the single incoming photons. Therefore, pile-up results in a distortion of the energy spectrum and, at the same time, in an underestimate of the correct counting rate and energy of the detected photons. The evaluation of the level of pile-up is therefore crucial. XRT data are mainly affected by this issue when taken in PC mode, but for bright sources, i.e. above 600 mCrab, a pile-up treatment becomes necessary also for observations taken in WT mode. In particular, the pile-up impact is considered negligible for count-rates below about 100 cts/s in WT mode (Romano et al. 2006). In this case a circular region can be used for the source extraction. If, on the other hand, the count-rate is above this threshold, we need to remove a central fraction of the PSF, replacing therefore a circular region with an annulus. The inner radius of the annulus depends in turn also on the estimated count-rate. In this thesis, I followed the guidelines of the *Swift*/XRT team, i.e. https://heasarc.gsfc.nasa.gov/lheasoft/ftools/headas/xrtgrblc.html.

3.3.2 Grouping spectra

The final step in data analysis before obtaining spectra which are ready to be exploited consists in grouping, i.e. rebinning the spectra in order to have a minimum of a certain number of counts per channel. Indeed the spectrum can be considered as an histogram containing the number of couts per channel, which is connected to an energy bin by means of the response. The size of the channel is regulated in this step. Channels too wide risk to smooth out the spectral features I want to analyze, resulting therefore in a loss of information. On the other hand a sampling too fine risks to distribute a number of counts per bin too small for allowing statistical tests, such as the χ^2 statistics. Furthermore, even a sampling which allows the use of e.g. χ^2 statistics, can still results in an **oversampling** of the energy response (see Appendix C in Kaastra and Bleeker 2016, for an example of this effect). Ideally, the grouping should be chosen in order to have a spacing between the bins comparable to the spectral resolution of the instrument (see, e.g. Lanzuisi et al. 2016; Basak et al. 2017). Indeed, I chose a grouping which guarantees a minimum of 150 counts per bins for *NuSTAR* 3-78 keV spectra in Ch. 4, while a routine[10] for optimal binning based on the instrumental resolution and based on Kaastra and Bleeker (2016) was used for *NuSTAR* spectra in Ch. 7, taken between 5 and 78 keV. Also XRT data (0.8-10 keV) have been grouped in order to avoid oversample, leaving a minimum of 100 counts per bin in Ch. 4 and a minimum of 150 counts per bin in Ch. 7.

[10] C. Ferrigno (ISDC Geneva), *private communication*.

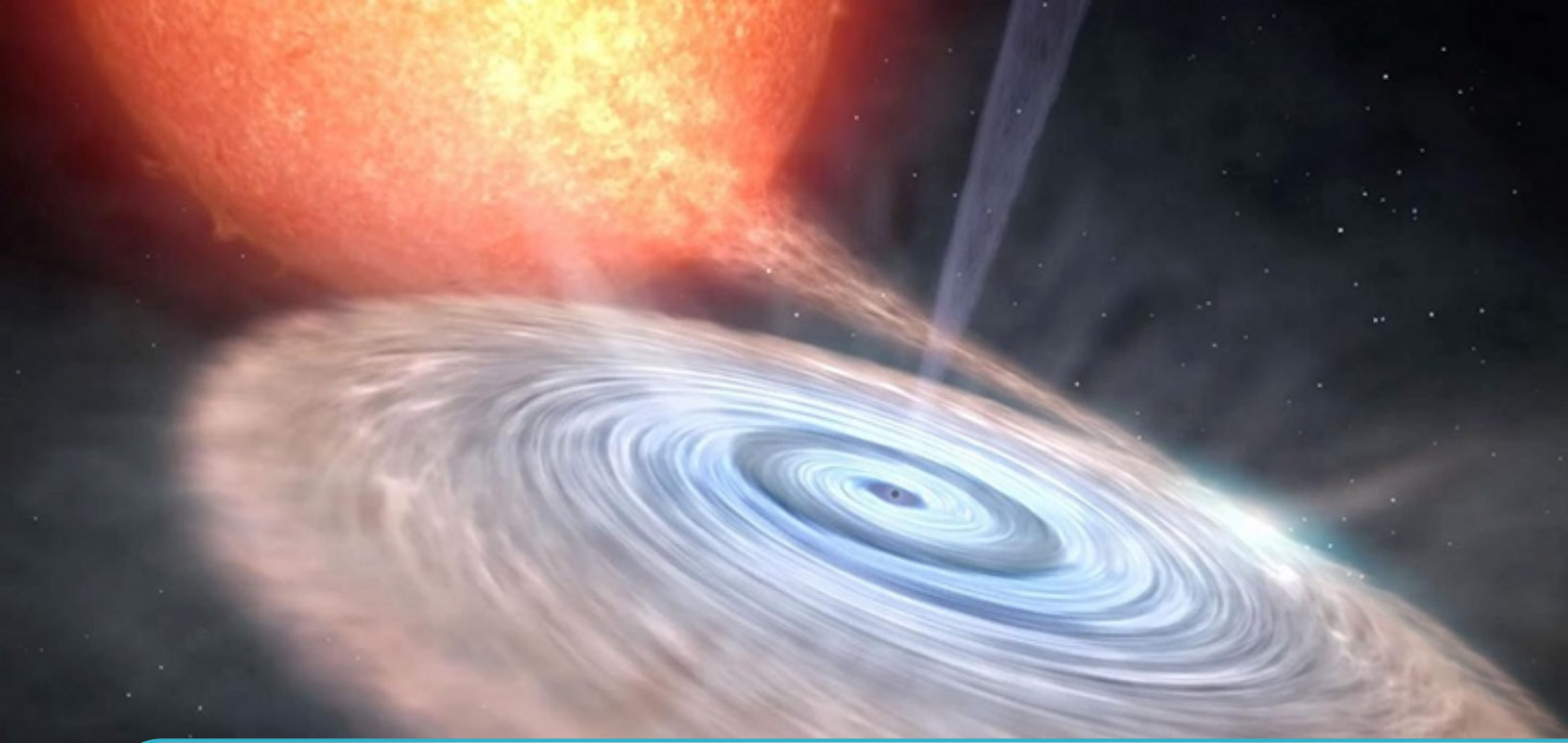

4. New insigths on the puzzling NS LMXB 1RXS J180408.9-342058

SUMMARY

1RXS J180408.9–342058 is a NS LMXB which shows X-ray activity at very different mass-accretion regimes, from very faint to almost the Eddington luminosity. In this work, I present a comprehensive X-ray study of this source using data from the Neil Gehrels Swift Observatory, NuSTAR and INTEGRAL/JEM-X. In order to follow the spectral evolution, I analysed the 2015 outburst using Swift data and three NuSTAR observations. Besides the canonical hard and soft spectral states, I identified the rarely observed intermediate state. This was witnessed by the appeareance of the accretion disk emission in the spectrum (at $kT_{\rm disk}$ ∼0.7 keV) and the simultaneous cooling of the hot corona. In addition, I also unveiled a hard tail above 30 keV in this state. In the hard state, a thermal Comptonization model with two seed photons populations ($kT_{\rm s,1} \sim 1.5$ keV and $kT_{\rm s,2} \sim 0.4$ keV, respectively) and a hot Comptonising plasma, represents the physically best motivated scenario to describe the data. I also estimated a reflection fraction below 20% in all states, while no constraints on the inclination and only lower limits on the inner disk radius could be inferred. Finally, I studied a number of type-I X-ray bursts displayed from the source, one of them at the Eddington limit (observed with JEM-X). Their characteristics, combined with the clocked behaviour observed during the intermediate state, point to H/He composition for the accreted material, which makes unlikely the proposed helium dwarf nature for the companion.

4.1 The "inbetweeners": "faint" and "very faint" X-ray binaries

Transient LMXBs are usually thought as systems showing two different accretion regimes, namely the outburst and the quiescence. The luminosity (and presumably mass accretion rate) differ

of at least three orders of magnitude in the two regimes. However nature is very rarely black and white and indeed, aside of these two accretion regimes, a third, less known regime seems to exist at intermediate luminosities between outburst and quiescence. The systems in this class, called **Very Faint X-ray Transients** (VFXTs), are one the main topics of this chapter.
VFXTs are a peculiar class of transients showing considerably faint outbursts, with peak luminosities within 10^{34} and a few 10^{36} erg s^{-1} (in the 2-10 keV; Muno et al. 2005; Wijnands et al. 2006). A consistent number of this non-homogeneous class of transients have been classified as Low Mass X-ray Binaries with neutron stars (e.g. Degenaar and Wijnands 2009, 2010; Armas Padilla et al. 2013; van den Eijnden et al. 2018a). These systems have been observed accreting at very low X-ray luminosities even over relatively long (months or years) time-scales (e.g. Del Santo et al. 2007; in't Zand et al. 2009; Degenaar et al. 2017). This behavior is associated with very low mass-accretion rate, although the exact physical origin is still an object of debate. According to some of the most common theories, at least a number of VFXTs could be Ultra-Compact X-ray Binaries (UCXB) i.e. binaries with orbital periods below 1 hr, with physically small (and faint) accretion disks (King and Wijnands 2006; in't Zand et al. 2007; Hameury and Lasota 2016). Other authors suggested accretion via stellar wind and the existence of a "period gap" as in CVs (Maccarone and Patruno 2013), planetary or brown dwarf companion stars (King and Wijnands 2006) or even inclination angle related effects (Muno et al. 2005; King and Wijnands 2006). Finally, some authors proposed that part of the mass transferred from the companion could be removed from the system before being accreted due to a magnetic **propeller effect** (Heinke et al. 2015; Degenaar et al. 2017, see also Subsection 5.1.1), reducing this way the amount of gravitational energy available to be converted in radiation.

A systematic study of these puzzling and fascinating objects is quite challenging, as none of the current (BAT onboard *Swift* and *MAXI*) or past (ASM oboard *RXTE*) X-ray all-sky monitors were/are sensitive enough to observe these systems. Only pointed observations with telescopes like *Swift*/XRT or *XMM-Newton* could in principle allow for a detection of these systems in a "faint" outburst. However, these systems are transients and finding them in (faint) outbursts via pointed observations turns out to be a matter of fortune.
A subgroup of VFXTs is represented by the so-called "burst-only" sources. This class of NS-LMXBs were discovered from the long monitoring of the Galactic center with *BeppoSAX* in the early 2000s (Cocchi et al. 2001; Cornelisse et al. 2002). Due to their low persistent luminosity, these sources were detected only during type-I X-ray burst events (see Section 4.2). Bursts are ignited by matter accretion, therefore these systems were accreting but at a luminosity lower than the detection threshold of the instrument which caught the burst. Some of the "burst-only" systems, e.g. SAX J1806.5–2215, SAX J1753.5–2349, 1RXS J180408.9–342058, have been also episodically displayed luminous outburst with peak luminosity above 10^{36} erg s^{-1} . These sources, observed at both "very faint" luminosity and standard luminosity regimes, are defined as "hybrid" VFXTs (see, e.g. Degenaar and Wijnands 2009; Del Santo et al. 2010, 2011).

4.2 Type-I X-ray Bursts

Some LMXBs sources display sudden and violent rises of X-ray luminosity, followed by a quasi-exponential decay in very short time-scales, e.g. from seconds to minutes: these phenomena are called **type-I X-ray bursts** (Grindlay and Heise 1975), bursts hereafter. It is nowadays well established that type-I X-ray bursts are thermonuclear explosions which occur on the NS surface

when the layer of matter piled up onto it undergoes unstable ignition (see, for a recent review, Galloway and Keek 2017). The strongest clue supporting this interpretation comes once again from the spectra; during the burst, the spectrum of the source is drastically changed and can be satisfactorily described by a blackbody of temperature $kT \sim 3$ keV coming from a spherical region of about 10 km radius. Subsequently, type-I X-ray bursts are a strong signature for the NS nature of the primary: indeed BHs do not have a solid surface, while WDs are not as compact as NSs.
The ignition of H-rich (or mixed H/He) material originates bursts lasting ~ 100 s and characterized by the typical "Fast Rise Exponential Decay" profile. Otherwise, if the material is H-poor, bursts are usually shorter, i.e. 10-s long flashes (in't Zand et al. 2005). Hydrogen burns more slowly with respect to helium or carbon, as it requires beta decays which undergo longer time-scales. An exception is represented by the case of the "superbursts", which last from hours to half a day (see, e.g. Strohmayer and Markwardt 2002) and are likely ignited by the unstable burning of C deeper in the neutron star envelope (Cumming and Bildsten 2001; Wijnands et al. 2001).
Bursts can therefore provide valuable information on the nature of the accretor and, from the composition of the accreted material, on the donor. The timing of the burst can in principle reveal also the spin of the NS through the identification of **burst oscillations** (Strohmayer et al. 1996). Burst oscillations have been detected in only 17 sources (Galloway and Keek 2017) so far and are usually seen at high accretion rates (see, e.g. Ootes et al. 2017) and during the rise of the burst. Being able to detect more and more oscillations represents one of the most important challenges of burst science for the future X-ray missions.

4.2.1 Photospheric Radius Expansion

During the burst, the X-ray luminosity increases by several orders of magnitude and sometimes can even reach the Eddington limit. When the limit is reached, the NS photosphere is temporarily lifted up by its own radiation pressure, a phase called **Photospheric Radius Expansion** (PRE). Knowing that the system reached the Eddington limit, it is possible to compare their luminosity with the measured flux to estimate the distance (Kuulkers et al. 2003). This is likely the most common method to constrain the distance of NS LMXB (Galloway et al. 2008), and it has been vastly employed to NS-LMXBs in the past. However, the method suffers from systematic uncertainties. Indeed, not all the bursts showing PRE from one source reach the same peak flux, but they rather scatter around a mean value, with variations usually within 15% (Kuulkers et al. 2003; Galloway et al. 2003, 2008). Furthermore, without precise information on the mass and the radius of the NS or on its atmospheric composition, the value used for the Eddington luminosity may not be accurate for the source.
With these caveats in mind, the study of PRE bursts remains sometimes the only way to obtain even rough estimates of the distance of NS LMXBs and, sometimes, of its mass and radius (Özel and Freire 2016): correctly identifying a PRE burst turns out to be therefore vital. A number of ways to catch a PRE phase in a burst exist. First of all, light curves of PRE bursts, when limited to soft X-rays, often show double peaks: when the burst reaches the Eddington limit, the photosphere radius $R_{\rm ph}$ expands and, as the luminosity has reached $L_{\rm Edd}$ and it is therefore fixed, its blackbody temperature $T_{\rm bb}$ is forced to decrease, since in this case $L_{\rm Edd} = 4\pi R_{\rm ph}^2 \sigma T_{\rm bb}^4$. This cooling would not be detectable in the bolometric light curve, but causes a sensible breakdown in a light curve limited to below 10 keV. A second peak would then appear when the photosphere halts the expansion and starts contracting back to its original size, giving to the burst its typical "double horn" shape (see Fig. 4.1, left panel). The same phenomenon can be observed performing **time-resolved spectroscopy**,

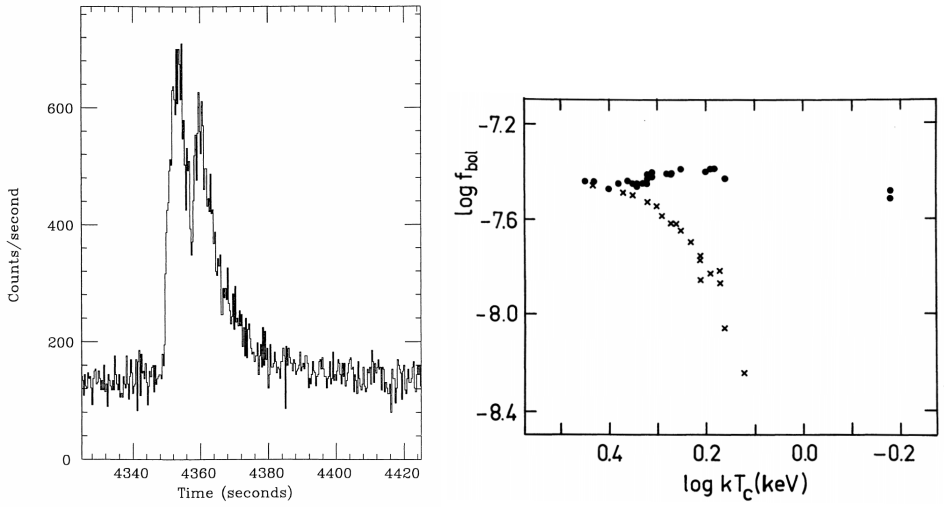

FIGURE 4.1: (*Left*) Example of a PRE type-I X-ray burst light curve exhibiting the typical double peak profile (Lewin et al. 1993). (*Right*) Flux-temperature diagram for a PRE type-I X-ray burst. In the plot dots indicate the expansion/contraction phase, while crosses are relative to the cooling track (van Paradijs et al. 1990).

i.e. modelling the spectrum of the system with a simple black body model at different moments of the burst and observing the evolution of the radius and the temperature. Finally, a third tool, less common but potentially useful, to infer a PRE phase in the burst can be identified in building a *bolometric flux vs. temperature* diagram (e.g. van Paradijs et al. 1990). In such diagrams, the saturation of the flux during the peak is witnessed by the $F_{\rm bol}$ values following an horizontal trend, the so-called "expansion track", during the peak. An example is reported in Fig. 4.1, right panel.

4.3 The puzzling case of the hybrid VFXT 1RXS J180408.9-342058

1RXS J180408.9–342058 (hereafter RX1804) was discovered by *ROSAT* in 1990 during the all-sky survey performed in the first half year of the mission (Voges et al. 1999). It was an unclassified X-ray source until 2012 April 16 when a burst was caught by JEM-X on board *INTEGRAL* and associated to the source (Chenevez et al. 2012). Thus, the source was classified as LMXB with NS showing a burst-only behaviour due to the very faint persistent luminosity (only an upper limit of 6 mCrab was inferred by JEM-X). Assuming that the burst reached the Eddington limit at the peak, Chenevez et al. (2012) estimated an upper limit to the distance of ∼5.8 kpc and to the persistent luminosity of roughly 10^{35} erg s^{-1} . From the analysis of the same burst, with a different method for the peak flux estimation, Chelovekov et al. (2017) derived an upper limit for the distance to the source of 9.7±1.6 kpc.

On January 2015, the Burst Alert Telescope (BAT) on board the Neil Gehrels *Swift* Observatory (hereafter *Swift*) detected the source at ∼40 mCrab (Krimm et al. 2015a), revealing RX1804 to be a "hybrid" VFXT. Then, a number of follow-up observations were triggered, i.e. with *MAXI/GSC* (Negoro et al. 2015), *Swift*/XRT (Krimm et al. 2015b) and *INTEGRAL* (Boissay et al. 2015), among the others. During the 4.5 months long outburst, the source exhibited both hard and soft states. Ludlam et al. (2016) performed a broad-band spectral analysis of the source between 0.45 and 50 keV using *NuSTAR* and *XMM-Newton* observations taken during the hard state. These authors modeled the reflection spectrum with RELXILL (García et al. 2014), which allowed them to estimate

an inclination $i \sim 18^\circ - 29^\circ$ and a strict upper limit on the inner disc radius (~ 22 km). Parikh et al. (2017) reported on unusual very hard spectra observed in three LMXBs with NS, including RX1804. In a number of XRT spectra (0.5-10 keV) they measured a very low value of the power-law photon index ($\Gamma \sim 1$), significantly lower than the typical spectral indices observed in these sources in the hard state ($\sim$1.5-2).
The soft state was studied by Degenaar et al. (2016) using *NuSTAR*, *Swift* and *Chandra* observations obtained around the X-ray peak of the outburst. From the study of the reflection component, the authors reported on a broad iron line, signature of a disk extending close to the NS. Using the reflection model REFLIONX, an inner disk radius lower than 17 km and an inclination of the system around 30° were inferred. Baglio et al. (2016) performed a detailed near-infrared/optical/UV study of the source, with the aim of classifying the companion star. The lack of H and He I emission lines was considered by these authors as an evidence for an out-of-the-main-sequence secondary star. However, the marginal detection of the He II line would indicate the presence of He in the disk, possibly related to a helium white dwarf nature of the companion. Under this hypothesis, the authors classified the system as ultra-compact X-ray binary (UCXB) with an orbital period of about 40 min.
In this chapter I present a study of the temporal and spectral evolution of RX1804 during the bright 2015 outburst. Taking advantage of the almost continuous monitoring performed by *Swift*, I was able to individuate the two main hard and soft states and, for the first time for this source, the intermediate state, rarely observed in NS-LMXBs. In order to study the reflection component, I combined the three *NuSTAR* data archival observations with XRT and BAT. Two of them have already been reported in previous works (the hard state by Ludlam et al. (2016) and the soft state by Degenaar et al. (2016)). The *NuSTAR* observation performed during the intermediate state is reported in this Chapter for the first time. Furthermore, I report on results from the unpublished type-I X-ray burst observed by *INTEGRAL* in 2012 and the bursts detected during the Nustar intermediate state. This work was carried on in collaboration with Dr. Massimo Cocchi from IAPS Rome and Dr. Carlo Ferrigno from ISDC Geneva. The results of this chapter have been published in Marino et al. (2019a).

4.4 Observations & Data reduction

In the present chapter, I used data from several X-ray telescopes, such as *Swift*/XRT , *Swift*/BAT and *NuSTAR* to study the evolution of the 2015 outburst and *INTEGRAL*/JEM-X, *NuSTAR* and *Swift*/XRT for the type-I X-ray bursts study. I refer to Section 3.3 for the data reduction procedure followed for XRT, BAT, *NuSTAR* and JEM-X. For this work I used the software package HEASOFT (v. 6.25).
The 2015 outburst was monitored by XRT, between MJD 57059 (February 2nd) and MJD 57166 (May 24th), with 24 pointings for a total exposure time of $\approx$31 ks. All these observations, with obsID: 00324360, 006300470 and 0008145, were performed in Window Timing (WT) mode. In the selected observations I found 4 pointings, i.e. obsID 0032436029-32, affected by pile-up, for which an annulus region with an inner radius of 6 pixels was required to correctly take into account the pile-up distortion effect.
The BAT survey data, from MJD 57060 to MJD 57165, retrieved from the HEASARC public archive, were processed again according to the procedure described in Section 3.3.
NuSTAR observed RX1804 three times in 2015: on March 5 for $\sim$34 ks exposure time, on April 1 for $\sim$23 ks, and on April 14 for $\sim$20 ks (see Table 4.1). Finally, *INTEGRAL* observed the 2012 type-I X-ray burst during the Science Window 116100100010, MJD 56033.350506, with exposure time of $\sim$1800 s. From this science window, I extracted 2 s light curves of the burst in the 3-20 keV energy

ObsID	Start Time		Exposure	Ref.
	(UTC)	(MJD)	ks	
80001040002	2015-03-05	57086.4	37.3	L16
80001040004	2015-04-01	57113.7	23.4	This work
90101003002	2015-04-15	57126.5	20.2	D16

TABLE 4.1: List of the *NuSTAR* observations of RX1804 used in this work. L16 = Ludlam et al. (2016), D16 = Degenaar et al. (2016).

	XRT			BAT		
ObsID (*)	Obs. Date (MJD)	Obs. Date (yyyy-mm-dd)	Exp. (ks)	Obs. Date start (MJD)	Obs. Date end (MJD)	Exp. (ks)
*20	57085.63121	2015-03-04	2.2	57060	57100	657.0
*27	57105.94254	2015-03-24	0.6	57105.8	57112	131.8
*28	57112.98183	2015-03-31	1.1	57112	57114	35.3
*29	57115.83525	2015-04-03	1.2	57115	57117	47.2
*30	57118.17901	2015-04-06	1.0	57117	57119.5	46.4
*31	57121.17200	2015-04-09	1.0	57119.5	57122.5	59.5
*32	57124.16573	2015-04-12	1.0	57122.5	57125.5	71.5
**01	57126.54499	2015-04-14	1.0	57125.5	57130	99.7
*34	57166.75520	2015-05-24	1.6	57130	57165	714.2

TABLE 4.2: Details of the Swift data used in the analysis of the 2015 outburst; *=000324360, **=000814510.

range using data from both the JEM-X monitors, i.e. JEM-X1 and JEM-X2, with the *INTEGRAL* data analysis software, OSA11. The light curve of each XRT and *NuSTAR* observation was checked in order to individuate any flare and/or burst. On the 25 XRT analyzed observations, I found and time-filtered 5 bursts for XRT. Five and ten type-I X-ray bursts were instead observed in the light curve of the source in the first and second *NuSTAR* observation, respectively. Also in this case I time filtered the spectra by removing the time intervals around these bursts; depending on the burst intensity and profile this resulted in a reduced exposure of 36.6 ks and 20.6 ks respectively.
Spectra were grouped with GRPPHA in order to have a minimum of 100 counts per bin for XRT and 150 counts per bin for *NuSTAR*.

4.5 1RXS J180408.9-342058 in intermediate state

The XRT and BAT light curves and hardness ratios (HRs) collected during the bright 2015 outburst are shown in Fig. 4.2.
The flux increasing by an order of magnitude in the soft X-rays band around MJD 57115 and the corresponding decay in the XRT hardness ratio are signatures of the transition to the soft state (Degenaar et al. 2015a). A peculiar increase of the count rate in the hard X-rays, especially evident in the 15-20 keV range (Fig. 4.2), seems to anticipate the soft rise by ~ 5 days. The nature of this hard rise will be discussed in the following. The XRT light curve profile shows a gap after the softening (see Fig. 4.2), but the flux decay can be followed using the *MAXI* monitoring (see fig. 1 in Degenaar et al. 2016), which reveals the expected exponential decrease after the peak.
According to the two HR evolutions, I individuated three different phases (indicated with dashed lines in Fig. 4.2) until the soft X-rays peak: one long *plateau* state, between ~57060 and ~57100

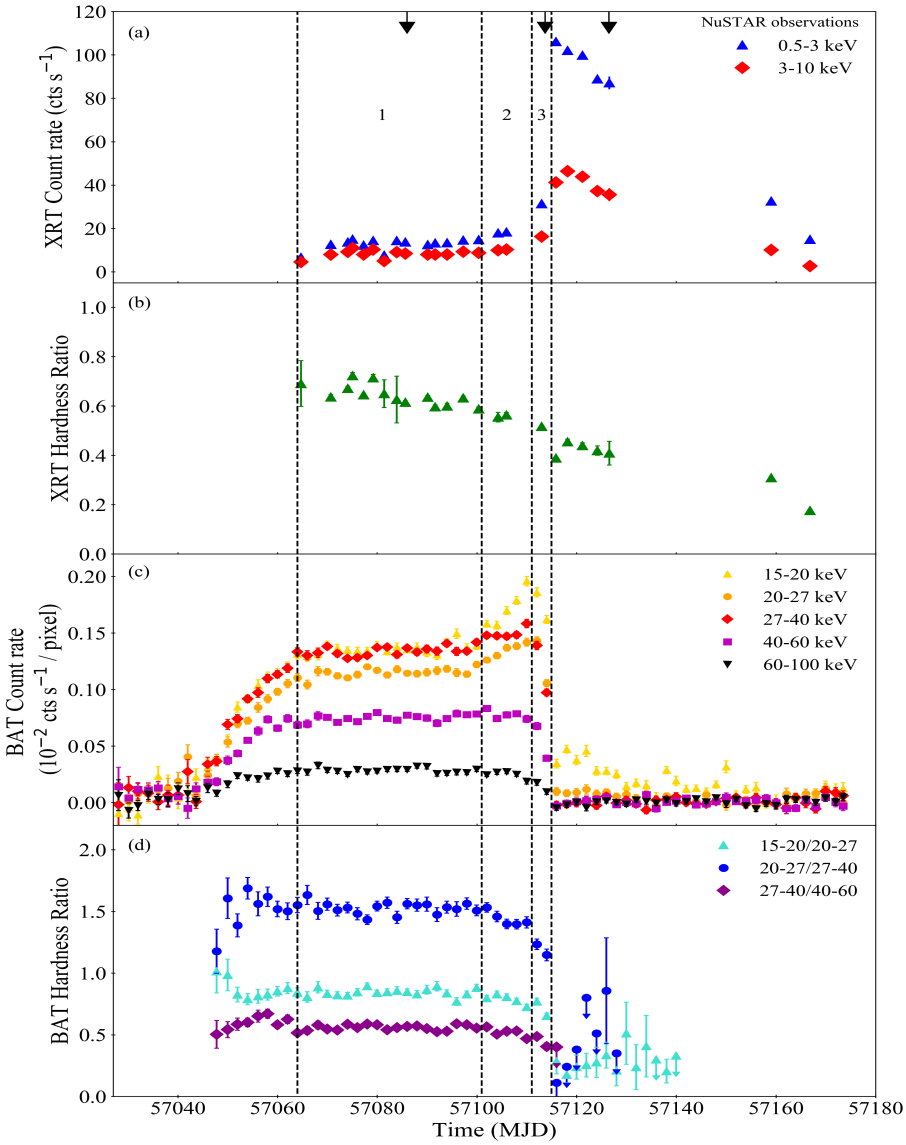

FIGURE 4.2: XRT and BAT light curves (subpanels (a) and (c), respectively) and hardness ratios (subpanels (b) and (d), respectively) of RX1804 during the 2015 outburst. The time intervals chosen for the first three BAT spectra used in this work are identified by dashed lines and labeled with numbers from 1 to 3. Onto the XRT light curve, the times of the three *NuSTAR* observations are flagged by arrows. In the BAT HR (d), points with large error bars are not shown for clarity.

MJDs, characterized by a constant HR for both data-sets, a second shorter phase from ∼57106 MJD to ∼57112 MJD with two XRT observations, where an increase in the soft X-rays comes along with a simultaneous softening in the BAT data and finally a third phase, prior to the transition to the soft state, until 57114 MJD. According to this selection I performed a broad-band spectral analysis for each phase. Three time-averaged BAT spectra were therefore extracted, with number of channels chosen according to the statistics, i.e. 51 channels in the first two spectra and 18 in the third one. A single XRT observation representative of each phase was associated to each BAT spectrum.
For Phase 1, for which a sample of 14 XRT pointings were available with compatible flux and hardness ratio, I selected the observation placed in the middle of the time interval of interest (ObsID 00032436020). Between the two spectra in Phase 2, with consistent flux and HR, I chose the second, ObsID 00032436027, characterized by a better constrained HR. Finally, only one XRT observation was present within Phase 3 and it was paired with the corresponding BAT spectrum (Tab. 4.2).
The variable HR in the soft state did not allow for a similar grouping, therefore I proceeded differently. I extracted 5 subsequent BAT spectra, each one with a time-bin of ≈3 days and 12 channels, and I associated them to its corresponding XRT pointing. The sixth XRT spectrum is relative to an observation taken more than one month later: in order to collect as much statistics as possible and according to the constant BAT light curve in that period, I paired the spectrum with a six-weeks long BAT spectrum. In the final XRT observation, the low exposure, i.e. around 10 s, and the resulting low statistics did not enable for a reliable spectral analysis, therefore I decided to exclude the observation from our sample. The details about the observations used and the XRT and BAT pairings are reported in Table 7.1.
In every model used in this work, the component TBABS was included to take into account the photoelectric absorption due to neutral matter between the source and the observer, with photoelectric cross sections from Verner et al. (1996) and element abundances from Wilms et al. (2000). Furthermore a CONSTANT component was included to serve as intercalibration constant. I also applied a systematic error of 2%, according to the *Swift* calibration guidelines. In the following, the quoted errors are computed at 90% confidence levels.

4.5.1 Spectral modelling

Based on the *NuSTAR* spectral analysis reported by Ludlam et al. (2016), RX1804 was in hard state during the BAT plateau, therefore I started testing a standard scenario for NS-LMXBs in hard state, i.e. a multi-color disk black body plus a thermal Comptonization spectrum. I performed the spectral analysis of these three broad band XRT and BAT spectra in the energy range 1.0-120 keV. The Comptonization spectrum was described with the model COMPTB (Farinelli et al. 2008), used as a pure thermal one, i.e. with the logarithm of the illuminating factor A and the bulk parameter δ frozen to respectively 8 and 0 (as in Cocchi et al. 2010). The γ parameter of the seed-photons distribution was fixed to the standard value of 3, corresponding to a pure black body distribution. The main parameters of this model are the corona temperature $kT_{\rm e}$, the temperature of the seed photons $kT_{\rm s,1}$ and α, the energy index of the Comptonization spectrum. An estimate of the optical depth τ can be derived from the following equation (Titarchuk and Lyubarskij 1995):

$$\alpha = -\frac{3}{2} + \sqrt{\frac{9}{4} + \frac{\pi^2}{C_T} \frac{m_e c^2}{kT_e \left(\tau + \frac{2}{3}\right)^2}} \tag{4.1}$$

with the parameter C_T equal to 3 in spherical geometry.
The emission from the disk was modeled with the XSPEC model DISKBB (Mitsuda et al. 1984), whose normalization parameter K is related to the apparent inner disk radius, given an assumed distance and inclination.

Assuming a 10 kpc distance, the real inner radius of the disk was then found as a function of the inclination, using the correction factor κ=1.7 and a ξ correction factor for the torque-free boundary condition of 0.4[1] (Kubota et al. 1998; Gierliński and Done 2002).
Although in Obs. *20 and *27 the fits led to statistically good results, with a reduced χ^2_ν (d.o.f.) of 1.04 (312) and 0.99 (151), respectively, the derived physical parameters are quite odd: the seed-temperature of the Comptonization spectrum $kT_{s,1}$ and the disk temperature kT_{disk}, are indeed above 3 and 1.7 keV, respectively. The disk temperature seems hard to reconcile with a physically consistent scenario, since usually NS-LMXBs in hard state shows kT_{disk} much below 1 keV (see, e.g., D'Aì et al. 2010; Di Salvo et al. 2015; Mazzola et al. 2019). I checked if these results can be related to the lack of modeling of the reflection component, which was detected by Ludlam et al. (2016) in the same state. I therefore applied the REFLECT convolution model (Magdziarz and Zdziarski 1995) to the Comptonization spectrum in the three observations considered, fixing the abundances to the solar abundances and the inclination to 30° (according to the best-fit value found by Ludlam et al. 2016; Degenaar et al. 2016). In both observations, the inclusion of this component was not statistically significant and did not modify the values of the two temperatures. A more detailed study of the reflection component with the high statistics *NuSTAR* data is presented in Subsection 4.5.2.
Due to these results, I decided to rule out a COMPTB+DISKBB model for the first two spectra in the hard state.
I tried then to apply a double seed-photons Comptonization model, as suggested by several authors (e.g. Cocchi et al. 2011). In this model, both populations of photons from the NS and the disk are seeds for the Comptonizing corona, characterized by a single electron temperature kT_e and a single optical depth. In order to describe this scenario, I summed in XSPEC two different COMPTB components, with the cloud parameters, i.e. kT_e and the energy index of the Comptonization spectrum α, tied between each other in the analogous models, following the prescription by Titarchuk and Shaposhnikov (2005). On the other hand, I left the temperatures of the photon sources $kT_{s,1}$, $kT_{s,2}$ free and untied. The fit was unable to give any constraints on the N_H value, therefore this parameter was kept frozen to the best-fit value I found, i.e. 0.22×10^{22} cm^{-2}.
On the contrary, Obs. *28 is not only statistically (χ^2_ν (d.o.f.)=1.07(272)), but also physically well described by a COMPTB+DISKBB model, with best-fit temperatures of ∼1.4 keV and ∼0.7 keV, respectively. For consistency, I applied the Comptonization model with double seed photons also to this spectrum. In this scenario, the seed photons temperatures obtained are physically consistent and compatible with NS (*boundary layer*) and disk temperatures in hard state ($kT_{s,1}$ ∼1.4 and $kT_{s,2}$ ∼0.3 keV, respectively). However, while the values found for kT_e and τ in the first two spectra are typical of the hard states in NS-LMXBs (H1 and H2 in Tab. 4.3), in the third spectrum a cooler kT_e has been found (∼12 keV) with both models. A cooler corona implies the arising of a cooling source, e.g. the accretion disk, therefore a model including the direct emission from the disk, such as COMPTB+DISKBB, could be a more physically acceptable scenario. Indeed, the observed increasing of the soft X-rays flux between the second and the third observation (see Fig. 4.2) is consistent with the arising of a contribution from a disk black body in the third spectrum. Based on these clues, I classified this spectrum as belonging to an intermediate state (I1 in Tab. 4.3).

[1]This assumption is probably not valid for NS-LMXBs, therefore these values for the inner disk radius are likely underestimated.

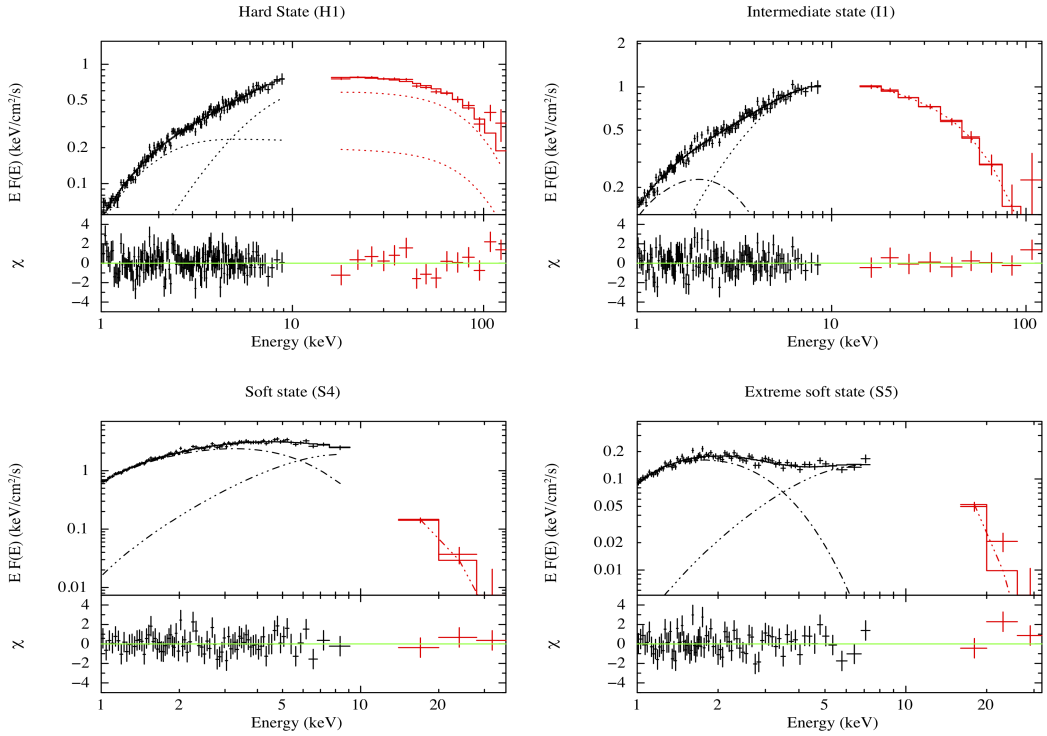

FIGURE 4.3: XRT (*black*) and BAT (*red*) spectra of Obs. labeled as: H1 (*top, left*), I1 (*top, right*), S4 (*bottom, left*) and S5 (*bottom, right*) and relative residuals. In H1 I used the model COMPTB+COMPTB, in I1 I used DISKBB+COMPTB while a BBODY+DISKBB model was employed for both S4 and S5. I adopted different linestyles to distinguish between the different components, in particular I used: dot for COMPTB, dash-dot for DISKBB and dash-dot-dot-dot for BBODY

.

The energy spectra, the model components and the residuals for H1 and I1 are shown in Fig. 4.3 (*top*).

In the soft state spectra I ignored all the data beyond 40 keV, due to the lack of significant emission above that threshold. Furthermore, the poor spectral resolution of XRT, did not allow us to model the reflection features below 1 keV, apparent in the residuals in all the spectra in this state. Therefore, all data below this threshold were ignored.
In order to be coherent with the analysis performed for I1, I applied a COMPTB+DISKBB model to Obs. *29, finding an acceptable fit (χ^2_ν/d.o.f.=1.07(324)), but as long as I kept the (totally unconstrained) α parameter frozen to its best fit value of 1.2. The ongoing transition to the soft state is witnessed by the decreasing value of the corona temperature, about 3 keV and, by the increase of $kT_{\rm disk}$. Such a low value for $kT_{\rm e}$, with a higher τ compared to the previous spectrum (see Table 4.3), indicates the arising of a saturated Comptonization spectrum, typical of this state (see, e.g. Barret et al. 2000; Gambino et al. 2019). It is noteworthy that, in spite of the increasing $kT_{\rm disk}$, the disk is found at a higher $R_{\rm in}$, which is odd. This is probably due to the higher best-fit value of $N_{\rm H}$, which is known being strongly correlated with the DISKBB normalization factor. Thus, I adopted the canonical soft state model, composed of a black body emission mimicking the saturated Comptonization (BBODY in XSPEC) and the multicolor disk black body (DISKBB). The fit with this model is acceptable as well (χ^2_ν =1.13(325)), and the physical parameters $kT_{\rm bb}$ and $kT_{\rm disk}$ are also compatible with those from the previous models.

Spectral modelling of the hard and intermediate state with *Swift*)

Parameters	**Spectra**			
	H1	H2	I1	I2
Model:TBABS×(COMPTB+COMPTB)				
$N_{\rm H}$ (10^{22} cm^{-2})	(0.22)	(0.22)	(0.22)	-
$kT_{\rm e}$ (keV)	$20.0^{+3.0}_{-1.5}$	$17.6^{+2.0}_{-1.7}$	$11.8^{+2.0}_{-1.5}$	-
$kT_{\rm s,1}$ (keV)	$2.1^{+1.2}_{-0.5}$	$1.5^{+0.3}_{-0.2}$	$1.20^{+0.11}_{-0.10}$	-
$kT_{\rm s,2}$ (keV)	$0.52^{+0.07}_{-0.06}$	0.36±0.04	0.24±0.02	-
α	$1.04^{+0.11}_{-0.05}$	1.20±0.06	1.15±0.13	-
τ	4.00±0.06	3.65±0.14	4.80±0.40	-
χ^2_ν (d.o.f.)	1.03(312)	0.93(151)	1.08(242)	-
Model:TBABS×(COMPTB+DISKBB)				
$N_{\rm H}$ (10^{22} cm^{-2})	-	-	(0.22)	$0.36^{+0.04}_{-0.03}$
$kT_{\rm e}$ (keV)	-	-	$13.0^{+3.0}_{-2.0}$	<3.4
$kT_{\rm s}$ (keV)	-	-	$1.36^{+0.19}_{-0.14}$	$1.2^{+3.0}_{-0.4}$
$kT_{\rm disk}$ (keV)	-	-	$0.70^{+0.09}_{-0.08}$	$1.0^{+0.4}_{-0.3}$
$R_{\rm in}\cos i$ (km)	-	-	$13.4^{+0.6}_{-0.5}$	$23.9^{+3.0}_{-1.6}$
α	-	-	1.24±0.13	(1.2)
τ	-	-	4.4±0.4	10.7±0.2
χ^2_ν (d.o.f.)	-	-	1.07(242)	1.07(324)
Model:TBABS×(BBODY+DISKBB)				
$N_{\rm H}$ (10^{22} cm^{-2})	-	-	-	0.25±0.02
$kT_{\rm bb}$ (keV)	-	-	-	$2.0^{+0.4}_{-0.3}$
$kT_{\rm disk}$ (keV)	-	-	-	1.18±0.15
$R_{\rm in}\cos i$ (km)	-	-	-	$17.8^{+0.9}_{-0.7}$
χ^2_ν (d.o.f.)	-	-	-	1.13(325)
$F_{\rm Bol}$ ($\times10^{-9}$erg cm^{-2} s^{-1})	3.7	3.9	4.7	16.6
$F_{\rm Disk}$($\times10^{-9}$erg cm^{-2} s^{-1})	-	-	0.7	7.9

TABLE 4.3: Fit results of the combined XRT and BAT spectra collected during the 2015 outburst in the hard and intermediate spectral state. Quoted errors reflect 90% confidence level. The parameters which were kept frozen during the fits are reported between round parentheses. The reported flux values have associated errors of 10%.

In the remaining five observations, the latter model provides an acceptable fit and spectral parameters all in accordance with each other, with the exception of $kT_{\rm disk}$ in Obs. *34, which is significantly decreased in this last spectrum. On the contrary, a DISKBB+COMPTB model does not provide a good fit in any of the last five spectra. So that, I have classified Obs. *29 as still an intermediate state, and labeled it as I2, and the observations from *30 to *34 as fully soft states (and labeled them from S1 to S5 in Tab. 4.4). In Fig. 4.3 (*bottom*), the model components and residuals for S4 and S5 are shown.

4.5.2 Studying the reflection component with *NuSTAR*

The spectral analysis performed in Subsection 4.5.1 had the goal to study the spectral evolution of the source during the outburst. Since the poor statistics of our *Swift* spectra did not allow us to probe the presence of the reflection, I combined our broad band XRT and BAT spectra with three

Spectral modelling of the soft state with *Swift*

Model:TBABS×(BBODY+DISKBB)					
Parameters	**Spectra**				
	S1	S2	S3	S4	S5
$N_{\rm H}$ (10^{22} cm^{-2})	0.39±0.03	0.46±0.04	0.27±0.02	0.22±0.02	0.29±0.08
$kT_{\rm bb}$ (keV)	1.9±0.2	$2.1^{+0.5}_{-0.3}$	$2.4^{+0.7}_{-0.4}$	2.3±0.4	$1.8^{+0.3}_{-0.2}$
$kT_{\rm disk}$ (keV)	$1.08^{+0.12}_{-0.11}$	1.20±0.17	$1.27^{+0.20}_{-0.17}$	$1.39^{+0.16}_{-0.13}$	0.69±0.04
$R_{\rm in}\cos i$ (km)	$21.0^{+1.0}_{-0.8}$	17.7±0.6	$14.0^{+0.9}_{-0.6}$	$13.0^{+0.6}_{-0.4}$	$15.7^{+0.8}_{-0.6}$
χ^2_ν (d.o.f.)	1.15(287)	1.13(297)	1.14(250)	0.98(267)	1.13(180)
$F_{\rm Bol}$ ($\times10^{-9}$erg cm^{-2} s^{-1})	17.0	18.6	13.3	12.0	1.8
$F_{\rm disk}$ ($\times10^{-9}$erg cm^{-2} s^{-1})	9.2	10.2	7.6	8.0	1.2

TABLE 4.4: Fit results of the combined XRT and BAT spectra collected during the 2015 outburst in the soft spectral state. Quoted errors reflect 90% confidence level. The parameters which were kept frozen during the fits are reported between round parentheses. The reported flux values have associated errors of 10%.

NuSTAR observations (see Table 4.1).

I first performed a preliminary analysis of the iron line using only *NuSTAR* data. The continuum was modeled with the same models used in this work for the XRT and BAT in hard, intermediate and soft states, while a simple GAUSSIAN component was included to describe the iron line. In all the three *NuSTAR* spectra, the line was found at an energy comprised between 6.5 and 6.7 keV, indicating a relatively high ionisation for the accreting material in all states. Furthermore, the equivalent width of the line was found around 50-70 eV, 75-110 eV and 40-100 eV, respectively. This points out a higher contribution of reflection in the intermediate state with respect to the hard state, while a similar consideration for the soft state is not possible, since the high uncertainties. Then, I associated each of the *NuSTAR* observations to the quasi-simultaneous *Swift* spectrum in Table 7.1. In particular I coupled *NuSTAR* Observation 80001040002 with H1, Obs. 80001040004 with I1 and Obs. 90101003002 with S4.

I used the convolution model RFXCONV (Done and Gierliński 2006; Kolehmainen et al. 2011), which is a self-consistent model including the effects of the absorption edges and the emission lines expected for reflection from accretion disks in X-ray binaries. I also applied the convolution model RDBLUR to smear the spectrum simulating the relativistic effects due to the NS gravitational field and the dynamics of the accretion disk. I applied RDBLUR×RFXCONV to both the Comptonization components[2] in the hard state, and to the single COMPTB component in the other two states.

In order to reduce the number of degeneracies, the outer radius of the disk was fixed to 1000 R_G and the iron abundance to the solar abundance. The emissivity index *Betor*[3] was not well constrained by the fit, i.e. it was found in a wide range between 2 and 3.5. It was then fixed to the reasonable value of -2.7. I left free, instead, the ionization parameter and the inclination. However, due to the strong correlation between the inclination and the inner disk radius, I was not able to find constraints on both the parameters. I considered fixing the inclination a viable way to obtain constraints on the inner disk radius. Moreover, due to the ignorance about the real inclination of the system, I attempted to calculate $R_{\rm in}$ considering a high and a low inclination cases, corresponding to 60° (since no dips and/or eclipses have been ever found) and 20° respectively. The fit to the broad band XRT,

[2] I tied together all the parameters in the reflection components applied to the two Comptonization spectra, as again I am considering in this scenario a single hot electron plasma.

[3] The exponent of the distance r to the center of the disk if I scale emissivity as r^{Betor}.

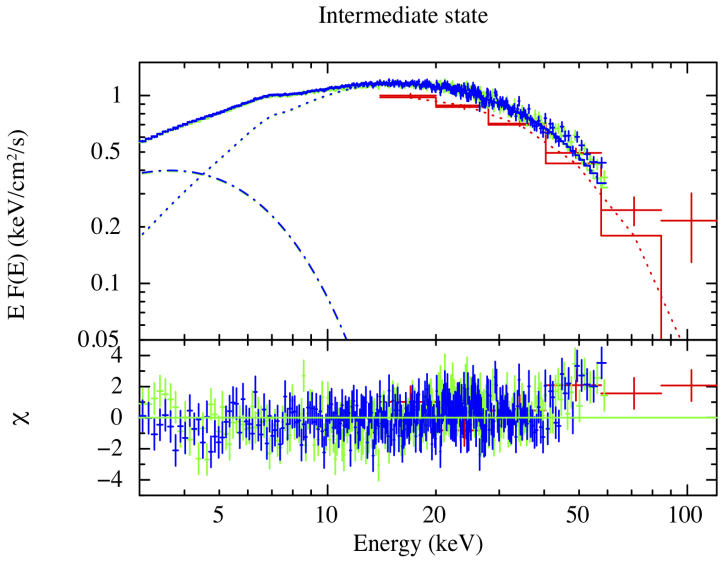

FIGURE 4.4: BAT+*NuSTAR* energy spectrum in the intermediate state fitted with a Comptonization (dot line) plus a disk model (dash-dot line). Reflection component is also included. Residuals at high energy (above 40 keV) are significant.

NuSTAR and BAT spectrum with the reflection-inclusive best-fit models individuated in Subsection 4.5.1, reveals unmodeled residuals above ∼40 keV and a general bad accordance with the data in the intermediate state (I1). Since the spectra in this state were taken during the rapid hard-to-soft state transition, I checked whether XRT and *NuSTAR* observations, performed only ∼17 hours apart, could have incompatible spectral shapes fitting them separately with a POWERLAW model and allowing the Γ index to vary between the two spectra. The best-fit indices are not compatible within the errors, pointing out that the RX1804 spectrum was varied, so that XRT and *NuSTAR* observations should not be fitted together. I then paired *NuSTAR* with BAT, since the spectrum of the latter was averaged over a large time interval, compatible with the exposure time of the *NuSTAR* spectrum. Fitting *NuSTAR* and BAT with the same model used before gives an acceptable fit, but in both spectra residuals can be clearly seen at high energies, which reveal the presence of a hard tail (see Section 2.6), as evident from Fig. 4.4. In order to improve the fit, I included a POWERLAW component, convolved with RDBLUR×RFXCONV. The new component improves significantly the fit, i.e. *F-test* probability of improvement by chance of $\sim 10^{-11}$, confirming the arising of a hard tail in the intermediate state, with a flux of $\sim 4\times10^{-10}$ erg cm^{-2} s^{-1} in the 30-100 keV energy band, a factor of 2 lower of the total flux in the same band.

I added a power-law component also to the models used for the analysis of the hard and soft states, in order to check for the presence of any hard tail in these states. In the hard state, the introduction of a reflected power-law component improves significantly the fit (*F-test* probability of $\sim 10^{-14}$), but at the cost of making the other physical parameters of the fit, especially kT_e, undetermined. A similar situation concerns the soft state spectra, where in spite of an improvement in the fit (*F-test* probability of $\sim 10^{-7}$), the Γ index of the reflected power-law was completely unconstrained by the fit. I therefore conclude that, while a hard tail contribution is likely to be taken into account at every spectral state of the source, the statistics to probe it properly is reached only in the intermediate state. The results of the fits of the three spectra are reported in Table 4.5-4.6, while the energy spectra plus

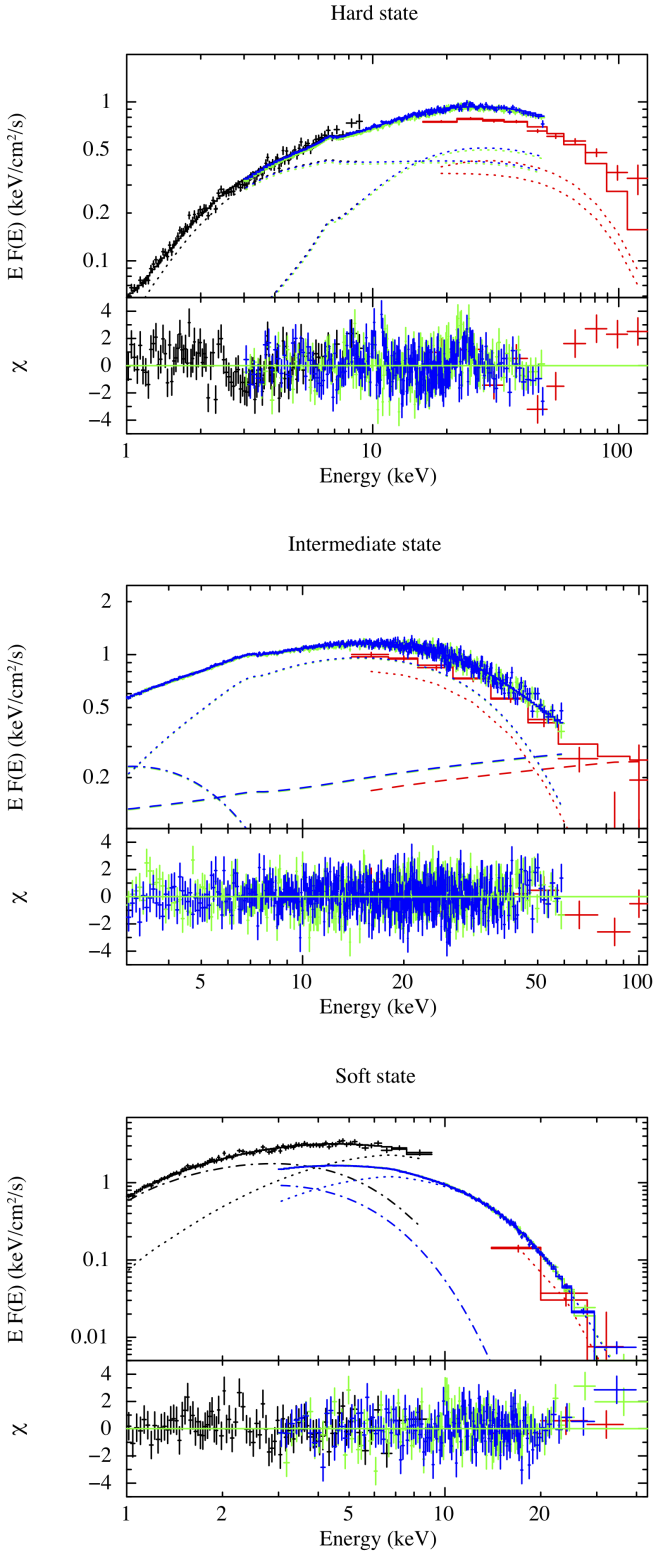

FIGURE 4.5: Energy spectra and residuals of RX1804 in hard (*top*), intermediate (*middle*) and soft (*bottom*) state including XRT + BAT + *NuSTAR* for the *top* and *bottom* spectra and only BAT + *NuSTAR* for the *middle* one. I adopted different linestyles to distinguish between the different components, in particular I used: dot for COMPTB, dash-dot for DISKBB and dash for POWERLAW.

Spectral modelling of the 2015 outburst with *NuSTAR+Swift*
High inclination case

Parameters	**Spectra**		
	H1	I1	S4
$N_{\rm H}$ (10^{22}cm^{-2})	(0.22)	(0.22)	0.31±0.03
$kT_{\rm s,1}$ (keV)	$3.19^{+0.14}_{-0.15}$	1.70±0.20	1.31±0.03
$kT_{\rm s,2}$ (keV)	0.75±0.02	-	-
$kT_{\rm disk}$ (keV)	-	$1.30^{+0.10}_{-0.16}$	(1.16)
$kT_{\rm e}$ (keV)	$17.3^{+0.7}_{-0.6}$	$7.5^{+0.5}_{-0.4}$	$2.41^{+0.04}_{-0.03}$
$f_{\rm refl}$	$0.16^{+0.05}_{-0.04}$	0.13±0.3	$0.07^{+0.10}_{-0.09}$
$R_{\rm in}$ ($R_{\rm G}$)	30^{+60}_{-20}	27^{+12}_{-8}	>25
i		(60)	
α	0.97±0.02	$0.96^{+0.05}_{-0.02}$	(1.2)
τ	4.39±0.07	7.0±0.2	11.1±0.1
$\log\xi$	$2.37^{+0.05}_{-0.03}$	$2.84^{+0.10}_{-0.05}$	$3.0^{+0.1}_{-0.3}$
χ^2_ν (d.o.f.)	1.16(1462)	0.99(1561)	1.08(1074)

TABLE 4.5: Fit results from the combined XRT, BAT and *NuSTAR* spectra. Quoted errors reflect 90% confidence level. Fixed parameters are in round brackets. The models used are: RDBLUR×RFXCONV×(COMPTB+COMPTB) for H1, RDBLUR×RFXCONV×(COMPTB+POWERLAW)+DISKBB for I1, and RDBLUR×RFXCONV×COMPTB+DISKBB for S4. See text for the parameters definition.

residuals are shown in Figure 4.6.
A comparison between these results and the results in Table 4.3-4.4 reveals how the inclusion of the reflection component does not change significantly the values for the tempeatures $kT_{\rm s,1}$, $kT_{\rm s,2}$, $kT_{\rm e}$ and $kT_{\rm disk}$, except for H1, where the value of $kT_{\rm s,1}$ increases significantly. This might be due to a hidden contribution of an unmodeled power-law component at high energies, which drives the free parameters, and in particular $kT_{\rm s,1}$, to a physically odd minimum. In the three spectra the reflection fraction was always found lower than 20%, indicating a consistent but not extremely strong reflection component. Ionization was found relatively high, i.e. $\log\xi$ ≈2-3, in all the spectra, which is in accordance with the simple line analysis performed with a GAUSSIAN model in the *NuSTAR*-only spectra. This value is also in agreement with those found by Ludlam et al. (2016) and Degenaar et al. (2016) in hard and soft state, respectively. The wide uncertainties in the inner radius values in the three states do not allow us to strongly identify constraints for $R_{\rm in}$, which was found to be <90 $R_{\rm G}$ in H1, between 16 and 40 $R_{\rm G}$ in I1 and >13 $R_{\rm G}$ in S4.
The bolometric unabsorbed fluxes found from the broad band analysis are compatible within the errors with the fluxes found in the *Swift*only analysis, i.e. $F_{0.1-150{\rm keV}}$ ∼4.0×10^{-9} erg cm^{-2} s^{-1}for H1, $F_{0.1-150{\rm keV}}$ ∼5.0×10^{-9} erg cm^{-2} s^{-1}for I1 and $F_{0.1-50{\rm keV}}$ ∼11.0×10^{-9} erg cm^{-2} s^{-1}for S4.

4.5.3 Discussion

The spectral evolution of the source in the 2015 outburst: evidence of an intermediate state
The *Swift* spectral analysis highlights how the RX1804 spectrum evolves during the outburst. In Fig. 4.6 I show the best-fit models of the system in four phases of its evolution throughout the outburst, which displays four different spectral states. The hard state spectra H1 and H2, collected during the "plateau" in the light curve, are well described by a double-seeds Comptonization spectrum, arising

Spectral modelling of the 2015 outburst with *NuSTAR+Swift*
Low inclination case

Parameters	**Spectra**		
	H1	I1	S4
$N_{\rm H}$ (10^{22}cm^{-2})	(0.22)	(0.22)	0.28±0.02
$kT_{\rm s,1}$ (keV)	$3.64^{+0.14}_{-0.11}$	$1.59^{+0.10}_{-0.08}$	$1.03^{+0.07}_{-0.05}$
$kT_{\rm s,2}$ (keV)	$0.83^{+0.03}_{-0.02}$	-	-
$kT_{\rm disk}$ (keV)	-	$1.24^{+0.05}_{-0.02}$	(0.90)
$kT_{\rm e}$ (keV)	$18.5^{+0.9}_{-0.7}$	$7.4^{+0.3}_{-0.2}$	$2.49^{+0.06}_{-0.04}$
$f_{\rm refl}$	0.034±0.003	$0.052^{+0.006}_{-0.005}$	$0.09^{+0.05}_{-0.02}$
$R_{\rm in}$ ($R_{\rm G}$)	<21	25^{+11}_{-9}	23^{+65}_{-13}
i		(20)	
α	1.01±0.03	$0.91^{+0.03}_{-0.02}$	(1.2)
τ	4.04±0.09	7.5±1.2	10.9±0.01
$\log\xi$	$2.84^{+0.10}_{-0.05}$	(2.4)	3.3±0.1
χ^2_ν (d.o.f.)	1.14(1462)	0.98(1561)	1.07(1076)

TABLE 4.6: Fit results from the combined XRT, BAT and *NuSTAR* spectra. See the caption of Table 4.5 for further details.

from the interaction of the spectra by two different photon sources with the same hot electron plasma. Indeed, as suggested by Cocchi et al. (2011), NS-LMXBs in the hard state might be divided in two sub-classes: the one-photon population (1P) and the two-photon population (2P). In the former only one source of photons can be found, which can be the NS or the boundary layer, Comptonized by a hot corona. In the 2P systems also the photons emitted by the disk are Comptonized by the same medium, leading to a spectrum consisting of two different thermal Comptonization spectra. This is most likely related to the accretion luminosity observed in the hard state of 2P population, which is consistently higher than the hard state luminosity of the 1P sources (Cocchi et al. 2011). Indeed, RX1804 shows a luminosity in hard state of $\sim 4\times10^{37}$ erg s^{-1} .

I suggest here that the so-called "very hard" spectral state observed in this source by Parikh et al. (2017) might be explained, at least in the case of RX1804, in the framework of a thermal Comptonization spectrum with two seed photons populations. Indeed, for a corona temperature typical of NS-LMXBs in hard state, the presence of two Comptonization spectra with different seed photons makes the soft X-rays spectrum particularly flat, in particular with respect to a single Comptonization spectrum. Broad band X-rays spectral studies might point out whether the same explanation works for any of the other claimed "very hard" sources (Wijnands et al. 2015; Parikh et al. 2017; Wijnands et al. 2017b), with the exception of IGR J17361-4441, which was well-modeled by a single Comptonization spectrum (Del Santo et al. 2014). However, it is worth noting that the X-ray binary nature for IGR J17361-4441 is far from certain, as suggested by Del Santo et al. (2014) and Bozzo et al. (2014).

The corona electron temperature does not change between H1 and H2 (leveling off at a value around 18 keV), while a significant corona cooling is observed in I1, ∼12 keV. This phenomenon, combined with the arising of the direct disk emission in the data, points out that the source was in an intermediate state, which is quite common in black hole X-ray binaries, but rarely observed in NS-LMXBs. It is remarkable that the change in the spectral shape between the hard state and the intermediate happens right after the "peak" in the BAT light curve, only up to 40 keV (see Figure 4.2). This is

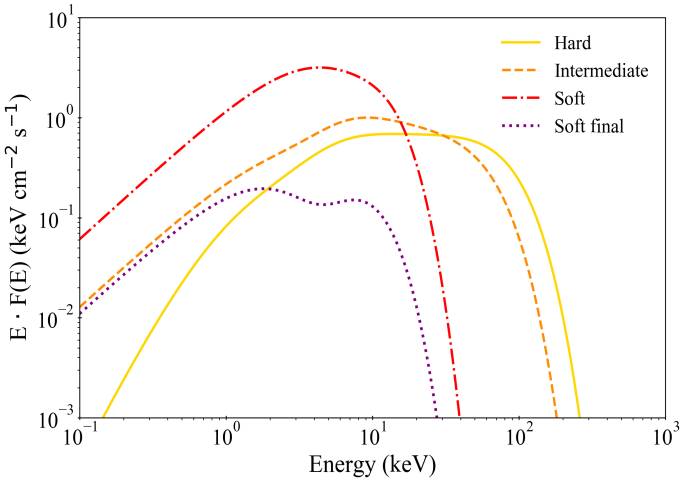

FIGURE 4.6: Best-fit models of observations H1 (yellow continuous line), I1 (orange dashed line), S4 (red dot-dashed line) and S5 (violet dotted line).

consistent with the pivot at 40 keV present between the hard and the intermediate state (see Fig. 4.6) due to the receding of the spectral cut-off, corresponding to the corona electron temperature decrease. In the soft state spectra from S1 to S4, steady values of the temperatures of both disk and NS are found, except for S5, where the disk is remarkably colder. This is coherent with the outburst fading and the disk depletion, witnessed by the increase of the inner disk radius from S4 to S5. Including *NuSTAR* data in S4, I am able to fit the spectrum with a more physically motivated model which replaces the BBODY model with a COMPTB with $\tau \approx 11$ (see Table 4.5-4.6). As expected, the black body model used in the soft state for the *Swift* spectra is only a crude approximation of a saturated Comptonization spectrum.
The discussed evolution of the spectral parameters of RX1804 throughout the outburst, in particular the increasing of the disk temperature, combined with the corona cooling, can be explained in the framework of a disk truncated at large gravitational radii in hard state and then approaching towards the compact object over the transition to the intermediate and soft states (e.g., Barret and Olive 2002; D'Aì et al. 2010; Gambino et al. 2019). The alternative plane-parallel corona scenario, which assumes an extended disk close to the NS surrounded by an optically thick corona in hard state and decreasing progressively in size going through the intermediate and soft states ("compactification"), seems unlikely since the relatively low τ values found in this work.

The reflection spectrum and the hard tail with *NuSTAR* The analysis carried out with *NuSTAR* provides the evidence of a low reflection fraction (<20%) and a relatively high ionization parameter, the latter in agreement with Ludlam et al. (2016); Degenaar et al. (2016), in all the three spectral states of RX1804. On the contrary, I was not able to give constraints on the inclination of the system, which was estimated with the same *NuSTAR* spectra as ∼18-29° in the hard state (Ludlam et al. 2016) and as ∼27-35° in the soft state (Degenaar et al. 2016), thus I estimated the spectral parameters assuming two different cases, i.e. for a low (20°) and high (60°) inclination. I suggest that this inconsistency with the previous results is possibly due to the different spectral binning chosen (see Subsection 3.1.2).

The fits result in wide inner disk radius ranges, which include the estimates found with the DISKBB model (this chapter) and the results by Ludlam et al. (2016) and Degenaar et al. (2016).
It is worth noticing that the bolometric flux estimations reported here for H1 and S4 are at least twice the values reported by Ludlam et al. (2016) and Degenaar et al. (2016). I suggest that this discrepancy is likely due to the procedure of co-adding the spectra, the background files and the ancillary response files using ADDASCASPEC (see Section 3.3).
Indeed I tried to sum FPMA and FPMB spectra in the hard state with ADDASCASPEC obtaining a 1.9×10^{-9} erg cm^{-2} s^{-1}flux in the 0.45-50 keV energy range, which is compatible within 10% with the estimate found by these authors. I verified that in this case the correct flux value is obtained by using ADDASCASPEC with the keyword `errmeth=GAUSS`, or using the SPECADD tool.
Unlike the *NuSTAR* study in the hard and soft states reported in the previously cited papers, I report here on the first broad band analysis of RX1804 including *NuSTAR* data in intermediate state. The physical parameters of the accretion found in the *NuSTAR*-including spectrum are compatible with the results by the *Swift*-only, confirming the evidence of the system being in a (rarely observed) intermediate state. The difficulty of catching intermediate spectral states in NS-LMXBs, witnessed by the very small number of reported intermediate states in literature, might be due to very rapid hard-to-soft transitions in this class of systems, significantly faster than the analogous transitions in BH X-ray binaries (as highlighted by Muñoz-Darias et al. 2014), presumably since the presence of the NS surface makes cooling more efficient.
The inclusion of *NuSTAR* analysis allowed me to individuate an additional power-law contribution in all the three states displayed by RX1804. In all three spectra, indeed, including a power-law results in a statistically significant improvement of the fit. Unfortunately, only in one case, i.e. I1, the introduction of the additional component resulted in a stable fit with a flux contribution to the total of $\sim$50% in the 30-100 keV energy band. It is noteworthy that the fit in the H1 spectrum gives odd results (i.e. a $kT_{s,1}$ of 3-4 keV) and rather unstable fits even including a power-law component. I suggest that the simple prescription of a double-seeds Comptonization scenario with two seed photons populations scenario with a single kT_e and τ for the hot corona might be either an oversimplification in this case, or that a spectral model capable to take into account properly both a thermal and non-thermal populations of photons is needed.

4.6 Looking for PRE bursts in RX1804

I have analysed the 2012 type-I burst observed by JEM-X (Chenevez et al. 2012) during the very faint emission period of RX1804, the five bursts found during the hard state within the XRT pointings, including the ones reported by Krimm et al. (2015b) and in't Zand et al. (2019b), and ten bursts observed by *NuSTAR* /FPMA during the intermediate spectral state. Each burst profile was fit with the BURS model included in the QDP tool, which well describes their Fast Rise Exponential Decay (FRED) shape. The duration of each burst lasts between 100 and 150 s. I found that the XRT bursts show similar characteristics in terms of peak luminosity, decay time (as in agreement with in't Zand et al. 2019b) and peak occurrence time, so that in the following I show results only for one of the sample (B2 in Tab. 4.7). The bursts observed by *NuSTAR* during the intermediate state are even more peculiar: they occur regularly every $\sim$4 ks with almost the same FRED profile (mean decay time of $\sim$36 s, with a standard deviation of $\sim$2 s). This behaviour is similar to the one displayed by other clocked bursters, the most famous being the "text-book" burster GS 1826–24, which has been regularly exhibiting bursts every $\sim$6 hr for at least 20 years (Ubertini et al. 1999; Chenevez et al. 2016). In order to confirm the regularity of the burst recurrence, which can be inferred by eye

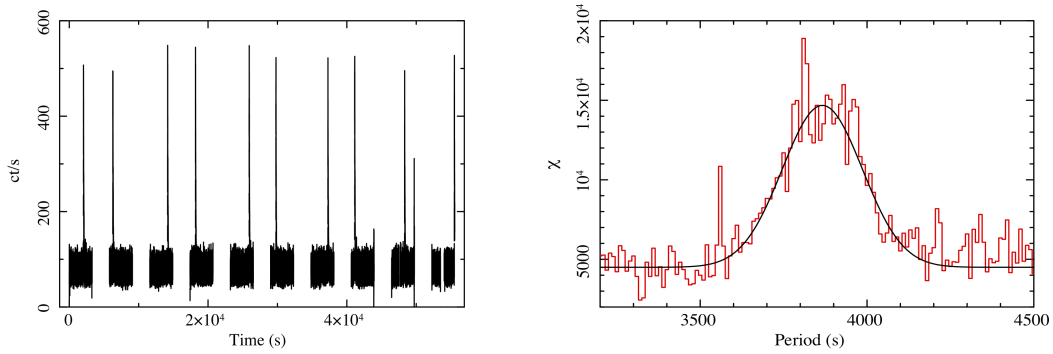

FIGURE 4.7: Light curve of the ten type-I bursts observed by *NuSTAR* in 2015 during the intermediate state (*left*) and folding of the light curve, fitted with a Gaussian model (*right*). The zero in the light curve corresponds to the Modified Julian Date (MJD) 57113.6798.

from Figure 4.7 (*Left*), I ran the XRONOS tool EFSEARCH, which performs an *e*-folding of the light curves. A 16-channels binning was chosen using a trial period of around 4000 s. Then, I performed a Gaussian fit finding a maximum at 3860 s with a FWHM of ∼140 s (see Figure 4.7, *right*). It is possible to conclude then that during the intermediate state the source did display quasi-periodic bursts, a behaviour which is thought to be related to a constant mass-accretion rate (Galloway et al. 2004). Finally, I chose one of the bursts to be representative of the sample of *NuSTAR* bursts, which in the following will be identified as B3 (see Table 4.7-4.8 and Figure 4.8).

Despite of the bursts observed by *Swift* and *NuSTAR* in 2015, the JEM-X burst (B1) shows different characteristics. In particular, in spite of the B1 light curve, the B2 and B3 profiles are well compatible with a standard FRED, without evidence of any wide structure in the peak, which is evident in B1 (Fig. 4.8, *top*). This could be considered a hint for a double peak, even though the bad statistics does not allow us to carry out a clear profile.
Thus, I performed a time-resolved spectral analysis of the three bursts. For B1, I extracted spectra in six time intervals, 10-s long, starting at 8:37:38 UTC, while for B2 and B3 I extracted four and five intervals, respectively of variable duration based on the statistics (see Table 4.8). For both B2 and B3, in order to neglect the contribution by the persistent emission, I used a spectrum taken ∼50 s before the start of each of the two bursts as the background spectrum. I did not apply a similar procedure for B1 since the persistent emission was below the telescope sensitivity. Spectra were then fitted by using a simple black body model (BBODYRAD in XSPEC), multiplied by the TBABS model. The interstellar equivalent absorption column $N_{\rm H}$ value was fixed at 0.22×10^{22} cm^{-2}. In B1, a simultaneous radius increasing and temperature decreasing can be observed around 40 s from the start of the burst, i.e. between the third and the fourth time segment (Tab. 4.8 and Fig. 4.8, *top*). On the contrary, in B2 and B3, the temperature evolution (see Figure 4.8, *middle* and *bottom*) suggests a simple cooling of the NS after the peak of the burst.
The bolometric unabsorbed flux at the burst peak is $3.2^{+1.5}_{-1.1}\times10^{-8}$ erg cm^{-2} s^{-1} in B1, $2.0^{+0.5}_{-0.4}\times10^{-8}$ erg cm^{-2} s^{-1} in B2 and $1.3\pm0.2\times10^{-8}$ erg cm^{-2} s^{-1} in B3. The flux errors have been derived by fixing the normalization factor of BBODYRAD to its lower and upper limits. Then, considering that the normalization K of BBODYRAD is connected to the black-body radius R through the relation: $K = R^2_{\rm km}/D^2_{10}$, where D_{10} is the source distance in units of 10 kpc, I computed the apparent radius of the NS for each spectrum (assuming d=10 kpc; see Tab. 4.8).

General properties of the bursts

	Bursts		
	B1	**B2**	**B3**
Instrument	JEM-X (3-20 keV)	XRT (0.5-10 keV)	*NuSTAR* (3-50 keV)
Occurrence Time (MJD)	56033.35986	57059.89270	57113.70346
Peak Time (s)	$17.0^{+3.0}_{-2.0}$	7.7±0.5	6.9±0.5
Decay Time (s)	$24.0^{+5.0}_{-4.0}$	67.0±3.0	38.0±5.0
Peak count rate (cts/s)	270±40	121^{+3}_{-4}	391^{+5}_{-4}

TABLE 4.7: Summary of the results obtained from the three selected type-I X-ray bursts, through light curves analysis. The decay time is the characteristic time interval for the count-rate to decay by a factor 1/e. Errors at 68% confidence level are reported.

A further argument in favour of a PRE nature for B1 can be found from the $F_{\rm bol}$-$kT_{\rm bb}$ diagram throughout the burst, as in van Paradijs et al. (1990) and Lewin et al. (1993). In order to have more points to trace the evolution of the burst in the diagram, I repeated the time resolved spectroscopy analysis with a finer time subdivision, i.e. of 14 5-seconds long intervals. In each of these intervals I calculated the 0.1-30 keV unabsorbed flux. As expected in the PRE case, the flux evolution is compatible with a constant up to a certain point (segment 8 in Fig. 4.9). Thereafter, the cooling phase, as witnessed by the flux decreasing, starts (9 in the same figure).
Finally, PRE bursts are more typically observed at low accretion regimes with He-rich material, when the fuel is more efficiently stored onto the NS surface, e.g. as in 4U 1812-12 (Cocchi et al. 2000). The 2015 bursts (including B2 and B3), on the contrary, are observed with likely short recurrence times in outburst, with duration and profiles fully compatible with the ignition of H-rich material, a trend which reminds of the "clocked burster" GS 1826-238 (see, e.g. Zamfir et al. 2012; Galloway et al. 2004), where PRE bursts are never observed. The 2012 burst (B1) occurred on the contrary during a low-level accretion phase and it might be more suggestive of a PRE episode.

4.6.1 Distance of RX1804 and its burst phenomenology

According to the time resolved spectral analysis (and the other clues presented in Section 4.6) of the 2012 type-I burst, it results that it underwent most likely a photospheric radius expansion, as assumed by Chenevez et al. (2012) and Chelovekov et al. (2017). Thus, the distance of RX1804 can be easily derived by using the critical Eddington luminosity reported in Kuulkers et al. (2003), i.e. $\simeq 3.79\times10^{38}$ erg s^{-1} with a 4% uncertainty. With a peak flux of $3.2^{+1.5}_{-1.1}\times10^{-8}$ erg cm^{-2} s^{-1}, I obtain a distance of $10.0^{+4.7}_{-3.5}$ kpc. The wide error range for the distance is a consequence of our conservative choice to estimate the errors of the peak flux (see subsection 4.6). If, alternatively, I consider a standard 10% uncertainty, I find a 10.0±1.4 kpc distance, which is compatible with the upper limit value reported by Chelovekov et al. (2017). This is significantly discrepant with the value of 5.8 kpc estimated by Chenevez et al. (2012). The reason is likely to rely on the method these authors used to estimate the burst peak flux, i.e. they compared the peak count-rate with the count-rate of the Crab, in order to express the flux in Crab units, and then converting this flux in c.g.s. This method can be reliable only when sources show Crab-like spectra or when fluxes are calculated within small energy bands. However, this is not the case for a type-I X-ray burst, whose spectrum has almost a black-body spectral shape, while the Crab spectrum is described by a power-law with Γ index of 2.1. The relatively high distance found for RX1804 would put the system likely beyond the Galactic

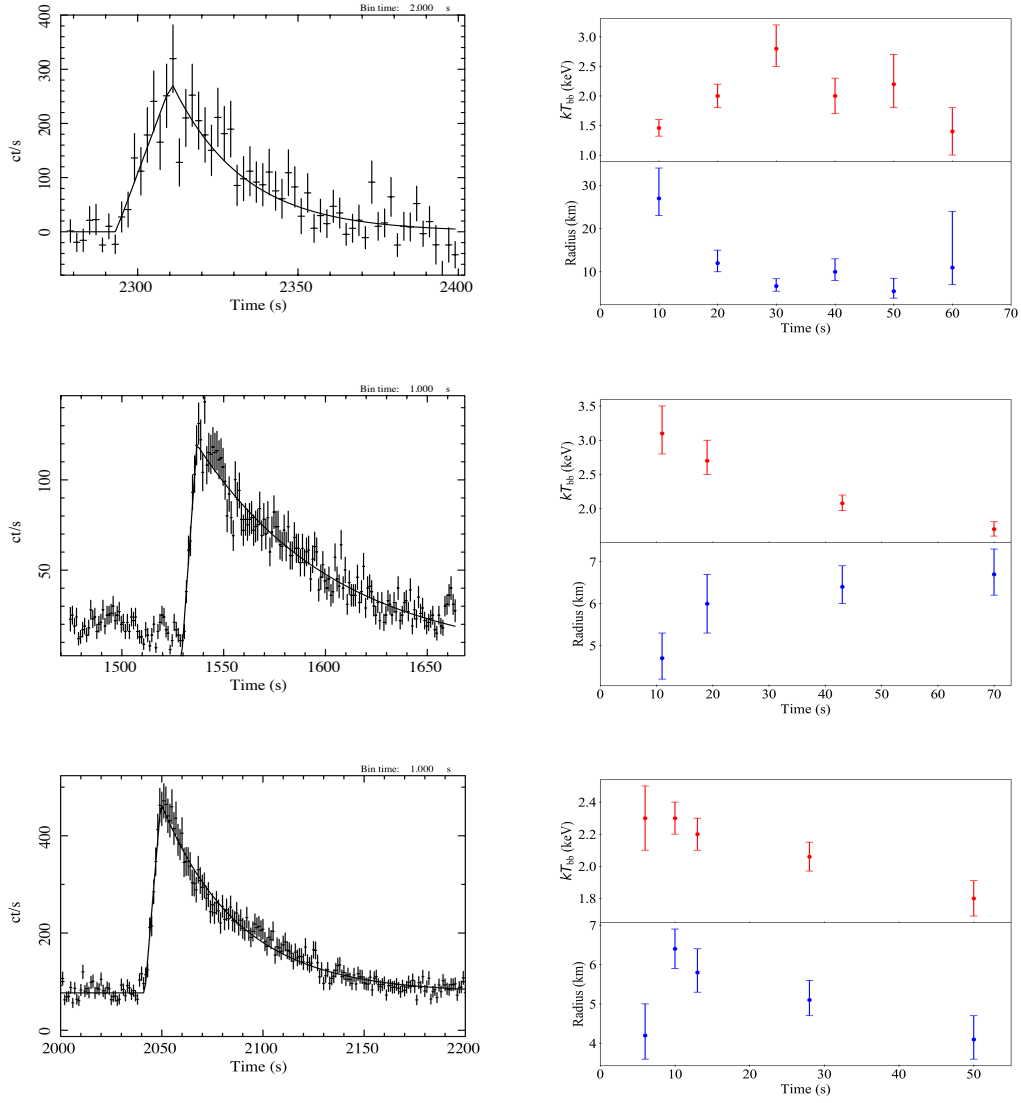

FIGURE 4.8: Light curve (*left*) and spectral parameters evolution over the whole burst duration (*right*) for the B1 (*top*), the B2 (*middle*) and the B3 bursts (*bottom*). Light curves have been fit by a BURS model. B1 is binned at 2 s, while B2 and B3 are binned at 1 s. The zero in the time interval was set to be equal to MJD56033.35963658 for B1, MJD57059.8920679 for B2 and MJD57113.70065027 for B3.

.

Time Resolved Spectroscopy

		Intervals					
		1	2	3	4	5	6
	Δt (s)	10	10	10	10	10	10
B1	$kT_{\rm bb}$ (keV)	1.46±0.14	2.00±0.20	$2.80^{+0.40}_{-0.30}$	2.00±0.30	$2.20^{+0.50}_{-0.40}$	1.40±0.40
	$R_{\rm bb}$ (km)	$27.0^{+7.0}_{-4.0}$	$12.0^{+3.0}_{-2.0}$	$6.7^{+1.7}_{-1.2}$	$10.0^{+3.0}_{-2.0}$	$5.5^{+3.0}_{-2.0}$	$11.0^{+13.0}_{-4.0}$
		1	2	3	4		
	Δt (s)	11.0	8.10	24.18	27.0		
B2	$kT_{\rm bb}$ (keV)	$3.1^{+0.4}_{-0.3}$	$2.7^{+0.3}_{-0.2}$	$2.08^{+0.12}_{-0.11}$	$1.70^{+0.11}_{-0.10}$		
	$R_{\rm bb}$ (km)	$4.7^{+0.6}_{-0.5}$	6.0±0.7	$6.4^{+0.5}_{-0.4}$	$6.7^{+0.6}_{-0.5}$		
		1	2	3	4	5	
	Δt (s)	6.0	10.0	13.0	28.0	50.0	
B3	$kT_{\rm bb}$ (keV)	2.3±0.2	2.3±0.1	2.2±0.1	2.06±0.09	1.80±0.11	
	$R_{\rm bb}$ (km)	$4.2^{+0.8}_{-0.6}$	6.4±0.5	$5.8^{+0.6}_{-0.5}$	$5.1^{+0.5}_{-0.4}$	$4.1^{+0.6}_{-0.5}$	

TABLE 4.8: Summary of the results obtained from the three selected type-I X-ray bursts, through time resolved spectroscopy. For B1 I used JEM-X1 and JEM-X2 combined data, while XRT data were used for B2 and *NuSTAR* data for B3. Spectra are fitted with a TBABS×BBODYRAD model. Errors at 68% confidence level are reported.

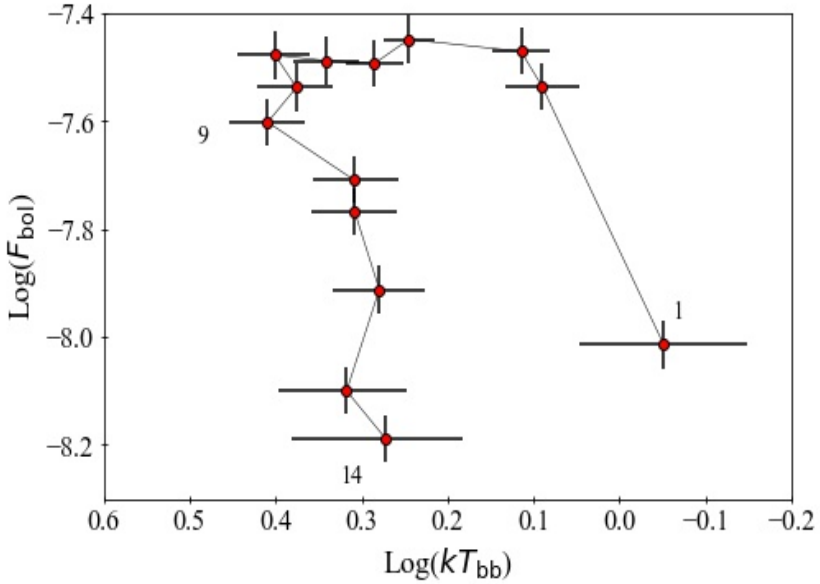

FIGURE 4.9: Flux-temperature diagram for B1, with a 14-intervals time subdivision. The start time is the same as interval 1 in Table 4.8. The data points have been connected to give chronological order.

Center. This is not troublesome, since the system has a ∼6.6° angular separation from Sgr A* and it is probably located in or right beyond the Galactic Bulge. This region seems to be inhabited by most of the VFXTs discovered so far (in't Zand 2001; Muno et al. 2005; Wijnands et al. 2006; Degenaar et al. 2012), therefore this new estimate of the distance seems reasonable. However, although using PRE bursts to infer distances is an extremely useful tool and it has been vastly employed to NS-LMXBs in the past, the method does suffer from systematic uncertainties (see 4.2), especially without precise information on the mass and the radius of the NS or on its atmospheric composition. It is therefore necessary to consider the distance estimates given in this Chapter with a bit of caution. The average duration of all the bursts reported in this work, i.e. around 100 s, seems compatible with low mass-accretion rates (Fujimoto et al. 1987) of a H/He mixed material, which usually gives bursts lasting less than 100 s (in't Zand et al. 2005). Furthermore, the "clocked burster" behaviour requires also accreted material with low metallicity (Galloway et al. 2004; Lampe et al. 2016). Although its burst phenomenology likely points out the presence of H and He in the accreted material, it is noteworthy that its optical spectrum seems somewhat lacking of hydrogen and He I lines, as reported by Baglio et al. (2016). This evidence, combined with the detection of a He II line, was used by the authors to propose RX1804 being an UXCB harbouring a helium white dwarf. However, a helium dwarf companion scenario seems hard to reconcile with the hydrogen/helium bursts exhibited by RX1804, therefore the UCXB nature of the system needs additional evidence to be confirmed. An alternative explanation could be that RX1804 harbours a brown dwarf (BD) companion, as in the case of SAX J1808.4–3658 (Bildsten and Chakrabarty 2001), which also shows bursts from mixed H/He material (Galloway and Cumming 2006). In addition, BDs have been proposed as donor stars in VFXT systems by King and Wijnands (2006). However, it is worth noticing that hydrogen lines are present in the optical spectrum of SAX J1808.4–3658 (Elebert et al. 2009). I conclude that the nature of the donor star in RX1804 remains a puzzle, which only new studies and observation could solve.

4.7 Summary & Conclusions

In this chapter I attempted to perform a comprehensive study of RX1804, an ex-"burst only" source, in two aspects of its X-ray activity: the long outburst occurred in 2015 and type-I X-ray bursts. I tried first to reconstruct the spectral behavior of the source during the whole 4-months outburst taking advantage of the broad band coverage by XRT and BAT together. I then paired three *NuSTAR* observations with three, quasi-simultaneous, XRT and BAT spectra to analyze the reflection continuum. On the other hand, I performed time resolved spectroscopy of three bursts, one observed by *INTEGRAL* one by XRT during the hard state and one by *NuSTAR* when the source was in intermediate state. The results of this work can be summarized as follows:

- I was able to follow the spectral evolution of the source all along the outburst, catching the source in an intermediate spectral state, rarely observed in NS-LMXBs.
- The *NuSTAR* and BAT data reveal the arising of a hard tail in the intermediate state, modelled as a power-law, pointing out that non-thermal processes are likely at play during the state transition.
- In the hard state, a model composed of two Comptonization spectra interacting with the same hot corona well describes the data, indicating that RX1804 belongs to the "two-photon" population, as e.g. the other bright burster GS 1826-238 (Cocchi et al. 2011). I suggest here

that the presence of two Comptonization spectra does explain the so-called "very hard" spectral state claimed for the source (Parikh et al. 2017).

- The *NuSTAR* analysis confirms the accretion physics scenarios resulted by the *Swift* spectra. In addition, it reveals a reflection contribution below 20% in all the states. However, with the applied Compton reflection modeling, only lower limits could be provided on the inner disk radius and no constraints on the inclination of the system.
- I found different hints suggesting that a Photospheric Radius Expansion burst occurred in 2012. This allowed me to confirm the distance of $\sim$10 kpc estimated by Chelovekov et al. (2017).
- Interestingly, during the intermediate state, I unveiled a "clocked burster" behaviour, with recurrence time of roughly 4000 s.

A study similar to the one presented here and led independently confirms a number of these conclusions (Fiocchi et al. 2019).
It is still unclear how systems like RX1804 exhibit different levels of X-ray activity in time-scales of years, transitioning from very faint outbursts to bright outbursts, as also observed in BH transients. This peculiar (and quite common) behaviour remains an open question in the framework of the Disk Instability Model, shedding light on how important and necessary are further investigations on the topic.

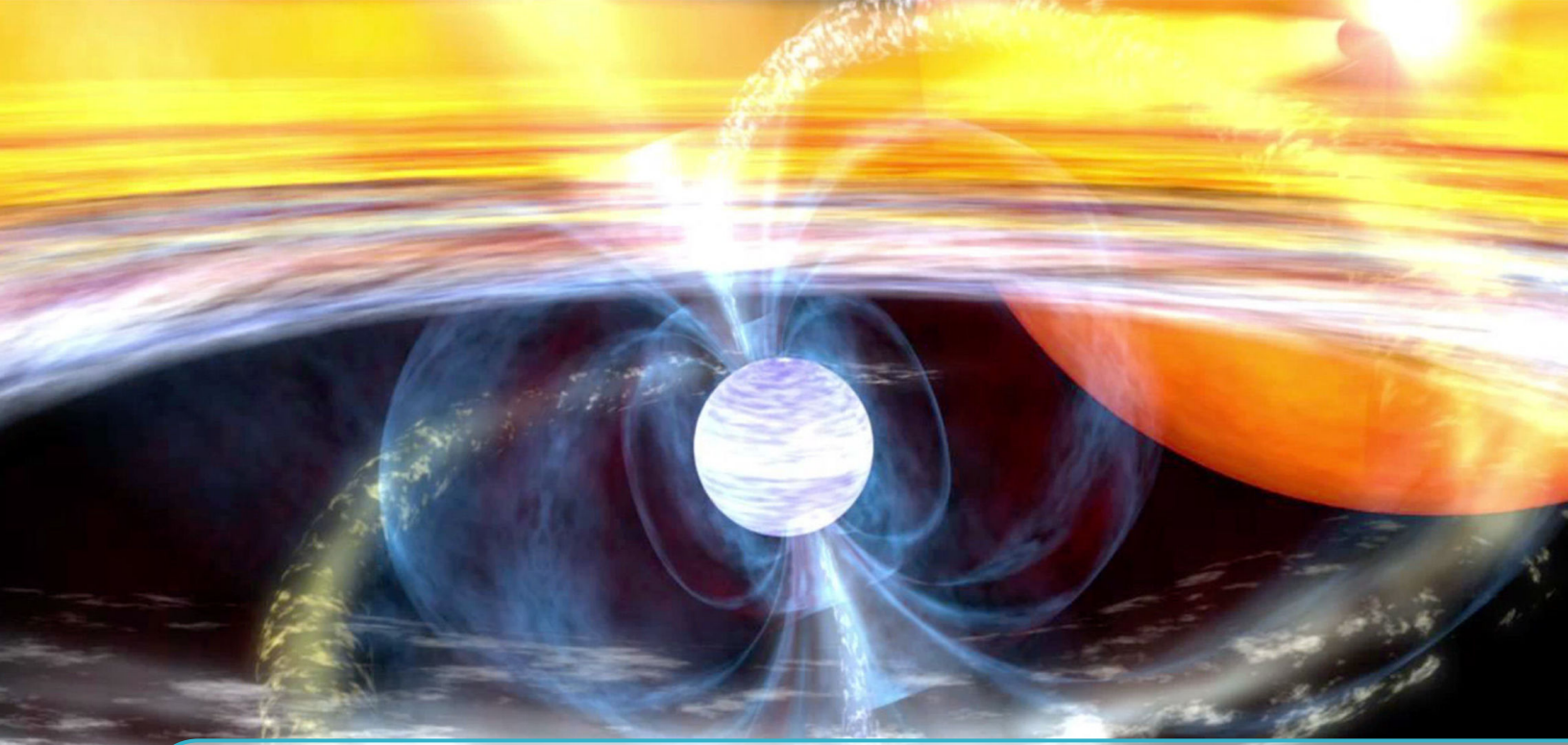

5. Indications of non-conservative mass-transfer in AMXPs

SUMMARY

Since the discovery of the first Accreting Millisecond X-ray Pulsar SAX J1808.4-3658 in 1998, the family of these sources kept growing on. Currently, it counts 22 members. All AMXPs are transients with usually very long quiescence periods, implying that mass accretion rate in these systems is quite low. Moreover, for at least three sources, a non-conservative evolution was also proposed. In this Chapter, I studied the long term averaged mass-accretion rates in all the Accreting Millisecond X-ray Pulsars discovered so far, to investigate a non-conservative mass-transfer scenario. I calculated the expected mass-transfer rate under the hypothesis of a conservative evolution based on their orbital periods and on the (minimum) mass of the secondary (as derived from the mass function), driven by gravitational radiation and/or magnetic braking. Using this theoretical mass-transfer, I determined the expected accretion luminosity of the systems. Thus, I achieved the lower limit to the distance of the sources by comparing the computed theoretical luminosity and the observed flux averaged over a time period of 20 years. Then, the lower limit to the distance of the sources has been compared to the value of the distance reported in literature to evaluate how reasonable is the hypothesis of a conservative mass-transfer. Based on a sample of 18 sources, I found strong evidences for a non-conservative mass-transfer for five sources, for which the estimated distance lower limits are higher than their known distances. I also report hints for mass outflows in other six sources. The discrepancy can be fixed under the hypothesis of a non-conservative mass-transfer in which a fraction of the mass transferred onto the compact object is swept away from the system, likely due to the (rotating magnetic dipole) radiation pressure of the pulsar.

5.1 The recycling scenario

At the end of Subsection 1.2.1 I left an intriguing question unanswered: how is the existence of old but yet extremely fast spinning radio pulsars as millisecond radio pulsars (MSPs) possible? The first clue to solve this mystery was already *hidden in plain sight* in the BP diagram in Figure 1.2 (*Right*), where the distribution of binary pulsars and MSPs almost overlap. Indeed, a vast majority of the known MSPs belong to binary systems with low-mass companions, i.e. with mass lower than about 1 $M_{\odot}$. While on its own a pulsar would evolve towards inactivity and rest peacefully in the pulsar graveyard, in a binary system the interaction with the companion star might somehow increase the spin frequency to such an extent that the "dead" pulsar becomes able to cross the *death line* and reappear as a radio pulsar. Indeed, this could happen in LMXBs, where the interaction between the accretion disk and the weak magnetic field of the pulsar can lead to phenomena of spin-up (or spin-down). This is the so-called **recycling scenario** (see, for a review, Bhattacharya and van den Heuvel 1991). The conditions for such fascinating mechanism to occur will be explored in the next subsection.

5.1.1 How to spin-up a pulsar

In Chapter 2 I mentioned several times that in LMXBs the disk is expected to be truncated, mainly in order to explain the observed spectral shape. Radius truncation, however, is crucial also to explain spin-up in recycled pulsars. In magnetized NSs, the magnetic field exerts a magnetospheric pressure on the infalling matter transferred from the companion and is in principle able to halts accretion. The pressure exerted by the magnetic field can be expressed as $B^2/8\pi$, which decays as r^{-6}, while the ram pressure of the infalling matter is given by ρv^2, with ρ density and v the (free-fall) velocity of the transferred matter, which goes as $r^{-1/2}$. By balancing these two pressures, it is possible to obtain the expression of a radius, i.e. the so-called **Alfven radius** $R_{\rm A}$:

$$R_{\rm A} = \left(\frac{\mu^4}{2GM_{\rm NS}\dot{M}} \right)^{1/7} \tag{5.1}$$

with μ the magnetic dipole momentum and $\dot{M}$ the mass-transfer rate. In order to extend Eq. 5.1 to the more specific case of an accretion disk, $R_{\rm A}$ must be multiplied for a factor ϕ which measures the distortion of the magnetic field lines due to the interaction with the accretion disc and it is usually comprised between 0.3 and 0.5 (see, e.g. Burderi et al. 1996). This more realistic description of the truncation radius for the accretion disk is defined as the **magnetospheric radius** $r_{\rm m}$. At the magnetospheric radius the disk and the magnetic field interact directly and eventually exchange angular momentum. In order to determine if this interaction leads to a spin-up (spin-down) it is useful to introduce another quantity, the **co-rotation radius** $r_{\rm CO}$, i.e. the radius at which the accretion disk, which I recall moves with Keplerian velocity, spins at the same frequency of the NS. Three possible scenarios can be envisaged:

- if $r_{\rm m} > r_{\rm CO}$ (i) at its inner radius, the disk is slower than the NS magnetic field lines anchored to it. The resulting torque exerted by the accretion flow forces the NS to spin-down. The fastly rotating magnetic field will also create a centrifugal barrier which prevents matter to penetrate further into the magnetosphere[1] (**propeller effect.**).

[1] However, in real life this is not necessarily true and at least a fraction of matter is likely able to avoid the centrifugal sweep and be accreted, as shown by magneto-hydrodynamical simulations (see, e.g. Romanova et al. 2005)

- if $r_m < r_{CO}$ (ii), the disk is moving faster than the NS and exerts a spin-up torque. This phenomenon is expected to occur in NS LMXBs (e.g. Ghosh and Lamb 1979), where the NS have "old" and thereby weak magnetic fields and the accretion flow is able to reach the proximity of the compact object.

- if $r_m = r_{CO}$ (iii) no exchange of angular momentum occurs and the system reaches a stable configuration.

The case illustrated in (ii) is what is believed happens in aging pulsars beyond the death line with a low-mass companion star. When the recycled pulsar crosses again the death line it becomes potentially observable as a radio millisecond pulsar; however, if the NS is still accreting matter, it is expected that the accreted material fills the NS magnetosphere, preventing the pulsar mechanism to work[2]. Indeed MSPs can be observed as radio pulsars if the companion evaporates or it is extremely small and degenerate, so that accretion is halted. In the latter case, it is common to distinguish between two "*Spider*" classes of sources depending on whether the secondary star is close to fill up its Roche lobe: in this case, the systems are called **redbacks**, while if the companion star is too small to fill the lobe the sources are labeled **black widows** (see, for a review, Roberts et al. 2018). In black widow systems, the companion star is slowly ablated by the impact of the pulsar wind, which will eventually lead them to evaporate. These systems are likely the evolutionary chain between binary MSPs and isolated MSPs.
The theory of recycling scenario is therefore able to explain how extremely fast and extremely old radio pulsars could exist, but until 20 years ago it lacked of an experimental confirmation, i.e. the evidence that accreting NSs in LMXBs could be spun up to such short spin periods. This evidence is represented by the existence of the so-called **Accreting Millisecond X-ray Pulsars**, which will be the topic of the following Section.

5.2 Accreting Millisecond X-ray Pulsars

The first observational confirmation of the recycling scenario arrived when the NASA X-ray Observatory Rossi X-ray Timing Explorer (*RXTE*) discovered the first LMXB exhibiting X-ray coherent pulsations, i.e. SAX J1808.4-3658 (Wijnands and van der Klis 1998). In this system, the matter accreted close to the NS surface, i.e. within the magnetospheric radius, was channeled along the magnetic field lines and accreted mainly onto the poles, so that the emitted X-ray radiation would appear pulsed for a lighthouse effect analogous to the one characteristic of radio pulsars.

Since 1998, other 22 AMXPs have been discovered with spin periods ranging between 1.7 and 9.5 ms (see, e.g. Patruno and Watts 2012; Campana and Di Salvo 2018), the most recent one discovered by *NICER* (Ng et al. 2020). AMXPs are usually found in compact binary systems, as witnessed by their relatively short orbital periods (with a few exceptions, the most relevant one is Aql X-1, which has an orbital period of 19 hr, Chevalier and Ilovaisky 1991; Welsh et al. 2000), from $\sim$ 40 min to a few hours, and therefore they probably host very low-mass donor stars, with $M \leq 0.2 M_{\odot}$. All AMXPs known so far are X-ray transients; some of them show outbursts every few years (such as SAX J1808.4-3658, which goes in outburst every $\sim$ 2.5 years) while others have been observed in outburst only once since their discovery, e.g. XTE J0929-314 and XTE J1807-294 (Galloway et al. 2002; Riggio et al. 2008). The duration of the outbursts can also be quite long, as in the case of HETE J1900.1-2455 (in outburst for $\sim$ 10 years, Šimon 2018) and MAXI J0911-655 (which is in an

[2]However, the reason for the lack of detected radio pulsations in LMXBs hosting pulsars is not completely established and other theories have been proposed, (see, for a discussion Patruno and Watts 2012).

ongoing outburst since 2016, Sanna et al. 2017c). Interestingly, when in outburst, pulsations could be intermittent and somehow disappear, as observed for three systems, e.g. HETE J1900.1-2455 (Patruno 2012), SAX J1748.9-2021 (Patruno et al. 2009a; Sanna et al. 2016) and Aql X-1, arguably the most exotic one as it showed coherent X-ray pulsations only during a single ∼150-s long data segment (out of ∼1 Ms of *RXTE* data, Casella et al. 2008). The origin of intermittency is still an enigma, even if the fact that all these intermittent AMXPs seem to have an average long term accretion rate higher than the other AMXPs (Campana and Di Salvo 2018) could point out that some screening effect of the magnetic field from the accreted matter could be at play (Patruno 2012).
AMXPs are usually faint LMXBs, with luminosities below 10% $L_{\rm Edd}$ and hard X-ray spectra, with little spectral evolution during the outburst (Campana and Di Salvo 2018). The perhaps only exception is represented by SAX J1748.9-2021, which was also found in the soft state (Pintore et al. 2016). In Table 5.1 I present a summary of the main properties of these sources[3], i.e. spin period P_{ms}, orbital period P_{orb}, mass function f_X, the minimum mass for the companion star $M_{2,min}$, the distance and the year when pulsations were observed for the first time. The table is an updated version of Table 1 in Campana and Di Salvo (2018). The minimum mass is estimated from the mass function f_X fixing the inclination of the system to 90°.
While many new AMXPs were discovered, a direct and so even stronger confirmation of the recycling scenario was found in 2013, when *XMM-Newton* observed a source previously classified as a radio millisecond pulsar, i.e. IGR J18245-2452, that behaved as an AMXP during one X-ray active state (Papitto et al. 2013b). The source showed swings between X-ray, accretion-powered pulsations to radio, rotation-powered pulsations over short time-scales (less than a couple of weeks). Along with PSR J1023+0038[4] (Archibald et al. 2009, 2013) and XSS J12270-4859 (de Martino et al. 2013; Bassa et al. 2014; Papitto et al. 2015), IGR J18245-2452 is part of a sub-class of MSPs dubbed **transitional millisecond pulsars**. These sources are the living proof that radio MSPs, AMXPs and LMXBs may be considered different seasons of the lifetime of a low-mass binary system hosting a neutron star (see, for a review Di Salvo and Sanna 2020).

5.3 Evidences of non-conservative mass-transfer

As explained in Subsection 2.3.2, binary stars follow a certain evolutionary path according mainly to the amount of angular momentum lost via Gravitational Radiation (GR) or Magnetic Braking (MB). Knowing the orbital evolution of such systems and how it leads to the formation of MSPs is vital to confirm the recycling scenario. Furthermore, it allows scientists to test alternative theories of Gravity with respect to General Relativity (Will 2006) or deviations from it (Psaltis 2008). In order to track the orbital evolution of a NS LMXB, one needs to take the time of passage of the NS through the ascending node at each orbit and to track how it changes over a certain time scale. AMXPs are transients, so that it is possible to measure the orbital period with high precision of the system only during an outburst. This aspect is critical since so far only for a handful of systems more than a single outburst was observed. For these systems, the variation of the orbital period points out that, as expected, they are undergoing an orbital expansion. However, only IGR J0029+5934 seems to expand at a rate which is compatible with the one expected including only

[3]The Table and the following work does not include IGR J17494-3030, since it was discovered as an AMXP after the writing of this chapter and the related paper.

[4]Note that it has been recently proposed that PSR J1023+0038 might not be in an accretion-powered pulsar phase even when the X-ray pulsations are clearly detected (Papitto et al. 2019).

TABLE 5.1: **List of the AMXPs discovered so far and their main properties**

Source	P_{orb} (hr)	P_s (ms)	f_X ($M_\odot$)	$M_{2,min}$ ($M_\odot$)	Year of discovery	Ref.
Aql X-1	18.95	1.7	1.4×10^{-2}	0.56	2008	[6], [14]
IGR J18245-2452	11.03	3.9	2.3×10^{-3}	0.17	2013	[17]
Swift J1749.4–2807	8.82	1.9	5.5×10^{-2}	0.59	2010	[3]
IGR J17591-2342	8.80	1.9	1.5×10^{-2}	0.42	2018	[23]
SAX J1748.9–2021	8.77	2.3	4.8×10^{-3}	0.10	2008	[1]
XSS J12270–4859	6.91	1.7	3.9×10^{-3}	0.27	2015	[18]
PSR J1023+0038	4.75	1.7	1.1×10^{-3}	0.20	2009	[4], [7]
XTE J1814–338	4.27	3.2	2.0×10^{-3}	0.17	2003	[13]
IGR J17498–2921	3.84	2.5	2.0×10^{-3}	0.17	2011	[16]
IGR J17511–3057	3.47	4.1	1.1×10^{-3}	0.13	2010	[15]
IGR J00291+5934	2.46	1.7	2.8×10^{-3}	0.039	2005	[9]
SAX J1808.4–3658	2.01	2.5	3.8×10^{-5}	0.043	1998	[25]
IGR J1737.9-3747	1.88	2.1	8.5×10^{-5}	0.056	2018	[21]
HETE J1900.1-2455	1.39	2.7	2.0×10^{-6}	0.016	2006	[10]
NGC6440 X–2	0.95	4.8	1.6×10^{-7}	0.00067	2010	[2]
Swift J1756.9–2508	0.91	5.5	1.6×10^{-7}	0.0070	2007	[11]
IGR J16597–3704	0.77	9.5	1.2×10^{-7}	0.0060	2017	[20]
MAXI J0911–655	0.74	2.9	6.2×10^{-6}	0.024	2016	[19]
XTE J0929–314	0.73	5.4	2.9×10^{-7}	0.0083	2002	[8]
XTE J1751–305	0.71	2.3	1.3×10^{-6}	0.014	2002	[12]
XTE J1807–294	0.67	5.3	1.5×10^{-7}	0.0066	2003	[5]
IGR J17062-6143	0.64	6.1	9.1×10^{-8}	0.00060	2017	[24]

In the table P_{orb} is the orbital period, P_s is the spin period of the pulsar, f_X is the mass function and $M_{2,min}$ is the minimum mass for the companion, evaluated from f_X for an inclination of 90°. References: [1]=Altamirano et al. (2008a), [2]=Altamirano et al. (2010a), [3]=Altamirano et al. (2011), [4]=Archibald et al. (2009), [5]=Campana et al. (2003), [6]=Casella et al. (2008), [7]=Coti Zelati et al. (2014), [8]=Galloway et al. (2002), [9]=Galloway et al. (2005a), [10]=Kaaret et al. (2006), [11]=Krimm et al. (2007), [12]=Markwardt et al. (2002b), [13]=Markwardt et al. (2003), [14]=Mata Sánchez et al. (2017), [15]=Papitto et al. (2010), [16]=Papitto et al. (2011a), [17]=Papitto et al. (2013b), [18]=Roy et al. (2015), [19]=Sanna et al. (2017c), [20]=Sanna et al. (2018a), [21]=Sanna et al. (2018b), [22]=Sanna et al. (2018d), [23]=Sanna et al. (2018c), [24]=Strohmayer et al. (2018), [25]=Wijnands and van der Klis (1998).

angular momentum losses via GR (see, e.g. Sanna et al. 2017a). For the other systems, i.e. SAX J1808.4-3658[5] (Di Salvo et al. 2008; Burderi et al. 2009), IGR J1737.9-3747 (Sanna et al. 2018b), Swift J1756.9-2508 (Mukherjee et al. 2015), IGR J17511-3057 and SAX J1748.9-2021 (Di Salvo and Sanna 2020), the observed strong orbital expansion rates are hard to explain. The observed orbital period derivatives would require high mass-transfer rates (see Eq. 2.10) which, in the case of a conservative mass-transfer scenario, would be translated in a high average mass-accretion rate, e.g. a high average X-ray luminosity. However, this seems not to be the case for AMXPs, which are transients and usually show sporadic and faint X-ray outbursts. On the contrary, if we admit that at least a fraction of the transferred mass somehow leaves the system and removes from it a fraction of angular momentum (**non-conservative mass-transfer scenario**, NCMT) we could explain both the observed faint X-ray activity and the fast orbital expansion. This scenario has been proposed for the AMXPs SAX J1808.4-3658 (Di Salvo et al. 2008; Burderi et al. 2009; Sanna et al. 2017a) and SAX J1748.9-2021 (Sanna et al. 2016). Matter ejections have been also suggested to explain the low, average, mass-transfer rate derived for XTE J1814-338 (Van et al. 2018).

It is still unclear the physical mechanism inhibiting a fully conservative mass-transfer in these systems. A model which would explain this phenomenon was proposed by Burderi et al. (2001) and it is known as the *radio ejection* model. It predicts that a non-conservative mass-transfer may arise in LMXBs hosting rapidly rotating pulsars when the radiative pressure of the pulsar, emitting as a magnetic-dipole rotator, overcomes the ram pressure of the accreting matter, throwing it away from the system. It is noteworthy that the arising of a phase where the electromagnetic pressure of the pulsar wind is strong enough to halt the accretion flow beyond the light cylinder has been predicted also using general-relativistic simulations by Parfrey and Tchekhovskoy (2017).

While the theory of a NCMT scenario seems promising, it can be directly tested only for a few AMXPs, i.e. the few sources for which more than one outbursts was observed. Most of them have been indeed observed in outburst only once and it is unknown how long will it take for catching them in outburst again. However, it is possible to test the NCMT scenario for an AMXP even ignoring its orbital evolution: Marino et al. (2017) invoked a non-conservative mass-transfer to explain the discrepancy between the observed averaged luminosity and the expected luminosity, estimated on the basis of a conservative evolutionary model driven by Gravitational Radiation (GR) (Verbunt and van den Heuvel 1995) for XTE J0929-314. Furthermore, a recent work by Ziółkowski and Zdziarski (2018) shows with a similar argument how also systems hosting BHs might undergo a secular evolution driven by non-conservative mass-transfer. In these systems, radio ejection is clearly out of the picture; in that case, matter outflows in the form of jets and winds have been invoked to explain the phenomenon.

In this chapter I use the same argument as for XTE J0929-314 and I apply it to almost the complete sample of AMXPs, with the aim of exploring how common (or uncommon) non-conservative mass-transfer is among such sources. The results of this chapter have been published in Marino et al. (2019b), which I wrote also in collaboration with the high energy astrophysics group of the University of Cagliari and Dr. Alessandro Papitto, from INAF Rome.

5.4 The method

The method applied here is based on the comparison between the expected average luminosity, L_{exp}, expected in the case of an orbital evolution induced by conservative mass-transfer, and the

[5] In the very last outburst, dated 2019, the observed curve for the times of passage showed an inversion of the trend and a puzzling flattening, for which no clear explanation has been found yet (Bult et al. 2020).

observed averaged X-ray luminosity. This comparison gives an estimation of the lower limit to the source distance, which is used as a test of how reliable the conservative hypothesis is. The same strategy has been already applied to several non-burster AMXPs in order to constrain their distances (Galloway 2006) and to the AMXP XTE J0929-314, with the aim of proving the unlikeliness of a conservative mass-transfer in this system (Marino et al. 2017).

5.4.1 Expected Luminosity

Recalling Equation 2.4, the expected luminosity of a LMXB might be simply expressed as $L_{exp} = -\frac{GM_1\dot{M}_2}{R}$, where M_1 is the mass of the accretor while $\dot{M}_2$ is the (intrinsically negative in the considered case) mass-transfer rate of the donor, in the hypothesis that the whole mass transferred from the secondary is accreted onto the NS. Assumptions can be made about M_1 and R according to the standard values associated to neutron stars and/or the latest results in the search for the NS mass and radius. In order to have a lower limit for the expected luminosity I should choose a lower limit for both the masses and an upper limit for the radius. Here I assumed the mass of the NS equal to 1.4 $M_\odot$, which is low enough to be considered a reasonable lower limit giving that the current record-holder for the least massive NS is PSR J0453+1559, with a mass of 1.174±0.001 $M_\odot$ (Martinez et al. 2015). Furthermore, according to Özel et al. (2012), the distribution of the NS masses is double-peaked, with two maxima corresponding to 1.28 $M_\odot$ (with a dispersion of 0.24 $M_\odot$) and 1.54 ± 0.23 $M_\odot$ (with a dispersion of 0.20 $M_\odot$), for NSs in non-recycled eclipsing high-mass binaries and for slow pulsars or NSs in recycled systems, which have experienced several episodes of accretion, respectively. The NSs inhabiting the sources analyzed in the present work belong to the second family, therefore a 1.4 $M_\odot$ seems like a reasonable choice. Concerning the radius, I chose 12 km as an upper limit, based on the 9.9-11.2 km range reported by Özel and Freire (2016).

The minimum donor mass for each system was determined on the basis of its mass function f, reported in Table 5.1. Considering the lack of eclipses and/or dips ever observed for all the systems in the class with the exception of one - Swift J1749.4–2807 (Altamirano et al. 2011) - I exclude inclination angles $i > 60°$, and then I estimated the lower limit for the secondary accordingly. Coherently, for the only eclipsing AMXP discovered so far, this lower limit was estimated fixing the inclination to 90°.

An estimate of $\dot{M}_2$ requires the introduction of a theoretical orbital evolution model. This model can be obtained from Eq. 2.11 by including the mechanisms of angular momentum loss $\dot{J}$ and extending it to a NCMT scenario.

In the following, I will start by combining the Kepler's third law with the condition that the neutron star is accreting matter from the companion via Roche Lobe overflow. The latter can be expressed as:

$$\frac{\dot{R}_2}{R_2} = \frac{\dot{R}_{L2}}{R_{L2}} \,, \tag{5.2}$$

where R_2 and R_{L2} are the radii of the secondary and of its Roche Lobe (see Eq. 2.8), respectively. Equation 5.2 guarantees that during the whole evolution of the system the secondary star fills the Roche Lobe. I assume then a mass-radius relation $R_2 \propto M_2^n$, with M_2 the mass of the secondary, and the Paczyński (1971) approximation for the Roche lobe radius $R_{L2} = 2/3^{4/3}[q/(1+q)]^{1/3}a$ (valid for $q = M_2/M_1 \leq 0.8$), where a is the orbital separation. I am also taking into account two possible mechanisms of angular momentum loss that, in turn, drive the mass-transfer process from

the donor star: gravitational radiation (GR) and magnetic braking (MB). According to this model, the mass-transfer rate $\dot{m}_{-9}$, in units of $10^{-9} M_{\odot} yr^{-1}$ can be expressed as:

$$\dot{m}_{-9} = 4.03\, m_1^{8/3} P_{2h}^{-8/3} \left[\frac{q^2}{\left(2g(\alpha,\beta,q) - \frac{1}{3} + n\right)(1+q)^{1/3}} \right] \times [1 + T_{MB}] \tag{5.3}$$

where:

$$g(\alpha,\beta,q) = 1 - \beta q - \frac{1-\beta}{1+q}\left(\frac{q}{3} + \alpha\right) , \tag{5.4}$$

(see Di Salvo et al. 2008; Burderi et al. 2009, 2010) where m_1 is the mass of the primary star in units of $M_{\odot}$, P_{2h} is the orbital period in units of 2hr, n is the index of the mass-radius relation, β is the fraction of mass lost by the donor and accreted onto the NS, α is the specific angular momentum carried by the matter ejected from the system in the case of a non-conservative mass-transfer and T_{MB} is the strength of the torque associated to MB. The parameter T_{MB} can be parametrised in units of the GR torque as in Burderi et al. (2010)[6], in line with Verbunt and Zwaan (1981); Verbunt et al. (1994); Tauris (2001), as:

$$T_{MB} = 8.4 (k^2)_{0.1} f^{-2} m_1^{-1} P_{2h}^2 q^{1/3} (1+q)^{2/3} \tag{5.5}$$

where k is the gyration radius of the secondary star and f is a dimensionless parameter which assumes a value of 0.79 or 1.78 (depending on Skumanich 1972; Smith 1979). In order to estimate the expected mass-transfer rate in the conservative case, I take $\beta = 1$.

The value of $\dot{m}$, given by Equation 5.3, is highly dependent on the mass of the secondary. On the one hand, because of the assumed mass-radius relation, the value of n changes according to M_2, on the other hand the MB is considered to become negligible (T_{MB}=0) in Ultra-Compact X-ray Binaries for fully convective stars with $M_2 \leq 0.3 M_{\odot}$ (Nelson and Rappaport 2003). However, the latter assumption has been questioned at least in one case. Indeed magnetic braking has been included to describe the evolutionary path of the AMXP SAX J1808.4-3658 during its whole history (Wang et al. 2013; Tailo et al. 2018), although its companion star is likely a brown dwarf with a mass ≤ 0.1 $M_{\odot}$. For uniformity, I considered both models, GR and GR+MB, to describe the mass-transfer in each system, fixing f to 1.78 in order to have a lower limit on T_{MB}. In the following, I will refer with $L_{exp,GR}$ to the expected luminosity in the GR-only case, and with $L_{exp,GR+MB}$ to the luminosity in the MB-included case.

Another assumption concerns the value attributed to n. In the case of a low-mass secondary star with $M_2 \leq 0.2 M_{\odot}$ I chose $n = -1/3$, the proper mass-radius index for fully convective or degenerate stars (Nelson and Rappaport 2003). On the other hand, for masses $M_2 \geq 0.40$ $M_{\odot}$, I assumed $n = 1$ to be a valid approximation (Chabrier and Baraffe 2000). Finally, I used the value of k computed for low-mass ($M_2 \sim 0.6$ $M_{\odot}$) stars (Claret and Gimenez 1990), i.e. $k = 0.378$. This value is expected to decrease for decreasing masses, therefore the estimated values for T_{MB} in the sources with secondary stars with masses $M_2 << 0.6\, M_{\odot}$ have to be considered as upper limits. Note, however, that the MB strength becomes negligible for small values of the orbital separation.

[6] In the cited equation two typos were present, in particular the constant was wrong and the factor $(1+q)^{2/3}$ was missing, therefore I report a corrected version of the same formula.

5.4.2 Observed Luminosity

To estimate the observed average luminosity I considered the energy released by the system during the outburst phase(s) as a good approximation of the whole amount of energy ever emitted by the source, ignoring both the energy released during type-I X-ray bursts and the energy radiated when the source was quiescent. Even if type-I X-ray bursts are among the most energetic displays of LMXBs activity, they usually last for less than an hour; therefore the amount of energy released is negligible if averaged over a baseline of several years. On the other hand, quiescence luminosity is likely at least 3 orders of magnitudes lower than the luminosity in outburst, a ratio which is significantly lower than the ratio between the duration of the outburst and the recurrence time between subsequent outbursts observed so far for AMXPs. Furthermore, accretion is considered to be almost shut off during quiescence (although residual accretion processes might still be ongoing in some quiescent LMXBs, see e.g. Wijnands et al. 2015), it is therefore reasonable to neglect the energy emitted during this phase.

A complication to this assumption could be represented by the possibility of "very faint" activity during quiescence, i.e. showing episodes of accretion at low luminosity (around 5×10^{33} erg s^{-1}) (see Section 4.1). Such outbursts would be too faint to be detected from any all-sky monitor and could be seen only with pointed observations. This type of peculiar behavior has been observed in transitional millisecond pulsars, lasting also for several years (Papitto et al. 2013b; Linares et al. 2014; Patruno et al. 2014), although also in this case the contribution of low-level accretion is not clear yet (see, e.g. Ambrosino et al. 2017). However, the correction to the calculated total energy output when considering these episodes would be significant, i.e. of the order of 10-20%, only in the case of decades of continuous accretion at $\sim 10^{33}$ erg s^{-1}). I then decided to neglect the energy emitted outside the outbursts.
Keeping this caveat in mind, the energy released during an outburst was then roughly estimated by calculating the area subtended by the light curve of the system in outburst, which is the observed fluence f, i.e. the total energy per unit area emitted during the outburst as received by the detector. To convert this fluence in the total energy radiated during the outburst, it is necessary to multiply it by a factor of $4\pi d^2$. I consider the distance as a free parameter for the moment and keep this total energy in the form $f \times 4\pi d^2$. In order to find the observed luminosity, i.e. $F_{av}\times 4\pi d^2$, where F_{av} is the average observed flux, one has to average the energy emitted during the outbursts, $f \times 4\pi d^2$, all along the period T the source was monitored by all-sky observatories.
I considered T equal to 20 years, because since 1996 the X-ray Sky was continuously monitored and any previous outburst would have been therefore recorded. In fact, in 1996, the ASM onboard *RXTE* and the Wide Field Cameras (WFC) onboard *BeppoSAX* started a continuous monitoring of the X-ray sky. This is today continued by *MAXI* onboard the International Space Station, the *Swift*/BAT (Burst Alert Telescope) hard X-ray monitor, *INTEGRAL*, and the Gamma-ray Burst Monitor (GBM) on board *Fermi*. A more conservative choice for T might have been the time elapsed since the discovery of the source, but it would leave out the most recently discovered AMXPs. However, in Section 5.6 a comparison between the results obtained with the 20 years-interval and the results obtained with the latter strategy will be presented.
Finally, under the hypothesis of a conservative mass-transfer, it is possible to solve the equation $F_{av}\times 4\pi d^2 = L_{exp}$ in order to find the distance d to the source; the discrepancy between my value of d and the value reported in literature is then used to quantify the unlikeliness of a conservative mass-transfer. Indeed, in the case of a non-conservative mass-transfer, the mass accretion rate would be lower than the mass transfer rate from the companion star, and this would result in a lower L_{exp}

and then in lower values for d, fixing in this way the discrepancy.

5.5 Data Analysis

I analyzed all the sources listed in Table 5.1, with the exclusion of three systems: Aql X-1, XSS J12270-4859, PSR J1023+0038. Aql X-1 is a peculiar source, given its relatively long orbital period with respect to every other AMXP and the fact that showed coherent X-ray pulsations only once since its discovery. Furthermore it displays a $\sim$ 70 days outburst per year (Ootes et al. 2018), therefore it is expected to have a high averaged mass-accretion rate, likely compatible with a conservative mass-transfer scenario. On the other hand the transitional MSPs XSS J12270-4859 and PSR J1023+0038 have been observed in X-rays only in short, sub-luminous outbursts or in flaring activity at low luminosity, i.e. $L_X \lesssim 10^{34}$ erg s^{-1}, under the detectability threshold of any X-ray all-sky monitor (Papitto et al. 2015; Coti Zelati et al. 2014). Quantifying the energy emitted during these episodes is not an easy task and, at least in the case of PSR J1023+0038, the emitted X-rays flux may not be related to accretion at all, as recently suggested by Papitto et al. (2019). Furthermore, a non-conservative mass-transfer scenario has been already hypothesized to explain the peculiar phenomenology of these systems (as suggested by Heinke et al. 2015). In the following I discuss the analysis carried out for the other nineteen sources. In this chapter, the results for XTE J0929-314 are also included for sake of completeness, even if its analysis has been extensively discussed by Marino et al. (2017).
For each source, I followed the methodology explained in subsection 5.4.1 in order to estimate the expected luminosity in both the case GR-only and MB-included. The results are reported in Table 5.3. For the moment, I used only the minimum mass M_2 for the companion, corresponding to the high inclination case, to have a lower limit on the distance of the source.

The estimation of the average observed flux F_{av} requires a study of the observational history of the sources in the last 20 years. I searched in the literature for published light curves of each outburst displayed by each AMXP in the sample. I analysed these light curves numerically, i.e. approximating their shape with a piecewise linear function and then calculating the area subtended by the function. In the analysed light curves, usually, the count rate of the instrument or the flux in a limited energy band is reported rather than the bolometric unabsorbed flux. I used the *HEASARC* Count Rate Simulator WEBPIMMS to convert count-rates and/or fluxes into unabsorbed 0.1-300 keV fluxes. In WEBPIMMS the spectrum of each source was described using a power-law, with the values of N_H and Γ reported in literature for that source. If the flux of the source was reported in Crab units, I assumed the Crab Γ index, i.e. $\Gamma = 2.1$, to convert the reported flux in bolometric flux. This procedure was not followed for IGR J00291+5934 and XTE J1751-305, whose outburst properties, including peak bolometric flux and outburst durations, were already reported in literature (respectively by De Falco et al. 2017b; Riggio et al. 2011). The spectral parameters of two sources during their outbursts were not available in literature, which are XTE J1814+338 and NGC 6440 X-2. While for the latter I described each of its short, subsequent outbursts with the same parameters reported by Heinke et al. (2010) for the first outburst, for XTE J1814+338 a rough spectral analysis of the source was performed using the *RXTE* standard products. Further details about this analysis are reported in the Appendix A. Finally, I followed a different procedure for IGR J17062-6143. Since the source has been persistently in a faint outburst from 2006 (Churazov et al. 2007), the year of its discovery, at a 2-20 keV luminosity of 5.8-7$\times 10^{35}$ erg s^{-1} (see Strohmayer et al. 2018, and references therein), I associated to the source a constant luminosity of 6.5$\times 10^{35}$ erg s^{-1} in the 2-20 keV band. Using the known distance of the source, i.e. 7.3 kpc (Keek et al. 2017), I estimated

the flux corresponding to this arbitrary, but compatible with the observations, luminosity. Finally I extracted the bolometric unabsorbed flux by means of WEBPIMMS and calculated $F_{av} \times 4\pi d^2$ accordingly.
The light curves of some outbursts of a few different sources have never been published in literature. This was the case for IGR J17591-2342, SAX J1748.9-2021, SAX J1808.4-3658, IGR J1737.9-3747 and Swift J1756.9-2508 (see Table 5.2). For these cases, I used the archival data of all-sky monitors such as *ASM* onboard *RXTE*, *BAT* onboard *Swift* and *MAXI*, in order to reproduce the light curves of their outbursts[7].
The outburst properties (duration and peak bolometric flux) of the AMXPs are summarized in Table 5.2. As shown in this Table, the phenomenology of AMXPs is far from being homogeneous; while most of the sources in the class (10 over 19, including XTE J0929-314) have undergone only one outburst in at least 20 years, almost the other half has shown multiple outbursts. An interesting case is represented by NGC 6440 X-2, which between 2009 and 2011 showed frequent but faint and short (around 3 days each) outbursts (Patruno and D'Angelo 2013).

The analysis of each outburst, by means of the values reported in Table 5.2, led to the estimation of the fluence of the source. Following the recipe of subsection 5.4.2, I calculated the observed luminosity of the source. By equating $L_{exp,GR}$ ($L_{exp,GR+MB}$) and $F_{av} \times 4\pi d^2$ I find the distance of the source under the hypothesis of a conservative mass-transfer. This distance is essentially a lower threshold for the distance of the source, due to the choice of fixing the donor mass to its minimum value. Furthermore, since switching on and off the magnetic braking in the adopted conservative model (Equation 5.3) gives two alternative expected luminosities, I will distinguish between two lower limits for the distance, i.e. the "GR-only" distance $d_{m,GR}$ and the "MB-included" distance $d_{m,GR+MB}$. The final results are presented in Table 5.3. In the same Table, the results for XTE J0929-314, already presented by Marino et al. (2017), are included in order to give a general picture of all the AMXPs to which this method has been applied. For ease of discussion, each source is labeled with an arbitrary number, as shown in Table 5.3, and in the following it will be indicated using this number.

5.6 Results

According to the general picture emerging from Table 5.3, I will discuss the sources distinguishing first between sources with unknown distance values and sources with a reported distance estimate (or at least an upper limit). For the latter sources, i.e. 14 over 19 sources in the sample, the comparison with the estimated distance lower limits is obviously easier, while in the discussion for the former sources the soundness of these distance limits will be considered. I checked if any of the available distance values could be updated using the public results of the Global Astrometric Interferometer for Astrophysics (*GAIA*) Gaia Collaboration et al. (2016), in the catalogue GAIA DR2 (Gaia Collaboration et al. 2018), excluding the Globular Clusters sources, since their distances are know with sufficient precision. For only 6 sources, i.e. S5, S7, S11, S17, S18 and S19 *GAIA* found counterparts within 2 arcsec error boxes. The distance ranges found for these optical counterparts are wide and always compatible with the distances reported in the literature (and in this chapter) and the association of these sources with the optical systems in the *GAIA* catalogue is not certain. I therefore decided not to include *GAIA* results in this work.
Among the 14 sources with a known distance, in 6 cases, i.e. SAX J1748.9-2021, SAX J1808.4-3658,

[7]The public data used here were downloaded from the online archives: https://heasarc.gsfc.nasa.gov/docs/xte/ASM/sources.html, https://swift.gsfc.nasa.gov/results/transients/ and http://maxi.riken.jp/top/index.html.

TABLE 5.2: **Outburst properties (until June 2019).**

Source	# of outbursts	Year	Duration (days)	Bolometric peak flux ($\times 10^{-8}$ erg cm^{-2} s^{-1})	References Light curves	References Spectral Parameters
IGR J18245-2452	1	2014	23	1.15	[4]	[4]
Swift J1749.4–2807	1	2010	11	1.52	[7]	[7]
IGR J17591-2342	1	2018	50	1.50	[b]	[32]
SAX J1748.9–2021	6	1998, 2001, 2005 2010, 2015, 2017	10, 53, 52 53, 58, 13	0.65, 1.30, 2.10, 4.20, 2.09, 1.73, 0.10	[1], [1], [1], [m], [m], [28]	[1], [1], [1], [25], [27], [28]
XTE J1814–338	1	2003	53	0.88	[11]	*
IGR J17498–2921	1	2011	37	2.00	[8]	[8]
IGR J17511–3057	2	2010, 2015	30, 25	0.40, 0.44	[20], [23]	[20], [23]
IGR J00291+5934	4	2004, 2008, 2008, 2015	14, 9, 15, 25	0.29, 0.15, 0.11, 0.35	[5] (all)	[5] (all)
SAX J1808.4–3658	7	1998, 2000, 2002, 2005, 2008, 2011, 2015	15, 14, 42, 28, 21, 16, 25	0.72, 0.12, 0.92, 0.63, 3.31, 2.24, 0.94	[11], [11], [11], [11], [3], [m], [19]	[12], [38], [18], [10], [3], [21], [6]
IGR J1737.9-3747	3	2004, 2008, 2018	50, 15, 10	0.330, 0.690, 0.014	[18], [18], [b]	[10], [10], [33]
HETE J1900.1-2455	1	2005	3784	2.40	[36]	[21]
NGC6440 X–2	10	2009, 2009, 2010, 2010, 2010, 2010, 2011, 2011, 2011, 2011	3 (all) 0.026	0.088, 0.35, 0.053, 0.088, 0.035, 0.079, 0.079, 0.026, 0.079,	[15] (all)	[13] (all)
Swift J1756.9–2508	3	2007, 2009, 2018	7, 15, 7	0.20, 0.26, 0.10	[15], [a], [2]	[15], [24], [34]
IGR J16597–3704	1	2018	17	1.80	[b]	[34]
MAXI J0911–655	1	2016†	910	0.13	[31],[x]	[31]
XTE J1751–305	4	2002, 2005, 2007, 2009	7, 3, 3 3	0.81, 0.11, 0.14, 0.22	[29] (all)	[29] (all)
XTE J1807–294	1	2004	100	0.49	[7]	[7]
IGR J17062-6143	1	2006†	4380	0.025	[37]	[14]

List of the AMXPs discovered so far and their main properties. The bolometric peak flux is the unabsorbed flux in the range 0.1-300 keV and an intrinsic standard 10% error was attributed to each value. The unpublished light curves were extracted from the public archives of: [a]=*All Sky Monitor* (ASM) onboard *RXTE*, [b]=*BAT* onboard Swift, [m]=*MAXI* and [x]=*XRT* onboard *Swift*. The references are divided in refereed publications where the light curve of the relative outburst is displayed and publications where the spectral parameters of the source during the outburst were reported. †: the outburst is still ongoing at the time of writing. References: [1]=Altamirano et al. (2008a), [2]=Bult et al. (2018), [3]=Cackett et al. (2009) [4]=De Falco et al. (2017a), [5]=De Falco et al. (2017b), [6]=Di Salvo et al. (2019), [7]=Falanga et al. (2005), [8]=Falanga et al. (2012), [9]=Ferrigno et al. (2011), [10]=Galloway et al. (2005b) [11]=Hartman et al. (2008), [12]=Heindl and Smith (1998), [13]=Heinke et al. (2010), [14]=Keek et al. (2017), [15]=Krimm et al. (2007), [16]=Linares et al. (2008), [17]=Markwardt et al. (2002a), [18]=Markwardt et al. (2008), [19]=Papitto et al. (2007), [20]=Papitto et al. (2010), [21]=Papitto et al. (2011b), [22]=Papitto et al. (2013a), [23]=Papitto et al. (2016), [24]=Patruno et al. (2009b), [25]=Patruno et al. (2010), [26]=Patruno and D'Angelo (2013), [27]=Pintore et al. (2016) [28]=Pintore et al. (2018), [29]=Riggio et al. (2011), [30]=Sanna et al. (2016), [31]=Sanna et al. (2017c), [32]=Sanna et al. (2018c), [33]=Sanna et al. (2018b), [34]=Sanna et al. (2018d), [35]=Sanna et al. (2018a), [36]=Šimon (2018), [37]=Strohmayer et al. (2018), [38]=Wijnands (2003)

TABLE 5.3: **Results**

#	**Source**	M_{min} $M_\odot$	$L_{exp,GR}$ (10^{35} erg s^{-1})	$L_{exp,GR+MB}$ (10^{35} erg s^{-1})	$F_{av} \times 4\pi d^2_{kpc}$ (10^{33} erg s^{-1})	**d** (kpc)	**Method**	$d_{m,GR}$ (kpc)	$d_{m,GR+MB}$ (kpc)
S1	IGR J18245-2452	0.21	0.21	1.40	1.32(13)	5.5 [4]	GC	3.97(19)	10.2(5)
S2	Swift J1749.4–2807	0.60	1.70	12.0	0.23(2)	<8[13]	B	27.1(1.4)	71.0(4.0)
S3	IGR J17591-2342	0.43	2.20	13.0	5.2(5)	<7 [14]	M	6.7(0.3)	16.1(0.8)
S4	SAX J1748.9–2021	0.12	0.11	0.44	45.0(4.)	8.5 [8]	GC	0.50(2)	0.99(5)
S5	XTE J1814–338	0.20	3.20	5.40	0.49(5)	<9.6 [10]	B	25.7(1.3)	33.2(1.7)
S6	IGR J17498–2921	0.20	1.80	3.70	0.61(6)	7.6 [7]	B	17.4(0.8)	24.8(1.2)
S7	IGR J17511–3057	0.16	2.50	3.80	2.30(20)	<7 [1]	B	10.4(5)	12.8(6)
S8	IGR J00291+5934	0.04	0.35	0.41	0.98(9)	<4.7 [2]	B	6.0(3)	6.4(3)
S9	SAX J1808.4–3658	0.008	0.95	1.01	14.0(1.4)	3.5 [3]	B	2.63(13)	2.77(14)
S10	IGR J1737.9-3747	0.07	2.30	2.50	2.20(20)	<4 [14]	M	10.1(4)	10.6(4)
S11	HETE J1900.1-2455	0.018	0.32	0.33	790.0(80)	<5 [5]	B	0.20(1)	0.20(1)
S12	NGC6440 X–2	0.0005	0.17	0.18	0.144(14)	8.5 [8]	GC	11.0(4)	11.0(4)
S13	Swift J1756.9–2508	0.008	0.19	0.20	0.41(4)	<14 [14]	M	6.9(7)	7.0(7)
S14	IGR J16597–3704	0.007	0.25	0.25	2.5(2)	9.1 [11]	GC	3.14(16)	3.15(16)
S15	MAXI J0911–655	0.027	4.00	4.05	8.9(9)	9.5 [12]	GC	6.7(7)	6.7(7)
S16	XTE J0929–314	0.01	0.55	0.56	0.80(8)	U	-	8.3(6)	8.4(6)
S17	XTE J1751–305	0.016	1.50	1.50	1.16(12)	<8.5 [9]	T	11.4(4)	11.5(4)
S18	XTE J1807–294	0.0077	0.41	0.42	5.7(6)	U	-	2.70(13)	2.71(13)
S19	IGR J17062-6143	0.0060	0.29	0.29	10.0(1.0)	7.3 [6]	B	1.66(8)	1.66(8)

List of the obtained expected and observed luminosities for the selected sample of AMXPs. The minimum masses for the companion star M_{min} reported in this Table have been inferred from the mass function of the source fixing i to 60°, with the exception of the eclipsing Swift J1749.4-2807, for which i was fixed to 90°. In the Table $L_{exp,GR}$ and $L_{exp,GR+MB}$ are the expected luminosity evaluated for a mass-transfer driven by GR and GR+MB respectively, F_{av} is the bolometric (0.1-300 keV) unabsorbed flux averaged over 20 years, d the distance known for the system, $d_{m,GR}$ and $d_{m,GR+MB}$ the distances evaluated using $L_{exp,GR}$ and $L_{exp,GR+MB}$ respectively. The label "U" indicates that the distance of the source is unknown at the moment. The cited values for d are upper limits on the distance, therefore I reported the value found on the refereed paper plus its upper error. In the "Method" column I indicate the method used to determine the upper limit on d reported here.

Methods: "B": study of type-I X-ray bursts. "GC": association to a Globular Cluster of known distance. "M": study of the extinction maps by Marshall et al. (2006). "T": theoretical argument.

References: [1]=Altamirano et al. (2010b), [2]=De Falco et al. (2017b), [3]=Galloway and Cumming (2006), [4]=Harris et al. (1996), [5]=Kawai and Suzuki (2005), [6]=Keek et al. (2017), [7]=Linares et al. (2011), [8]=Ortolani et al. (1994), [9]=Papitto et al. (2008), [10]=Strohmayer et al. (2003), [11]=Valenti et al. (2007), [12]=Watkins et al. (2015), [13]=Wijnands et al. (2009)., [14]=This paper.

HETE J1900.1-2455, MAXI J0911-655, XTE J1807-294 and IGR J17062-6143, this method gave a lower limit for the distance which is lower than the measured distances. The method in these cases must be considered inconclusive, since changing the assumptions made, e.g. on the secondary mass, might fix the discrepancy between the distance values and indicate a compatibility with a conservative scenario.

Not surprisingly, these sources have emitted huge amounts of energy in the time considered. Two of these five sources have indeed undergone several outbursts in the last 20 years and three of them, i.e. S11, S15 and S19, have been persistently in outburst for years (see Table 5.2), even if, in the latter case, at a faint luminosity.

Except for one source, i.e. S1, the remaining 7 sources with known distances have estimated values smaller than both the $d_{m,GR}$ and $d_{m,GR+MB}$ limits, indicating a likely non-conservative mass-transfer scenario. S1 is the only source where $d_{m,GR} < d < d_{m,GR+MB}$. While this result might be considered inconclusive, it is indeed remarkable that the relatively long orbital period of the system, i.e. 11.03 hr (Papitto et al. 2013b), seems to discourage a GR-only model, making the higher distance-limit (and the non-conservative scenario) more realistic.

The limits on the distance discussed so far rely strongly on the choice to fix the time interval T to 20 years. Taking into account smaller time intervals would also decrease the limits on the distance. In the following I release this assumption and assume T equal to the time elapsed since the first outburst of each source in the last 20 years[8] (see Table 5.2), in order to test the robustness of these results. The new choice for T leaves almost unchanged the situation for S2, S5, S6 and S17, because even the new limits for d (i.e. 17, 22, 10 and 10 kpc, respectively) exceed the current distance estimate. On the contrary, considering a shorter T changes substantially the results obtained for S1, S7, S8 and S12, which are now equal or even lower than the measured d, i.e. at 5, 7, 5, and 7 kpc, respectively. This result reflects also the fact that these sources, especially S1, have been discovered very recently. Therefore, I conclude that a strong evidence for non-conservative mass-transfer can be associated to S2, S5, S6 and S17, while this evidence is more troublesome for the other four sources in the group.

As stated before, for five sources in the sample I do not have available distance estimates. In this work, I attempt to find at least an upper limit on these distance values using the 3D extinction maps of radiation in the K_S band for our Galaxy computed by Marshall et al. (2006)[9], following the same steps by Gambino et al. (2016). Even if on the basis of its location, i.e. very close to the Galactic Center, an upper limit of 8.5 kpc was suggested for XTE J1751-305 (Papitto et al. 2008), no direct measurements of its distance are available so far, therefore I included the source in the sample and tried to evaluate its distance too. For a specific direction in the Galaxy, e.g. defined by the coordinates of a source, these maps give the evolution of the extinction in the K_S band, A_{K_S}, as a function of the distance. In order to evaluate A_{K_S}, I used the equations:

$$N_H = (2.21 \pm 0.09) \times 10^{21} A_V, \tag{5.6}$$

$$A_{K_S} = (0.062 \pm 0.005) A_V \text{ mag}, \tag{5.7}$$

by Güver and Özel (2009) and Nishiyama et al. (2008), respectively, where A_V is the extinction in the visual band. The references for the N_H values employed for each source are reported in the

[8] This time usually coincides with the time of discovery of pulsations for the source, displayed in Table 5.1, with the exception of S10 and S19.

[9] http://vizier.cfa.harvard.edu/viz-bin/VizieR?-source=J/A+A/453/635

"References Spectral Parameters" column in Table 5.2.
From the study of the extinction maps, I derived distance values of 5±2 kpc for S3, 12±2 kpc for S13 and an upper limit of 4 kpc for the distance of S10. My estimate for the distance of S3 is barely compatible with the lower limit posed by Russell et al. (2018) of 6 kpc.
Results for S17 are inconclusive, since the only constraints on the distance found is a lower limit of 2.7 kpc. S16 and S18 have relatively high Galactic latitude, in directions poorly mapped by Marshall et al. (2006), therefore even with this technique it is not possible to obtain constraining limits on the distances. The discussion about the non-conservativity of the mass-transfer has to shift towards how reasonable is the estimated threshold distance for these two sources. Taking into account the new distance upper limits, S10 results compatible with a non-conservative scenario according to both $d_{m,GR}$ and $d_{m,GR+MB}$, while the limits for S13 are below the known distance for the source, making the method inconclusive. The situation of S3, for which $d_{m,GR} < d < d_{m,GR+MB}$, recalls what found for S1. By the way, since the long orbital period of the source, i.e. 8.82 hr (Sanna et al. 2018c), strongly encourages a MB contribution in the dynamics of the system, the non-conservative case seems to be better-founded than the conservative case. The distance limits for S18 are reasonable and they have to be considered inconclusive for my purposes. Also S16 has a realistic distance threshold, although its relatively high Galactic latitude would place it in an empty region of the Galaxy, suggesting a non-conservative mass-transfer scenario (Marino et al. 2017). I applied the test of changing the choice for T to S3 and S10. While S3 was discovered only last year and it is clearly not suitable for such test, S10 has upper limits with the new T of $d_{m,GR}$=8.4±0.5 kpc and $d_{m,GR+MB}$=8.9±0.5 kpc, which are still suggestive of a non-conservative scenario. Therefore I include S10 in the sample of strong evidences sources.
It is noteworthy that if no activity is observed in the next few years, the limits for d found for the 19 sources analyzed in this paper will drift to higher values and some of the weak evidences for non-conservative mass-transfer might be strenghtened.

5.7 Discussion

The method described and applied in this paper strongly indicates a non-conservative mass-transfer for six sources (including the results for XTE J0929-314), and weakly for other five sources. I discuss here the possibility that any of the assumptions made in this work may have biased the results for the strong evidences. In the following, T was considered the time elapsed since the discovery of the source. First of all, I checked if decreasing the value assumed for the mass of the NS to 1.1 $M_\odot$ (lower than the lowest NS mass ever measured, i.e. 1.174±0.001, Martinez et al. 2015) and increasing the radius of the neutron star above 12 km (i.e. above the values expected according to most proposed Equations of state, Özel and Freire 2016) might give different results. Fig. 5.1 shows the distance as a function of $R^{-1/2}$, using for $F_{av} \times 4\pi d^2$ and $\dot{M}_{min}$ the values previously evaluated for the five strong evidence sources. For four sources out of five, an unrealistic value of $R > 20$ km would be needed to match the luminosity expected under the assumption of conservative mass transfer. In XTE J1751-305, on the contrary, the compatibility is restored for values of R >12 km. I therefore discard this source from the strong evidences sources.

Another assumption which might be relaxed concerns the inclination, fixed to 60° in all the sources but the only eclipsing one, i.e. Swift J1749.4-2807. However, allowing for a 90° inclination does not give substantial changes in the obtained values and the scenario proposed here is unchanged. Even in the extreme scenario of 90°-inclination systems (for which no eclipsing activity was ever observed), hosting bizarre neutron stars with high radii and the smallest mass value ever observed I

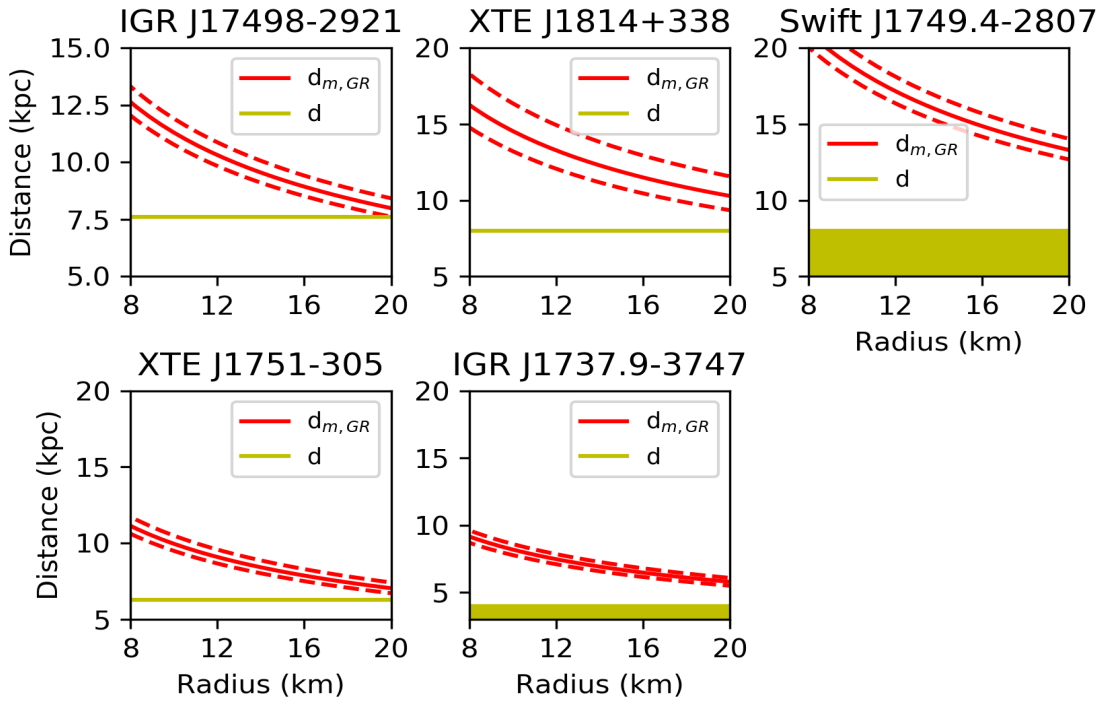

FIGURE 5.1: Distance-Radius curves (in red) with errors (dashed lines) compared with the distance value reported in literature (in yellow) for the four sources with stronger evidences for non-conservative mass-transfer.

am not able to find an accordance between data and the predictions of a conservative mass-transfer model for these sources.
Even considering wrong the distance measured for these sources, I still have to admit high inclinations and low-mass companions to obtain distances within the size of our Galaxy.
Finally, my choice for T in this discussion was the most conservative possible and replacing it with 20 years may only reinforce these evidences. Therefore, the Occam's razor leads us to consider these results as a strong evidence for non-conservative mass-transfer for IGR J17498-2921, XTE J1814+338, Swift J1749.4-2807, IGR J1737.9-3747. As stated in Section 5.3, a non-conservative mass-transfer has been proposed in three other AMXPs: XTE J0929-314, SAX J1808.4-3658 and SAX J1748.9-2021. The latter two sources have been analyzed as well in this paper, giving no evidence for a non-conservative mass-transfer. This should not be considered a contradiction, because the possibility of a non-conservative mass-transfer is not excluded by this method; allowing for higher companion masses might increase the expected luminosity and shift $d_{m,GR}$ ($d_{m,GR+MB}$) below the distance estimate for the system. It is impossible, however, with the current available information about the inclination and/or the secondary mass of these sources to discriminate between the conservative and non-conservative scenarios using this method. Furthermore, as recently demonstrated by Van et al. (2018), the chosen prescription for the MB term might not be the most adequate and may significantly underestimate the real contribution, i.e. by an order of magnitude, to the average theoretical mass-transfer. Indeed, the model used here neglects some physical aspects, e.g. the chemical or thermal evolution of the companion star, as well as any calculation of the convective and radiative zones of it, therefore these results have to be considered with a reasonable dose of caution. These arguments might explain why S4 and S9 do not give evidence for a non-conservative mass-transfer although a non-conservative evolution has been hypothesized (Di Salvo et al. 2008; Sanna et al. 2016, 2017b) with an independent argument, in order to justify the large value of the orbital period derivative measured for both systems[10].

5.8 Conclusions

This work aims at a discussion of the possibility of a non-conservative mass-transfer for almost all the AMXPs discovered so far by comparing their expected luminosity, calculated on the conservative evolution hypothesis, and the observed X-ray flux averaged over the last 20 years (or the time elapsed since their discovery). Recently a non-conservative mass-transfer has been claimed for three AMXP; including the four strong evidence cases presented here the count would increase to seven, suggesting that this physical phenomenon might be not rare at all in the family of the AMXPs. Furthermore, including also the sources with weak evidence of non-conservative mass-transfer and the two AMXPs which displayed only faint outbursts (for which conservative mass-transfer rates seem unlikely), more than half of the AMXPs would require a non-conservative scenario. It is also interesting to notice how, despite more than 20 years of continuous monitoring by several all-sky monitors, the number of transient LMXBs showing millisecond pulsations keeps rising (the latest discovered is IGR J17591-2342, Sanna et al. 2018c). This argument might be taken as a hint that the recurrence times could be even longer than 15 years, enlightening the inadequacy of conservative mass-transfer scenarios for many members of this class.

[10] A short-term variability induced by tidal dissipation and magnetic activity in the companion, which is required to be at least partially non-degenerate, convective, and magnetically active (Applegate and Shaham 1994; Hartman et al. 2008), has been alternatively invoked to explain the observed orbital period expansion, although this possibility appears quite unlikely (Sanna et al. 2017a)

The radio ejection model, developed several years before these pieces of evidence for non-conservative mass-transfer were found, might be able to explain what induces a non-conservative regime in the case of accreting fast pulsars and, if confirmed, it could be considered as a key feature in the complex phenomenology of this class of sources.

6. Testing jet geometries and disk-jet coupling with internal shocks

SUMMARY

Multi-wavelength spectral energy distributions of Low Mass X-ray Binaries (in hard state) are determined by the contribution of the jet in the low energies domain (up to mid-IR) and the accretion flow at high energies (from optical to X-rays). In the last few years, the flat radio-to-mid-IR spectra of BH X-ray binaries was described using the internal shocks model, which assumes fluctuations in the velocity of the ejected shells along the jet driven by the fluctuations in the accretion flow. The success of this model confirms the strong interconnection between accretion and ejection in BH systems. In the first part of this chapter, I sum up the basics of jets in X-ray binaries. In the second part, I attempt to model the broadband data-set of the Neutron Star LMXB 4U 0614+091, obtained in 2006 and comprising data from radio to X-rays, using an internal shocks model for the jet and an irradiated disc model for the accretion flow. The jet model builds a simulated spectral energy distribution based on a wide set of physical parameters and on the X-rays Power Density Spectrum. The latter is used as a tracer of the fluctuations of the Lorentz factors in the ejected shells and the resulting internal shocks dissipation pattern. Fitting the data set with the model results in good fits only in two alternative scenarios: using the X-rays PDS but using a non-conical geometry for the jet, i.e. a more confined jet, or either using a conical geometry but with a "flicker-noise" PDS, apparently unrelated to the observed X-ray variability.

6.1 Compact jets

The ejection of collimated outflows of matter in the form of jets is quite an ubiquitous phenomenon in astrophysics and it has been associated to a wide range of celestial objects, from Active

Galactic Nuclei (AGNs) to Young Stellar Objects (YSOs), from Gamma-Ray Bursts (GRBs) to, of course, Stellar X-ray Binaries (XRBs). Although jets are very common, there is a huge difference in scales depending on the type of source launching them: while jets in XRBs are typically around 10^{14}-10^{15} cm elongated (Miller-Jones et al. 2012), in GRBs jets can reach lenghts of about 10^{18} cm (Mészáros and Rees 1997; Wijers et al. 1997) and the giant radio lobes of AGNs jets are observed up to distances of the size of our Galaxy ($\sim 10^{23}$ cm, Alvarez et al. 2000). Besides of these two cases, jets are usually not directly observed as extended structures in short orbital period systems (Garcia et al. 2003) and are therefore dubbed as **compact jets**. X-ray binaries, however, are definitely not the only type of astrophysical source where jets have been observed. Furthermore, XRBs jets are believed to be only mildly relativistic ($\Gamma \sim 1-10$) while jets in AGNs and GRBs are relativistic, i.e. $\Gamma \gtrsim 10$, and highly relativistic , i.e. $\Gamma \gtrsim 100-1000$ (Pe'er 2014), respectively.

Jets are complex physical phenomena, about which many unsolved questions and open problems still exist. However, as pointed out by Jacquemin-Ide et al. (2019), at least three physical ingredients can be considered essential in order to produce a jet: (1) an accretion disk, (2) a large scale vertical magnetic field through the disk and (3) the possibility for mass diffusion through it. These ingredients are not hard to find in accreting objects and this explains the universality of jets accross all cosmic scales. Furthermore it points out how matter accretion is almost always paired with ejection, to such an extent that it is actually possible to think of accretion and ejection as *two faces of the same coin*.

As XRBs are the main focus of this thesis, in the following I will focus on jets in only this class of object, but almost all of the considerations made can be easily extended to the other mentioned objects. Furthermore, I will not consider jets in WD binaries (examples of works on this topic might be found in Rupen et al. 2008; Körding et al. 2008), but as in the previous chapters the focus will be on NS and BH binaries. In the last few decades, jets in X-ray binaries hosting BHs and their coupling with the disk have been object of extensive observational campaigns, simulations and theoretical studies. While jets are observed in X-ray binaries hosting NSs as well, the wealth of studies of jets phenomenology in BH X-ray binaries is unmatched when it comes to NS X-ray binaries. The study of jets in the latter class of systems is indeed challenging, mainly because they tend to have weaker radio emissions (from hundreds to tens of μJy), sometimes below the observational capabilities of the most sensitive interferometers on Earth, and somewhat faster state transition timescales (Muñoz-Darias et al. 2014, and also the results of Chapter 4), which make it harder to schedule coordinated space and ground observations. While jets are very common in NS LMXBs, which host NSs with weak ($B \lesssim 10^9$ G) magnetic fields, recently the phenomenon has been associated also to at least one highly magnetised NS in a High Mass X-ray Binary (van den Eijnden et al. 2018b). As far as I know, jets in NSs X-ray binaries have a few, but substantial, differences with respect to jets in BH X-ray binaries. As mentioned before, jets in NSs are less radio-loud than in BHs, i.e. a factor $\sim$30 than for BH binaries at similar X-ray flux levels (Fender and Kuulkers 2001; Migliari et al. 2003; Gallo et al. 2018). It is unclear if this observational evidence points out that the jet power is simply lower in NSs than in BHs or rather that the mass of the compact object or the radiative efficiency, e.g., play some role (Körding et al. 2006). Furthermore, in BHs binaries jet emission is always suppressed when the source is in soft state, while jets are never entirely quenched in NSs X-ray binaries (see, e.g. Migliari et al. 2004), with just a few exceptions (one example is RX1804, the source analyzed in Chapter 4, Gusinskaia et al. 2017). The emerging picture seems to point out that the nature of the compact object (and, as in the case of a NS, the presence of a magnetic field) likely plays some role in determining the characteristics of the launched jet.

In this chapter, I will briefly sum up the current understanding on jets, focusing on how they form, what powers them, how they radiate and what are they composed of.

6.2 Jets physical properties

Jets carry most likely a mixture of ions and electrons. However, from the point of view of emission models, they are usually considered as made essentially of leptons, in the sense that only leptons are accelerated to sufficiently high energy to contribute to the overall spectrum (see e.g. Bosch-Ramon et al. 2006, and references therein)[1].
The mechanisms at the base of launching and acceleration of particles in jets is also still debated. In the following I will try to sum up the main achievements in the field.

6.2.1 How the story starts: jet launching mechanisms

Historically, the models proposed to explain the launching of jets are two: the Blandford and Payne (1982) (B-P model) for disc-driven jets and the Blandford and Znajek (1977) (B-Z model) for jets powered by the rotation of the black holes. Both models require the presence of a strong magnetic field anchored to the disk. Since General Relativistic Magneto-Hydrodynamical (GRMHD) simulations support both models (Meier et al. 2001), at the moment there are not arguments to prefer one model over the other for BH X-ray binaries, while only the B-P mechanism is plausible for NSs[2] and WDs X-ray binaries. Other mechanisms have been hypothesized, which in turn are not suitable for black holes and rely crucially on the interaction between the NS magnetosphere and the disk, as e.g. the model developed by Parfrey et al. (2016) for jets in AMXPs.

Blandford-Payne model According to this model just a few ingredients are needed in order to produce a jet: a rapidly rotating disk surrounded by a less dense region, i.e. the atmosphere or a hot corona, and a magnetic field anchored to it. In the accretion disk matter is dense and fastly rotating, so that $\rho v^2 > \frac{B^2}{8\pi}$, with ρ the density of the plasma, v its velocity and B the magnetic field intensity. Under this condition the magnetic pressure is smaller than the ram pressure of the plasma, so that the magnetic field lines are *frozen* in the plasma and dragged by the movement of the disk. This condition does not hold in the tenuous atmosphere above and below the disk (or in the hot electron corona surrounding the disk); here density decreases drastically and the magnetic pressure dominates over gas pressure, i.e. $\frac{B^2}{8\pi} > \rho v^2$. Here the gas is pulled from the magnetic field lines and it is forced into corotation with the disk, on which the magnetic field lines are anchored. If field lines are not exactly aligned with the axis of rotation of the system but are at least slightly inclined outward, the plasma flow experiences a centrifugal force accelerating it away from the disk (magnetocentrifugal acceleration). This is a simple consequence of the fact that the magnetic field does not act on the velocity component of the particles parallel to it. As particles move along the field lines, the field strength decreases and a third *plot-twist* in this duel between magnetic field and plasma happens at the point where, again $\rho v^2 \geq \frac{B^2}{8\pi}$ (at the edge of the so-called **Alfvén radius**). Field lines start lagging behind the flow and get coiled into a spiral, which serves as the structure for the newly formed jet. The magnetic energy is gradually dissipated along the jet and it is used to accelerate the particles along the jet.

Blandford-Znajek model One of the most commonly thought facts about black holes is that nothing can escape from them, either mass, light or energy. This is not exactly correct: several

[1] However, several models of lepto-hadronic jets have been developed as well and they predict a significant contribution of the ultra-relativistic protons to the spectrum as well (see, e.g. Vila and Romero 2010; Pepe et al. 2015).

[2] But see also (Migliari et al. 2011) for a discussion on the possibility of having spin-powered jets also on NS LMXBs.

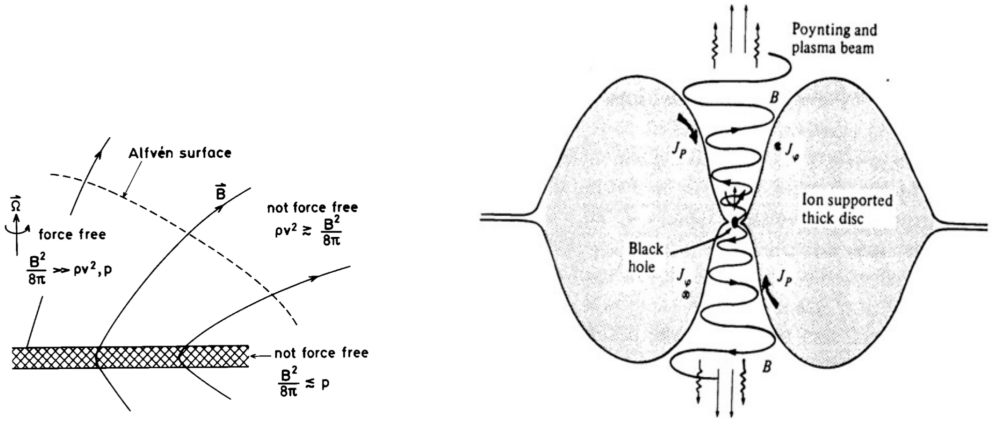

FIGURE 6.1: Jet-launching models sketches: Blandford-Payne (*left*) vs. Blandford-Znajek (*right*). *Credits for the figures*:Spruit (2010); Blandford and Znajek (1977).

processes are indeed known that highlight how nature provides some ways that allow energy to be extracted from rotating BHs, as the **Penrose mechanism**[3] and the **Blandford-Znajek mechanism**. The latter, in particular, it is thought to power relativistic jets and it was indeed delevoped to explain the tremendous amounts of energy liberated in AGNs and quasars[4]. A detailed treatment of the mechanism involves a review of General Relativity and Magneto-Hydrodynamics which are beyond the scopes of this chapter, therefore in the following I will simply summarise the basics of this process. Consider a black hole immersed in a magnetic field: an open magnetic field line which stretches from infinity to the edge of the event horizon is able to extract energy and angular momentum from inside the rotating the black hole which is used to power the jet. Such *open* field lines configuration is a consequence of frame dragging in the ergosphere and it is expected to arise mostly in black holes with a retrograde spin ($a < 0$) or black holes with rapid prograde[5] spin (($0.75 < a < 0.99$; see, e.g. Meier 2011).

6.2.2 How the story goes on: acceleration and collimation

When particles are injected in a jet, the environment they find is a particularly wild one: as jets are supersonic, turbulent and highly magnetised, particles can easily interact with strong shock waves, shear layers or reconnection sites. Jets are therefore ideal sites for particle acceleration (see, for a recent review, Matthews et al. 2020). Indeed, spectra of jet-emitting sources show clear signatures of power-law energy distributions of electrons (see Sec. 6.3), which is an indirect evidence of the existence of some particles acceleration mechanism within the jet.
The most widely discussed one is the **Fermi mechanism** (Fermi 1949, 1954). According to this mechanism, particles which cross back and forth a shock wave multiple times are accelerated to a final, power-law energy distribution (Longair 2011). Shock waves are likely a common ingredient in jets, since they are generated whenever two plasma shells propagating at different speed catch up and collide (this mechanism is therefore also a channel through which the energy losses in the jet are replenished, see Section 6.4). An alternative mechanism might be represented by **magnetic reconnection**, i.e. close magnetic field lines running in opposite directions which change their

[3] See Penrose (1969).

[4] Before the deeply influential paper by Blandford and Znajek (1977), a plethora of exotic theories existed, invoking clusters of billions of pulsars in the cores of the galaxies (Rees 1971) or either the presence of a single, giant, magnetised star (Morrison 1969).

[5] Retrograde and prograde spin is here intended with respect to the accretion flow.

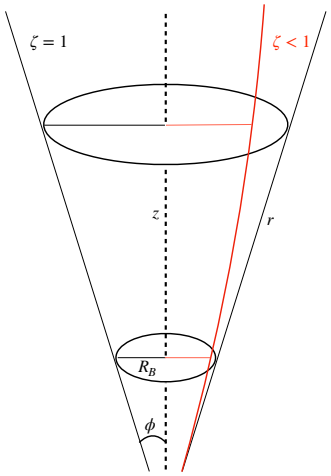

FIGURE 6.2: Schematic view of a jet in both conical and non-conical geometry.

topology and reconnect, liberating energy. The dissipated energy can be used to accelerate particles at high energies (see, e.g. Romanova and Lovelace 1992; McKinney and Uzdensky 2012).

Jets are usually assumed to be conical, i.e. the radius of the jet r at a height z follows a simple linear relation. In a conical jet the sideways velocity of the particles in the jet, responsible for the jet to expand, is constant along the whole jet axis. If, however, some internal or external agent reduces the radial velocity along the axis, the jet gets confined and its shape goes from conical to parabolic. More specifically, it is possible to describe the geometry of the jet with a parameter ζ such as: $r \propto z^{\zeta}$, where $\zeta = 1$ for the "standard" conical geometry, while $\zeta < 1$ holds for a parabolic jet (see Figure 6.2). The case of an "overpressured jet" with $\zeta > 1$ is not impossible, but it would be an highly unstable structure which will tend to evolve spontaneously to a situation where $\zeta \leq 1$ (Kaiser 2006). A non-conical geometry it is likely a physically more realistic description of the jet structure than the conical. The confinement agent necessary can be internal or external. In the first case, it has been proposed by several authors that collimation might be due to a toroidal component of the magnetic field which increases along the axis and that forces the jet to decrease its opening angle (see, e.g. Heyvaerts and Norman 1989; Pudritz et al. 2006, 2012). However, this mechanism has been questioned by Spruit (2010), according to which a magnetic self-confinement of the jet is not physically possible as the toroidal magnetic pressure within the jet would force them to expand. On the other hand the collimation necessary to "break" the conical geometry might be furnished by external pressure exerted by, e.g., the interstellar medium (e.g. Asada and Nakamura 2012) or an external magnetic field kept in place by the disk (e.g. Spruit et al. 1997).

6.3 Jet spectral emission

A magnetised plasma containing very energetic electrons with a power-law energy distribution will produce a power-law spectrum at high frequencies, which slope α is determined by the slope of the energy distribution p, i.e. $\alpha = (1-p)/2$. This is true, however, only above the critical self absorption frequency: below this threshold the radiating electrons will re-absorb some of the photons and produce a power-law spectrum of slope 5/2, entirely uncorrelated to the slope of the electron energy distribution. Each region of the jet emits as the magnetised plasma described above: at high

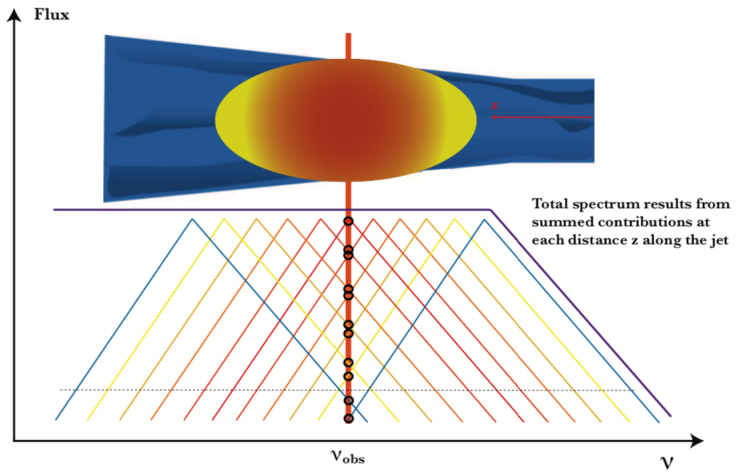

FIGURE 6.3: Plot showing how the different slabs of a compact jet, in the case of energy replenishment mechanisms, produces flat spectra by the superposition of the contribution of the various slabs the jet can be divided in (Markoff 2010).

energies emission is optically thin and the spectrum is steep, at low energies emission becomes optically thick and the spectrum is inverted and somewhere between these two extremal behaviours a spectral peak is expected. In the case of compact jets, i.e. since it is not possible to spatially resolve such regions, what is observed is the superposition of the spectra emitted by the different regions of the jet.

Moving along the jet, the magnetic field decays but also the particles lose energy through adiabatic expansion. Therefore the peaks of the single synchrotron spectra decrease in both intensity and frequency, leading to a power-law shape of the spectrum. However, jets have been usually observed with a "flat" radio-to-mid-IR spectrum (see, e.g. Corbel et al. 2000; Fender 2001; Corbel and Fender 2002). This is somewhat puzzling, since it would imply optically thin jets and a power-law energy distribution of the electrons of slope unity, which is very unlikely to arise for the usually assumed acceleration mechanisms at the shock fronts in the jet (see, e.g. Bell 1978). The currently accepted explanation for the flat spectra (see Fig. 6.3) invokes continuous energy replenishments in the jet, which might compensate the adiabatic losses due to the expansion of the jet (Blandford and Königl 1979). In the following, I will go beyond this simple picture and develop a proper physical model for the broadband spectral shape of jets.

6.3.1 Self-absorbed synchrotron emission from a jet: the model

I consider a jet with adiabatic losses where the magnetic field B is assumed to be tangled on scales larger than the Larmor radius and smaller than the emitting region[6]. This constitutes a good approximation of the magnetic field in a shocked region and the result is valid for any viewing angle (Crusius and Schlickeiser 1986).

I take the z-axis as the axis of a rotationally-symmetric jet.

In order to build this model, I need to describe how the geometrical shape, the magnetic field and the electron energy distribution varies along the jet. In particular:

- I describe the geometrical shape of the jet with the function $R(z)R_0\,(z/z_0)^{\zeta} = R_0 l(z)^{\zeta}$, with

[6]I refer to Kaiser (2006) for the same derivation with magnetic fields isotropic or parallel/perpendicular to the jet axis.

R_0 the radius at the base of the jet and l a dimensionless coordinate. For a discussion about the confinement of the jet see Subsection 6.2.2.

- I consider the magnetic field $B(R)$ as varying with R (and then with ζ), i.e. $B(R) = B_0(R/R_0)^{-b}$.
- Even if the energy distribution $p_{\rm el}$ of the electrons does not change over the jet, the number of accelerated electrons $N(\gamma) = N_0\gamma^{-p}$ can be modified as the scaling factor N_0 depends e.g. on B (see Marino et al. 2020).

Furthermore, I assume that the jet is made of homogeneous cylindric shells of proper vertical scale $\tilde{H}$, i.e. calculated in the shell frame[7], and radius following the parabolic dependence with z defined above. The **local cylinder approximation** will be adopted, i.e. for which the radius of the shell is negligible with respect to its height, i.e. $\tilde{H} >> R$. In this approximation the variations of the source function and absorption coefficients along the line of sight are neglected. This approximation is expected to be accurate at large inclination angles ($\theta \sim 90°$) where the observed emission is dominated by radiation travelling in the radial direction and does not experience significant gradients in the jet. In fact it turns out to be remarkably accurate even at smaller viewing angles and up to viewing angles comparable to the jet opening angle (i.e. up to $\tan\theta \sim R_0/Z_0$) [8].
Each of these shells emits an instantaneous observed flux F_j. The total jet flux is the time averaged flux of a shell as it crosses the whole jet, extending from z_0 to z_f, multiplied by the total number of shells $n_{\rm s}$ present at any time in the jet:

$$F_j = \frac{n_s}{t_{rf} - t_{r0}} \int_{t_{r0}}^{t_{rf}} F dt_r, \tag{6.1}$$

where $t_{rf} - t_{r0}$ is the shell jet crossing time as measured by the observer (assuming that the jet emitting region starts at z_0 and ends at z_f). The number of shells is given by the jet size divided by the observed length $\delta\tilde{H}$ of the shells and corrected by their volume filling factor f_v, i.e. $n_s = (z_f - z_0) f_v/\delta\tilde{H}$. The total jet flux can be then rewritten as:

$$F_j = \int_{z_0}^{z_f} \frac{f_v F}{\delta\tilde{H}} dz, \tag{6.2}$$

where F is the observed flux from a single shell.

A full derivation of F is presented in the Appendix of Marino et al. (2020). For the sake of simplicity I will just highlight here the main dependences of F, in order to discuss the physical implications of this formula:

$$F_j \propto \frac{\nu^{5/2}}{\tau_1^{a_1-1}} \int_{\tau_1}^{\tau_f} \tau^{a_1-2}(1 - e^{-\tau}) d\tau \tag{6.3}$$

where τ_1 and $\tau_{\rm f}$ are the optical depth at the base and at the termination of the jet and a_1 is defined as:

$$a_1 = 1 + \frac{2 + 2\zeta + \zeta b}{2\zeta\,(1 - b(3 + p/2))} \quad . \tag{6.4}$$

[7] In this section, tilted symbols represent quantities measured in the rest frame of the cylinder.
[8] For smaller jet inclinations, a different approach must be adopted (see, e.g. Zdziarski et al. 2016)

A derivation of τ_f and τ_1 is not trivial and it is given in the Appendix of Marino et al. (2020). Here I will just highlight the dependence of both τ_1 and τ_f on ν, i.e. $\tau_1, \tau_f \propto \nu^{-(p+4)/2}$.

Eq. 6.3 can be written as:

$$F_j \propto \frac{\nu^{5/2}}{\tau_1^{a_1-1}} \left[\Gamma(a_1-1,\tau) + \frac{1}{a_1-1}\tau^{a_1-1} \right]_{\tau_1}^{\tau_f} \tag{6.5}$$

with Γ the incomplete $\Gamma-$function, defined as:

$$\Gamma(a,z) = \int_z^\infty t^{a-1}e^{-t}\mathrm{d}t \quad . \tag{6.6}$$

For the purposes of studying the shape of F_ν, it is useful to express $\Gamma(a,z)$ in the following series representation (Gradshteyn et al. 2000):

$$\Gamma(a,z) = \Gamma(a) - \sum_{n=0}^{\infty} \frac{(-1)^n z^{a+n}}{n!(a+n)} \tag{6.7}$$

While the formula in Equation 6.5 is not easy to handle, some information can still be recovered on how F_ν evolves for some special cases:

- Frequencies at which the jet is **optically thin** ($\tau_f \ll 1$ & $\tau_1 \ll 1$): all terms beyond $n=1$ in the summation (Eq. 6.7) become negligible and the term in brackets in Equation 6.5 becomes: $\frac{1}{a_1}\left(\tau_\mathrm{f}^{a_1} - \tau_1^{a_1}\right)$. When multiplied to the term $1/\tau_1^{a_1-1}$ outside of the brackets, I obtain a quantity which depends simply on $\nu^{-4-p}/2$ which can therefore be singled out and multiplied by $\nu^{5/2}$, resulting in:

$$F_\nu \propto \nu^{(1-p)/2} \tag{6.8}$$

- Frequencies at which the jet is **optically thick** ($\tau_f \gg 1$ & $\tau_1 \gg 1$): since $\lim_{z\to\infty}\Gamma(a,z) = 0$ (Gradshteyn et al. 2000), what remains of the term in brackets is: $\frac{1}{a_1}\left(\tau_\mathrm{f}^{a_1-1} - \tau_1^{a_1-1}\right)$. Again both terms are proportional to $\nu^{(-4-2)/2}$, but the factor cancels out with $\tau_1^{-a_1}$, in Eq. 6.5, leaving:

$$F_\nu \propto \nu^{5/2} \tag{6.9}$$

- Frequencies at which the jet is **partially absorbed** ($\tau_\mathrm{f} \ll 1$ and $\tau_1 \gg 1$) using the results previously discussed, I find that the term in brackets results simply in $\Gamma(a-1)$, and therefore:

$$F_\nu \propto \nu^{[5+(a_1-1)(p+4)]/2} \tag{6.10}$$

  For typical values of p and ζ, i.e. 2 and 1 respectively, and $b = 4/3$ which is appropriate for a magnetic field behaving as a relativistic fluid in an isotropic expansion (Longair 2011), I obtain $\nu^{0.65}$, i.e. the spectrum slope changed abruptly with respect to the optically thick and optically thin frequencies.

The first two points describe the emission from the optically thin part of the jet, i.e. its base, and the optically thick part of the jet, its edge and predict that at high energies the spectrum has a power-shape of slope depending on the original p electron energy distribution index while at low energies the typical self-absorbed synchrotron spectrum shape is assumed. In the intermediate regime of frequencies, where the jet is "partially absorbed", the spectral shape depends not only on p but also on ζ and b.

It is possible to see that for a particular value of ζ[9] and intermediate frequencies, F_ν is independent of ν and it is simply *flat* (Kaiser 2006), i.e. $F_\nu \propto \nu^0$ in the partially absorbed regime. It is usually stated that flat spectra in jet imply the existence of energy replenishment mechanisms which compensate for the energy losses. As shown here, this statement is not completely correct as if we could finely tune the collimation of the jet to get to $\zeta_{\rm flat}$, we would have a flat jet spectrum without the need to invoke for any energy injection mechanism. However, this is likely not the case for the vast majority of jets and energy replenishment effect are likely playing some role in determining the final spectral energy distribution in jet-emitting sources (I will come back to this point in 6.4).

As electrons radiate, they lose energy and their energy distribution is at some level affected by it. In particular, this implies the existence of a high energy cut-off, the so-called **cooling break**, corresponding to the frequency where electrons start to lose energy more rapidly than how they gain it. This high-energy cut-off is found analytically putting in equation the typical acceleration time-scale $t_{\rm acc}$ and the *cooling* time-scale $t_{\rm cool}$ (see e.g. Pe'er 2014, for details), usually in the X-ray range or even at higher energies. Taking care of radiative energy losses may be relevant when spectral information at high energies is available. (see Bassi et al. 2020, for a further discussion of this effect in the context of ISHEM).

6.4 Internal shocks

In the previous paragraph I just assumed the existence of some mechanism that allows the electrons in the jet to gain back at least part of the energy lost in the expansion and emit the flat spectra typically associated to jets. As discussed in Subsection 6.3.1, flat spectra would arise from sufficiently collimated jets, but this would require such a fine tuning of the geometry of the jet to result unlikely. Magnetic reconnection is a physical process which might also play some role in accelerating particles in the jet and, therefore, compensate for the adiabatic losses (Lyubarsky 2010; Sobacchi and Lyubarsky 2020), but its dissipation profile, i.e. how the liberated energy is distributed along the jet axis, is hard to predict. An alternative option is represented by the so-called **Internal Shocks** models, which take into account the conversion from kinetic energy into internal energy which arise when two shells in the jet, ejected at different velocity, catch up and collide. In the past, these models have been applied to γ-ray bursts (Rees and Meszaros 1994; Daigne and Mochkovitch 1998), AGNs (Rees 1978; Spada et al. 2001; Boettcher 2010) and BH XRBs (Kaiser et al. 2000; Jamil et al. 2010; Malzac 2013). In the last decade, Malzac (2013, 2014) showed that internal shocks might also explain the flat SEDs of X-ray Binaries.

According to this model, jets can be modelled as the continuous launching of discretised plasma shells of constant mass[10], ejected at constant time intervals Δt comparable to the **dynamical time-scale** of the accretion flow, i.e. the Keplerian orbital period at a distance $r_{\rm dyn}$, assumed to be the inner radius of the accretion disk. Every single shell is then tracked and followed until they collide

[9] Which, according to this model is: $\zeta_{\rm flat} = \frac{6p+24}{(10p+50)} \sim 0.51$.

[10] Even if the constant mass hypothesis is not realistic, it is shown in Malzac (2013) that the choice of a constant or a variable mass affects very slightly the results of the code.

with a second shell, merge together and form a secondary shell, which is followed and tracked as well. If the shells are ejected with a constant Lorentz factor Γ, no collision happens, otherwise ejecta with variable velocity will collide and form a shock; the resulting emitted shock waves accelerate the electrons in the jet and compensate, even partially, for the adiabatic losses. As highlighted by Malzac (2014), a crucial role is played by the fluctuations frequency of the Γ-s of the ejected shells, as they determine how the energy is dissipated along the jet. In particular, low frequency fluctuations correspond to variability over long time scales and to shells which will catch up and merge only at large distances from the jet, while in the case of high frequency fluctuations, energy is dissipated mainly close to the base of the jet. It results that the ultimate spectral shape of the jet, as it is crucially determined by the energy dissipation pattern, is very sensitive to the the time-scale and amplitude of the fluctuations of Γ, i.e. to their **Fourier Power Spectral Density** or PSD $P(\nu)$. While a "flat" PSD, i.e. corresponding to "white noise", is not able to reproduce the observed spectral energy distribution (Beloborodov et al. 2000; Jamil et al. 2010), it was demonstrated by Malzac (2013) that a a power-law shaped PDS, where $P(\nu) \propto 1/\nu$, is a more appropiate choice. In this case the velocity fluctuations in the jet is dominated by the so-called "flicker noise", which occurs in many different processes of biological, economic and physical (see, e.g. Press 1978) nature but also in astrophysics, especially in the X-ray variability of X-ray binaries (Gilfanov 2010). As X-rays PSDs of XRBs in hard state can be roughly approximated to "flicker-noise"-shaped PSDs, the next step was to use it as a proxy of the fluctuations in the Γ of the ejecta (Drappeau et al. 2015). In the Internal Shocks model, dubbed ISHEM, the hierarchical merging of the shells and the subsequent energy dissipation pattern in the jet are built from a PSD, which is usually a power-law PDS or an observed X-rays PDS. The second case is particularly important since it highlights the inner connection between the variability in the accretion flow, observed in the X-rays, with the energetics of the ejecta, observed in radio-mid-IR.

While the dissipation pattern is defined by the PDS of the fluctuations, the final spectrum depends crucially on the geometry of the jet. As already discussed in Subsections 6.2.2-6.3.1, jets are likely non-conical and collimated, and for reasonable values of ζ the more collimated the jet, the flatter the spectrum. Furthermore, since the jet loses less energy for an increasingly less conical configuration, also the range of wavelengths emitted by the jet shrinks (for a fixed length of the jet). The flat spectrum of compact jets may result from the combination of non-conical ζ values and internal shocks. Finally, the last main ingredient in the model is p, which determines the slope $\alpha = (p-1)/2$ of the spectrum at high energies, in the optically thin part of the jet (see Equation 6.8).

ISHEM also requires several other additional physical parameters to be specified. However the values of these parameters do not affect the shape of the SED, they can only shift in frequency or rescale the normalisation of the whole SED. These parameters describe the system, the jet and the distribution of the radiating particles. The main parameters are: the distance (D) to the source, the inclination of the jet axis with respect to the line of sight, the mass of the compact object ($M_{\rm NS}$ in this case), the jet power ($P_{\rm J}$), the jet opening angle (ϕ), the radius at the base of the jet (R), the bulk Lorentz factor of the jet ($\Gamma_{\rm av}$) of the accelerated particles, the volume filling factor $f_{\rm V}$ (Malzac 2014), the maximum/minimum energy limits ($\gamma_{\rm max}$,$\gamma_{\rm min}$) of the electrons distribution. A study of how the resulting simulated SED depends on these parameters is presented in fig. 2, Péault et al. (2019).

The model has been successfully applied to three X-ray Binaries hosting black holes (BHs) as the primary star in the past (Drappeau et al. 2015; Péault et al. 2019; Bassi et al. 2020), but never to a neutron star (NS) X-ray binary. In this chapter, I report on the application of the Internal Shocks model to the Spectral Energy Density of 4U 0614+091, the first attempt ever to describe the entire SED of a NS LMXB with a jet model. Furthermore, ISHEM has been used so far only with

systems hosting a black hole and never for a neutron star LMXB, as in this work. The results of this Chapter are presented and discussed in Marino et al. (2020), written in collaboration with Dr. S. Migliari (*ESA*), Dr. D. Russell (NYU Abu Dhabi), Dr. R. Belmont (*CNRS*), Dr. M. Perucho and J. Lopez-Miralles (Univ. Valencia).

6.5 The source: 4U 0614+091

Discovered by the Uhuru survey in the 70s (Forman et al. 1978), 4U 0614+091 was later identified as a Low Mass X-ray binary hosting a NS by the detection of type-I X-ray bursts (Swank et al. 1978). From the study of the bursts a measure of the distance was obtained, i.e. around 3.2 kpc with a 15% uncertainty (Kuulkers et al. 2010). Due to its short orbital period of around 50 min (Shahbaz et al. 2008; Baglio et al. 2014), the system has been classified as an ultra compact X-ray binary or UCXB, implying a likely degenerate-helium dwarf or white dwarf nature for the companion star (see, e.g. Kuulkers et al. 2010, for an extensive discussion on the companion star nature). The source is classified as a persistent atoll source and is expected to spend in the hard ("island") spectral state almost 90% of its time (van Straaten et al. 2000), with a constantly high X-ray spectral variability level (higher than 5%) and only episodical transitions to softer states (Muñoz-Darias et al. 2014). In the past, a few authors gave evidence for the presence of a so-called hard tail in the spectrum, reaching energies beyond 100 keV, which was modeled with non-thermal models (Piraino et al. 1999; Migliari et al. 2010) or thermal Comptonization from a very hot corona (Ford et al. 1997; Piraino et al. 1999; Fiocchi et al. 2008). A reflection component has been commonly used to describe the X-ray spectral emission too, although the Fe K line was usually found to be absent or weak. The apparent absence (or weakness) of this feature may be related to an underabundance of Fe (Madej et al. 2014; Ludlam et al. 2019) in the secondary star with respect to solar abundances and it is compatible with the hypothesis of an out-of-main-sequence companion.
The flat radio to mid-IR spectrum, reported by Migliari et al. (2010) in the first complete multi-wavelengths spectral study of the source, witnesses the presence of a compact jet in the system, as confirmed by the polarimetric study by Baglio et al. (2014).
In this chapter, I report on the application of the Internal Shocks model to the Spectral Energy Density of 4U 0614+091, the first attempt ever to describe the entire SED of a NS LMXB with a model including both the jet and the accretion flow emission. Furthermore, ISHEM has been used so far only with systems hosting a black hole and never for a NS LMXB, as in this work.

6.6 Data

The ISHEM model depends on three essential ingredients: (1) a multi-wavelength SED, (2) a PDS which is used as tracer of the accretion flow variability, and (3) a synthetic spectrum, simulated on the basis of the PDS to be compared with the real SED. In the previous applications of ISHEM (see, Drappeau et al. 2015; Malzac et al. 2018; Péault et al. 2019; Bassi et al. 2020), it was proven that the X-ray PDS quasi-simultaneous to the SED can be satisfactorily used as ingredient (2). The methods to obtain these three ingredients are described in the following sections, in particular in this Section I describe the data set and the timing analysis while the model used, the main parameters adopted and the spectral fitting procedure will be described in Section 6.7-6.8.
This work takes advantage of the multi-wavelength observational campaign performed on the source within 5 days, between October 30 and November 4 2006, from radio to X-ray. For the radio-to-IR realm, I used radio observations collected by the Karl G. Jansky Very Large Array (*VLA*), mid-IR/IR

observations taken by the Infrared Array Camera (IRAC) onboard *Spitzer Space Telescope*. I used near-IR/optical data by the ground based Small and Moderate Aperture Research Telescope System (*SMARTS*), while the optical/UV observations were taken with UVOT onboard the Neil Gehrels Swift Observatory (*Swift* in the following). Finally X-ray data were obtained with the Proportional Counter Array (PCA) and the High Energy X-ray Timing Experiment (HEXTE) onboard the Rossi X-ray Timing Explorer (*RXTE*) and XRT onboard *Swift*. This vast data set was already used for a comprehensive spectral analysis by Migliari et al. (2010). I refer to this paper for the details concerning the data reduction and analysis performed on the observations, except for the *Swift*/UVOT data, which were re-extracted in this work.

6.6.1 *SMARTS*-UVOT data treatment

As pointed out by Migliari et al. (2010), the data in the optical-ultraviolet (covered by *SMARTS*-UVOT) region of the electromagnetic spectrum show indeed an unexpected shape, which can not be ascribed to irradiation of the outer disk or to the blackbody emission from the (likely very faint, Nelemans et al. 2004; Shahbaz et al. 2008) companion star. In order to check if a different treatment of the data might improve their results, I re-analysed UVOT data (ObsID 00030812001), in collaboration with my colleague Dr. A. D'Aí from IASF Palermo, with HEASOFT v. 6.26 following the standard procedure[11] and we used the calibration files updated to the latest available version (CALDB 2017-09-22). This observation was carried out using all the six UVOT filters. By using the task UVOTDETECT, we clearly detected 4U 0614+091 in each image. We defined a source region with a 5 arcsec radius and several different background regions for each filter around the source. Finally, the photometry of 4U 0614+091 has been performed with the task Uvotsource.
The de-reddening applied by Migliari et al. (2010) on the *SMARTS* data was removed by using equation (1) and the values reported in table 3 (for the bands V, I and J) of Cardelli et al. (1989) and considering A_V=2, as reported in Migliari et al. (2010) in order to get $A(\lambda)$, i.e. the absorption at wavelength λ. Considering then $F_\lambda = F_{\lambda,0} \times e^{-A(\lambda)/1.086}$, with F_λ and $F_{\lambda,0}$ the absorbed and unabsorbed fluxes at wavelength λ, respectively, I obtained the required values for the uncorrected *SMARTS* data. The new UVOT data and the uncorrected *SMARTS* data have been then de-reddened by us via XSPEC, using a proper model (see Subsection 6.8.2).
With the new treatment of the optical-UV data the odd IR-UV spectral shape reported by Migliari et al. (2010) has now disappeared. In Figure 6.4 I compare the "old" and the new data sets de-reddened, in order to investigate the nature of the previously reported tricky result. I therefore retain this discrepancy arises from the different extraction methods, in particular on the choice and sizes of source and background regions used for the photometric measures.

6.6.2 X-ray Timing Analysis

The timing analysis performed here was carried on by my collaborators Dr. S. Migliari (*ESA*) and J. Lopez-Miralles (Univ. Valencia). The observation 92411-01-06-07 (30 October 2006) was used, performed by the RXTE Proportional Counting Array (PCA). Data were taken in the *event* mode configuration with a time resolution of $\sim$125 μs, allowing to obtain PDS up to a Nyquist frequency of 4096 Hz. We averaged multiple PDS data calculated over 128 seconds subintervals covering a total data set of 2048 seconds, using Fast Fourier Transform (FFT) techniques. No deadtime corrections nor background subtraction were performed before creating the PDS. We subtracted the Poisson noise power, derived from the PDS in the frequency range 1536 and 2048 Hz, following

[11] reported in https://www.swift.ac.uk/analysis/uvot

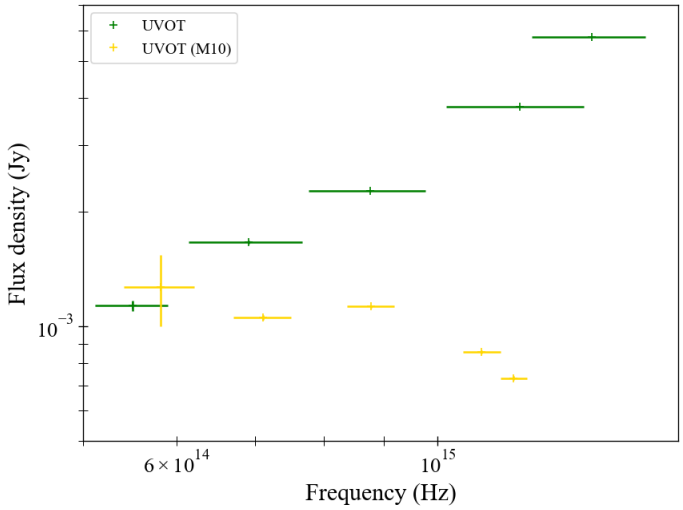

FIGURE 6.4: Comparison between the unabsorbed UVOT data in Migliari et al. (2010) (yellow points) and the unabsorbed UVOT data used in this paper (green points). In particular, for the new UVOT data set I corrected for an absorption coefficient of $A_V \sim 1.5$, found using the model REDDEN on XSPEC (see subsection 6.8.2-6.8.3 for further details).

Lorentzian Component	ν_0	Δ	r
1	(0)	62.0 ± 5.0	$0.106^{+0.003}_{-0.006}$
2	650^{+30}_{-24}	<250	$0.030^{+0.010}_{-0.008}$
			$\chi^2_\nu(\mathbf{d.o.f.}) = 1.49(126)$

TABLE 6.1: Fit results of the PDS described with a sum of two Lorentzians, each of them given by $P(\nu) = r^2/\pi\left[\Delta^2 + (\nu - \nu_0)^2\right]$, with r the integrated *rms* over the full range of frequencies $-\infty$ to $+\infty$, Δ the Full Width Half Maximum of the Lorentzian and ν_0 its central frequency. Values in round parentheses were kept frozen during the fit. Quoted errors reflect 68% confidence levels.

Zhang et al. (1995). Figure 6.5 shows the traditional ν, P_ν representation where we applied the Leahy normalisation (Leahy et al. 1983) before converting the PDS to squared fractional rms. The resulting PDS was eventually fitted with a model consisting of the sum of two Lorentzians, each of them given by $P(\nu) = r^2/\pi\left[\Delta^2 + (\nu - \nu_0)^2\right]$, with r. We used one broad Lorentzian to fit the low frequency noise and one narrow Lorentzian to fit the QPO in the range ~500-700 Hz. The best-fit parameters found were used as input for ISHEM and are listed in Table 6.1. Although the fit is poor, I highlight that since the PDS is used only as a proxy of the variability in the Lorentz factors of the ejecta, even a rough description of the PDS serves satisfactorily my scopes.

6.7 Simulating the jet with ISHEM

The PSD is fundamental in order to perform a simulation of the jet emission with ISHEM, since it is used as a tracer of the fluctuations in the Lorentz factor of the ejecta, but it is not the only ingredient. The shape of the simulated SED depends critically on other two ingredients: (1) the index of the electron distribution p_{el} and (2) the geometry of the jet. The first one was fixed to 2, as the IR slope of the synchrotron spectrum α has been found to be 0.5 (Migliari et al. 2010) and

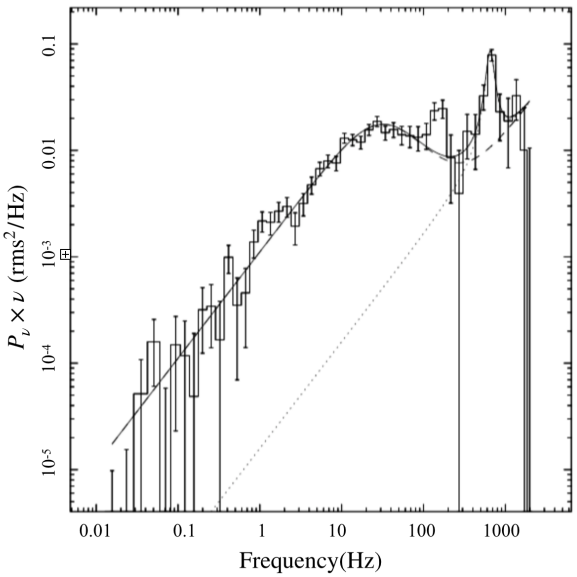

FIGURE 6.5: PDS in the normalized power (P_ν) times frequency (ν) representation, with the best fit multi-Lorentzian model.

$p_{\rm el} = 2\alpha + 1$. In this work, I will also allow ζ to change over finite values between 1.0 and 0.5, in order to test which geometry is the more appropriate for the source.

6.7.1 The impact of geometry and simulation times on the simulated spectra

In the previous applications of ISHEM, the geometry was assumed to be conical and ζ was fixed to 1 by default. This is the first time that the dependency of the results on ζ is tested. In order to correctly take into account a non-conical geometry, the code used in this work has been updated with respect to the previous versions used by, e.g., Drappeau et al. (2015); Péault et al. (2019). The new version of the model also includes some improvement of the treatment of radiation transfer, detailed in Appendix, Marino et al. (2020). Some examples of simulations illustrating the effects of a non-conical geometry are shown in Fig. 6.6. As shown in the Figure, reducing ζ allows for a more collimated jet, where the energy losses are reduced and the spectrum is naturally flatter. Furthermore, for a fixed length of the jet, the range of wavelengths emitted by the different regions will shrink as a result of the contained energy losses. This leads to the appearence of a low frequency turn-over which marks a transition from the flat partially absorbed region of the SED to optically thick emission $F_\nu \propto \nu^{5/2}$ at lower frequencies. This optically thick emission arises from the terminal part of the jet at the largest scale. As can be seen in Fig. 6.6, the low frequency termination turn-over gradually moves toward higher frequencies at lower ζ and might be observable if the jets are strongly confined. Lowering ζ results also in an increase of the overall flux emitted, as both the amount of energy lost and the frequency range over which jet power is distributed diminishes. The frequency of the termination break in the SED of the source also depends on the size of the jet, which, in the model corresponds to the distance to which the shells have been able to propagate during the time of the ISHEM simulation i.e. $\sim ct_{\rm simu} \simeq 3 \times 10^{15}$ cm in the spectra shown in Fig. 6.6[12]. As shown in

[12]Note that in the real world, the extension of the jet depends not only on the time since the ejection started, but also on the interaction of the jets with their ambient medium at large scales which is not modelled here.

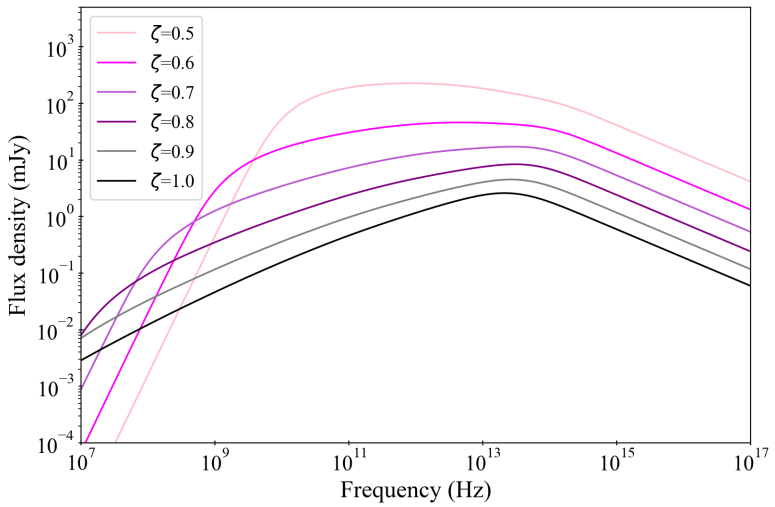

FIGURE 6.6: Simulated SEDS with ISHEM using several values of ζ, from 1.0 to 0.5, without rescaling or shift factors applied, showing the impact of geometry on the flux and the shape of the emitted jet spectrum. In order to simulate these spectra, the X-ray PDS was used as input.

Fig. 6.7, in the case of strongly parabolic jets, increasing the simulation time pushes the spectral turnover towards lower frequencies, without affecting the shape of the spectrum (see Fig. 6.8 for a distinction between the effect of reducing ζ and increasing $t_{\rm simu}$). In contrast, in the conical jet model the SED is barely affected by the duration of the simulation.

6.7.2 ISHEM parameters

As for the other parameters involved in the simulation (see 6.4), a summary is reported in Table 6.2. As mentioned in Section 6.5, the distance of the source is well constrained to be around 3.2 kpc, while no constraints have been ever reported at my knowledge on the mass of the NS, which in the following will be fixed to 1.5 $M_\odot$[13], or to the inclination of the system. However, the lack of observed eclipses or dips shows that it should be lower than 60°-70°, therefore I fixed it to 60°. The jet power is not known, but since the simulations are only roughly dependent on this parameter, I fixed it to be of the same order of magnitude of the X-rays luminosity of the source, i.e. 0.01 $L_{\rm Edd}$ (Migliari et al. 2010). I chose f_V=0.7 (Malzac 2014) and R equal to 10 R_G, which is plausible for X-ray binaries, but the impact of these parameters on the overall results is negiglible. For $\Gamma_{\rm av}$, which for X-ray binaries is expected to vary between 1 and 10 (see, e.g. Casella et al. 2010), I started with a value of 2 (Gallo et al. 2003; Heinz 2004). For the lower and upper limits of the electron distribution and its index, I started with some standard values for X-ray Binaries, i.e. 10, 10^6 and 2.5 respectively (Gandhi et al. 2011; Malzac 2014; Drappeau et al. 2015). A study of how the resulting simulated SED depends on the values chosen for the cited parameters is presented in fig. 2 of Péault et al. (2019). The dependence of the results on these parameters will be explored in this chapter as well.

As already discussed in subsection 6.7.1, in the case of non-conical jets ($\zeta < 1$), the choice for $t_{\rm simu}$

[13] Which is close to the peak for recycled NSs in the expected NSs mass distribution (Özel et al. 2012).

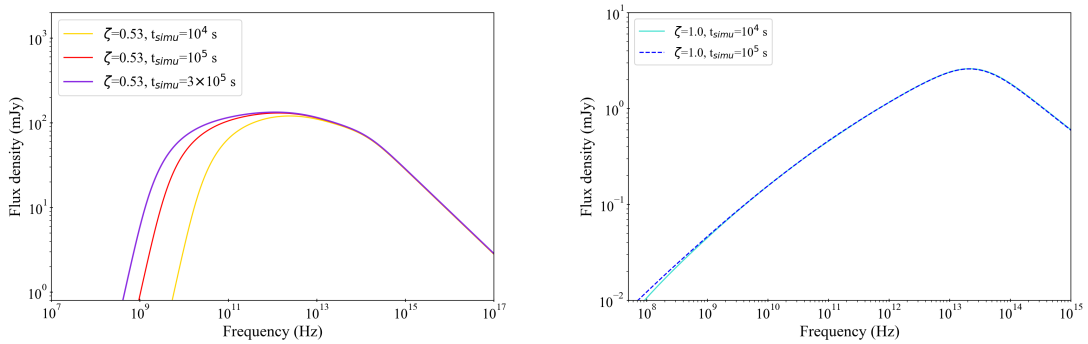

FIGURE 6.7: Simulated SEDS with ISHEM using several values for $t_{\rm simu}$ in both non-conical (*left*) and conical (*right*) geometry, showing how for strongly non-conical jets the low frequency turnover is dependent on the choice for $t_{\rm simu}$. For both plots, $t_{\rm simu}$ was fixed to 10^5 s.

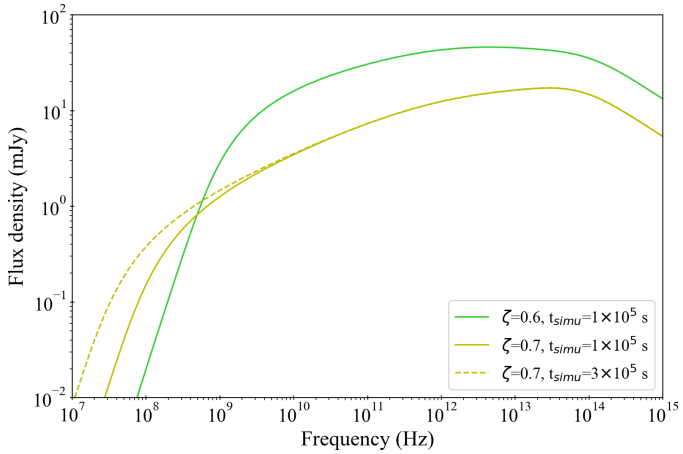

FIGURE 6.8: Simulated SEDS with ISHEM using several values for $t_{\rm simu}$ and ζ in order to show the separate effect of reducing ζ and increasing $t_{\rm simu}$.

becomes crucial because it determines both the size of the jet and the location of the low-frequency jet termination turn-over. I choose to set this parameter to 10^5 s, which corresponds to a final jet extension of $\sim 3 \times 10^{15}$ cm. As the observed radio spectrum in 4U 0614+091 is rather flat, reproducing the data with a strongly non-conical model will require to have the spectral turn-over well below 10 GHz. So the jet should be as large as possibly allowed by the observational constraints. Regarding 4U 0614+091, the constraints on the jet extension are very poor. Namely, the jets from 4U 0614+091 should not be significantly bigger than $\sim 10^{17}$ cm, otherwise they would have been resolved with the VLA. In general, however, the observations of compact jets suggest much smaller dimensions for the radio emitting region. In the case of the resolved jet of Cyg X-1 the extension of the radio jet at 8.4 GHz indicates scales of the order of $10^{14} - 10^{15}$ cm (see, e.g Stirling et al. 2001). My choice for $t_{\rm simu}$ is therefore the most favourable for non-conical jet models while being still roughly compatible with the expected scale of the radio jet.

A summary of the parameters used in the simulation is reported in Table 6.2.

Simulation parameters	
M_{NS} ($M_\odot$)	1.5
t^a_{simu} (s)	10^5
r^b_{dyn} (R_G)	10
ϕ (°)	2.0
f_{vol}	0.7
γ^d_a	4/3
$\gamma_{average}$	2.0
Ejecta scheme	constant shell mass
P_{jet} (L_{Edd})	0.01
γ_{min}	10
γ_{max}	1e+06
i (°)	60

TABLE 6.2: Parameters used in the ISHEM code which were kept fixed in all the simulations run in this paper. *a*: Simulation running time; *b*: Initial radius of the ejecta, imposed of approximately the same order of magnitude of the inner radius of the accretion disk; *c*: effective adiabatic index of the flow, (Malzac 2013).

6.7.3 Simulations

In the previous sections, I gave details on the data set and on the model. In order to test if data and model are compatible it is necessary first of all to compute a simulated, *synthetic* SED using ISHEM. The code simulates over a fixed simulation running time t_{simu} the ejection of shells with velocity variable according to the input PDS in an environment which is set-up by the choice of p, ζ and the parameters described in Subsection 6.7.2. The simulated SED is produced to build a local model on XSPEC (v. 12.10.1f) called ISH used to fit the data. The model is characterized by basically two parameters, i.e. a re-normalization parameter and a shift parameter, which allow me to rescale or shift in frequency the synthetic SED but not to change its shape, determined by the parameters set-up in ISHEM. The model ISH is therefore used to fit the data. In the case of a poor fit, a different combination of PDS, ζ and p needs to be used in order to change the spectral shape. When a good fit is found, the best-fit scaling and shift parameters can be used to improve the original set of parameters in Subsection 6.7.2. The shift parameter scales as the frequency break ν_b and the renormalization parameter scales as the flux at this frequency F_{ν_b}. The following system of relation holds for these parameters:

$$F_{\nu_b} \propto \frac{R_b^{\zeta-1}}{\tan^\zeta \phi} \frac{\delta^{\frac{3p+7}{p+4}}}{D^2_{kpc}} \frac{\sin\theta^{\frac{p-1}{p+4}} \quad i_\gamma^{\frac{5}{p+4}} \quad P_J^{\frac{2p+13}{2p+8}}}{[(\Gamma_{av}+1)\Gamma_{av}\beta]^{\frac{2p+13}{2p+8}+\zeta-1}} \tag{6.11}$$

$$\nu_b \propto \frac{R_b^{\zeta-1}}{\tan^\zeta \phi} \delta^{\frac{p+2}{p+4}} \frac{\sin\theta^{\frac{-2}{p+4}} \quad i_\gamma^{\frac{2}{p+4}} \quad P_J^{\frac{p+6}{2p+8}}}{[(\Gamma_{av}+1)\Gamma_{av}\beta]^{\frac{3p+14}{2p+8}+\zeta-1}} \tag{6.12}$$

where $\beta = \sqrt{1-\Gamma_{av}^{-2}}$, $\delta = [\Gamma_{av}(1-\beta\cos i)]^{-1}$ and $i_\gamma^{-1} = \int_{\gamma_{min}}^{\gamma_{max}} \gamma^{-p}(\gamma-1)d\gamma$. Playing with these equations, once I obtained a couple of values for the shift and renormalization parameters, gives the possibility to obtain new values for the parameters appearing in these equations, which could then be used in ISHEM to simulate SEDs with the right scale and break frequency position. The reported

equations represent an extension of equations (1) and (2) reported by Péault et al. (2019) to the non-conical geometry with also a more realistic angle dependence of the jet emission which reflects also the improvements in the new version of ISHEM used in the present work. A full derivation of these scaling relations is presented again in Appendix, Marino et al. (2020). Finally, since the spectral emission from the source is largely dominated by the accretion flow beyond the optical wavelengths, I was not able to constrain the "cooling break" of the spectrum, which is expected at high energies (see, e.g Pe'er 2014). I then assume the jet optically thin synchrotron emission to extend with a power-law shape at least up to the hardest X-ray bands of the observed SED. I note that the extrapolation of the observed IR power-law spectrum at high energies implies that the jet has a negligible contribution in the hard X-ray band (see Subsection 6.8.3).

6.8 Spectral Analysis

In NS Low Mass X-ray Binaries the jet emission is expected to dominate only the radio-to-IR wavelengths, while the emission from optical to X-ray should be mainly ascribed to the accretion disk (since usually the radiation emitted by the faint companion is negligible). Therefore, I began with a separate analysis for the radio-to-IR data, fitted with ISH. Then, the optical-to-X-ray data were described mainly with DISKIR, an irradiated disc plus Comptonization model (Gierliński et al. 2008). However, although X-ray reprocessing from the outer disk or even direct emission from the outer disk is expected to dominate the Near Infrared (NIR) - optical region in NS LMXBs (Russell et al. 2006, 2007), some level of contribution from the jet emission might still be present (several examples can be found in, e.g. Lewis et al. 2010; Harrison et al. 2011; Baglio et al. 2016, 2019). Therefore, I performed a fit of the whole data set, in order to check if accretion and ejection do dominate over two separate frequency ranges or either if there is a border territory, i.e. the NIR-optical region, where these phenomena can not be easily singled out and have to be taken into account together.

6.8.1 From radio to IR: the jet emission

I first tried to reproduce the observed SED with a standard set of parameters, which are listed in Table 6.2, with $p = 2.0$, the X-ray PDS and adopting the usual conical geometry (ζ=1). I chose $p = 2.0$ according to the fit to the optically thin part of the jet spectrum by Migliari et al. (2010) and also to the standard diffusive shocks acceleration theory. I then tested the "synthetic" spectrum on XSPEC, using the ISH model built on it to fit the data. I also checked if using a one-Lorentzian model instead of a double-Lorentzian model, i.e. ignoring the component for the high frequency QPO (see 6.6.2) which could probably be related to the orbital motion of the system (Stella and Vietri 1998), could influence the results of the fit. I found that both models lead to the same results, therefore in the following, I will refer only to the results obtained including the QPO.
Even if IR fluxes are expected to be only slightly affected by interstellar reddening, I included the model REDDEN, which estimates the extinction in the optical band, $E(B-V)$. The latter was frozen to 0.5 (see Sec. 6.8.2), since it was left unconstrained by the fit. The outcome of the fit is quite poor, as witnessed by the resulting χ^2_ν (d.o.f.) of 3.96 (5). Furthermore, using Equations 6.11-6.12 to explore the parameters needed to improve the simulation, I found that, in order to have reasonable values for the jet power of the expected order of magnitude, i.e. 0.01 $L_{\rm Edd}$, one has to invoke oddly high opening angles (see Section 6.9). As mentioned in Section 6.4 the shape of the SED can be affected by only three elements: the shape of the electron distribution (which modifies the slope of the optically thin part of the spectrum), the geometry chosen and the dissipation pattern of the ejecta, in this case based on the X-ray PDS. Since the IR data are well fitted by the optically thin region of

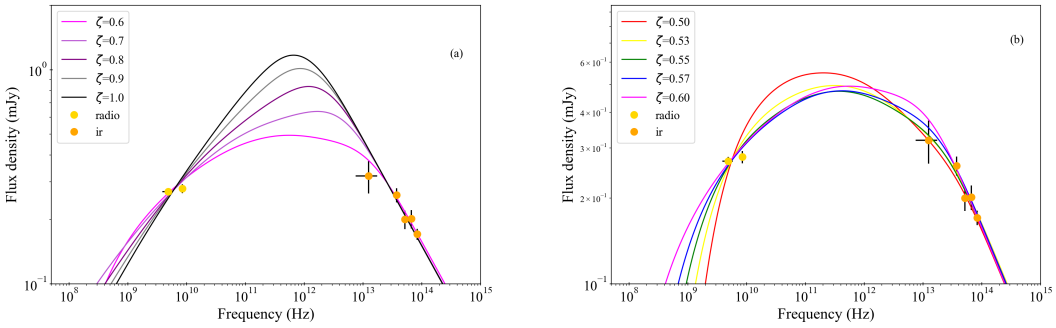

FIGURE 6.9: Simulated SEDS with ISHEM using several values of ζ, from 1.0 to 0.6 (panel *a*) and in the critical region 0.5 to 0.6 (panel *b*), normalized and shifted in order to fit the data. In all these models, the X-ray PDS was used as an input for ISHEM. Panel *b* shows the interesting evolution of the SED for values of ζ spanning in the crucial region between $\zeta = 0.6$ and $\zeta = 0.5$: when the jet becomes too collimated, the contribution from the external regions of the jet (the lower frequencies) becomes dominant and it leads again to an inverted spectrum.

the synthetic SED, the chosen value of p seems to be correct, as expected. In the following I will then try to change the geometry first and the PDS then in order to see if, with a different choice for these ingredients, I can still find a good model for the data. In order to check if a different value for ζ might improve the results of the fit, I run again the simulations with different ζ between 0.5 and 1.0, and I repeated the whole procedure. The resulting best fits as a function of ζ is shown in Figure 6.9, *a-b*. The results of each fit is reported in Table 6.3. The values of ζ for which I have the lowest χ^2_ν are 0.57 and 0.6 (1.08 and 1.13 respectively, both with 5 d.o.f.). A paraboloidal jet with ζ in this range of values therefore represents an acceptable fitting scenario, contrary to the typical conical geometry.

As mentioned in Subsection 6.7.2, for strongly non-conical geometries, spectra obtained with longer simulation times could produce flatter spectra. I show in Table 6.4 the results of the fits for three values of ζ, i.e. 0.53, 0.60 and 0.7 with $t_{\rm simu} = 1 \times 10^5$ and $t_{\rm simu} = 3 \times 10^5$. As expected, the values of χ^2_ν are generally lowered by increasing the simulation time, with the exception of the fit with $\zeta = 0.7$, which is mostly unaffected by changing $t_{\rm simu}$. Even with higher simulation times I found the best fit for ζ around 0.6. While an even higher simulation time would still be physically acceptable (see Subsection 6.7.2), it would very likely only confirm the results presented here with shorter and more feasible $t_{\rm simu}$.

I also notice that the conclusion on the best value of ζ should not be considered definitive, as further investigations in the range between ζ =0.53 and ζ =0.6, with possibly higher $t_{\rm simu}$ could, in principle, lead to even more accurate estimates of the best ζ. However, a precise estimate of ζ goes beyond the scopes of this work and would likely provide no or very little improvement to the results.

I therefore conclude that a non-conical geometry, with ζ around 0.6 and possibly even below, improves significantly the fit with ISHEM using the X-ray PDS.

I then tested the other possible scenario, where the observed X-ray variability does not reflect the fluctuations of ejection velocity, using a "flicker-noise" PDS in conical geometry. I assumed a rms fractional amplitude of 30% and included a range of frequencies ranging from $f_1 = 10^{-5}$ Hz to $f_2 = 10^3$ Hz. Using the same set of parameters shown in Table 6.2, I obtained a synthetic SED which is in quite good accordance with the data, i.e. χ^2_ν (d.o.f.)=0.27(5). The best-fit model is shown in Figure 6.10, in comparison with the data and a pair of best-fit models obtained with the X-ray

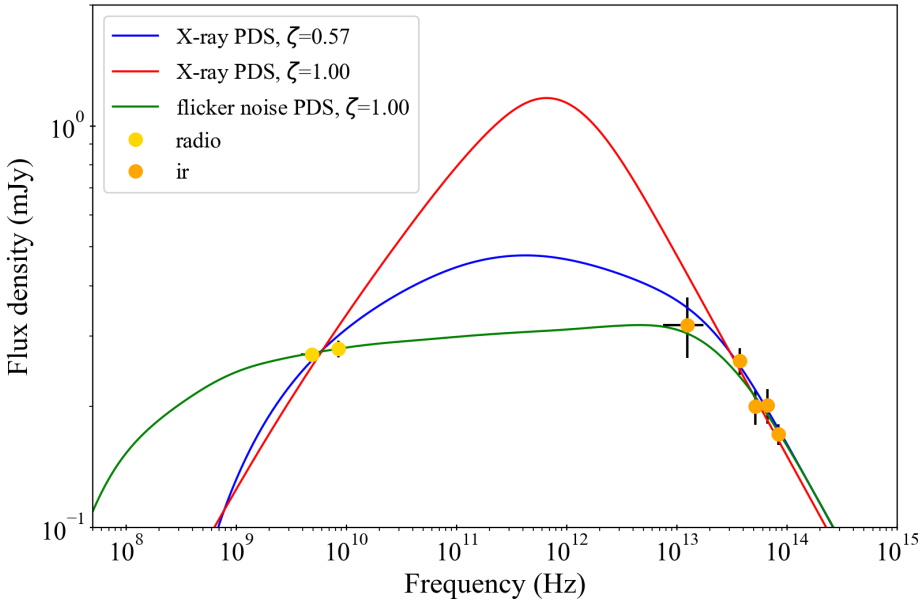

FIGURE 6.10: Simulated SEDS with ISHEM for varying geometries and input PDS as compared with the radio-to-IR data set.

Fit results for different jet geometries									
	ζ								
	0.50	0.53	0.55	0.57	0.60	0.70	0.80	0.90	1.00
χ^2_ν	5.95	2.34	1.46	1.08	1.13	2.11	2.84	3.37	3.96

TABLE 6.3: Results of the *VLA-Spitzer*/IRAC fits with ISH with different ζ values. In all the fits the number of degrees of freedom is equal to 5.

Fit results for different jet geometries and simulation times						
	ζ					
	0.50		0.60		0.70	
$t_{\rm simu}$ ($\times 10^5$ s)	1	3	1	3	1	3
χ^2_ν	2.34	1.36	1.13	0.80	2.11	2.13

TABLE 6.4: Results of the *VLA-Spitzer*/IRAC fits with ISH with different ζ and $t_{\rm simu}$. In all the fits the number of degrees of freedom is equal to 5.

PDS and variable values of ζ.

6.8.2 From optical to X-ray: the disk emission

While in the previous section I focused on the part of the SED dominated by the jet, in this section I will focus on the optical-to-X-rays data, which are expected to be dominated by the disc and the hot corona emission.
First of all, I used DISKIR (Gierliński et al. 2008), which includes the disk emission, Comptonization from a hot corona and the X-ray illumination of the disk, relevant in the presence of data coverage in the optical-UV domain (as in my case). The main parameters of the model are: the temperature of the disk at its inner radius $kT_{\rm disk}$, the Γ index of the power-law reproducing the Comptonization spectrum, the electron temperature of the corona $kT_{\rm e}$, the ratio $L_{\rm C}/L_{\rm D}$ between the luminosity of the Comptonized emission and the disk luminosity, the fraction of the flux of the Compton tail which is thermalized in the inner and outer radius ($f_{\rm in}$ and $f_{\rm out}$ respectively), the radius of the illuminated disk $r_{\rm irr}$, the outer disk radius $\log r_{\rm out}$ (both in units of the inner disk radius) and the normalization K, which can be used to derive the inner disk radius.
The value $L_{\rm C}/L_{\rm D}$ is generally used as an indicator of the spectral state and it is usually higher than 1 in intermediate/hard states. In the following fits I fixed $f_{\rm in}$ and $r_{\rm irr}$ to the standard values of, respectively, 0.1 and 1.1 (Gierliński et al. 2008). Furthermore, as 4U 0614+091 is known to be an Ultra-Compact Binary, I fixed $\log r_{\rm out}$ to the value of 3. This value is reasonable considering that, since the system has an orbital period of about 50 mins, the orbital separation is expected to be around 3×10^5 km and a factor of 10^3 guarantees that even with large inner disk radii, say 100 $R_{\rm G}$, as expected in hard state, it is larger than the extension of the disk. A black-body model in the spectrum (BBODY in XSPEC) was also included, already present in the fit by Migliari et al. (2010), which accounts for the emission of the NS surface (or the boundary layer). Finally, I included the two Gaussian components used by the authors, i.e. at 0.67 keV for the O VIII line and at 6.6 keV for the Fe K fluorescence line. I applied to the model the components REDDEN and TBABS to take into account interstellar extinction in both the UV and X-ray band. Finally, I included CONSTANT to serve as a cross-calibration constant and then checked that its value was always around 1, i.e. in the range 0.8-1.2.
The fit did not constrain $L_{\rm C}/L_{\rm D}$, which was therefore tentatively fixed to 10, which is a reasonable value for hard states (see, e.g. Del Santo et al. 2008). The fit is unable to constrain the parameters of the GAUSSIAN component at 6.6 keV, due to a marginal contribution of this component to the fit, i.e. a 9% probability of improvement by chance (calculated via FTEST). This is not surprising, since the iron line in 4U 0614+091 is known to be weak (see, e.g Piraino et al. 1999). In the following, I will therefore not include this GAUSSIAN component. On the other hand, I confirmed the presence of a broad line at $\sim$ 0.67 keV, likely associated to O VIII (see Section 6.5 for references). The fit provides E(B-V) (from REDDEN) of about 0.5, which corresponds to a value[14] of $A_{\rm V}$ slightly lower than the one reported in Migliari et al. (2010), equal to 2. Only a relatively high lower limit to the corona temperature could be found, i.e. 110 keV, which might be probably due to the lack of a proper modeling of the high energy hard tail (see, e.g Di Salvo et al. 2001; Iaria et al. 2001; D'Aí et al. 2007; Del Santo et al. 2013, and references therein) rather than such a hot electron plasma. The results of the fit led as well to a significantly colder disk with respect to Migliari et al. (2010), i.e. $kT_{\rm disk} < 0.1$ keV, but correlations with the disk normalization K and/or with the imposed values of $L_{\rm C}/L_{\rm D}$ might be at play. The normalization of the disk K is bound to the inner radius of the disk

[14] Keeping in mind the relation $A_{\rm V} = R_{\rm V} \times E(B-V)$, with $R_{\rm V}$ fixed to 3.1 (Seaton 1979b,a).

Spectral analysis			
REDDEN	**E(B-V)**		$0.48^{+0.07}_{-0.06}$
TBABS	$\mathbf{N}_H$	$\times 10^{22}$ cm^{-2}	0.21±0.02
	$kT_{\rm disk}$	keV	0.077±0.003
	$kT_{\rm e}$	keV	>110
	Γ		2.24±0.02
	$L_{\rm C}/L_{\rm D}$		(10)
DISKIR	$f_{\rm in}$		(0.10)
	$f_{\rm out}$	($\times 10^{-3}$)	$2.0^{+9.0}_{-1.3}$
	$R_{\rm in}/\sqrt{\cos i}$	($R_{\rm G}$)	73^{+5}_{-4}
	$R_{\rm irr}/R_{\rm in}$		(1.01)
	$R_{\rm out}/R_{\rm in}$		(10^3)
GAUSSIAN	$E_{\rm line}$	(keV)	0.671±0.009
	σ	(keV)	0.077±0.006
BBODY	$\mathbf{kT}_{\rm bb}$	(keV)	1.38±0.02
		χ^2_ν(**d.o.f.**) = 1.49(442)	

TABLE 6.5: Fit results of the disk-dominated SED region, with data from UVOT, XRT, PCA and HEXTE. Quoted errors reflect 90% confidence level. The parameters which were kept frozen during the fits are reported between round parentheses.

$R_{\rm in}$ by the relation: $K = (R^2_{\rm in}/D^2_{\rm 10kpc}) \times \cos i$, with $D_{\rm 10kpc}$ is the distance of the system in units of 10 kpc. I found an apparent inner disk radius of $\sim$ 160 km ($\sim$ 73 $R_{\rm G}$), which has to be taken as a lower limit since it does not take into account the proper (unknown) inclination of the system and the correction factor (for a more detailed calculation of the inner disk radius based on K see, e.g. Marino et al. 2019a, and references therein). The few differences in my results with respect to the results obtained by Migliari et al. (2010) on the same X-ray data are likely due to either the inclusion, in my data set, of the SMARTS-UVOT data or to the different models used in the two papers.

6.8.3 Global multi-wavelength analysis

The spectral analyses conducted in subsections 6.8.1-6.8.2 allowed us to characterize separately the emission from the jet and from the disk, under the hypothesis that the spectral domains of the two were independent. In the following, I report on the global dataset fitted with both accretion and ejection models, in order to confirm the previous assumption and provide a final, multi-wavelength study of the spectral energy distribution of 4U 0614+091.

Starting from the best-fit model for the optical-to-X-ray data, whose main parameters are reported in Table 6.5, I included the *VLA* and *Spitzer* data used in Subsection 6.8.1 and added ISH to the spectral model employed. Since it is not possible to exclude *a priori* that the results reported here on the jet might have been biased by the lack of higher frequencies data, I performed several fits trying different ISHEM models with ζ spanning from from 1.0 to 0.5. Unfortunately each fit results in approximately the same χ^2_ν (d.o.f.) value of 1.49(451)[15]. Similarly, using the ISHEM model based on the "flicker noise" PDS, the fit results in a χ^2_ν (d.o.f.) value of 1.43(451). This situation is not surprising because the fit is indeed dominated by the higher statistics data in the X-ray and only slightly affected by the modeling of the few data points in the radio-IR domain. Leaving the same model, i.e. including

[15]Even if the χ^2_ν is still quite poor, I notice that (i) it is very similar to the fit reported by Migliari and Fender (2006), on which the present Chapter is based and (ii) a more sophisticated X-ray spectral analysis is far beyond the scopes of this chapter and (iii) the inclusion of the fit to the optical-to-X-rays data only confirms what found in the previous Section.

DISKIR and BBODY, but neglecting all the data but radio and IR, results in fits which are similar to the fits performed in Subsection 6.8.1: among the different fits with X-ray PDS with varying ζ, the best fit is obtained again with $\zeta = 0.57$, i.e. for which the fit goes from χ^2/d.o.f.=671.9/451 (including optical-to-X-rays data) to χ^2/d.o.f.=5.25/5, while choosing the flicker noise PDS the fit goes from χ^2/d.o.f.=644.9/451 to a χ^2/d.o.f. of 3.55/5. However, the extension of the data set does have some effects on the ISHEM best-fit parameters, i.e. the shift frequency and re-normalization factors, which are different with respect to the previous set of fits. In the next section I use Equations 6.11-6.12 in order to check whether the best fit shifts and normalization allows for 'reasonable' physical parameters of the jet. Finally, I checked if the results are dependent on the values assumed by the cross-calibration constant for the IR and the radio data, which were assumed to be equal to 1.0 for the radio and IR data; leaving the cross-calibration parameters free to vary between 0.8 and 1.2 does not change significantly the values obtained for the χ^2_ν (d.o.f.). In the following, I will only refer to the fits with the parameters fixed to 1.0.
I refer to Figure 6.11 for the SED, overimposed to the best-fitting ISHEM model. The best-fit parameters of the accretion flow model found with the lower frequencies extension of the dataset are all perfectly compatible with the results reported in Table 6.5.

6.9 Discussion

The analysis limited to the radio-IR domain carried out in Subsection 6.8.1 suggests two possible scenarios to describe the jet emission for 4U 0614+091 within the internal shocks scenario: on one hand the variability in the Lorentz factors of the ejecta is related to the X-ray variability, i.e. the variability in the accretion flow, but the jet is non-conical (in the following scenario *a*), on the other hand it is also possible that, at least in this source, a flicker noise power spectrum, unrelated to the X-ray variability, is a better proxy for the fluctuations of the jet Lorentz factor (scenario *b*). Including the optical-to-X-rays portion of the data set in Subsection 6.8.3 revealed furthermore inconclusive in discerning between the two proposed scenarios, due to the lack of data around 10^{11}-10^{12} Hz. The availability of data in this region, e.g. from the Atacama Large Millimeter/submillimeter Array (ALMA), would have been crucial to distinguish between the two scenarios. For example, ALMA data for other NS LMXBs in hard state (see, e.g., the SEDs shown by Díaz Trigo et al. 2017, 2018) indicate a small rise in flux density in this region which, if observed also in my data set, would have likely favored scenario *a*.
I will instead explore and discuss both scenarios *a* and *b* in the following section, on the basis of the global fit reported in Subsection 6.8.3. In both cases there is evidence that it is not possible to completely disentangle the disc contribution to the IR domain or the jet contribution to the optical domain as well. In particular, it results that there is a jet contribution varying from 30% to 6% in the *SMARTS* wavelengths range within scenario *a*, while this contribution is less prominent in scenario *b*, i.e. from 20% to 3%. These results confirm the study led by Russell et al. (2006), according to which in NS LMXBs the main emission process to be taken into account in the optical domain is the X-ray reprocessing from the disc[16], even though they also point out how the jet contribution might not be negligible at all.

[16]Contrarily to black holes, where the jet emission is usually extended until the optical wavelengths (see, e.g Péault et al. 2019)

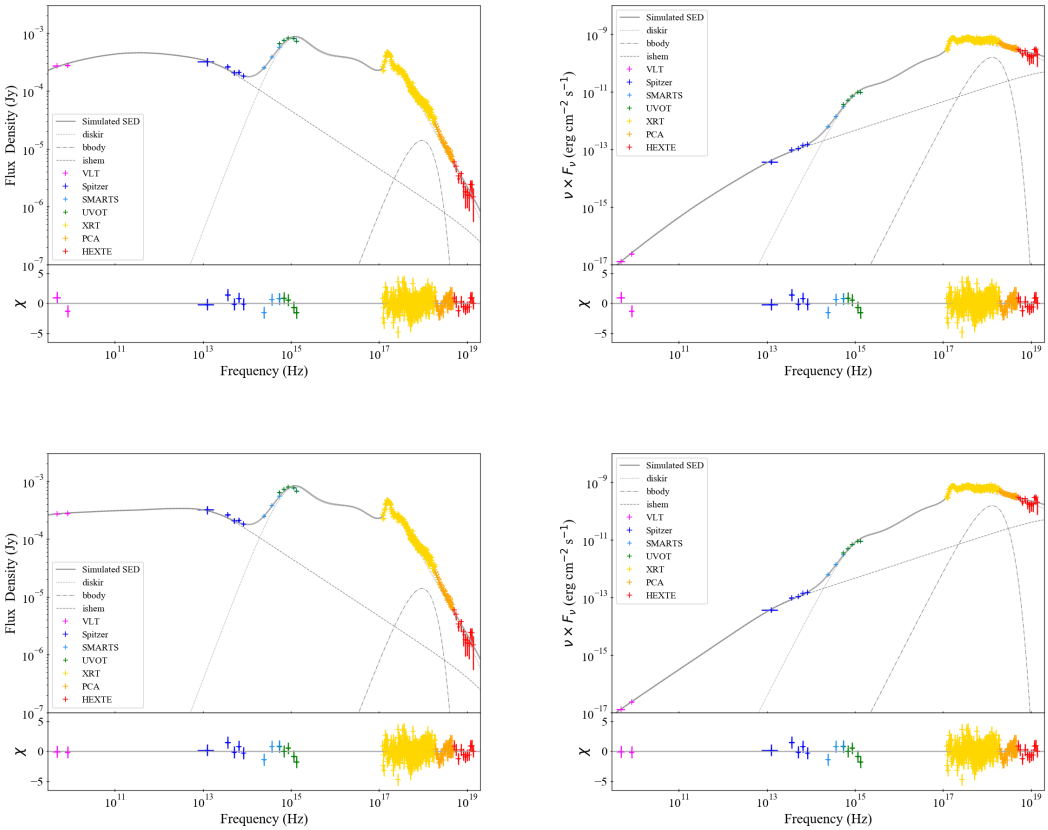

FIGURE 6.11: Best-fit unabsorbed spectral energy distribution compared with the whole multiwavelength dataset available for 4U 0614+091, in both Flux Density (*Left*) and $\nu \times F_\nu$ (*Right*) representation. The optical-to-X-ray data set has been analysed with an irradiated disk + black-body model, while the radio-to-IR data set was modeled with ISHEM. In this plot both best-fit ISHEM models found in this paper are shown: on *Top* the model built with the X-ray PDS and corresponding to a non-conical geometry ($\zeta = 0.6$) and on (*bottom*) the model corresponding to a "flicker noise" PDS in conical geometry.

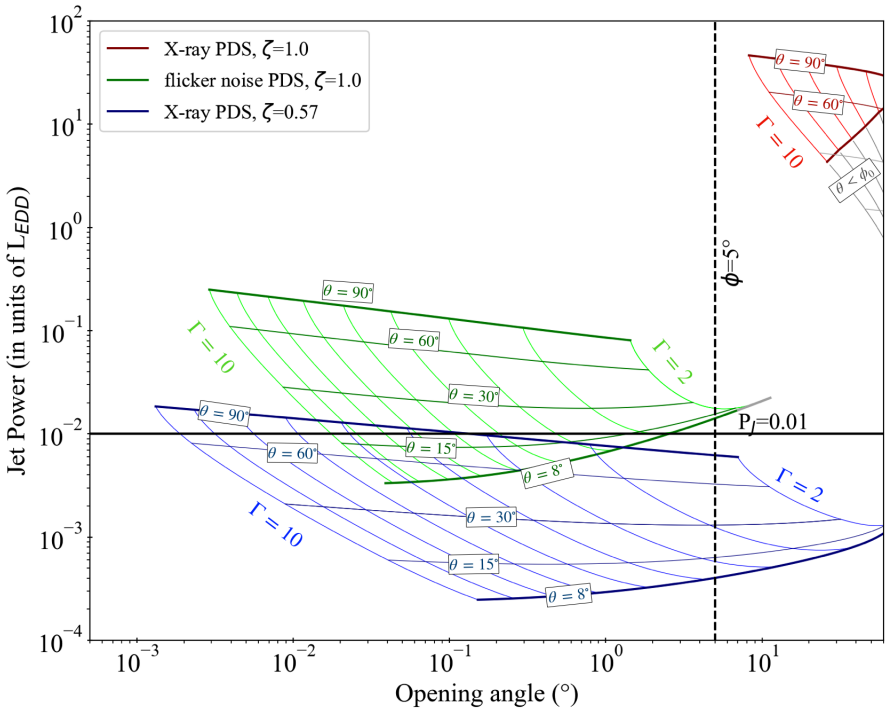

FIGURE 6.12: Jet power - (observed) opening angles curve (from Equations 6.11-6.12) for a different combinations of ζ and PDS to a range of possible values for the inclination θ and a range of Γ_{av} between 2 and 10. In particular, in each "region" (identified by a specific color) the inclination increases going upwards, while the Lorentz factor increases going from right to left. Curves for specific fixed values of Γ and θ are identified to help the eye. In each area, the sub-region for which the condition $\theta > \phi_0$ is not satisfied are colored in grey and have to be discarded, as the used scaling relations are no longer valid. In this plot, the black solid line indicates the expected jet power, while the dashed black line points out the upper limit for the opening angle.

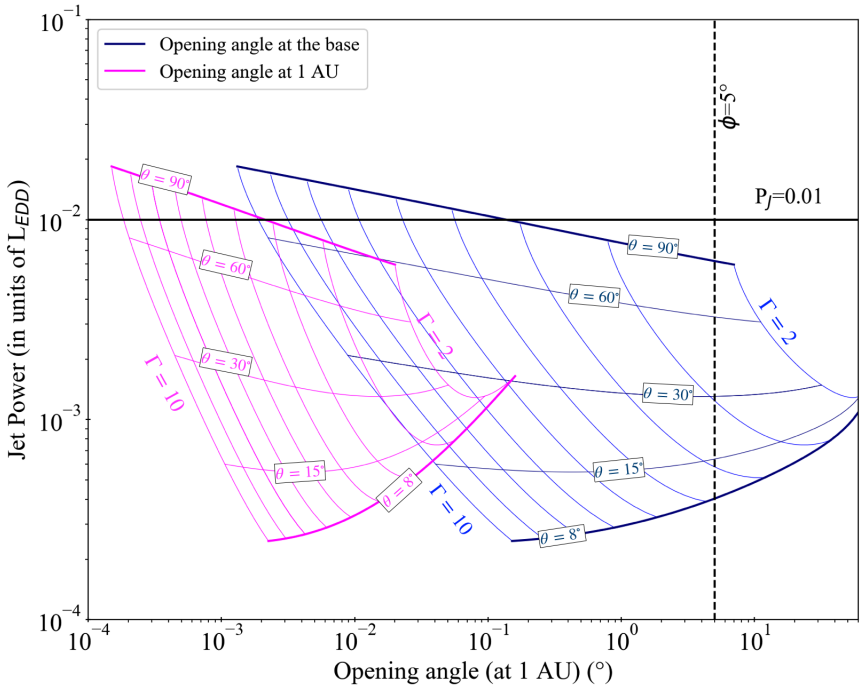

FIGURE 6.13: Jet power - opening angle curves for the particular case of $\zeta = 0.57$, using the opening angles at the base of the jet (blue) and the opening angles hypothetically observed at 1 AU (magenta). I refer to the caption of Fig. 6.12 for further details.

6.9.1 Scenario *a*: a non-conical jet?

Due to the high statistics in the X-rays, the fit to the whole dataset gives comparable values χ^2_ν values for each of the tested geometries, contrary to what happens in the fits limited to the radio-IR data. In order to determine the most likely values of ζ, I use Equation 6.11-6.12 to convert the values of the shift and renorm factors found by ISH in couples of P_J-ϕ. I explored also how these results were influenced by my choice for θ and Γ_{av}, allowing for both to change in some physically reasonable ranges. In particular, since the scaling relations used in this work, i.e. Eq. 6.11-6.12, are valid in the approximation of $\phi_0 \lesssim \theta$ (see **??**), with ϕ_0 the opening angle at the emitting region, the lower limit for the inclination θ was fixed to 8°. On the other hand, Γ_{av} was allowed to vary in the 2-10 range. Running these tests draw areas of possible results in a P_J-ϕ plot, corresponding to specific values of ζ. I show in Figure 6.12 the resulting area for $\zeta = 1.0$ (red) and $\zeta = 0.57$ (blue). In each of the resulting skewed areas, the bottom of the areas corresponds to $\theta = 8°$, the top corresponds to $\theta = 90°$, while Γ_{av} increases from right (where $\Gamma_{av} = 2$) to left ($\Gamma_{av} = 10$). The sub-regions where the condition $\theta < \phi_0$ are colored in grey and they have to be excluded. It is important to notice that for a non-conical geometry, the opening angle depends on distance z along the jet and the emitting region, located at about 1 AU from the base of the jet and comparable to the angle observed in the radio band, will have a different opening angle than the values encompassed by the blue area in Fig. 6.12 (which thereby *can* violate the condition $\theta < \phi$). Indeed, for a fixed geometry parameter $\zeta = 0.57$, using the opening angle at a distance of 1 AU ϕ_0 results in significantly smaller angles, i.e. below 0.1°, as shown in Fig. 6.13. Such extreme values are not implausible, as small opening angles have been suggested for jets in XRBs (see, e.g. Zdziarski et al. 2016). Both the ranges of jet powers and opening angles individuated by the $\zeta = 0.57$ areas can be accepted and a $\zeta \approx 0.6$ value appears

still consistent with the best physically motivated scenario.
For $\zeta = 1.0$, on the contrary, the area found by this procedure does not allow for reasonably small opening angles and requires very high jet powers for the whole range of explored $\Gamma_{\rm av}$. This represents another point in favor of ruling out the conical geometry scenario.

It is interesting to compare these results with those previously found by applying the same ISHEM model to jets in BH-XRBs, where the conical geometry assumption worked correctly. In a few cases, see for example the radio residuals for some spectra in figure 3 of Péault et al. (2019), it is reasonable that flatter models could even improve the already acceptable fits and in this sense a non-conical geometry could be necessary. Any comparison between NS and BH XRBs is therefore premature for at least two reasons: a non-conical geometry was not tested for BH XRBs and, also, it is necessary to test more NS LMXBs to draw any conclusion on a possible difference between jets in these two classes of systems.

6.9.2 Scenario *b*: X-ray variability is not a good proxy for the Lorentz factor fluctuations

In the second scenario, the dissipation pattern of the shells internal energy in the jet is not related to the X-ray timing properties, i.e. the timing properties of the accretion flow, but it is mainly due to "flicker noise". The plausibility of this scenario is confirmed by the $P_{\rm J}$-ϕ diagram in Fig. 6.12, since the corresponding area encompasses the expected range of jet powers-opening angle.
This is not groundbreaking either (I refer again to, e.g., Jamil et al. 2010; Malzac 2013) but it would be certainly different to the results obtained on the other sources to which the ISHEM model has been applied in the past. In this case the fact of having a NS instead of a BH might play a role. Under the hypothesis of a disk-jet coupling, the variability in the emission from the NS/boundary layer may not be transmitted to the ejecta in the jet, breaking subsequently the connection between the ejection pattern of the shells and the X-ray PDS. Alternatively, one might also consider differences in the jet launching mechanism in NSs with respect to BHs. For instance Parfrey et al. (2016) shows how the interaction between a fastly rotating low magnetized NS and the disk may lead to a state where the magnetic field lines are open and provide the energy necessary for the ejection of particles. In this case I do not expect that the dissipation pattern in the ejecta and the accretion flow fluctuations in the disk to be exactly matched. Such a mechanism could be at work in Accreting Millisecond X-ray Pulsars and analogous systems, which might possibly include 4U 0614+091. Indeed, the system, with a 415 Hz frequency spin (see, e.g van Doesburgh and van der Klis 2017, and references therein), belongs to the family of binaries hosting millisecond NSs. However, the NS magnetic field is likely buried, as witnessed by the lack of observed X-ray pulsations, and this would make the attribution of the aforementioned mechanism to the system unlikely.
I also suggest the possibility that the lack of correlation between X-ray variability and ejecta in the jet proposed here for 4U 0614+091 may not necessarily be representative for the whole class of NS LMXBs in hard state. As apparent from the *VLA* data used in this paper, the jet spectrum looks quite flat, which, I recall from Subsection 6.3.1, requires also an almost flat PDS. The X-ray PDS used has evidently not the required shape and it is therefore not surprising that it may not be the best tracer for the variability in the shells velocity. Similar PDS have been observed frequently in the atoll LMXBs, when in island state (IS) (see, e.g van Straaten et al. 2002, 2003). On the other hand PDS dominated by broad, flat-topped noise, similar to what observed in BH XRBs in hard state, have been found also in several atoll sources at low luminosity in the so-called Extreme Island State (EIS) (Belloni et al. 2002; Reig et al. 2004; van Straaten et al. 2005), which was already introduced in Section

2.8. Indeed spectra of NS LMXBs in EIS are typically described with power-laws of $\Gamma \sim 1.8$ (see e.g Barret et al. 2000; Linares et al. 2008), unlike e.g 4U 0614+091 which displays spectra usually steeper, $\Gamma \sim 2.2-2.4$, as in this paper and, e.g. Piraino et al. (1999); Migliari et al. (2010); Ludlam et al. (2019). In addition, the X-ray variability is significantly stronger (i.e. 30-40% rms amplitude, Wijnands et al. 2017a) in EIS than sources in IS. The ensemble of these clues suggests that atoll sources in EIS are likely associated to a physical scenario where the disk is truncated far from the compact object and the NS surface is not very hot (Reig et al. 2004; Bult et al. 2018), while in IS the contribution from the disk and/or from the NS increases, cools down the corona and reduces the X-ray variability. The distinction between sources in IS and EIS is not strict, and some sources, like 4U 0614+091 itself, have been found in both states (see panel 1 in Figure 2 of van Straaten et al. 2002). Assuming that radio jet spectra in NS LMXBs are usually flat[17], it is plausible that X-ray PDS can be used as proxy of the variability in the ejecta for NS LMXBs in EIS. In this sense, AMXPs and/or low luminosity bursters, usually found in EIS, could be good candidates to test ISHEM in the future.

6.10 Conclusions

In this work I presented the first ever attempt to describe the broadband emission of a NS LMXB, i.e. 4U 0614+091, with a model taking into account both the jet and the accretion flow emission. I took advantage of the same multi-wavelength data set presented by Migliari et al. (2010), with the only exception for the *Swift*/UVOT data, which were re-analyzed. I modelled the radio-to-IR spectrum with the ISHEM code, which calculates the expected spectral energy distribution in the low energy part of the SED taking into account the X-ray variability (connected in turn to the internal shocks temporal pattern). In particular, I used the quasi-simultaneous *Swift*/XRT PDS as input for the "synthetic" SED. While the ISHEM model has been applied several times in the past to X-ray binaries hosting BHs as the accreting object, this is the first time that the model is applied to a system hosting a NS. In addition, optical-to-X-ray data were modelled with an irradiated disc model.
I found that the compatibility between the SED built using the X-ray PDS and the data set is critically dependent on the geometry of the jet, enclosed in the geometrical parameter ζ. In particular, a highly non-conical geometry, with $\zeta \approx 0.6$, results in an acceptable fit. Alternatively, an acceptable fit is found within a conical geometry scenario but using in input a "flicker-noise" PDS instead of the X-ray PDS. This scenario might imply that for NS LMXBs the X-ray PDS are not good tracers for the fluctuations in the Lorentz factors of the ejecta, possibly due to some contribution from the boundary layer/NS emission. The scarce statistics does not allow for the moment to choose one scenario over the other. New observations and/or further studies like the one presented here are definitely necessary to provide an answer to this issue and in general for a better understanding of the accretion-ejection coupling in NS LXMBs.

[17] Aside of 4U 0614+091, a couple of other examples can be found in Díaz Trigo et al. (2017).

7. An accretion/ejection paradigm: the case of MAXI J1820+070

SUMMARY

Many aspects of accretion, ejection and their interplay in X-ray binaries remain unexplained to date. Recently a new paradigm was proposed for BH X-ray binaries to address both aspects together, according to which the accretion flow at any spectral state is composed of two disks, an outer standard Shakura-Sunyaev disk (SAD) and an inner optically thin disk called JED and serving as the hot corona. Since the jet is launched only by the JED, the disruption of it in the transition to the soft state coincides with the quenching of the jet. This model is aimed at describing both the X-ray spectrum and the radio jet power emitted in hard state. In this Chapter I am using NuSTAR *and* Swift *data to describe eight observations of the BH LMXB MAXI J1820+070 in hard state. According to the performed spectral analysis, two reflection components, likely associated to different regions of the SAD, are required. Furthermore, in order to avoid oddly reflection-dominated fits, it is necessary to leave the sonic Mach number parameter m_s free to vary in the fits. The results point out that the accretion material in the JED goes from supersonic to transonic when the system goes from hard to the hard-intermediate state, highlighting that m_s is likely playing a crucial role in driving the evolution of the accretion flow.*

7.1 The need for a unified accretion-ejection paradigm

In Chapter 2 it was discussed how LMXBs can be found in a variety of spectral states, i.e. mainly hard, intermediate and soft state, corresponding to different accretion flow properties. In

particular spectra in hard states are dominated by the emission from a hot optically thin corona, while systems in soft state show quasi-blackbody spectra associated to Shakura-Sunyaev accretion disks. Interestingly, systems evolve through such states following a well established hysteretical cycle, going from hard to soft and then back from soft to hard but at a decreased flux level. While running the cycle, also ejection properties change accordingly: jets, which have been the focus of Chapter 6, are present only in the right region of the q-diagram, i.e. in the hard/intermediate states, and disappear instead in soft states (at least for BH and many NS LMXBs). While much has been discovered about each of these phenomena, a general theory able to put together all of them as pieces of a particularly challenging puzzle is still somehow missing.

A first attempt to describe globally such complex behavior was addressed by Esin et al. (1997) who, I recall from Section 2.6, introduced the idea of a multi-flow configuration for the disk, i.e. consistent of an outer Shakura-Sunyaev accretion disk and an inner, less dense ADAF. In this scenario the transition radius between the two types of accretion flow becomes crucial, as the closer it is to the event horizon, the smaller the ADAF-dominated region and therefore the softer the emitted spectrum. Such model effectively describes many observational features but had also critical weak spots. Indeed, the model assumes a low density plasma condition for the ADAF realm which in turn required low X-ray luminosity (Oda et al. 2012), while BH XRBs in hard state can be observed up to very high luminosities, sometimes above the Eddington limit (see, e.g. Dunn et al. 2010). The very existence of the ADAF solution in many cases was therefore not granted. This problem was partially solved by the introduction of the so-called hot luminous accretion flows or LHAFs (Yuan 2001), a variant of the ADAF solution which predicts a sign inversion for advection at high luminosity in the inner accretion flow, i.e. going from a local cooling to a local heating mechanism, and therefore allowing for low density coronae close to the BH. However, these solutions initially neglected the energy transfer in the disk from the magnetic fields to the electrons, a factor which, when considered, made these solutions less likely to physically exist (Xie and Yuan 2012). Furthermore, the original ADAF model did not address hysteresis or the dynamical link between the accretion flow and the jet. Taking into account the evaporation effect of the accretion disk due to the illumination coming from the central light source, a convincing model for hysteresis within the ADAF paradigm was provided by Meyer-Hofmeister et al. (2005).

The second issue remained instead open: the correlation between accretion flow and jets is not implicit in the ADAF model and neither in the updates provided for it in the following years. The hesitation in including jets production and distruction in accretion models probably arises partially from the debated origin of jets itself: assuming a B-Z model for jet launching (see 6.2.2) a strong interplay between jet and disk is not expected[1], while the same is not true in the framework of the B-P model. However observations reveal how some kind of correlation exists between accretion and ejection. Furthermore, even if the B-Z model could in principle relieve any accretion flow model of the need to address its dynamical link with jets, it works only for BH XRBs, while also NS LMXBs do launch jets.

An attempt in the direction of connecting accretion and ejection features in a unified model has been recently done by the high energy astrophysics group in Grenoble in a series of papers: Ferreira et al. (2006); Marcel et al. (2018a,b, 2019, 2020). In the following, I will illustrate the main characteristics of their paradigm in order to then apply it to the data taken during the hard/intermediate of the puzzling BH LMXB MAXI J1820+070.

[1] Even if an accretion flow is necessary in order for B-Z to take place.

7.2 The JED-SAD model

7.2.1 Basics of the model

The basic assumption underlying the model is the existence of a large scale vertical magnetic field B_Z threading the disk. This is not a strong assumption, as such magnetic field configuration is expected to build up due to, e.g., in-situ generation of magnetic fields by dynamo (Romanova et al. 1998) or alternatively by magnetic advection from the accreting material, as also predicted by numerical simulations (see, e.g. Liska et al. 2018). Furthermore, I notice that the existence of this magnetic field is unavoidable in order to produce B-P jets.
Due to the presence of this magnetic field, at each radius of the disk the dynamics of the particles is determined by the competition between the pressure exerted from this magnetic field, i.e. $P_{\rm mag} = B_Z^2/\mu_0$, with μ_0 the vacuum permeability, and the pressure exerted by the surrounding regions of the disk and the photons in the environment. In the following I will define the **magnetization** $\mu(r)$ the ratio between the magnetic pressure and the sum of radiation and gas pressure acting on the electrons in the disk $P_{\rm tot}$, i.e.:

$$\mu(r) = \frac{B_Z^2(r)}{\mu_0 P_{\rm tot}} \quad . \tag{7.1}$$

In the classic Shakura-Sunyaev disk the large scale magnetic field plays a negligible role so that $\mu \ll 1$. However, for a larger μ, i.e. $\mu \gtrsim 0.1$, the magnetic pressure becomes high enough to launch magnetocentrifugally (B-P) driven jets. These jets carry away mass, energy and angular momentum and therefore exert a torque on the underlying accretion disk. I recall from Section 5.6 that in order for the accretion flow to spiral-in and build up the disc some mechanism of dissipation of angular momentum must exist; in the classic Shakura-Sunyaev disk internal turbulent viscosity transports angular momentum radially outwards so that matter can fall deeper down in the gravitational potential and be accreted onto the compact object. The torque exerted by the launched jet acts analogously but is able to exert an even stronger torque (see, e.g. Ferreira and Pelletier 1993, 1995) which allows accretion to proceed at supersonic velocity, i.e. higher than in the Shakura-Sunyaev accretion disk. As a consequence, the accretion flow lauching a jet is sparser and less dense with respect to an accretion flow which does not.
In the following, I will distinguish between:

- an accretion flow dominated by the viscous (turbulent) torque and defined by Shakura and Sunyaev (1973), labeled as Shakura-Sunyaev Accretion Disk or **SAD**;
- an accretion flow dominated by the torque exerted by magnetocentrifugally launched jets, labeled as Jet Emitting Disks or **JED**;

Nature hints to the existence of both these solutions, as accretion flows found only in the SAD mode would never launch jets but on the other hand accretion flows choosing only the JED mode would always launch jets, leaving jet quenching in soft spectral states unexplained (see the study performed by Marcel et al. 2018b). Indeed, it is very plausible that the accretion flow surrounding a BH (and presumably also a NS) in a XRB can be considered as a multi-flow configuration composed by a few basic ingredients (see Fig. 7.1): (1) a SAD in the outer regions of the flow, (2) a JED close to the event horizon driving a jet (3), which could in turn be composed of an outer non-relativistic and an inner ultra-relativistic region under adequate conditions (Ferreira et al. 2006). Quite intuitively, each spectral state could be obtained by mixing these ingredients with different quantities, i.e. with a

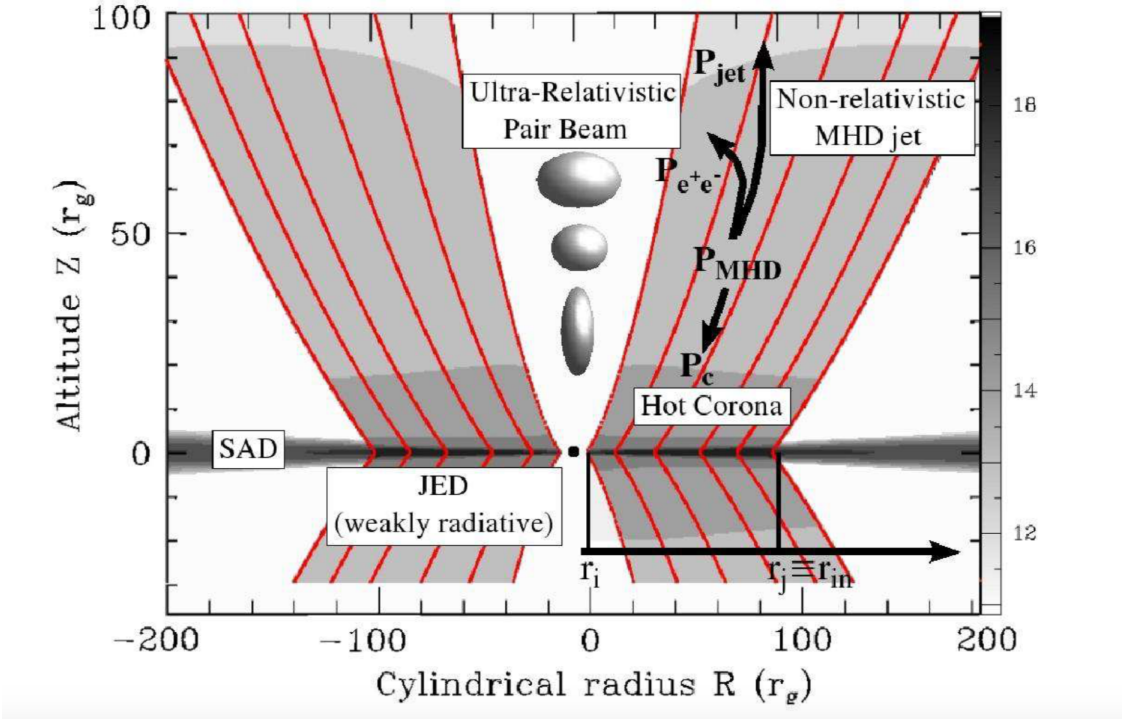

FIGURE 7.1: Sketch representing the multi-flow configuration in the typical JED-SAD geometry (Ferreira et al. 2006).

hybrid **JED-SAD** configuration where the two realms extend over regions of different scale. In this sense, such configuration is fundamentally determined by two control parameters: (1) the **transition radius** R_J between the JED and the SAD disk and (2) the inner mass accretion flow $\dot{M}_{\rm in}$ feeding the BH. Playing with these *knobs* ideally any spectral state could be reproduced.

The accretion flow on one side of R_J is obviously very different from the other. The main difference is represented by jet production but as a consequence, JED and SAD have very different properties. In order for jets to be launched, first of all, magnetization μ must change abruptly from SAD to JED. As jets are launched they carry away mass, energy and angular momentum; how much of these are taken away deeply modify the structure of the underlying jet. In a JED disk accretion rate can be written as:

$$\dot{m} = \dot{m}_{\rm in}\left(\frac{r}{r_{\rm in}}\right)^{\xi} \tag{7.2}$$

with $\dot{m} = \dot{M}/\dot{M}_{\rm Edd}$, $\dot{m}_{\rm in} = \dot{M}_{\rm in}c^2/L_{\rm Edd}$, $r_{\rm in}$ the innermost radius of the accretion disk and ξ the **ejection efficiency**. The value of ξ, which is always lower than 1, determines the type of jets the JED is lauching, as $\xi \sim 0.01$ is associated to fast but cold and tenuous jets (Ferreira 1997), while higher ξ, i.e. $\xi \sim 0.1-0.5$ are attributed to slow but warm and dense ejections (Casse and Ferreira 2000). In the following b will be defined as the fraction of the total energy budget $P_{\rm acc}$ of the accretion disk which is exhausted in the jet, i.e.:

$$b = \frac{2P_{\rm jet}}{P_{\rm acc}} \tag{7.3}$$

where the factor 2 accounts for the fact that jets are launched from both sides of the disk.
The torque exerted to the accretion flow by either viscosity or jet launching allows matter to accrete at a certain speed $u_{\rm R}$. As already anticipated, jet launching tends to increase $u_{\rm R}$ making as a consequence the accretion flow less dense. It is therefore apparent that another important parameter describing the JED/SAD configuration is the sonic Mach number $m_{\rm s}$ in the accretion flow at a certain radius R, determined by both types of torques i.e.:

$$m_{\rm s} = m_{\rm s,turb} + m_{\rm s,jet} = \alpha\varepsilon + 2q\mu \quad , \tag{7.4}$$

with α the viscosity parameter (see Sec. 5.6), ε the aspect ratio given by the ratio between the disk height $H(R)$ and R and q a magnetic field related parameter which describes the ratio between the toroidal magnetic field on the disk surface B_ϕ^+ over $B_{\rm Z}$ (Ferreira 1997). The SAD is slightly subsonic, while the JED is at least sonic and more likely supersonic, with an exact value of $m_{\rm s}$ depending on μ. Finally, it is not possible to neglect how the outer SAD affects the inner JED: energy from the outer SAD is indeed flowing to the inner JED by advection and the radiation emitted from the SAD is intercepted by the JED, cooling it. The impact of the second effect depends critically on the geometry of the JED and it is embodied in a dilution factor ω, which assumes values between 0 and 1 (I refer to Marcel et al. 2018a, and references therein for further discussion on this topic). A JED-SAD configuration is therefore determined by (3) μ, (4) b, (5) ξ, (6) $m_{\rm s}$ and (7) ω. Furthermore the mass of the compact object $M_{\rm BH}$ (8), the innermost radius $R_{\rm in}$ (9) of the accretion disk and the distance of the system d (10) are also to be specified.

7.2.2 Reproducing X-ray and radio luminosity with the model

In the following, I will only give a summary of the analytical structure of the JED-SAD model, as a detailed description of the model would go beyond the scopes of this Chapter[2]. Once a subset of parameters (1)-(10) is fixed, the model can be run to describe a two-temperature plasma $T_{\rm e}$-$T_{\rm i}$ for the whole extension of the JED in thermal equilibrium. In particular, the radial distribution of $T_{\rm e}, T_{\rm i}, \varepsilon$ and $P_{\rm rad}$ can be computed, up to R_J. The same thing is done for the SAD, for which of course ξ and b are equal to zero, as the jet production is inhibited, and μ and $m_{\rm s}$ assume the typical values for this mode. The extension of such region goes from $R_{\rm J}$ up to $R_{\rm out}$.
Once a pair R_J-$\dot{m}$ is chosen, a spectrum can be computed. An important test for the model is then to reproduce the observed spectral states in a known source. Furthermore, to a particular pair R_J-$\dot{m}$ it is possible to associate also a $P_{\rm jet}$. Indeed:

$$P_{\rm jet} = bP_{\rm acc,JED} = b\left[\frac{GM\dot{M}}{2R}\right]_{R_{\rm J}}^{R_{\rm in}} = \frac{b}{2}\frac{\dot{m}_{\rm in}}{r_{\rm in}}\left[1-\left(\frac{r_{\rm j}}{r_{\rm in}}\right)^{\xi-1}\right]L_{\rm Edd} \tag{7.5}$$

with $r_{\rm in}$ ($r_{\rm j}$) is $R_{\rm in}$ ($R_{\rm j}$) expressed in $R_{\rm G}$ units. Assuming b constant, I obtain that $P_{\rm jet}$ is a function of solely $\dot{m}_{\rm in}$ and $R_{\rm J}$. Knowing how much energy is carried by the jet, it is possible to use this information to compute the expected radio luminosity from the source, i.e. using a model (in this case by Heinz and Sunyaev 2003) describing self-absorbed synchrotron emission from non-thermal particles (see e.g. Sec. 6.3). Operatively, what has been done in Marcel et al. (2019) was to compare the radio flux F_R at a certain frequency ν with the pair R_J-$\dot{m}$ used to describe a quasi-simultaneous

[2] I refer again to Marcel et al. (2018b,a) and the relative Appendices for it

X-ray observations by means of this formula:

$$F_R = \tilde{f}\dot{m}^{17/16} R_{\rm J} \left(R_{\rm J} - R_{\rm in}\right)^{5/6} \frac{L_{\rm Edd}}{4\pi d^2} \tag{7.6}$$

with $L_{\rm Edd}$ the Eddington luminosity, d the distance of the source and $\tilde{f}$ a normalization constant which encloses all the usual uncertainties and can be tuned to fit the data. If the formula works, one should be able to find one value of $\tilde{f}$ valid for all the observations of the system in one outburst.The model described here is therefore able on the one hand to describe the physical structure of the accretion flow and the jet and on the other to predict the multi-wavelength emission from it. The next step would be to check if it is possible to reproduce each one of the canonical spectral states with values by playing with $R_{\rm J}$ and $\dot{m}$. In order to perform such task, Marcel et al. (2018b) simulated a large number of synthetic spectra each one corresponding to a different pair $R_{\rm J}$-$\dot{m}$ and fitted them by means of XSPEC with simple models, i.e. disk and power-law models, in order to get their corresponding position in a disk fraction luminosity diagram[3] (DFLD; Körding et al. 2006). The whole domain usually covered by observations of XRBs in this type of diagrams can be successfully reproduced with the previously computed synthetic observations. This procedure allowed Marcel et al. (2018b) to codify each of the canonical spectral states in terms of $R_{\rm J}$-$\dot{m}$ pairs and further to associate to each of them the expected radio luminosity coming from the jet. In the following, I will summarize these results:

- Before the beginning of the outburst, the source is in quiescence (Q). The accretion rate is low, a few percent of the Eddington mass accretion rate at best, while $R_{\rm J}$ is of the order of hundreds of $R_{\rm G}$. The observed luminosity is below $10^{-3} L_{\rm Edd}$. The observed spectrum is consistent with a hard power-law ($\Gamma \sim 1.5 - 2.0$) and a high energy cut-off, above 200 keV. Jets are launched but, since only a fraction of an already low energy budget is injected onto them, they are hardly detectable.

- In the high hard state (HHS) $\dot{m}_{\rm in}$ increases up to a value of several times the Eddington mass-accretion rate, while $r_{\rm j}$ tends to decrease rapidly, going from $\sim 100 R_{\rm G}$ to $\sim 10 R_{\rm G}$. The observed X-ray luminosity can reach values up to 30% the Eddington Luminosity and beyond[4]. The spectrum is still best described by a power-law with high energy cut-off, but with a value of the cut-off which goes from 200 keV to around 50 keV. In this state, the jets are very bright as expected. A particular state arises for very high accretion rate, i.e. $\dot{m} \gtrsim 3$, where the JED switches to a denser and cooler configuration, labeled as **slim disk** (described for the first time by Abramowicz et al. 1998). Slim disks are geometrically and optically thick spectra which, unlike SADs, are advection-dominated. Their spectral emission is characterized by the sum of the blackbody spectra emitted from each radius but extends up to high energies (100-200 keV), since the effective temperature follows a different profile due to advection (Marcel et al. 2018b). Indeed,a 3-200 keV spectra could be satisfactorily modeled with a simple cutoff power-law of index $\Gamma \sim 1.2$ and a cut-off energy below 100 keV.

- When the system transitions to the soft state (HSS), $\dot{m}$ is still around 1 while $R_{\rm J}$ finally coincides with $R_{\rm in}$: the JED has disappeared and the disk is entirely in SAD mode. Subsequently no

[3] A diagram where the total luminosity is plotted versus the luminosity of one of the components, e.g. the power-law or the disk blackbody.

[4] Note that even if $\dot{m}_{\rm in}$ can exceed the Eddington mass accretion rate, the $\dot{m}$ rate which determines the final X-ray luminosity is lower since it hides the accretion efficiency η, of the order of 10% for a Schwarzschild BH (see Section 2.2).

jet is launched. The emission is well described by a multi-color blackbody with temperature around 1 keV or below.

- The decrease of $\dot{m}$ to about 0.5 $\dot{m}_{\rm Edd}$ witnesses the transition to the low soft state (LSS), as we travel to the bottom part of the q-diagram. While the JED is still absent, the SAD is found colder, with an effective temperature of around 0.6-0.7 keV.

- At such low mass accretion rate, the inner regions switch back to the JED mode and $R_{\rm J}$ increases accordingly. The system is found in the low hard state (LHS). Spectrally this state is analogous to the HHS, but it is characterized by a lower luminosity due to the lower value of $\dot{m}$. Together with the JED, also the jet and its signature radio emission resuscitate.

The computed geometrical shape of the hybrid JED-SAD corresponding to each of these enlisted state is shown in Figure 7.2.

The step further was of course to put this paradigm to a test. Marcel et al. (2019) used indeed the JED-SAD paradigm to describe the observed cycle of X-ray activity displayed by the BH XRB GX 339-4 between 2010 and 2011 (Tetarenko et al. 2016), reproduced in Fig. 7.3 (*left*). The various spectral states exhibited by the source are color-coded in the figure, i.e. green for hard states, blue for hard/intermediate states, yellow for soft/intermediate state and red for soft state. Interestingly, Marcel et al. (2019) found that all the observed spectra could be well reproduced by changing only $r_{\rm J}$ and $\dot{m}$ (see Fig. 7.3, right). During the outburst $\dot{m}$ tends to slowly increase until the transition to the intermediate state, while it later follows a decreasing trend. On the other hand, $R_{\rm J}$ decreases when the system moves from hard to soft states, stays fixed to the innermost radius during the soft state while it increases again during the back transition to the hard state. Within this framework, hysteresis is reflected on the different levels of mass-accretion rate in the hard-to-soft and soft-to-hard branch. The exact reason for such trend could be related to the strength and distribution of $B_{\rm Z}$, as suggested by (Ferreira et al. 2006), but this topic still requires more investigations. The replication of the 2010-2011 outburst of GX 339-4 is not limited to the X-ray activity: also the radio light curve was satisfactorily reproduced by using the synthetic radio flux calculated from the pairs $R_{\rm J}$-$\dot{m}$ (Marcel et al. 2019).

Finally, it has been recently shown that also some timing features could be explained within the JED-SAD paradigm framework. Indeed, a direct proportionality between the Keplerian frequency of the transition radius $R_{\rm J}$ and the type C QPO frequency in four different outbursts of GX 339-4 (Marcel et al. 2020). According to these results, this type of QPO could originate in the interface between two regions of different values of μ, i.e. being then strictly related to the existence of two different types of accretion flow in the hard and hard/intermediate states of BH LMXBs.

The JED-SAD paradigm has been proven successful in explaining much of the accretion and ejection phenomenology in GX 339-4. However, the variety of different behaviours observed in three decades of BH XRBs studies (I refer again to Dunn et al. 2010, for an observational review) demands for other tests of this model. In the following, I report on the application of the JED-SAD model to the BH LMXB MAXI J1820+070. The results presented and discussed in these chapter are the fruit of a very inspiring collaboration with the high energy astrophysics group of IPAG, Grenoble (France), in particular with Dr. Pierre-Olivier Petrucci and Samuel Barnier. Furthermore part of the analysis on the XRT data has been carried on by Dr. Sara Elisa Motta (INAF Milano). A paper on this work is currently in preparation.

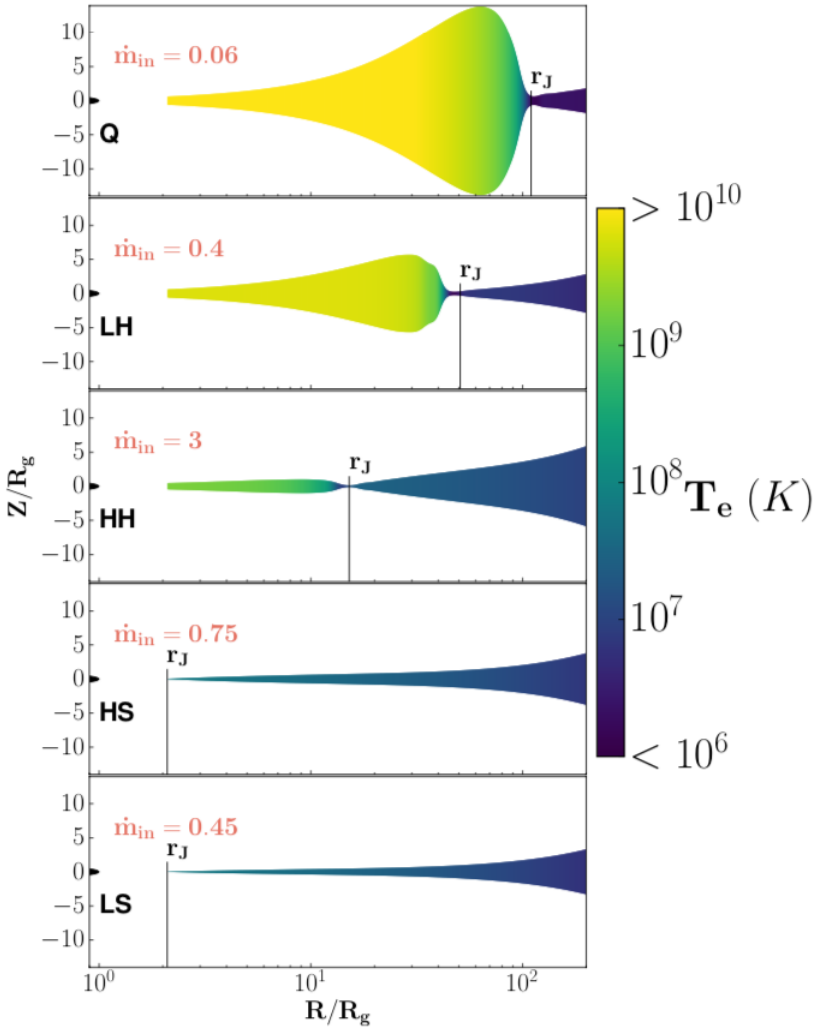

FIGURE 7.2: Sketches representing the geometry and electron temperature distribution of the JED-SAD configuration corresponding to each of the canonical spectral states, i.e. from top to bottom: Quiescence (Q), Low Hard state (LH), High Hard state (HH), High Soft state (HS) and Low Soft state (LS). Credits: Marcel et al. (2018a).

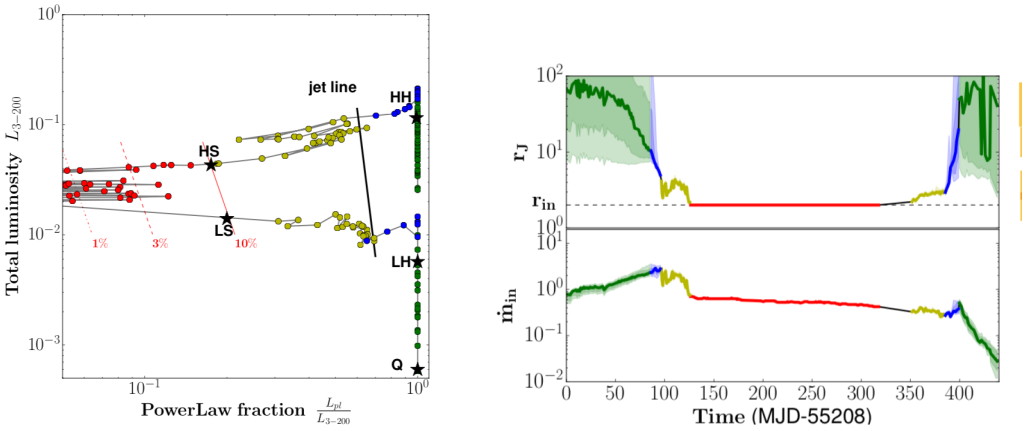

FIGURE 7.3: Evolution of GX 339-4 during its 2010–2011 outburst in a DFLD (*left*) where the total luminosity (in Eddington units) in the range 3-200 keV is plotted versus the power-law fraction. In the plot the observations are color-coded in base of the spectral state (see text). (*Right*) Evolution of the corresponding R_J and $\dot{m}$ found to model the same outburst. Credits: Marcel et al. (2019).

7.3 MAXI J1820+070

MAXI J1820+070 is a recently discovered transient low-mass X-ray binary, observed for the first time in the optical band by the All-Sky Automated Search for SuperNovae ASSAS-SN (Shappee et al. 2014) on March 3 2018 and one week later by *MAXI* in X-rays (Kawamuro et al. 2018). Detailed studies of the optical counterpart revealed that the system is hosting a stellar-mass black hole (~ 8.5 $M_\odot$) accreting from a ~ 0.4 $M_\odot$ companion star (Torres et al. 2019, 2020). Since its discovery the source underwent a long (approximately one year) and bright outburst, becoming at its peak the second brightest object in the X-ray sky. Due to its brightness, the system was object of an impressive multi-wavelength campaign of observations (see, e.g. Shidatsu et al. 2018; Paice et al. 2019; Hoang et al. 2019; Trushkin et al. 2018) and following investigations, which allowed the scientific community to characterize in detail the physical properties of the system. The most recent and precise measure of the distance was determined via radio parallax and it is about 3.0±0.3 kpc (Atri et al. 2020). Furthermore, the system shows X-rays dips (Kajava et al. 2019) but not eclipses, suggesting an inclination between 60° and 80°. Other evidences of the high inclination of the system are provided by optical spectroscopy (Torres et al. 2019) and by the estimate of the inclination of the jet axis (Atri et al. 2020), i.e. about 60°. The orbital period of the system is also known, i.e. around 0.68 days (Patterson et al. 2018; Torres et al. 2020). In X-rays, the outburst was studied in detail in hard (see, e.g. Bharali et al. 2019), soft (Fabian et al. 2020) and in the terminal phases of the outburst (Xu et al. 2020). Several authors have recently proposed that in the spectral hard state of MAXI J1820+070, the hot corona contracts while the accretion disk remains stable at the ISCO: the intriguing scenario was first proposed by Kara et al. (2019) based on *NICER* X-ray timing analysis and then corroborated by modeling the reflection component in *NuSTAR* spectra with two lamppost coronae (Buisson et al. 2019).

7.4 Observations

The whole 2018 outburst of the source was monitored in detail by *Swift*/XRT, i.e. between MJD 58191 (March 14 2018) and MJD 58280 (November 6 2018), with a total of 75 observations,

performed in Window Timing (WT) mode. In order to produce the light curve, I used the Data Analysis software available at https://www.swift.ac.uk/user_objects/ (Evans et al. 2007, 2009), adopting a 100 cts s^{-1} limit for the pile-up correction and using the standard settings. I extracted the data in a soft, i.e. 0.5-2.0 keV, and a hard, 2.0-10 kev, energy bands. The resulting light curve and hardness ratio is presented in Figure 4.2.
In this Chapter, I will only focus on the spectral analysis of the source in the high hard state, i.e. up to $\approx$ MJD 58300. With the aim of analyzing broadband X-ray spectra, I included also *NuSTAR* and BAT data. However, I selected only the *NuSTAR* observations which were performed within the same day of an XRT observation. Furthermore, in a few cases two or more *NuSTAR* observations were performed the same day: whenever this occurred, I chose the one which was the closest in time with the XRT pointing. These criteria led me to narrow down the list of the available *NuSTAR* to eight epochs, highlighted in Fig. 7.4 with vertical lines. It is noteworthy that this set of observations has been already analyzed by Buisson et al. (2019), which allows for a direct comparison. I refer to these authors for further details on the whole set of *NuSTAR* observations taken prior to the hard-to-soft transition. In order to avoid any discrepancy between BAT and *NuSTAR* due to the spectral variability of the source, I extracted BAT spectra exactly over the duration of each *NuSTAR* observation and processed them according to the procedure described in Section 3.3.

In the following, I will refer to these observations as Epochs and I will label them with numbers from 1 to 8 in chronological order. Details on the selected Epochs are reported in Table 7.1. In all these Epochs I exploit a broad data set composed of quasi-simultaneous XRT, *NuSTAR* and BAT data, with the sole exception of Epoch 6, for which no BAT data were available during the duration of the corresponding *NuSTAR* pointing. Among these observations, Epoch 1 was taken in full hard state, while Epochs 2 to 8 belong to a hard/intermediate state and have almost the same hardness ratio (see Fig. 7.4). Even if it is not evident from the XRT hardness ratio, Epoch 8 likely corresponds to a short episode of re-hardening, as better highlighted in the *NICER* Hardness Intensity Diagram, Fig. 7.5. I refer to Section 3.3 for the detailed procedure of data reduction on both XRT and *NuSTAR*. For both procedures I used HEASOFT (v. 6.26.1) and the latest updated CALDB version. Since all the XRT observations had a quite high count-rate, i.e. always well above 100 cts s^{-1}, I used an annulus region in order to remove the pile-up effects (see Subsection 3.3.1). The outer radius was always chosen to be $\sim$47", while for the inner radius I used a $\sim$18" inner radius for Epoch 1, a $\sim$24" inner radius for Epochs 2, 3, 5, 6 and a $\sim$28" inner radius for Epoch 4, 7 and 8.

Each XRT spectrum was rebinned with GRPPHA in order to have 150 counts per bin, which allows the use of the χ^2 statistics.

I instead grouped the FPMA and FPMB spectra using the optimal grouping recipe by Kaastra and Bleeker (2016) in order to have a grouping which reflects the spectral resolution of the instrument in a given energy range, so to avoid any oversampling issue (see 3.3.2).

7.5 Spectral analysis

The final broadband spectra were obtained keeping data in the range 0.8-10 keV for XRT, 5-78 keV for *NuSTAR* and 30-190 keV for BAT. Indeed, *NuSTAR* data below 5 keV show a remarkable (and unexpected) mismatch between FPMA and FPMB, likely due to a known instrumental issue (Madsen et al. 2020), so that I decided not to include the data in this region, since already covered by XRT. Also BAT data show an unexpected mismatch with *NuSTAR* below 30 keV, which can be

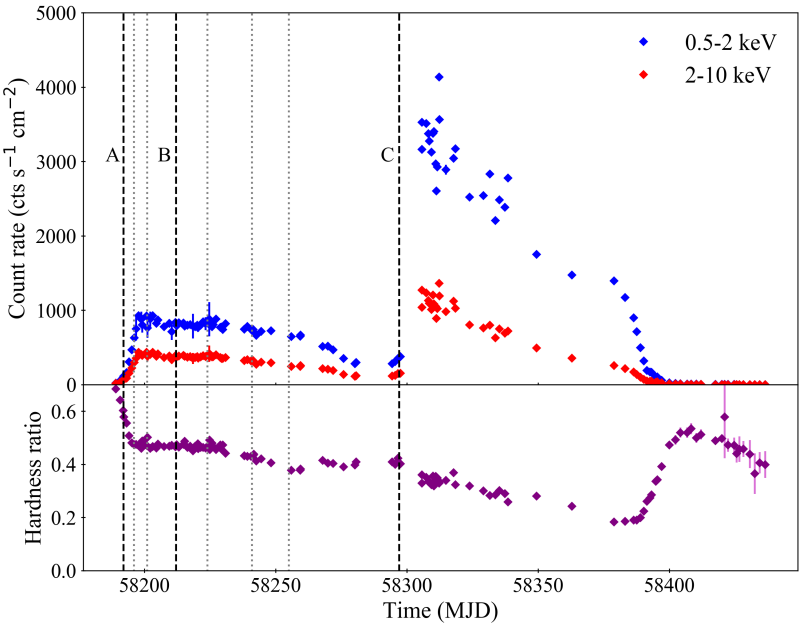

FIGURE 7.4: (*Top*) *Swift*/XRT light curve of the source between MJD 58189.0 and MJD 58436.6 in a soft and hard X-rays bands and (*Bottom*) hardness ratio. The XRT-*NuSTAR* epochs are highlighted as black dashed lines, while the other *NuSTAR* observations in the hard state are indicated with grey dotted lines.

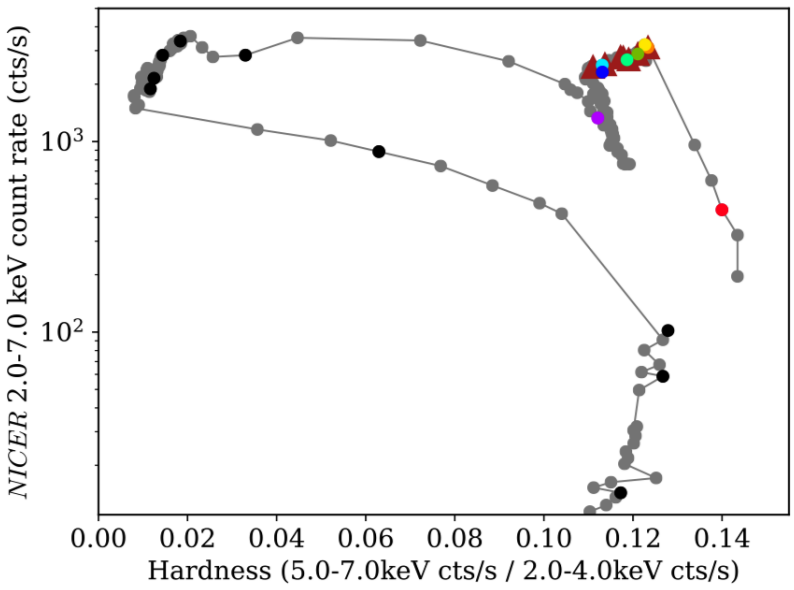

FIGURE 7.5: Hardness Intensity Diagram of the whole 2018 outburst of the source as observed by *NICER*. In the plot, the eight *NuSTAR* epochs are highlighted with different colors, i.e. Epoch A (in this chapter) is colored in red, Epoch B is azure and Epoch C is purple. The Figure is adapted from Buisson et al. (2019).

XRT					
Epoch	ObsID	Start Time		Exposure	Ref.
		(UTC)	(MJD)	ks	
1	00010627001	2018-03-14	58191.9	1.0	Bh19
2	00010627008	2018-03-19	58196.8	0.98	This work
3	00010627013	2018-03-24	58201.1	0.98	This work
4	00088657001	2018-04-04	58212.2	1.0	This work
5	00010627038	2018-04-15	58223.3	1.7	This work
6	00010627055	2018-05-04	58240.6	1.0	This work
7	00088657004	2018-05-18	58255.9	1.9	This work
8	00088657006	2018-06-28	58297.3	1.8	This work
NuSTAR					
Epoch	ObsID	Start Time		Exposure	Ref.
		(UTC)	(MJD)	ks	
1	90401309002	2018-03-14	58191.9	11.8	Bu19
2	90401309004	2018-03-21	58198.0	2.8	Bu19
3	90401309008	2018-03-24	58201.5	3.0	Bu19
4	90401309012	2018-04-04	58212.2	12.3	Bu19
5	90401309013	2018-04-16	58225.0	1.8	Bu19
6	90401309016	2018-05-03	58241.8	13.7	Bu19
7	90401309019	2018-05-17	58255.6	9.4	Bu19
8	90401309021	2018-06-28	58297.2	21.4	Bu19

TABLE 7.1: List of the XRT and *NuSTAR* observations of the source used in this work. Bh19 = Bharali et al. (2019), Bu19 = Buisson et al. (2019)

hardly connected to any physical nature. I therefore ignored BAT data up to 30 keV.
I analyzed each of the eight observations with the JED-SAD model, which consists in the sum of two models, one for the JED and one for the SAD region, with all the parameters tied to each other. The tables for the models are produced by fixing the parameters (3)-(6) (see Subsection 7.2.1) to values selected by the user. As explored in detail by Marcel et al. (2018b), a reasonable set of values, i.e. the one which best describes the JED emission in the archetypal object GX 339-4, is: μ=0.5, b=0.3 and ξ=0.01. The same set of values was adopted for MAXI J1820+070.
The main free parameters in the model are the transition radius between the JED and the SAD disks $R_{\rm J}$ and the mass accretion rate $\dot{m}$. Besides the $R_{\rm J}-\dot{m}$ pair, the other parameters involved are: $m_{\rm s}$, which was fixed to 1.5 in accordance with Marcel et al. (2018a), the inner radius of the JED disk $R_{\rm in,JED}$ (presumably coincident with the ISCO), fixed to 2 $R_{\rm G}$, the geometry dilution parameter ω, fixed to 0.2, the redshift parameter ζ, fixed to 0 and the JED-SAD normalization $K_{\rm JEDSAD}$, which is determined by the distance $D_{\rm kpc}$ in kpc of the system following the formula:

$$K_{\rm JEDSAD} = \left(\frac{10}{D_{\rm kpc}}\right)^2 \tag{7.7}$$

The distance of the system has been found in the range 2.7-3.3 kpc (Atri et al. 2020), so that I fixed $D_{\rm kpc}$ to 3 and calculated $K_{\rm JEDSAD}$ accordingly. I also included TBABS to take into account the effect of interstellar absorption, using the photoelectric cross sections from Verner et al. (1996) and element abundances from Wilms et al. (2000), and CONSTANT to serve as cross-calibration constant. Finally, as each data-set was showing apparent systematics, I applied a 1% systematic error to the analyzed spectra.

A first fit without any reflection component results in extremely poor fits and strongly unmodelled residuals in the iron line and Compton hump regions, showing that a proper reflection treatment is necessary in order to fit these spectra.

I included then a reflection component which tied to the JED-SAD parameters predicts the reprocessing of the JED emission by the SAD and the expected resulting reflection spectrum, i.e. labelled REFL. This reflection table is based on the XILLVER reflection model (García et al. 2013) and it is produced by simulating spectra for different combinations of $R_{\rm J}-\dot{m}$ pairs, fitting them with a simple cut-off power-law models and finally injecting the fits in the XILLVER table. More details on this model will be given in Barnier et al., in preparation.
This component has the iron abundance $A_{\rm Fe}$, the ionization parameter $\log\xi$ and a normalization K. However, the component does not take into account the relativistic blurring effects, so that I applied the convolution model KDBLUR, which smooths the reflection spectrum according to the original calculations by Laor (1991). This model is composed by four other parameters: the emissivity parameter ε, i.e. the power-law index of R if we assume the emissivity in the disk scales as $\propto R^{\varepsilon}$, the inner and outer radius of reflection $R_{\rm in,KDBLUR}$ and $R_{\rm out}$ and the inclination i. In order to further reduce the number of degrees of freedom, I fixed ε to the reasonable value of 3 (see, e.g. Dauser et al. 2013; Xu et al. 2020). Furthermore, according to the JED-SAD model geometry, it is expected that the reflecting region coincides with the SAD disk, so that I tied the inner reflection radius $R_{\rm in,KDBLUR}$ to transition radius $R_{\rm J}$.

The model I applied reads therefore:

$$\text{Model 1 :TBABS} \times (\text{ATABLE(JED)} + \text{ATABLE(SAD)} + \text{KDBLUR} \times \text{ATABLE(REFL)}) \tag{7.8}$$

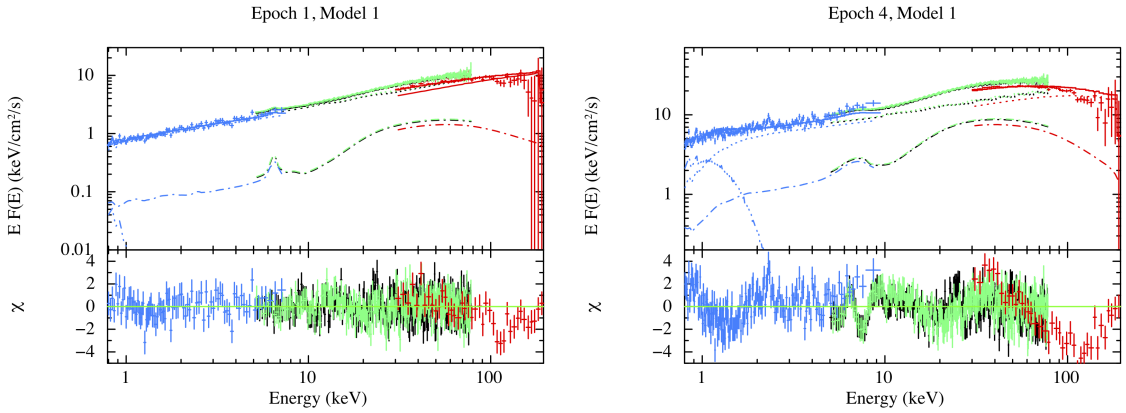

FIGURE 7.6: Residuals for Epochs 1 and 4 with **Model 1**. Data: XRT (blue), *NuSTAR* (green-black) and BAT (red). I adopted different linestyles to distinguish between the different components, in particular: dot for JED, dash for REFL and dash-dot-dot-dot for SAD

Epochs 1 and 8 are well enough modeled by Model 1, with a χ^2_ν(d.o.f.)=1.15(630) and χ^2_ν(d.o.f.)= 1.16(737), respectively. In Figure 7.6 (*Left*) the best-fit models and residuals are presented. The best-fit values for $R_{\rm J}$-$\dot{m}$ are respectively of $\sim$ 44 $R_{\rm G}$-0.9 $\dot{m}_{\rm Edd}$ and 23 $R_{\rm G}$-0.8 $\dot{m}_{\rm Edd}$. On the other hand, Epochs from 2 to 7 are poorly fitted by Model 1, with χ^2_ν values all above 1.25 and, most importantly, evident unmodelled structures around the iron line region in the residuals (I am showing the fit to Epoch 4 as an example in Fig. 7.6, right).

7.5.1 The need for a second reflection component

The unacceptable fits obtained for six out of eight Epochs points out the possibility of an unmodelled additional reflection component. It is noteworthy that a model with two reflection component was used in the spectral analysis of these *NuSTAR* observations from Buisson et al. (2019); Chakraborty et al. (2020) and suggested on the basis of its lag behaviour and the observed *NICER* spectral residuals by Kara et al. (2019). The results of these authors point out the presence of both a remote, low ionisation reflection component and a highly ionised inner reflection component, which contribute to the observed iron line profile providing respectively a narrow core and a broad base. I therefore added a second reflection component in the model, from now on Model 2. In the following I use the pedices '1' and '2' to refer to the parameters of the inner and remote reflection components, respectively. The purpose of this model is to reproduce a physical scenario where reflection comes from two distinct regions, characterized by different ionisations and therefore presumably placed at different distances from the illuminating JED. I therefore tied $R_{\rm in,1}$ to $R_{\rm J}$ and $R_{\rm out,1}$ to $R_{\rm in,2}$, in order to place the two reflection regions at separate but neighboring regions[5]. The outer radius of the remote reflection is instead left free. The ionization parameter was left free as well in both components, so that we have two different ionization values ξ_1 and ξ_2. All the other parameters were tied between the two components. The best-fit model found including this new component requires always one of them, the inner one, to be highly-ionized ($\log \xi_1 \sim$ 2.9-3.5) while the outer one has lower, i.e. $\log \xi_2 < 1$, ionisation. The fits are mostly insensitive to $R_{\rm in,1}$ and $R_{\rm out,2}$ and can only finds upper limits on ξ_2. I therefore fixed $R_{\rm in,1}$ and $R_{\rm out,2}$ to 300 and 10^4 $R_{\rm G}$ respectively (the choice is reasonable but arbitrary, but the results of the fit are barely affected by changes in these

[5]This is only a working assumption, as it cannot be excluded that regions may not be exactly adjacent to each other.

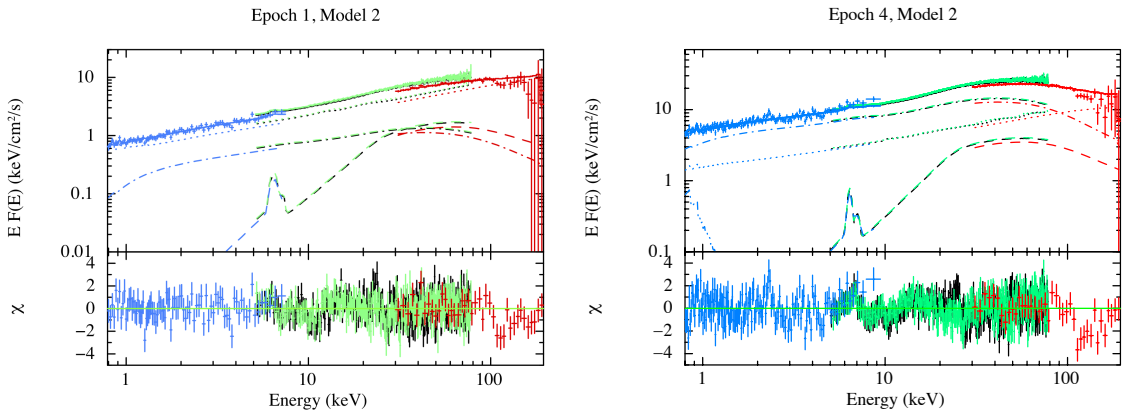

FIGURE 7.7: Residuals for Epochs 1 and 4 with **Model 2**. Data: XRT (blue), *NuSTAR* (green-black) and BAT (red). I adopted different linestyles to distinguish between the different components, in particular: dot for JED, dash-dot for the inner REFL, dash for the outer REFL and dash-dot-dot-dot for SAD

parameters), while ξ_2 was frozen to 0.
In all cases the best-fit model consists in the highly ionized reflection component being prominent with respect to the remote neutral reflection component. Epochs 1 and 8 are slightly better fitted with Model 2 with respect to Model 1, with χ^2_ν(d.o.f.) of 0.99(629) and 1.14(736). I tested how significant is the improvement in the fit going from Model 1 to Model 2 in both Epochs by means of F-test: I found in both cases a significant improvement, with probability of improvement by chance of respectively 1×10^{-14} and 5×10^{-4}. It results that a two-model reflection is in every Epoch a statistically preferable scenario to fit the data (see Fig. 7.7, *left* for the best-fit and residuals of Epoch 1 with Model 2). In both Epoch 1 and 8, Model 2 gives slightly different values for $R_{\rm J}$-$\dot{m}$ with respect to Model 1, in particular lower $\dot{m}$ values, i.e. around 0.8 $\dot{m}_{\rm Edd}$ and 0.7 $\dot{m}_{\rm Edd}$ respectively. This is not surprising as Model 1 lacks of one reflection component, so that it needs to increase the flux in the continuum by increasing $\dot{m}$.
Model 2 improves strongly the results of the fits to the remaining six Epochs, for which a one-reflection scenario has been ruled out. While the χ^2_ν values are now in all cases around 1, also the unmodelled residuals in the iron line are less defined, but still slightly present. The best-fit values of $R_{\rm J}$ ($\dot{m}$) are all found in the range 17-28 $R_{\rm G}$ (0.5-0.7 $\dot{m}_{\rm Edd}$), as expected since these Epochs have very similar spectral shapes. However, the most striking aspect of the fits with Model 2 to Epochs 2 to 6 is that the solution found to fit the broadband spectrum has always the inner reflection at a higher flux with respect to the JED spectrum, as shown in Figure 7.7, *right* for Epoch 4. Such reflection-dominated spectra are challenging to explain, especially in the framework of the proposed JED-SAD geometry (see 7.6). Similarly high reflection fractions have been explained in the past with, e.g., a large covering fraction of the disk due to the presence of clouds (Malzac and Celotti 2002), with a compact corona close to the BH emitting anisotropically due to light bending (Miniutti et al. 2003) or to mildly-relativistic motion of the corona towards the disc (Beloborodov 1999). Unfortunately, all of these scenarios are hard to reconcile with the proposed JED-SAD geometry.

7.5.2 The role of m_s

The spectral shape outlined by the *NuSTAR*-BAT data in Epoch 4 reveals a curvature which could hint at a spectral cut-off around 100-200 keV. However XSPEC seems to prefer fitting such curvature by enhancing the inner reflection normalization instead of properly using the JED model. Playing with the model reveals indeed that in order for the the JED component to assume a proper curvature at these energies, one needs to decrease R_J below $\sim 13\ R_G$ and at the same time increasing $\dot{m}$ beyond 1 $\dot{m}_{Edd}$. However with this pair of parameters, also the SAD component, whose parameters I recall are strictly tied to the JED ones, becomes quite strong. As a consequence the accordance between the model and the data, which do not require such strong disk component in the soft X-rays, is lost again and the only way to fit the broadband data is using a highly-ionized reflection component as continuum.
A possible solution lies in the choice of the sonic Mach number m_s: allowing for the accretion flow to proceed at lower speed in the JED realm results indeed in a denser JED and therefore a more saturated Comptonization spectrum. I therefore left m_s free in all the fits. To ease the following paragraph, I will refer to Model 2 with m_s free as Model 3. Thawing m_s results finally in not only good fits, but in removing the physically odd scenario of having a reflection dominated spectrum. The spectral curvature, which was hardly modelled with a supersonic JED, is indeed well reproduced by allowing m_S to decrease down to around 0.7 in Epochs 2 to 5. m_s increases instead in Epochs 6 to 7, until finally reaching the 1.5 value again in Epoch 8. Less variability is found on the other hand in R_J and $\dot{m}$: the first parameter decreases abruptly going from Epoch 1 to 2, i.e. from hard to hard-intermediate state, and then decreases more slowly until Epochs 7-8, while the latter parameter is almost stable at $\sim$0.6 $\dot{m}_{Edd}$ for all the first 5 Epochs and increases again after Epoch 6, i.e. to $\sim$ 0.8 $\dot{m}_{Edd}$. The results of all the fits are reported in Table 7.2, while the best fit models and residuals are displayed in Figure 7.8-7.9.

It is noteworthy that A_{Fe} and the inclination i are consistent in the eight observations with the values of respectively 2 and 70°.

7.6 Preliminary discussion & ongoing work

In the previous section I tested the JED-SAD model with a dataset of XRT+*NuSTAR*+BAT observations taken during the hard state. I tested both a standard one reflection model (Model 1) and a more complex reflection model with two components, originating from different but neighboring regions of the SAD disk (Model 2). According to these preliminary results, all the three Epochs are best described with Model 2, but in order to avoid a best-fit solution where the reflection is dominant some freedom in the parameter m_s needs to be provided (Model 3). Using the best-fit values found for R_J-$\dot{m}$ with Model 3, it is possible to produce diagrams for the geometry, optical depth and temperature distribution in the corresponding hybrid JED-SAD configuration. These diagrams have been produced by my collaborator in Grenoble, Samuel Barnier, and are presented in Fig. 7.10-7.11 for Epoch 1 and 2. The results obtained raise several issues and interesting prospects, which put the basis for the continuation of this work.

The first interesting result is indeed the need for a two-reflection model, which arises with m_s both free to vary or fixed. The co-existence of two reflection spectra has been already proposed for the source by other authors, (e.g. Kara et al. 2019; Buisson et al. 2019; Chakraborty et al. 2020), mainly to describe the odd iron line profile. These authors explained the double reflection

Spectral analysis					
Epochs		1	2	3	4
N_H	$\times 10^{22}$ cm^{-2}	0.45±0.03	$0.223^{+0.014}_{-0.023}$	0.27±0.02	0.25±0.02
R_J	R_G	$51^{+4.7}_{-7.5}$	$23.8^{+2.0}_{-0.4}$	$25.5^{+2.3}_{-1.8}$	23.6±0.5
$\dot{M}_{in}$	$\dot{M}_{Edd}$	$0.61^{+0.04}_{-0.02}$	0.58±0.02	$0.62^{+0.04}_{-0.03}$	$0.63^{+0.02}_{-0.01}$
m_s		$1.26^{+0.07}_{-0.02}$	$0.75^{+0.06}_{-0.02}$	$0.728^{+0.014}_{-0.015}$	$0.76^{+0.07}_{-0.02}$
A_{Fe}		1.9±0.5	2.1±0.2	(2)	(2)
$R_{in,1}$	R_G			$=R_J$	
$R_{in,2}$	R_G			(300)	
$R_{out,1}$	R_G			$=R_{in,2}$	
$R_{out,2}$	R_G			(10^4)	
i	$^\circ$	>35	(70)	(70)	(70)
$\log \xi_1$		$4.32^{+0.03}_{-0.10}$	$3.79^{+0.07}_{-0.03}$	3.79±0.04	$3.78^{+0.03}_{-0.04}$
$\log \xi_2$				(0)	
K_1	$(\times 10^{-6})$	$0.17^{+0.05}_{-0.02}$	$4.3^{+0.6}_{-1.0}$	4.4±0.7	$3.7^{+0.6}_{-0.5}$
K_2	$(\times 10^{-4})$	0.83±0.06	200±30	207^{+27}_{-29}	176^{+28}_{-24}
χ^2_ν	(d.o.f.)	0.94(627)	1.14(741)	0.98(640)	1.08 (735)

Epochs		5	6	7	8
N_H	$\times 10^{22}$ cm^{-2}	0.24±0.02	$0.36^{+0.04}_{-0.02}$	$0.366^{+0.04}_{-0.05}$	0.40±0.02
R_J	R_G	$21^{+2.0}_{-1.3}$	$16.0^{+0.5}_{-0.9}$	$15.2^{+1,4}_{-1.1}$	16.7±0.4
$\dot{M}_{in}$	$\dot{M}_{Edd}$	$0.62^{+0.05}_{-0.03}$	$0.82^{+0.03}_{-0.02}$	0.78±0.04	$0.770^{+0.003}_{-0.007}$
m_S		$0.75^{+0.05}_{-0.01}$	$1.32^{+0.08}_{-0.06}$	>1.46	>1.49
A_{Fe}		1.97±0.02	$2.1^{+0.12}_{-0.20}$	$1.92^{+0.30}_{-0.20}$	(2)
$R_{in,1}$	R_G			$=R_J$	
$R_{in,2}$	R_G			(300)	
$R_{out,1}$	R_G			$=R_{in,2}$	
$R_{out,2}$	R_G			(10^4)	
i	$^\circ$	84^{+1}_{-44}	(70)	(70)	75^{+8}_{-7}
$\log \xi_1$		$3.75^{+0.06}_{-0.05}$	$3.61^{+0.09}_{-0.08}$	$3.58^{+0.12}_{-0.08}$	$3.18^{+0.03}_{-0.04}$
$\log \xi_2$				(0)	
K_1	$(\times 10^{-6})$	3.8±0.8	$4.8^{+0.8}_{-0.6}$	$4.9^{+0.8}_{-1.0}$	$5.8^{+1.0}_{-0.6}$
K_2	$(\times 10^{-4})$	155^{+20}_{-17}	99^{+17}_{-13}	100^{+18}_{-21}	$4.3^{+1.3}_{-0.4}$
χ^2_ν	(d.o.f.)	1.04(827)	1.03(771)	1.07(743)	1.13(735)

TABLE 7.2: Fit results for all epochs with **Model 3**. Quoted errors reflect 90% confidence level. The parameters which were kept frozen during the fits are reported between round parentheses.

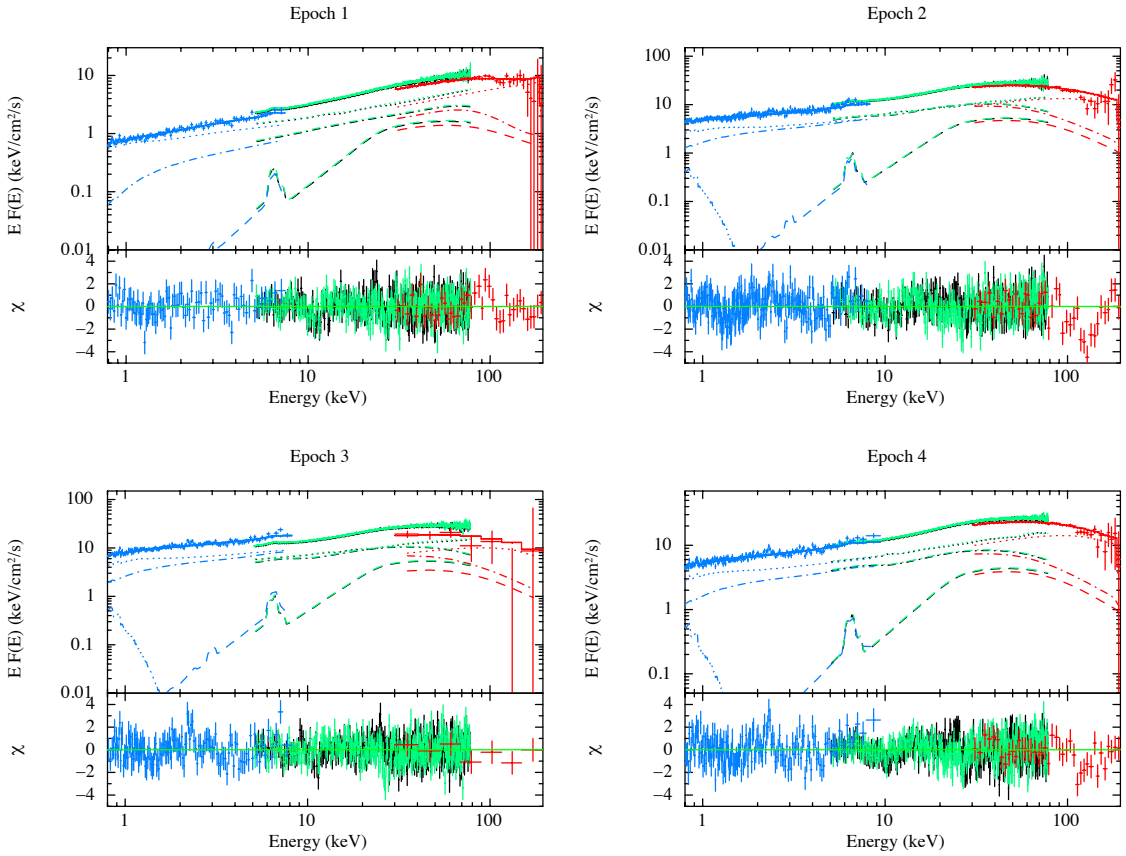

FIGURE 7.8: Residuals for Epochs 1 to 4 with **Model 3**. Data: XRT (blue), *NuSTAR* (green-black) and BAT (red). I adopted different linestyles to distinguish between the different components, in particular: dot for JED, dash-dot for the inner REFL, dash for the outer REFL and dash-dot-dot-dot for SAD.

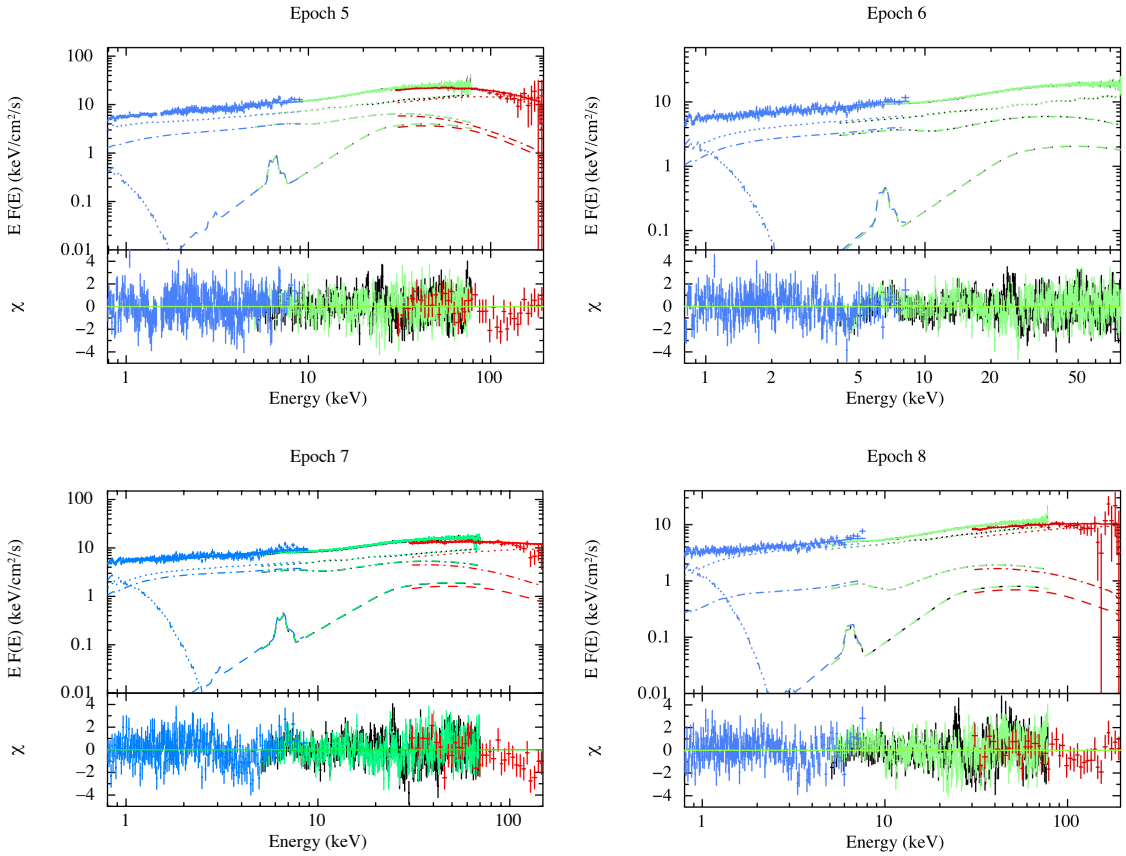

FIGURE 7.9: Residuals for Epochs 1 to 4 with **Model 3**. Data: XRT (blue), *NuSTAR* (green-black) and BAT (red). I adopted different linestyles to distinguish between the different components, in particular: dot for JED, dash-dot for the inner REFL, dash for the outer REFL and dash-dot-dot-dot for SAD.

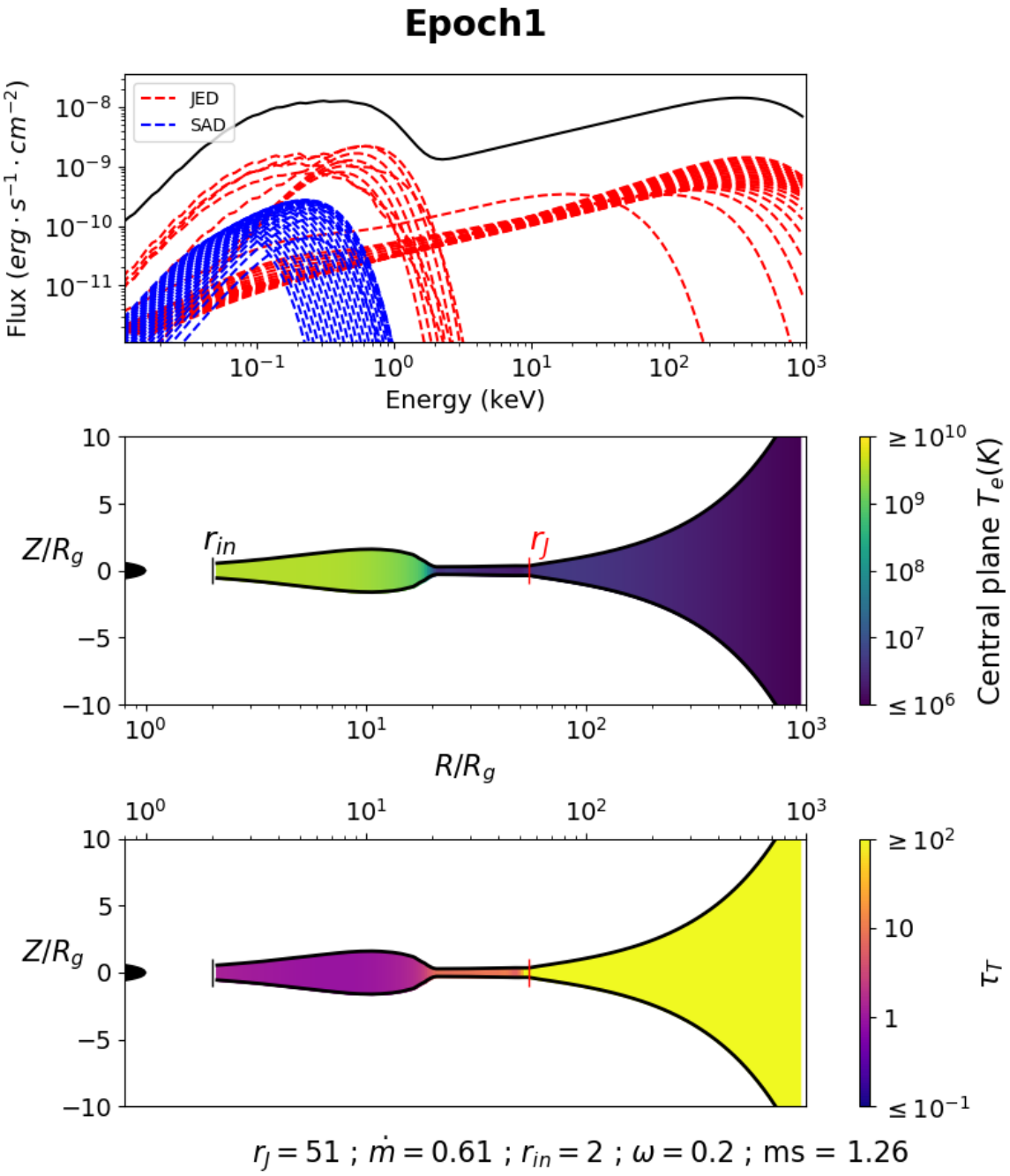

FIGURE 7.10: Sketch representing the geometry, electron temperature and optical depth distribution for MAXI J1820+070 in Epoch 1 with the best-fit parameters found with Model 3.

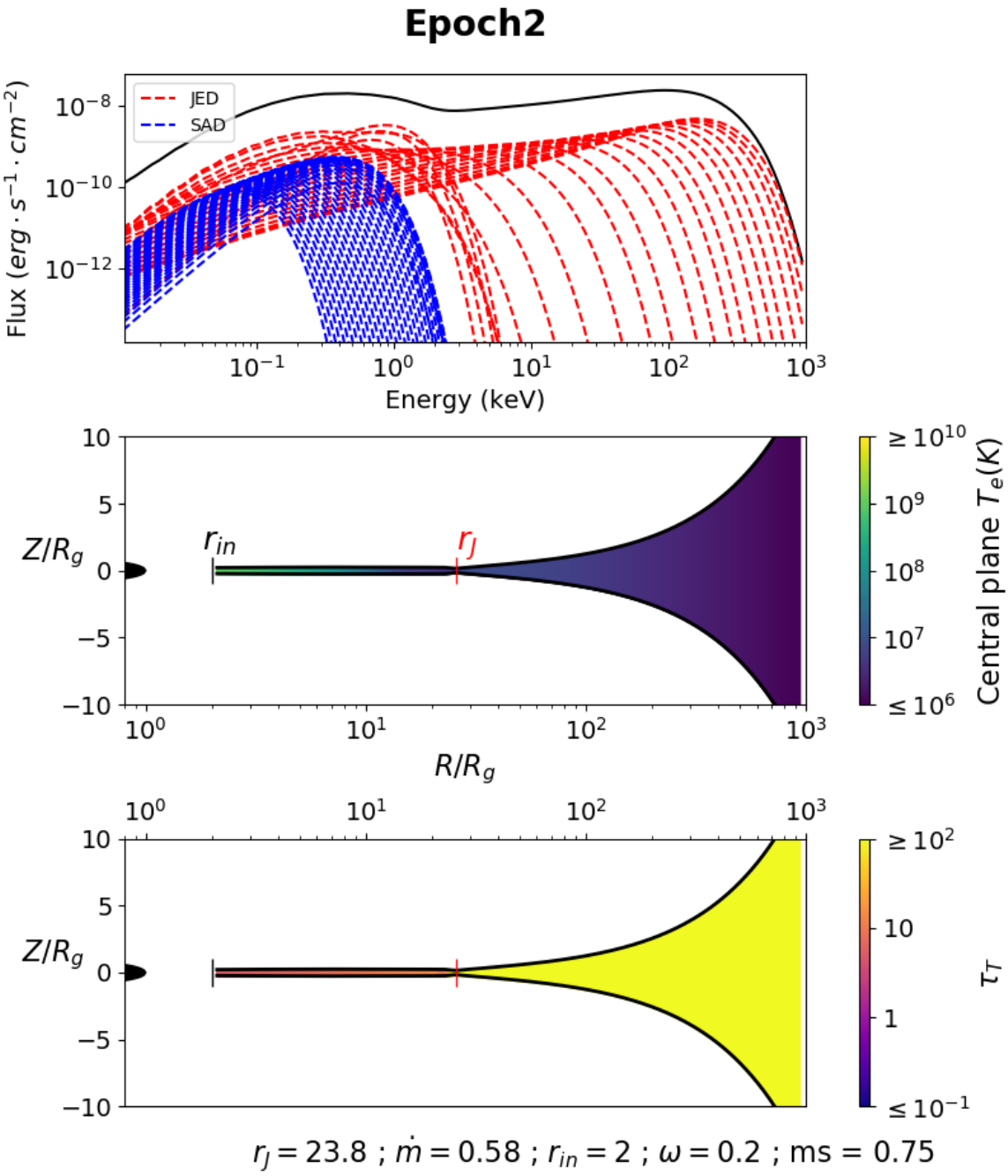

FIGURE 7.11: Sketch representing the geometry, electron temperature and optical depth distribution for MAXI J1820+070 in Epoch 2 with the best-fit parameters found with Model 3.

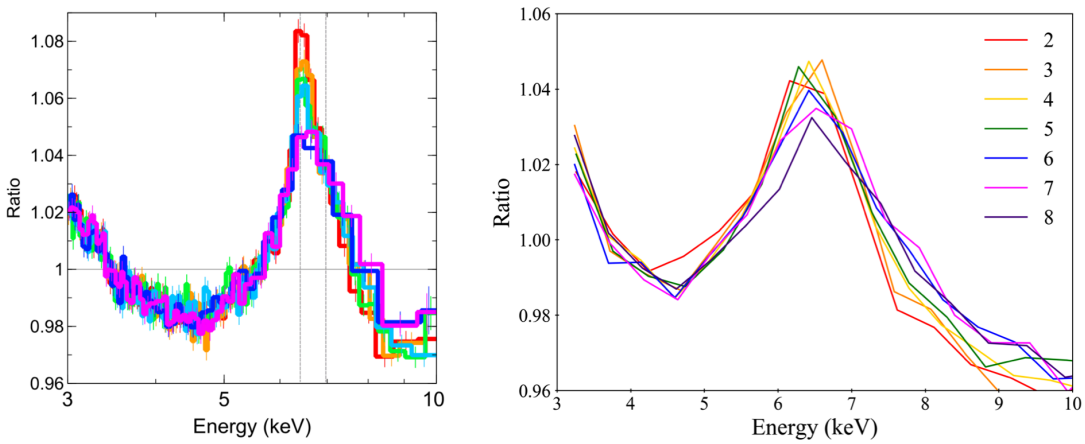

FIGURE 7.12: Evolution of the best-fit parameters for R_J, $\dot{m}$ and m_s over the eight analyzed Epochs.

component by invoking the existence of an elongated corona above the BH. In this geometry the top of this corona would illuminate mainly a remote region of the disk, which produces the narrow line, contrarily to the bottom which would instead illuminate an inner region of the disk, where a strongly blurred line arises. In the JED-SAD configuration the corona is not lamppost so that an analogous explanation is not available. I suggest instead that the origin of such double feature would be due to a self-shielding effects of the disk which, since observed at high inclination, might obscure part of the reflection incoming between $R_{in,1}$ and $R_{in,2}$. Alternatively the outer reflection could be associated either to the presence of a torus of neutral matter surrounding the disk, as observed in AGNs (see, e.g. Petrucci et al. 2007) or even to reflection from the companion star surface (Di Salvo et al. 2001). A point which however needs to be addressed concerns the variability in the reflection spectrum. In Kara et al. (2019) the line profile displayed by *NICER* data was evidently evolving across the hard state (see Fig. 7.12, *left*) shrinking the narrow core while keeping the same, broad, blurred base. This has been interpreted invoking a contracting lamppost corona, which produces two reflection components, one stable (the inner) and one variable (the outer). I do not see an analogous evolution with the *NuSTAR* data, which are well fitted keeping the outer reflection component parameters fixed in all the observations. In *NuSTAR* data, which are taken with a similar cadence with respect to the *NICER* data in Kara et al. (2019), the line profile is indeed more stable, showing only a slight broadening from Epoch 5 to 6 (see Fig. 7.12, *right*). The origin behind this difference between *NuSTAR* and *NICER* could be due to the poorer spectral resolution of the former or to calibration issues in the latter instrument. Interpreting the reflection variability in *NICER* data in accordance with the accretion flow geometry proposed here is challenging. It is however possible to imagine that the outer "torus" might become progressively thinner so that the narrow core in the iron line becomes less and less important. This is going to be fully addressed in the paper in preparation.

However, as extensively discussed in the previous Section, a two-reflection model, while required for a good accordance with the data, was not enough to obtain physically solid best-fit parameters. In particular, I found that allowing for a slightly subsonic or *transonic*, i.e. with m_s around 1, accretion flow is also necessary, unveiling that the previously used strong reflection component was not of physical origin but rather due to an inappropriate fit of the continuum. Subsequently the evolution of the accretion flow in MAXI J1820+070 seems to be determined by three main *actors*, i.e. R_J, $\dot{m}$ and

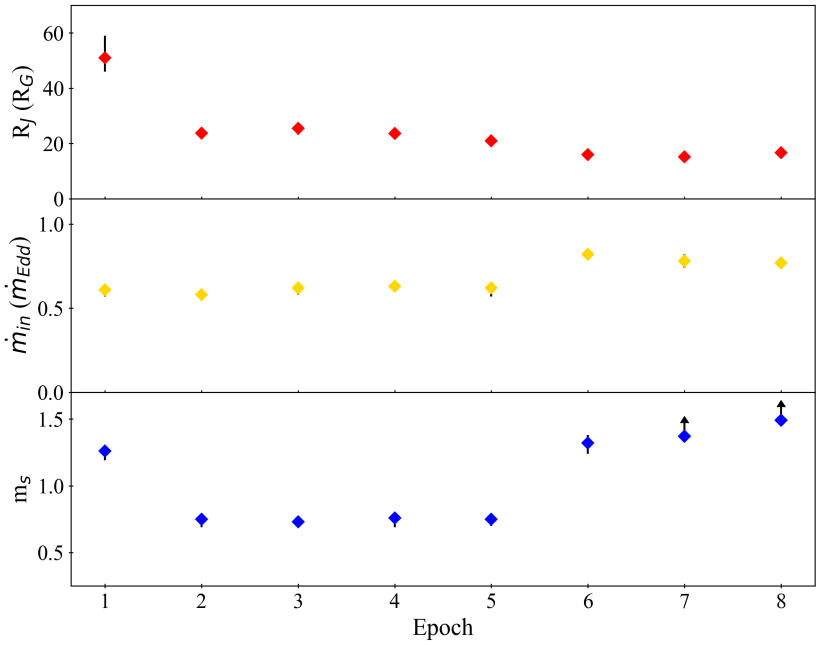

FIGURE 7.13: Evolution of the best-fit parameters for R_J, $\dot{m}$ and m_s over the eight analyzed Epochs.

m_s. The observed trends in the eight analysed Epochs are displayed in Figure 7.13. Interestingly the most variable parameter seems to be m_s. The transition from hard to hard-intermediate state (Epoch 1 to 2) is indeed determined by a decrease in both R_J and m_s, while $\dot{m}$ remains mostly unchanged. From Epoch 5 to 6 m_S is again above 1 and this evolution seems to be correlated with a slight increase in $\dot{m}$ and a slight decrease in R_J. Further investigations are required to confirm and to better explain this scenario. It is noteworthy that this solution is different with respect to the modelling of GX 339-4 with JED-SAD, in which m_s was fixed to 1.5 and the interplay between R_J and $\dot{m}$ was sufficient to describe the data (Marcel et al. 2019).
Several authors reported that a low inclination, i.e. $\sim 30°$-$50°$ was necessary to fit the iron line (Buisson et al. 2019; Bharali et al. 2019; Xu et al. 2020). Such finding is in direct contrast with the evidence of dips in the system (Kajava et al. 2019), which would require at least an inclination of 60°, so that a warped disk was proposed. In this work, when constrained, I found inclination values compatible with the expected high inclination of the systems. When instead the inclination was not well constrained I kept the value frozen to 70°, finding nonetheless acceptable fits.

Finally, my future activity will be also devoted to analyse the radio jet power of the source by means of JED-SAD. Indeed the fits performed in this Chapter allow me to describe each of the selected Epochs with a pair of $\dot{m}$-R_J. From Equation 7.6 it is possible to associate to each of these a radio flux. The system was monitored in radio in the hard state, e.g. with the RATAN-600 radio telescope at 4.7, 8.2 and 11.2 GHz for approximately 30 days, i.e. during the period MJD 58195-58225 (Trushkin et al. 2018). The obtained radio light curve at 4.7 GHz is shown in Figure

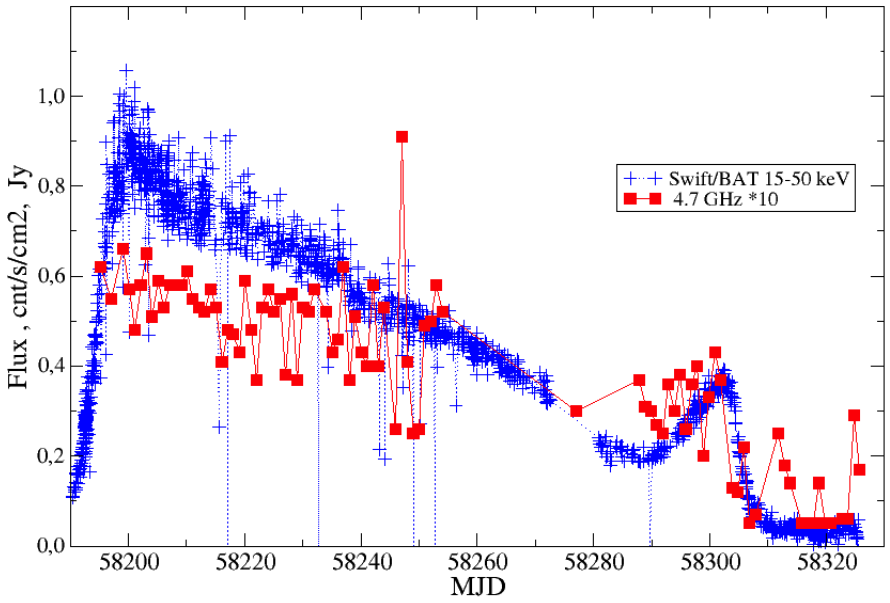

FIGURE 7.14: *RATAN-600* radio lightcurve at 4.7 GHz and *Swift*/BAT lightcurve of the source, showing both the high energies and low energies emission of the source prior to the transition to the soft state. Figure adapted from Trushkin et al. (2018).

7.14.

A further test of the JED-SAD model would be then to check the validity of the aforementioned Equation, especially in the framework of an evolving m_s. This is actually work in progress and it will be reported in Marino et al., *in preparation*.

Conclusions

In this thesis, I worked on four different projects with the aim to focus each time on a different aspect of the broad and complex topic of accretion/ejection of matter onto NSs or BHs, i.e. the accretion flow (Chapter 4), outflows in general (Chapter 5), jets (Chapter 6) and the interconnection between them (Chapter 7). In the first project, I analyzed X-rays spectra of the NS LMXB 1RXS J180408.9-342058 taken across different spectral states during its 2015 outburst and in a selection of type-I X-ray bursts, with the aim of constraining the properties of the accretion flow and of the system itself. A more global approach was followed in the following Chapter, where I hunted for evidences of non-conservative mass-transfer, i.e. matter outflows, in a sample of sources containing almost all the discovered AMXPs. The method used in this chapter consisted in comparing their expected luminosity, calculated on the conservative evolution hypothesis and the observed X-ray flux averaged over the last 20 years. I later dedicate my attention specifically to a specific form of outflows, i.e. to jets and to the modelling of their spectral emission. I applied the Internal Shocks Model (Malzac 2013) to the radio-to-mid-IR spectrum of the NS LMXB 4U 0614+091, using the observed X-rays Fourier Power Density Spectrum as a proxy of the velocity fluctuations in the ejecta. This model allows not only to describe the jet emission but also to test the correlation between variability in the accretion flow and variability in the jet. Testing the accretion/ejection interplay becomes the core of the fourth and final project I worked on, in which I tried to model a number of X-rays observations of the BH transient MAXI J1820+070 in hard/intermediate state with the JED-SAD model (Marcel et al. 2018b). On the basis of a strong interconnection between jet and accretion flow, the model aims at describing simultaneously the configuration of the accretion flow - described as a combination of a typical Shakura-Sunyaev disk (SAD) and a less dense and magnetised jet-emitting disk (JED) - and the jet power.
The main results obtained from these different projects are summarized in the following:

- I caught the system RX1804 in the intermediate spectral state, a state where NS systems are rarely found, and found indications that within this state the spectrum of the system was evolving over very short time scales, i.e. $\sim$ hours.

- I identified a Photospheric Radius Expansion burst occurred in 2012 in RX1804. The study of this burst allowed me to confirm the distance of $\sim$10 kpc proposed by Chelovekov et al. (2017). I have also observed a "clocked burster" behaviour during the intermediate state of RX1804, with recurrence time of about 4000 s. The observed burst phenomenology would suggest H-rich accreted material and therefore gives hints on the nature of the companion star.

- I developed a method which allowed me to obtain indications of non-conservative mass-transfer from the study of the average observed X-rays flux from a XRB and applied it to (almost) all the AMXPs discovered so far. Over the 19 AMXPs analyzed, I found strong

evidences for a non-conservative mass-transfer scenario for five systems, and weaker, i.e. more assumptions-dependent, evidences for other six systems. The majority of the systems in the sample manifests therefore at least indications for a non-conservative mass-transfer scenario. This result highlights how ejection mechanisms could be very common in this class of objects and very likely influence the orbital evolution of these systems.

- I performed the first ever multi-wavelength spectral analysis of a NS LMXB, i.e. 4U 0614+091, including both a physical model (ISHEM) for the jet and a model for the accretion flow. The application of ISHEM to the source suggested two alternative scenarios: the jet is parabolic (instead of the standard conical geometry) or the X-rays variability cannot be used as a proxy for the jet variability. None of these possibilities was suggested for the BH binaries this model was applied to in the past.

- In a preliminary analysis, I found the JED-SAD paradigm to be compatible with the X-ray observations of MAXI J1820+070. I also found that in order to model the reflection spectrum of the systems two reflection components are necessary, which likely originate from different parts of the accretion disk. Moreover, an evolution in the sonic Mach number of the JED region seems to be necessary to describe the data with physically reliable spectral parameters.

The work carried on in this thesis (and in the linked publications) paves the way to new research to be done. The evidence of somehow faster hard-to-soft transitions in NS LMXBs needs a physical explanation. In this thesis, I proposed that this is consequence of the role played by the surface of the NS as an extra-cooling mechanism, but I can not exclude other possible explanations. Concerning the nature of the companion star, in the past it was suggested on the basis of its optical spectrum that RX1804 is a UCXB harbouring a white dwarf (Baglio et al. 2016). However, the burst phenomenology enlightened in this thesis would rather point out that the companion star is a H-rich star instead, i.e. a main sequence star or a brown dwarf. The second possibility would also explain the VFXT behavior exhibited by the system in the past. The nature of the donor star in RX1804 remains therefore a conundrum, which only new investigations might solve.
The indication of outflows in the majority of the AMXPs class confirms the expectation that ejection is a key phenomenon for this class of system, which could likely play a role in the strong orbital expansion observed in several AMXPs (see, e.g. Di Salvo and Sanna 2020). Furthermore, a non-conservative mass-transfer could be at play also in other types of binaries, e.g. as observed by Ziółkowski and Zdziarski (2018) who applied the same method developed here to the BH binary V404 Cyg and found also hints for an analogous scenario. However this method gives indeed *indications*; in the future I plan to attempt on obtaining more detailed descriptions of the secular evolution of these systems following the approach of e.g. Tailo et al. (2018) or using open source numerical codes for the binary evolution like `MESA` (Paxton et al. 2010).
The puzzling results for 4U 0614+091 raise several question marks. One of the two possible scenarios consisted in a more collimated jet with respect to the standard conical jet usually assumed in the past for other BH binaries (e.g. Drappeau et al. 2015; Péault et al. 2019; Bassi et al. 2020). More investigations are necessary to understand why 4U 0614+091 is the first source to specifically require a non-conical jet and if this is somehow representative of systems hosting NSs instead of BHs. Even more troublesome is the other scenario envisaged, where the accretion flow variability is not transmitted to the jet. Does it mean that the disc-jet coupling works differently with respect to the other BH XRBs studied in the past with `ISHEM`? And more crucially is also this scenario related to the nature of the compact object? The answer to these questions might be closer with

new multi-wavelength observational campaigns of NS (or BH) binaries emitting jets and so new applications of ISHEM. In particular, exploiting radio data from *ALMA*, which would allow me coverage on the crucial energy range 10^{11}-10^{12} Hz, together with Infrared, optical and X-rays data with good time resolution would provide a very useful opportunity in this direction. It would be indeed extremely fascinating to study if the jet properties and the disc-jet coupling change in an AMXP with respect to a non-pulsating NS LMXB, as it would highlight the role of the NS magnetic field in the jet/accretion flow coupling.
Finally, the preliminary results for MAXI J1820+070 with the JED-SAD model point out that the model satisfactorily describes the X-ray spectrum of the system. If confirmed this could be the second time that the paradigm is found successful. Another intriguing result is represented by the fact that two reflection components were necessary to model the iron line region and the Compton hump in the spectrum. A double reflection component was also adopted by other authors for the same sources (e.g. Buisson et al. 2019) but using toy models, i.e. the lamp-post corona model, while in this thesis I used a physical model which describes in detail also the physical properties of the accretion flow. It is noteworthy that a truncated disk geometry was found for the hard state of both RX1804 and MAXI J1820+070, despite having different types of accreting compact objects.

However the JED-SAD model is not been adapted to NS systems yet. It is plausible that, since several hard state NS LMXBs seem to fit as well in the truncated disk geometry scenario and jets are observed in these systems as well, that a JED-SAD paradigm could be valid also for this class. However, the results obtained in this thesis for 4U 0614+091, together with evidences like e.g. the lack of jet quenching in soft state and the existence of models of jet launching like in Parfrey et al. (2016) which are specifically designed for NSs, cast a shadow on the belief that the accretion/ejection engine is the same for NS and BH XRBs.
While much has been done in this field, it is clear that the accretion and ejection mechanisms of matter onto compact objects are far to be fully understood. It is natural to wonder if the future X-ray missions would bring us any closer to solve these questions. The future is indeed presumably *bright* in this sense. In the next decade the enhanced X-ray timing polarimeter (*eXTP*, Zhang et al. 2019) first and the Advanced Telescope for High Energy Astrophysics (*Athena*, Barcons et al. 2015) later could provide data with unprecedented statistics and excellent spectral resolution, especially for the second mission. The analysis of the Fe line profile with these next generation telescopes could lead to strong constraints on the inner disk radius, which in turn could put the debate on the geometry of the accretion flow during the hard spectral state to an end. Furthermore, the combination of the good timing and polarimetry capabilities of *eXTP* will enable parallel ways to constrain the accretion geometry, e.g. by studying time lags between the different spectral components or the polarization of the incoming radiation (in't Zand et al. 2019a). It is also noteworthy that analogous polarimetry studies will be possible even before *eXTP* with the Imaging X-ray Polarimetry Explorer (*IXPE* Weisskopf et al. 2016), scheduled to be launched in 2021.

The very good spectral resolution of X-IFU on board *Athena*, combined with its high sensitivity, could in principle allow for observations of the outflows due to the disruption of the disk at the onset of a propeller phase in LMXBs at low accretion rates.
Finally, the high sensitivity of the just launched X-ray telescope eROSITA (Merloni et al. 2012) and of future missions like *Athena* and *eXTP*, will provide in the near future the unique opportunity to gain insights on the elusive Very Faint X-ray Transients population, i.e. like RX1804, during their most interesting and exotic behavior, i.e. their 10^{34}-10^{36} erg s^{-1} luminosity outbursts. Of course, in order to actually catch these systems in one of these faint outbursts it is fundamental to have a good X-ray survey mission; this role could be played in the near future by the Transient High Energy Sky

and Early Universe Surveyor (*THESEUS*), if the mission will actually be picked by ESA.
This section was aimed to give the reader *conclusions* and instead it rather focused on how the conclusion of this work could potentially coincide with the opening of many others. As it (almost) always happens in science, indeed any result leads to more questions and more research to be done. The tales of the Universe rarely have an ending of any kind. And maybe this is for the best, maybe research, as a product of human curiosity, should never get one.

Acknowledgements

I wrote this thesis during a global pandemic, confined in the loneliness of my own room with little or no contact at all with the outside world. And yet, as much as solitary it has felt, it is impossible not to see how many people helped me in writing this manuscript. This last page is dedicated to all of you who played a role in the last three years of my life.

First of all, I am very grateful to my referees, Sergio Campana and Guillame Dubus, for the detailed and careful revision of this manuscript. The comments and suggestions you made helped improve substantially the quality of this thesis.

I have to thank my supervisors: Tiziana, Julien and Melania. One might think that having not one, not two but three supervisors could only mean more and more work to do, but at least for me it was a blessing. I had the chance to study with three different mentors, each of them with their own specific area of interest, method, approach. I never felt neglected but I also never felt overlooked. You all guided me with care at the beginning, when I most needed a guide, and then gave me the trust to develop my research autonomously, always certain of your support, if needed. I could not be more grateful for the time and the effort you dedicated to teach me and supervise my work and I would be anything but honored to keep working with you in the future.

I also have to thank all the extremely skilled scientists I had the chance to work with. The collaboration with Rosario Iaria and Luciano Burderi not only helped me enormously with my understanding of accretion physics but was also punctuated by brilliant and memorable conversations, sometimes not only about science. Andrea Sanna in Cagliari has always been the first to comment on my drafts and his contributions were often crucial. Antonino D'Aí helped me countless times with the Swift *and* NuSTAR *data analysis, while Alberto Segreto was the one who actually extracted all the BAT data used here, so thank you both, sincerely. I want to thank also Carlo Ferrigno, who was my tutor for only a week in Geneva and yet he had the time to teach me about* INTEGRAL*, python and how to do a presentation which was good enough to actually win the best talk prize. Chapter 6 of this thesis could never have been done without the outstanding work done by Simone Migliari and his student, José Lopez Miralles. For Chapter 7, on the other hand, I have to credit Pierre-Olivier Petrucci, who I might consider my fourth, uncredited supervisor, and his student Samuel Barnier: the work performed on MAXI J1820+070 was not easy itself, COVID-19 outbreak did not help either but your support, patience and contribution made it possible. Finally, I want to thank Massimo Cocchi, in Rome, for his precious and sometimes severe lessons, because sometimes a harsh critique is what you really need to get out of your comfort zone and grow up.*

A long list of colleagues has also been there since day one and I am extremely grateful to them for sharing what sometimes felt like a burden. Me and Roberta were flatmates during our first year of PhD and she was with me during one of the most exciting, and yet terrifying, moments of my life: thanks. To Simona and Angelo goes my gratitude for all the data- and science-related problems we

solved together, I really felt like we were a team. "Tizianina" supported me a lot and also helped me many times when I moved to Toulouse - I am sure it would have been so much worse without you. Living in France, at least before COVID, was a wonderful adventure because of all the amazing people in IRAP: Andres, Sujay, Abe, Gabi, Jakob and all the others. I felt part of a family and it was nice sharing PhD experiences together.

A special thanks goes to my family: my parents, my brothers and my grandparents. You supported me all the time, helping me when needed, cheering me up when I felt sad. The work carried on in this PhD brought me away for a long time, I missed so many things and spent only a tiny fraction of these years with you. I am deeply sorry for this, but at least, I hope I made you proud in the end.

I can not articulate with words how much I feel grateful for my friends. Thanks for the nights out, the dinners, the walks, the laughs, the drama. Thanks for being always by my side. With you I spent the best moments of this three-years-long adventure. So thanks Andrea, Cesare, Daniele, Elia, Elsa, Enrico, Fabio, Peppe, Toti and all the others.

At last, I want to thank Sid. You always believed in myself, often way more than I do. You made me feel seen and appreciated even when I was at my worst. We wrote our theses together, during the worst historical time I could think of. It was a hell of a ride. But with you, I would do it all again without hesitation.

Bibliography

Abbott, B. P., Abbott, R., Abbott, T. D., Abernathy, M. R., Acernese, F., Ackley, K., Adams, C., Adams, T., Addesso, P., Adhikari, R. X., and et al.: 2016, *Physical Review Letters* **116(6)**, 061102 20

Abramowicz, M. A. and Igumenshchev, I. V.: 2001, **554(1)**, L53 33

Abramowicz, M. A., Igumenshchev, I. V., and Lasota, J.-P.: 1998, **293(4)**, 443 130

Agol, E. and Krolik, J. H.: 2000, **528(1)**, 161 26

Altamirano, D., Casella, P., Patruno, A., Wijnands, R., and van der Klis, M.: 2008a, **674**, L45 83, 90

Altamirano, D., Cavecchi, Y., Patruno, A., Watts, A., Linares, M., Degenaar, N., Kalamkar, M., van der Klis, M., Rea, N., Casella, P., Armas Padilla, M., Kaur, R., Yang, Y. J., Soleri, P., and Wijnands, R.: 2011, **727**, L18 83, 85

Altamirano, D., Patruno, A., Heinke, C. O., Markwardt, C., Strohmayer, T. E., Linares, M., Wijnands, R., van der Klis, M., and Swank, J. H.: 2010a, **712**, L58 83

Altamirano, D., van der Klis, M., Méndez, M., Jonker, P. G., Klein-Wolt, M., and Lewin, W. H. G.: 2008b, **685(1)**, 436 45

Altamirano, D., Watts, A., Linares, M., Markwardt, C. B., Strohmayer, T., and Patruno, A.: 2010b, **409**, 1136 91

Alvarez, H., Aparici, J., May, J., and Reich, P.: 2000, **355**, 863 98

Ambrosino, F., Papitto, A., Stella, L., Meddi, F., Cretaro, P., Burderi, L., Di Salvo, T., Israel, G. L., Ghedina, A., Di Fabrizio, L., and Riverol, L.: 2017, *Nature Astronomy* **1**, 854 87

Applegate, J. H. and Shaham, J.: 1994, **436**, 312 95

Archibald, A. M., Kaspi, V. M., Hessels, J. W. T., Stappers, B., Janssen, G., and Lyne, A.: 2013, *ArXiv e-prints* 82

Archibald, A. M., Stairs, I. H., Ransom, S. M., Kaspi, V. M., Kondratiev, V. I., Lorimer, D. R., McLaughlin, M. A., Boyles, J., Hessels, J. W. T., Lynch, R., van Leeuwen, J., Roberts, M. S. E., Jenet, F., Champion, D. J., Rosen, R., Barlow, B. N., Dunlap, B. H., and Remillard, R. A.: 2009, *Science* **324**, 1411 82, 83

Armas Padilla, M., Degenaar, N., and Wijnands, R.: 2013, **434**, 1586 56

Armas Padilla, M., Ueda, Y., Hori, T., Shidatsu, M., and Muñoz-Darias, T.: 2017, **467(1)**, 290 37, 39

Asada, K. and Nakamura, M.: 2012, **745(2)**, L28 101

Atri, P., Miller-Jones, J. C. A., Bahramian, A., Plotkin, R. M., Deller, A. T., Jonker, P. G., Maccarone, T. J., Sivakoff, G. R., Soria, R., Altamirano, D., Belloni, T., Fender, R., Koerding, E., Maitra, D., Markoff, S., Migliari, S., Russell, D., Russell, T., Sarazin, C. L., Tetarenko, A. J., and Tudose, V.: 2020, **493(1)**, L81 133, 137

Baade, W. and Minkowski, R.: 1954, **119**, 215 40

Baade, W. and Zwicky, F.: 1934, *Physical Review* **46(1)**, 76 17

Bachetti, M., Harrison, F. A., Walton, D. J., Grefenstette, B. W., Chakrabarty, D., Fürst, F., Barret, D., Beloborodov, A., Boggs, S. E., Christensen, F. E., Craig, W. W., Fabian, A. C., Hailey, C. J., Hornschemeier, A., Kaspi, V., Kulkarni, S. R., Maccarone, T., Miller, J. M., Rana, V., Stern, D., Tendulkar, S. P., Tomsick, J., Webb, N. A., and Zhang, W. W.: 2014, **514(7521)**, 202 27

Baglio, M. C., D'Avanzo, P., Campana, S., Goldoni, P., Masetti, N., Muñoz-Darias, T., Patiño-Álvarez, V., and Chavushyan, V.: 2016, **587**, A102 59, 77, 114, 150

Baglio, M. C., Mainetti, D., D'Avanzo, P., Campana, S., Covino, S., Russell, D. M., and Shahbaz, T.: 2014, **572**, A99 107

Baglio, M. C., Vincentelli, F., Campana, S., Coti Zelati, F., D'Avanzo, P., Burderi, L., Casella, P., Papitto, A., and Russell, D. M.: 2019, **631**, A104 114

Balbus, S. A.: 2005, in J. M. Hameury and J. P. Lasota (eds.), *The Astrophysics of Cataclysmic Variables and Related Objects*, Vol. 330 of *Astronomical Society of the Pacific Conference Series*, p. 185 31

Baldassare, V. F., Reines, A. E., Gallo, E., and Greene, J. E.: 2015, **809(1)**, L14 20

Barcons, X., Nandra, K., Barret, D., den Herder, J. W., Fabian, A. C., Piro, L., Watson, M. G., and the Athena Team: 2015, in *Journal of Physics Conference Series*, Vol. 610 of *Journal of Physics Conference Series*, p. 012008 151

Barret, D. and Olive, J.-F.: 2002, **576(1)**, 391 71

Barret, D., Olive, J. F., Boirin, L., Done, C., Skinner, G. K., and Grindlay, J. E.: 2000, **533(1)**, 329 64, 124

Barthelmy, S. D., Barbier, L. M., Cummings, J. R., Fenimore, E. E., Gehrels, N., Hullinger, D., Krimm, H. A., Markwardt, C. B., Palmer, D. M., Parsons, A., Sato, G., Suzuki, M., Takahashi, T., Tashiro, M., and Tueller, J.: 2005, **120**, 143 48

Basak, R., Zdziarski, A. A., Parker, M., and Islam, N.: 2017, **472(4)**, 4220 39, 54

Bassa, C. G., Patruno, A., Hessels, J. W. T., Keane, E. F., Monard, B., Mahony, E. K., Bogdanov, S., Corbel, S., Edwards, P. G., Archibald, A. M., Janssen, G. H., Stappers, B. W., and Tendulkar, S.: 2014, **441**, 1825 82

Bassi, T., Del Santo, M., D'Aı, A., Motta, S. E., Malzac, J., Segreto, A., Miller-Jones, J. C. A., Atri, P., Plotkin, R. M., Belloni, T. M., Mineo, T., and Tzioumis, A. K.: 2019, **482(2)**, 1587 41, 42

Bassi, T., Malzac, J., Del Santo, M., Jourdain, E., Roques, J. P., D'Aì, A., Miller-Jones, J. C. A., Belmont, R., Motta, S. E., Segreto, A., Testa, V., and Casella, P.: 2020, *arXiv e-prints* p. arXiv:2003.07822 105, 106, 107, 150

Begelman, M. C., McKee, C. F., and Shields, G. A.: 1983, **271**, 70 40

Bell, A. R.: 1978, **182**, 147 102

Belloni, T.: 2010, *The Jet Paradigm*, Vol. 794 43

Belloni, T., Mendez, M., van der Klis, M., Hasinger, G., Lewin, W. H. G., and van Paradijs, J.: 1996, **472**, L107 40

Belloni, T., Parolin, I., Del Santo, M., Homan, J., Casella, P., Fender, R. P., Lewin, W. H. G., Méndez, M., Miller, J. M., and van der Klis, M.: 2006, **367(3)**, 1113 42

Belloni, T., Psaltis, D., and van der Klis, M.: 2002, **572(1)**, 392 44, 123

Beloborodov, A. M.: 1999, **510(2)**, L123 139

Beloborodov, A. M., Stern, B. E., and Svensson, R.: 2000, **535(1)**, 158 106

Bharali, P., Chauhan, J., and Boruah, K.: 2019, **487(4)**, 5946 133, 136, 147

Bhattacharya, D. and van den Heuvel, E. P. J.: 1991, **203**, 1 19, 80

Bildsten, L. and Chakrabarty, D.: 2001, **557(1)**, 292 77

Blandford, R. D. and Begelman, M. C.: 1999, **303(1)**, L1 33

Blandford, R. D. and Königl, A.: 1979, **232**, 34 102

Blandford, R. D. and Payne, D. G.: 1982, **199**, 883 99

Blandford, R. D. and Znajek, R. L.: 1977, **179**, 433 99, 100

Boettcher, M.: 2010, *arXiv e-prints* p. arXiv:1006.5048 105

Boissay, R., Chenevez, J., Wilms, J., Grinberg, V., Del Santo, M., Bazzano, A., Capitanio, F., Tarana, A., Paizis, A., Watanabe, K., Rodriguez, J., Goetz, D., Kuulkers, E., and Ferrigno, C.: 2015, *The Astronomer's Telegram* 7096 58

Bosch-Ramon, V., Romero, G. E., and Paredes, J. M.: 2006, **447(1)**, 263 99

Bouchet, L., del Santo, M., Jourdain, E., Roques, J. P., Bazzano, A., and DeCesare, G.: 2009, **693(2)**, 1871 37

Bozzo, E., Papitto, A., Ferrigno, C., and Belloni, T. M.: 2014, **570**, L2 70

Bradt, H. V., Rothschild, R. E., and Swank, J. H.: 1993, **97(1)**, 355 50

Brocksopp, C., Corbel, S., Fender, R. P., Rupen, M., Sault, R., Tingay, S. J., Hannikainen, D., and O'Brien, K.: 2005, **356(1)**, 125 41

Buisson, D. J. K., Fabian, A. C., Barret, D., Fürst, F., Gandhi, P., García, J. A., Kara, E., Madsen, K. K., Miller, J. M., Parker, M. L., Shaw, A. W., Tomsick, J. A., and Walton, D. J.: 2019, **490(1)**, 1350 39, 133, 134, 135, 136, 138, 140, 147, 151

Bult, P., Arzoumanian, Z., Cackett, E. M., Chakrabarty, D., Gendreau, K. C., Guillot, S., Homan, J., Jaisawal, G. K., Keek, L., Kenyon, S., Lamb, F. K., Ludlam, R., Mahmoodifar, S., Markwardt, C., Miller, J. M., Prigozhin, G., Soong, Y., Strohmayer, T. E., and Uttley, P.: 2018, **859(1)**, L1 90, 124

Bult, P., Chakrabarty, D., Arzoumanian, Z., Gendreau, K. C., Guillot, S., Malacaria, C., Ray, P. S., and Strohmayer, T. E.: 2020, **898(1)**, 38 84

Burderi, L., Di Salvo, T., Riggio, A., Papitto, A., Iaria, R., D'Aì, A., and Menna, M. T.: 2010, **515**, A44 86

Burderi, L., King, A. R., and Wynn, G. A.: 1996, **457**, 348 80

Burderi, L., Possenti, A., D'Antona, F., Di Salvo, T., Burgay, M., Stella, L., Menna, M. T., Iaria, R., Campana, S., and d'Amico, N.: 2001, **560**, L71 13, 84

Burderi, L., Riggio, A., di Salvo, T., Papitto, A., Menna, M. T., D'Aì, A., and Iaria, R.: 2009, **496**, L17 84, 86

Burrows, D. N., Hill, J. E., Nousek, J. A., Kennea, J. A., Wells, A., Osborne, J. P., Abbey, A. F., Beardmore, A., Mukerjee, K., Short, A. D. T., Chincarini, G., Campana, S., Citterio, O., Moretti, A., Pagani, C., Tagliaferri, G., Giommi, P., Capalbi, M., Tamburelli, F., Angelini, L., Cusumano, G., Bräuninger, H. W., Burkert, W., and Hartner, G. D.: 2005, **120**, 165 48

Bussard, R. W., Alexander, S. B., and Meszaros, P.: 1986, **34**, 440 18

Cackett, E. M., Altamirano, D., Patruno, A., Miller, J. M., Reynolds, M., Linares, M., and Wijnands, R.: 2009, **694**, L21 90

Campana, S. and Di Salvo, T.: 2018, *ArXiv e-prints* 81, 82

Campana, S., Ravasio, M., Israel, G. L., Mangano, V., and Belloni, T.: 2003, **594**, L39 83

Cardelli, J. A., Clayton, G. C., and Mathis, J. S.: 1989, **345**, 245 108

Casella, P., Altamirano, D., Patruno, A., Wijnands, R., and van der Klis, M.: 2008, **674**, L41 82, 83

Casella, P., Belloni, T., and Stella, L.: 2005, **629(1)**, 403 44

Casella, P., Maccarone, T. J., O'Brien, K., Fender, R. P., Russell, D. M., van der Klis, M., Pe'Er, A., Maitra, D., Altamirano, D., Belloni, T., Kanbach, G., Klein-Wolt, M., Mason, E., Soleri, P., Stefanescu, A., Wiersema, K., and Wijnands, R.: 2010, **404(1)**, L21 111

Casse, F. and Ferreira, J.: 2000, **361**, 1178 128

Chaboyer, B.: 2001, in T. von Hippel, C. Simpson, and N. Manset (eds.), *Astrophysical Ages and Times Scales*, Vol. 245 of *Astronomical Society of the Pacific Conference Series*, p. 162 19

Chabrier, G. and Baraffe, I.: 2000, **38**, 337 86

Chadwick, J.: 1932, **129(3252)**, 312 17

Chakraborty, S., Navale, N., Ratheesh, A., and Bhattacharyya, S.: 2020, **498(4)**, 5873 138, 140

Chelovekov, I. V., Grebenev, S. A., Mereminskiy, I. A., and Prosvetov, A. V.: 2017, *Astronomy Letters* **43(12)**, 781 58, 74, 78, 149

Chenevez, J., Galloway, D. K., in 't Zand, J. J. M., Tomsick, J. A., Barret, D., Chakrabarty, D., Fürst, F., Boggs, S. E., Christensen, F. E., Craig, W. W., Hailey, C. J., Harrison, F. A., Romano, P., Stern, D., and Zhang, W. W.: 2016, **818(2)**, 135 72

Chenevez, J., Kuulkers, E., Brandt, S., Wijnands, R., Alfonso-Garzón, J., Beckmann, V., Bird, T., Del Santo, M., Domingo, A., Ebisawa, K., Jonker, P., Kretschmar, P., Markwardt, C., Oosterbroek, T., Paizis, A., Pottschmidt, K., and Sánchez-Fernández, C.: 2012, *The Astronomer's Telegram* 4050 58, 72, 74

Chevalier, C. and Ilovaisky, S. A.: 1991, **251**, L11 81

Churazov, E., Gilfanov, M., and Revnivtsev, M.: 2001, **321(4)**, 759 39

Churazov, E., Sunyaev, R., Revnivtsev, M., Sazonov, S., Molkov, S., Grebenev, S., Winkler, C., Parmar, A., Bazzano, A., Falanga, M., Gros, A., Lebrun, F., Natalucci, L., Ubertini, P., Roques, J. P., Bouchet, L., Jourdain, E., Knödlseder, J., Diehl, R., Budtz-Jorgensen, C., Brandt, S., Lund, N., Westergaard, N. J., Neronov, A., Türler, M., Chernyakova, M., Walter, R., Produit, N., Mowlavi, N., Mas- Hesse, J. M., Domingo, A., Gehrels, N., Kuulkers, E., Kretschmar, P., and Schmidt, M.: 2007, **467**, 529 88

Church, M. J. and Bałucińska-Church, M.: 2004, **348(3)**, 955 39

Claret, A. and Gimenez, A.: 1990, **169**, 215 86

Cocchi, M., Bazzano, A., Natalucci, L., Ubertini, P., Heise, J., Kuulkers, E., Cornelisse, R., and in't Zand, J. J. M.: 2001, **378**, L37 56

Cocchi, M., Bazzano, A., Natalucci, L., Ubertini, P., Heise, J., Kuulkers, E., Muller, J. M., and in't Zand , J. J. M.: 2000, **357**, 527 74

Cocchi, M., Farinelli, R., and Paizis, A.: 2011, **529**, A155 39, 63, 70, 77

Cocchi, M., Farinelli, R., Paizis, A., and Titarchuk, L.: 2010, **509**, A2 62

Coppi, P. S.: 1999, in J. Poutanen and R. Svensson (eds.), *High Energy Processes in Accreting Black Holes*, Vol. 161 of *Astronomical Society of the Pacific Conference Series*, p. 375 37

Corbel, S., Coriat, M., Brocksopp, C., Tzioumis, A. K., Fender, R. P., Tomsick, J. A., Buxton, M. M., and Bailyn, C. D.: 2013, **428(3)**, 2500 41

Corbel, S. and Fender, R. P.: 2002, **573(1)**, L35 102

Corbel, S., Fender, R. P., Tzioumis, A. K., Nowak, M., McIntyre, V., Durouchoux, P., and Sood, R.: 2000, **359**, 251 41, 102

Coriat, M., Corbel, S., Prat, L., Miller-Jones, J. C. A., Cseh, D., Tzioumis, A. K., Brocksopp, C., Rodriguez, J., Fender, R. P., and Sivakoff, G. R.: 2011, **414(1)**, 677 12, 41

Cornelisse, R., Verbunt, F., in't Zand, J. J. M., Kuulkers, E., Heise, J., Remillard, R. A., Cocchi, M., Natalucci, L., Bazzano, A., and Ubertini, P.: 2002, **392**, 885 56

Coti Zelati, F., Campana, S., D'Avanzo, P., and Melandri, A.: 2014, **438**, 2634 83, 88

Crusius, A. and Schlickeiser, R.: 1986, **164(2)**, L16 102

Cumming, A. and Bildsten, L.: 2001, **559**, L127 57

D'Aì, A., di Salvo, T., Ballantyne, D., Iaria, R., Robba, N. R., Papitto, A., Riggio, A., Burderi, L., Piraino, S., Santangelo, A., Matt, G., Dovčiak, M., and Karas, V.: 2010, **516**, A36 39, 63, 71

D'Aì, A., Iaria, R., Di Salvo, T., Riggio, A., Burderi, L., and Robba, N. R.: 2014, **564**, A62 24, 40

D'Aí, A., Życki, P., Di Salvo, T., Iaria, R., Lavagetto, G., and Robba, N. R.: 2007, **667(1)**, 411 117

Daigne, F. and Mochkovitch, R.: 1998, **296(2)**, 275 105

Dauser, T., Garcia, J., Wilms, J., Böck, M., Brenneman, L. W., Falanga, M., Fukumura, K., and Reynolds, C. S.: 2013, **430(3)**, 1694 137

Davis, S. W., Blaes, O. M., Hubeny, I., and Turner, N. J.: 2005, **621(1)**, 372 37

De Falco, V., Kuiper, L., Bozzo, E., Ferrigno, C., Poutanen, J., Stella, L., and Falanga, M.: 2017a, **603**, A16 90

De Falco, V., Kuiper, L., Bozzo, E., Galloway, D. K., Poutanen, J., Ferrigno, C., Stella, L., and Falanga, M.: 2017b, **599**, A88 88, 90, 91

De Marco, B., Ponti, G., Muñoz-Darias, T., and Nand ra, K.: 2015, **454(3)**, 2360 39

de Martino, D., Belloni, T., Falanga, M., Papitto, A., Motta, S., Pellizzoni, A., Evangelista, Y., Piano, G., Masetti, N., Bonnet-Bidaud, J.-M., Mouchet, M., Mukai, K., and Possenti, A.: 2013, **550**, A89 82

Degenaar, N., Altamirano, D., Deller, A., Heinke, C., Hessels, J., Joadand, A., Miller-Jones, J., Moldon, J., and Wijnands, R.: 2015a, *The Astronomer's Telegram* 7352 60

Degenaar, N., Altamirano, D., Parker, M., Miller-Jones, J. C. A., Miller, J. M., Heinke, C. O., Wijnands, R., Ludlam, R., Parikh, A., Hessels, J. W. T., Gusinskaia, N., Deller, A. T., and Fabian, A. C.: 2016, **461**, 4049 59, 60, 63, 69, 71, 72

Degenaar, N., Miller, J. M., Chakrabarty, D., Harrison, F. A., Kara, E., and Fabian, A. C.: 2015b, **451**, L85 35

Degenaar, N., Pinto, C., Miller, J. M., Wijnands, R., Altamirano, D., Paerels, F., Fabian, A. C., and Chakrabarty, D.: 2017, **464**, 398 56

Degenaar, N. and Suleimanov, V. F.: 2018, *arXiv e-prints* p. arXiv:1806.02833 18

Degenaar, N. and Wijnands, R.: 2009, **495**, 547 56

Degenaar, N. and Wijnands, R.: 2010, **524**, A69 56

Degenaar, N., Wijnands, R., Cackett, E. M., Homan, J., in't Zand, J. J. M., Kuulkers, E., Maccarone, T. J., and van der Klis, M.: 2012, **545**, A49 77

Del Santo, M., Belloni, T. M., Tomsick, J. A., Sbarufatti, B., Cadolle Bel, M., Casella, P., Castro-Tirado, A., Corbel, S., Grinberg, V., Homan, J., Kalemci, E., Motta, S., Muñoz-Darias, T., Pottschmidt, K., Rodriguez, J., and Wilms, J.: 2016, **456**, 3585 42

Del Santo, M., Malzac, J., Belmont, R., Bouchet, L., and De Cesare, G.: 2013, **430(1)**, 209 37, 117

Del Santo, M., Malzac, J., Jourdain, E., Belloni, T., and Ubertini, P.: 2008, **390(1)**, 227 37, 117

Del Santo, M., Nucita, A. A., Lodato, G., Manni, L., De Paolis, F., Farihi, J., De Cesare, G., and Segreto, A.: 2014, **444(1)**, 93 70

Del Santo, M., Romano, P., Sidoli, L., Mereghetti, S., Ferrigno, C., Degenaar, N., Wijnands, R., Kuulkers, E., Nucita, A., and Savchenko, V.: 2011, *The Astronomer's Telegram* **3210**, 1 56

Del Santo, M., Sidoli, L., Mereghetti, S., Bazzano, A., Tarana, A., and Ubertini, P.: 2007, **468**, L17 56

Del Santo, M., Sidoli, L., Romano, P., Bazzano, A., Wijnands, R., Degenaar, N., and Mereghetti, S.: 2010, **403**, L89 56

Dhawan, V., Mirabel, I. F., and Rodríguez, L. F.: 2000, **543(1)**, 373 40

Di Salvo, T., Burderi, L., Riggio, A., Papitto, A., and Menna, M. T.: 2008, **389**, 1851 13, 84, 86, 95

Di Salvo, T., Goldoni, P., Stella, L., van der Klis, M., Bazzano, A., Burderi, L., Farinelli, R., Frontera, F., Israel, G. L., and Méndez, M.: 2006, **649(2)**, L91 37

Di Salvo, T., Iaria, R., Matranga, M., Burderi, L., D'Aí, A., Egron, E., Papitto, A., Riggio, A., Robba, N. R., and Ueda, Y.: 2015, **449**, 2794 35, 63

Di Salvo, T., Robba, N. R., Iaria, R., Stella, L., Burderi, L., and Israel, G. L.: 2001, **554(1)**, 49 39, 117, 146

Di Salvo, T. and Sanna, A.: 2020, *arXiv e-prints* p. arXiv:2010.09005 82, 84, 150

Di Salvo, T., Sanna, A., Burderi, L., Papitto, A., Iaria, R., Gambino, A. F., and Riggio, A.: 2019, **483(1)**, 767 39, 90

Díaz Trigo, M., Altamirano, D., Dinçer, T., Miller-Jones, J. C. A., Russell, D. M., Sanna, A., Bailyn, C., Lewis, F., Migliari, S., and Rahoui, F.: 2018, **616**, A23 119

Díaz Trigo, M., Migliari, S., Miller-Jones, J. C. A., Rahoui, F., Russell, D. M., and Tudor, V.: 2017, **600**, A8 119, 124

Díaz Trigo, M., Parmar, A. N., Boirin, L., Méndez, M., and Kaastra, J. S.: 2006, **445(1)**, 179 40

Done, C. and Gierliński, M.: 2003, **342(4)**, 1041 27, 39

Done, C. and Gierliński, M.: 2006, **367**, 659 66

Done, C., Gierliński, M., and Kubota, A.: 2007, **15**, 1 37, 39, 40, 42

Drappeau, S., Malzac, J., Belmont, R., Gandhi, P., and Corbel, S.: 2015, **447(4)**, 3832 106, 107, 110, 111, 150

Drappeau, S., Malzac, J., Coriat, M., Rodriguez, J., Belloni, T. M., Belmont, R., Clavel, M., Chakravorty, S., Corbel, S., Ferreira, J., Gandhi, P., Henri, G., and Petrucci, P. O.: 2017, **466(4)**, 4272 41

Dunn, R. J. H., Fender, R. P., Körding, E. G., Belloni, T., and Cabanac, C.: 2010, **403(1)**, 61 126, 131

Eggleton, P. P.: 1976, in P. Eggleton, S. Mitton, and J. Whelan (eds.), *Structure and Evolution of Close Binary Systems*, Vol. 73 of *IAU Symposium*, p. 209 30

Eggleton, P. P.: 1983, **268**, 368 28

Egron, E., di Salvo, T., Burderi, L., Papitto, A., Barragán, L., Dauser, T., Wilms, J., D'Aì, A., Riggio, A., Iaria, R., and Robba, N. R.: 2011, **530**, A99 35

Elebert, P., Reynolds, M. T., Callanan, P. J., Hurley, D. J., Ramsay, G., Lewis, F., Russell, D. M., Nord, B., Kane, S. R., Depoy, D. L., and Hakala, P.: 2009, **395**, 884 77

Esin, A. A., McClintock, J. E., and Narayan, R.: 1997, **489(2)**, 865 33, 39, 126

Espinasse, M. and Fender, R.: 2018, **473(3)**, 4122 41

Evans, P. A., Beardmore, A. P., Page, K. L., Osborne, J. P., O'Brien, P. T., Willingale, R., Starling, R. L. C., Burrows, D. N., Godet, O., Vetere, L., Racusin, J., Goad, M. R., Wiersema, K., Angelini, L., Capalbi, M., Chincarini, G., Gehrels, N., Kennea, J. A., Margutti, R., Morris, D. C., Mountford, C. J., Pagani, C., Perri, M., Romano, P., and Tanvir, N.: 2009, **397(3)**, 1177 134

Evans, P. A., Beardmore, A. P., Page, K. L., Tyler, L. G., Osborne, J. P., Goad, M. R., O'Brien, P. T., Vetere, L., Racusin, J., Morris, D., Burrows, D. N., Capalbi, M., Perri, M., Gehrels, N., and Romano, P.: 2007, **469(1)**, 379 134

Fabbiano, G.: 2006, **44(1)**, 323 11

Fabian, A. C., Buisson, D. J., Kosec, P., Reynolds, C. S., Wilkins, D. R., Tomsick, J. A., Walton, D. J., Gandhi, P., Altamirano, D., Arzoumanian, Z., Cackett, E. M., Dyda, S., Garcia, J. A., Gendreau, K. C., Grefenstette, B. W., Homan, J., Kara, E., Ludlam, R. M., Miller, J. M., and Steiner, J. F.: 2020, **493(4)**, 5389 133

Fabian, A. C., Iwasawa, K., Reynolds, C. S., and Young, A. J.: 2000, **112**, 1145 35

Fabian, A. C. and Lasenby, A. N.: 2015, *Astrophysical Black Holes*, Vol. 28, pp 7–66 16

Fabian, A. C., Rees, M. J., Stella, L., and White, N. E.: 1989, **238**, 729 36

Falanga, M., Bonnet-Bidaud, J. M., Poutanen, J., Farinelli, R., Martocchia, A., Goldoni, P., Qu, J. L., Kuiper, L., and Goldwurm, A.: 2005, **436**, 647 90

Falanga, M., Kuiper, L., Poutanen, J., Galloway, D. K., Bozzo, E., Goldwurm, A., Hermsen, W., and Stella, L.: 2012, **545**, A26 90

Falcke, H., Körding, E., and Markoff, S.: 2004, **414**, 895 33

Farinelli, R., Titarchuk, L., Paizis, A., and Frontera, F.: 2008, **680**, 602 62

Fender, R.: 2010, *'Disc-Jet' Coupling in Black Hole X-Ray Binaries and Active Galactic Nuclei*, Vol. 794, p. 115 25

Fender, R. and Belloni, T.: 2004, **42(1)**, 317 27

Fender, R., Belloni, T., and Gallo, E.: 2005, **300(1-3)**, 1 42

Fender, R., Corbel, S., Tzioumis, T., McIntyre, V., Campbell-Wilson, D., Nowak, M., Sood, R., Hunstead, R., Harmon, A., Durouchoux, P., and Heindl, W.: 1999, **519(2)**, L165 41

Fender, R. P.: 2001, **322(1)**, 31 102

Fender, R. P. and Kuulkers, E.: 2001, **324(4)**, 923 41, 98

Fermi, E.: 1949, *Physical Review* **75(8)**, 1169 100

Fermi, E.: 1954, **119**, 1 100

Ferreira, J.: 1997, **319**, 340 128, 129

Ferreira, J. and Pelletier, G.: 1993, **276**, 625 127

Ferreira, J. and Pelletier, G.: 1995, **295**, 807 127

Ferreira, J., Petrucci, P. O., Henri, G., Saugé, L., and Pelletier, G.: 2006, **447(3)**, 813 12, 126, 127, 128, 131

Ferrigno, C., Bozzo, E., Del Santo, M., and Capitanio, F.: 2012, **537**, L7 42

Ferrigno, C., Bozzo, E., Falanga, M., Stella, L., Campana, S., Belloni, T., Israel, G. L., Pavan, L., Kuulkers, E., and Papitto, A.: 2011, **525**, A48 90

Fiocchi, M., Bazzano, A., Bruni, G., Ludlam, R., Natalucci, L., Onori, F., and Ubertini, P.: 2019, **887(1)**, 30 78

Fiocchi, M., Bazzano, A., Ubertini, P., Bird, A. J., Natalucci, L., and Sguera, V.: 2008, **492**, 557 107

Fiocchi, M., Bazzano, A., Ubertini, P., and Jean, P.: 2006, **651(1)**, 416 37

Fomalont, E. B., Geldzahler, B. J., and Bradshaw, C. F.: 2001, **558(1)**, 283 41

Ford, E. C., Kaaret, P., Chen, K., Tavani, M., Barret, D., Bloser, P., Grindlay, J., Harmon, B. A., Paciesas, W. S., and Zhang, S. N.: 1997, **486**, L47 107

Forman, W., Jones, C., Cominsky, L., Julien, P., Murray, S., Peters, G., Tananbaum, H., and Giacconi, R.: 1978, **38**, 357 107

Frank, J., King, A., and Raine, D. J.: 2002, *Accretion Power in Astrophysics: Third Edition* 26, 28, 30, 32

Fuchs, Y., Rodriguez, J., Mirabel, I. F., Chaty, S., Ribó, M., Dhawan, V., Goldoni, P., Sizun, P., Pooley, G. G., Zdziarski, A. A., Hannikainen, D. C., Kretschmar, P., Cordier, B., and Lund, N.: 2003, **409**, L35 40

Fujimoto, M. Y., Sztajno, M., Lewin, W. H. G., and van Paradijs, J.: 1987, **319**, 902 77

Gaia Collaboration, Brown, A. G. A., Vallenari, A., Prusti, T., de Bruijne, J. H. J., Babusiaux, C., Bailer-Jones, C. A. L., Biermann, M., Evans, D. W., Eyer, L., and et al.: 2018, **616**, A1 89

Gaia Collaboration, Prusti, T., de Bruijne, J. H. J., Brown, A. G. A., Vallenari, A., Babusiaux, C., Bailer-Jones, C. A. L., Bastian, U., Biermann, M., Evans, D. W., and et al.: 2016, **595**, A1 89

Gallo, E., Degenaar, N., and van den Eijnden, J.: 2018, **478(1)**, L132 41, 98

Gallo, E., Fender, R. P., and Pooley, G. G.: 2003, **344(1)**, 60 12, 111

Gallo, E., Fender, R. P., and Pooley, G. G.: 2004, *Nuclear Physics B Proceedings Supplements* **132**, 363 41

Galloway, D. K.: 2006, in F. D'Amico, J. Braga, and R. E. Rothschild (eds.), *The Transient Milky Way: A Perspective for MIRAX*, Vol. 840 of *American Institute of Physics Conference Series*, pp 50–54 85

Galloway, D. K., Chakrabarty, D., Morgan, E. H., and Remillard, R. A.: 2002, **576**, L137 81, 83

Galloway, D. K. and Cumming, A.: 2006, **652**, 559 77, 91

Galloway, D. K., Cumming, A., Kuulkers, E., Bildsten, L., Chakrabarty, D., and Rothschild, R. E.: 2004, **601**, 466 73, 74, 77

Galloway, D. K. and Keek, L.: 2017, *ArXiv e-prints* 57

Galloway, D. K., Markwardt, C. B., Morgan, E. H., Chakrabarty, D., and Strohmayer, T. E.: 2005a, **622**, L45 83

Galloway, D. K., Muno, M. P., Hartman, J. M., Psaltis, D., and Chakrabarty, D.: 2008, **179**, 360 57

Galloway, D. K., Psaltis, D., Chakrabarty, D., and Muno, M. P.: 2003, **590(2)**, 999 57

Galloway, D. K., Schulz, N. S., and Chakrabarty, D.: 2005b, *The Astronomer's Telegram* 517 90

Gambino, A. F., Iaria, R., Di Salvo, T., Del Santo, M., Burderi, L., Matranga, M., Pintore, F., Riggio, A., and Sanna, A.: 2016, **589**, A34 92

Gambino, A. F., Iaria, R., Di Salvo, T., Mazzola, S. M., Marino, A., Burderi, L., Riggio, A., Sanna, A., and D'Amico, N.: 2019, **625**, A92 64, 71

Gandhi, P., Bachetti, M., Dhillon, V. S., Fender, R. P., Hardy, L. K., Harrison, F. A., Littlefair, S. P., Malzac, J., Markoff, S., Marsh, T. R., Mooley, K., Stern, D., Tomsick, J. A., Walton, D. J., Casella, P., Vincentelli, F., Altamirano, D., Casares, J., Ceccobello, C., Charles, P. A., Ferrigno, C., Hynes, R. I., Knigge, C., Kuulkers, E., Pahari, M., Rahoui, F., Russell, D. M., and Shaw, A. W.: 2017, *Nature Astronomy* **1**, 859 41

Gandhi, P., Blain, A. W., Russell, D. M., Casella, P., Malzac, J., Corbel, S., D'Avanzo, P., Lewis, F. W., Markoff, S., Cadolle Bel, M., Goldoni, P., Wachter, S., Khangulyan, D., and Mainzer, A.: 2011, **740(1)**, L13 111

García, J., Dauser, T., Lohfink, A., Kallman, T. R., Steiner, J. F., McClintock, J. E., Brenneman, L., Wilms, J., Eikmann, W., Reynolds, C. S., and Tombesi, F.: 2014, **782**, 76 58

García, J., Dauser, T., Reynolds, C. S., Kallman, T. R., McClintock, J. E., Wilms, J., and Eikmann, W.: 2013, **768(2)**, 146 137

García, J. A., Steiner, J. F., McClintock, J. E., Remillard, R. A., Grinberg, V., and Dauser, T.: 2015, **813(2)**, 84 39

Garcia, M. R., Miller, J. M., McClintock, J. E., King, A. R., and Orosz, J.: 2003, **591(1)**, 388 98

Gehrels, N., Chincarini, G., Giommi, P., Mason, K. O., Nousek, J. A., Wells, A. A., White, N. E., Barthelmy, S. D., Burrows, D. N., Cominsky, L. R., Hurley, K. C., Marshall, F. E., Mészáros, P., Roming, P. W. A., Angelini, L., Barbier, L. M., Belloni, T., Campana, S., Caraveo, P. A., Chester, M. M., Citterio, O., Cline, T. L., Cropper, M. S., Cummings, J. R., Dean, A. J., Feigelson, E. D., Fenimore, E. E., Frail, D. A., Fruchter, A. S., Garmire, G. P., Gendreau, K., Ghisellini, G., Greiner, J., Hill, J. E., Hunsberger, S. D., Krimm, H. A., Kulkarni, S. R., Kumar, P., Lebrun, F., Lloyd-Ronning, N. M., Markwardt, C. B., Mattson, B. J., Mushotzky, R. F., Norris, J. P., Osborne, J., Paczynski, B., Palmer, D. M., Park, H.-S., Parsons, A. M., Paul, J., Rees, M. J., Reynolds, C. S., Rhoads, J. E., Sasseen, T. P., Schaefer, B. E., Short, A. T., Smale, A. P., Smith, I. A., Stella, L., Tagliaferri, G., Takahashi, T., Tashiro, M., Townsley, L. K., Tueller, J., Turner, M. J. L., Vietri, M., Voges, W., Ward, M. J., Willingale, R., Zerbi, F. M., and Zhang, W. W.: 2004, **611**, 1005 48

Ghosh, P. and Lamb, F. K.: 1979, **234**, 296 81

Giacconi, R.: 1974, in C. Dewitt-Morette (ed.), *Gravitational Radiation and Gravitational Collapse*, Vol. 64 of *IAU Symposium*, pp 147–180 24

Giacconi, R., Gursky, H., Paolini, F. R., and Rossi, B. B.: 1962, **9(11)**, 439 24

Gierliński, M. and Done, C.: 2002, **337(4)**, 1373 63

Gierliński, M., Done, C., and Page, K.: 2008, **388(2)**, 753 32, 114, 117

Gierliński, M., Zdziarski, A. A., Poutanen, J., Coppi, P. S., Ebisawa, K., and Johnson, W. N.: 1999, **309(2)**, 496 37

Gilfanov, M.: 2010, *X-Ray Emission from Black-Hole Binaries*, Vol. 794, p. 17 38, 43, 106

Gilfanov, M., Churazov, E., and Revnivtsev, M.: 1999, **352**, 182 39

Gilfanov, M., Churazov, E., and Revnivtsev, M.: 2000, in *Proceedings of 5-th Sino-German workshop on Astrohpysics*, Vol. 1, pp 114–123 38

Gillon, M., Jehin, E., Lederer, S. M., Delrez, L., de Wit, J., Burdanov, A., Van Grootel, V., Burgasser, A. J., Triaud, A. H. M. J., Opitom, C., Demory, B.-O., Sahu, D. K., Bardalez Gagliuffi, D., Magain, P., and Queloz, D.: 2016, **533(7602)**, 221 51

Gradshteyn, I. S., Ryzhik, I. M., Jeffrey, A., and Zwillinger, D.: 2000, *Table of Integrals, Series, and Products* 104

Grindlay, J. and Heise, J.: 1975, **2879**, 1 56

Gusinskaia, N. V., Deller, A. T., Hessels, J. W. T., Degenaar, N., Miller-Jones, J. C. A., Wijnands, R., Parikh, A. S., Russell, T. D., and Altamirano, D.: 2017, **470(2)**, 1871 41, 98

Güver, T. and Özel, F.: 2009, **400**, 2050 92

Haardt, F., Maraschi, L., and Ghisellini, G.: 1994, **432**, L95 40

Hameury, J.-M. and Lasota, J.-P.: 2016, **594**, A87 56

Harris, D. E., Forman, W., Gioa, I. M., Hale, J. A., Harnden, Jr., F. R., Jones, C., Karakashian, T., Maccacaro, T., McSweeney, J. D., Primnini, F. A., Schwarz, J., Tananbaum, H. D., and Thurman, J.: 1996, *VizieR Online Data Catalog* 9013 91

Harrison, F. A., Craig, W. W., Christensen, F. E., Hailey, C. J., Zhang, W. W., Boggs, S. E., Stern, D., Cook, W. R., Forster, K., Giommi, P., Grefenstette, B. W., Kim, Y., Kitaguchi, T., Koglin, J. E., Madsen, K. K., Mao, P. H., Miyasaka, H., Mori, K., Perri, M., Pivovaroff, M. J., Puccetti, S., Rana, V. R., Westergaard, N. J., Willis, J., Zoglauer, A., An, H., Bachetti, M., Barrière, N. M., Bellm, E. C., Bhalerao, V., Brejnholt, N. F., Fuerst, F., Liebe, C. C., Markwardt, C. B., Nynka, M., Vogel, J. K., Walton, D. J., Wik, D. R., Alexander, D. M., Cominsky, L. R., Hornschemeier, A. E., Hornstrup, A., Kaspi, V. M., Madejski, G. M., Matt, G., Molendi, S., Smith, D. M., Tomsick, J. A., Ajello, M., Ballantyne, D. R., Baloković, M., Barret, D., Bauer, F. E., Blandford, R. D., Brandt, W. N., Brenneman, L. W., Chiang, J., Chakrabarty, D., Chenevez, J., Comastri, A., Dufour, F., Elvis, M., Fabian, A. C., Farrah, D., Fryer, C. L., Gotthelf, E. V., Grindlay, J. E., Helfand, D. J., Krivonos, R., Meier, D. L., Miller, J. M., Natalucci, L., Ogle, P., Ofek, E. O., Ptak, A., Reynolds, S. P., Rigby, J. R., Tagliaferri, G., Thorsett, S. E., Treister, E., and Urry, C. M.: 2013, **770(2)**, 103 48

Harrison, T. E., McNamara, B. J., Bornak, J., Gelino, D. M., Wachter, S., Rupen, M. P., and Gelino, C. R.: 2011, **736(1)**, 54 114

Hartman, J. M., Patruno, A., Chakrabarty, D., Kaplan, D. L., Markwardt, C. B., Morgan, E. H., Ray, P. S., van der Klis, M., and Wijnands, R.: 2008, **675**, 1468 90, 95

Hasinger, G. and van der Klis, M.: 1989, **225**, 79 37

Hawking, S.: 1971, **152**, 75 20

Hawking, S. W.: 1975, *Communications in Mathematical Physics* **43(3)**, 199 20

Heindl, W. A. and Smith, D. M.: 1998, **506**, L35 90

Heinke, C. O., Altamirano, D., Cohn, H. N., Lugger, P. M., Budac, S. A., Servillat, M., Linares, M., Strohmayer, T. E., Markwardt, C. B., Wijnands, R., Swank, J. H., Knigge, C., Bailyn, C., and Grindlay, J. E.: 2010, **714**, 894 88, 90

Heinke, C. O., Bahramian, A., Degenaar, N., and Wijnands, R.: 2015, **447**, 3034 56, 88

Heinz, S.: 2004, **355(3)**, 835 111

Heinz, S. and Sunyaev, R. A.: 2003, **343(3)**, L59 129

Hessels, J. W. T., Ransom, S. M., Stairs, I. H., Freire, P. C. C., Kaspi, V. M., and Camilo, F.: 2006, *Science* **311(5769)**, 1901 33

Heyvaerts, J. and Norman, C.: 1989, **347**, 1055 101

Hoang, J., Molina, E., Lopez, M., Ribó, M., Blanch, O., Cortina, J., Maier, G., Park, N., De Naurois, M., de Oña Wilhelmi, E., Ernenwein, J. P., Malyshev, D., Mitchell, A., Ohm, S., and Zanin, R.: 2019, in *36th International Cosmic Ray Conference (ICRC2019)*, Vol. 36 of *International Cosmic Ray Conference*, p. 696 133

Homan, J. and Belloni, T.: 2005, **300**, 107 42

Homan, J., Wijnands, R., van der Klis, M., Belloni, T., van Paradijs, J., Klein-Wolt, M., Fender, R., and Méndez, M.: 2001, **132(2)**, 377 42

Iaria, R., Burderi, L., Di Salvo, T., La Barbera, A., and Robba, N. R.: 2001, **547(1)**, 412 117

Ingram, A. and Motta, S.: 2020, *arXiv e-prints* p. arXiv:2001.08758 44, 45

Ingram, A., van der Klis, M., Middleton, M., Done, C., Altamirano, D., Heil, L., Uttley, P., and Axelsson, M.: 2016, **461(2)**, 1967 39

in't Zand, J.: 2001, in A. Gimenez, V. Reglero, and C. Winkler (eds.), *Exploring the Gamma-Ray Universe*, Vol. 459 of *ESA Special Publication*, pp 463–470 77

in't Zand, J. J. M., Bozzo, E., Qu, J., Li, X.-D., Amati, L., Chen, Y., Donnarumma, I., Doroshenko, V., Drake, S. A., Hernanz, M., Jenke, P. A., Maccarone, T. J., Mahmoodifar, S., de Martino, D., De Rosa, A., Rossi, E. M., Rowlinson, A., Sala, G., Stratta, G., Tauris, T. M., Wilms, J., Wu, X., Zhou, P., Agudo, I., Altamirano, D., Atteia, J.-L., Andersson, N. A., Baglio, M. C., Ballantyne, D. R., Baykal, A., Behar, E., Belloni, T., Bhattacharyya, S., Bianchi, S., Bilous, A., Blay, P., Braga, J., Brandt, S., Brown, E. F., Bucciantini, N., Burderi, L., Cackett, E. M., Campana, R., Campana, S., Casella, P., Cavecchi, Y., Chambers, F., Chen, L., Chen, Y.-P., Chenevez, J., Chernyakova, M., Jin, C., Ciolfi, R., Costantini, E., Cumming, A., D'Aì, A., Dai, Z.-G., D'Ammando, F., De Pasquale, M., Degenaar, N., Del Santo, M., D'Elia, V., Di Salvo, T., Doyle, G., Falanga, M., Fan,

X., Ferdman, R. D., Feroci, M., Fraschetti, F., Galloway, D. K., Gambino, A. F., Gandhi, P., Ge, M., Gendre, B., Gill, R., Götz, D., Gouiffès, C., Grandi, P., Granot, J., Güdel, M., Heger, A., Heinke, C. O., Homan, J., Iaria, R., Iwasawa, K., Izzo, L., Ji, L., Jonker, P. G., José, J., Kaastra, J. S., Kalemci, E., Kargaltsev, O., Kawai, N., Keek, L., Komossa, S., Kreykenbohm, I., Kuiper, L., Kunneriath, D., Li, G., Liang, E.-W., Linares, M., Longo, F., Lu, F., Lutovinov, A. A., Malyshev, D., Malzac, J., Manousakis, A., McHardy, I., Mehdipour, M., Men, Y., Méndez, M., Mignani, R. P., Mikusincova, R., Miller, M. C., Miniutti, G., Motch, C., Nättilä, J., Nardini, E., Neubert, T., O'Brien, P. T., Orlandini, M., Osborne, J. P., Pacciani, L., Paltani, S., Paolillo, M., Papadakis, I. E., Paul, B., Pellizzoni, A., Peretz, U., Pérez Torres, M. A., Perinati, E., Prescod-Weinstein, C., Reig, P., Riggio, A., Rodriguez, J., Rodríguez-Gil, P., Romano, P., Różańska, A., Sakamoto, T., Salmi, T., Salvaterra, R., Sanna, A., Santangelo, A., Savolainen, T., Schanne, S., Schatz, H., Shao, L., Shearer, A., Shore, S. N., Stappers, B. W., Strohmayer, T. E., Suleimanov, V. F., Svoboda, J., Thielemann, F. K., Tombesi, F., Torres, D. F., Torresi, E., Turriziani, S., Vacchi, A., Vercellone, S., Vink, J., Wang, J.-M., Wang, J., Watts, A. L., Weng, S., Weinberg, N. N., Wheatley, P. J., Wijnands, R., Woods, T. E., Woosley, S. E., Xiong, S., Xu, Y., Yan, Z., Younes, G., Yu, W., Yuan, F., Zampieri, L., Zane, S., Zdziarski, A. A., Zhang, S.-N., Zhang, S., Zhang, S., Zhang, X., and Zingale, M.: 2019a, *Science China Physics, Mechanics, and Astronomy* **62(2)**, 29506 151

in't Zand, J. J. M., Cumming, A., van der Sluys, M. V., Verbunt, F., and Pols, O. R.: 2005, **441**, 675 57, 77

in't Zand, J. J. M., Jonker, P. G., Bassa, C. G., Markwardt, C. B., and Levine, A. M.: 2009, **506**, 857 56

in't Zand, J. J. M., Jonker, P. G., and Markwardt, C. B.: 2007, **465**, 953 56

in't Zand, J. J. M., Kries, M. J. W., Palmer, D. M., and Degenaar, N.: 2019b, **621**, A53 72

Irwin, J. A., Brink, T. G., Bregman, J. N., and Roberts, T. P.: 2010, **712(1)**, L1 20

Israel, G. L., Papitto, A., Esposito, P., Stella, L., Zampieri, L., Belfiore, A., Rodríguez Castillo, G. A., De Luca, A., Tiengo, A., Haberl, F., Greiner, J., Salvaterra, R., Sandrelli, S., and Lisini, G.: 2017, **466(1)**, L48 27

Jacquemin-Ide, J., Ferreira, J., and Lesur, G.: 2019, **490(3)**, 3112 98

Jamil, O., Fender, R. P., and Kaiser, C. R.: 2010, **401(1)**, 394 105, 106, 123

Kaaret, P., Feng, H., and Roberts, T. P.: 2017, **55(1)**, 303 27

Kaaret, P., Morgan, E. H., Vanderspek, R., and Tomsick, J. A.: 2006, **638**, 963 83

Kaastra, J.: 1999, *Iron Line Spectroscopy of Clusters of Galaxies*, Chandra Proposal 34

Kaastra, J. S. and Bleeker, J. A. M.: 2016, **587**, A151 54, 134

Kaiser, C. R.: 2006, **367(3)**, 1083 101, 102, 105

Kaiser, C. R., Sunyaev, R., and Spruit, H. C.: 2000, **356**, 975 105

Kajava, J. J. E., Motta, S. E., Sanna, A., Veledina, A., Del Santo, M., and Segreto, A.: 2019, **488(1)**, L18 133, 147

Kalemci, E., Tomsick, J. A., Rothschild, R. E., Pottschmidt, K., Corbel, S., and Kaaret, P.: 2006, **639(1)**, 340 44

Kallman, T. R., Palmeri, P., Bautista, M. A., Mendoza, C., and Krolik, J. H.: 2004, **155(2)**, 675 40

Kalogera, V. and Baym, G.: 1996, **470**, L61 16

Kara, E., Steiner, J. F., Fabian, A. C., Cackett, E. M., Uttley, P., Remillard, R. A., Gendreau, K. C., Arzoumanian, Z., Altamirano, D., Eikenberry, S., Enoto, T., Homan, J., Neilsen, J., and Stevens, A. L.: 2019, **565(7738)**, 198 39, 133, 138, 140, 146

Kawai, N. and Suzuki, M.: 2005, *The Astronomer's Telegram* 534 91

Kawamuro, T., Negoro, H., Yoneyama, T., Ueno, S., Tomida, H., Ishikawa, M., Sugawara, Y., Isobe, N., Shimomukai, R., Mihara, T., Sugizaki, M., Nakahira, S., Iwakiri, W., Yatabe, F., Takao, Y., Matsuoka, M., Kawai, N., Sugita, S., Yoshii, T., Tachibana, Y., Harita, S., Morita, K., Yoshida, A., Sakamoto, T., Serino, M., Kawakubo, Y., Kitaoka, Y., Hashimoto, T., Tsunemi, H., Nakajima, M., Kawase, T., Sakamaki, A., Maruyama, W., Ueda, Y., Hori, T., Tanimoto, A., Oda, S., Morita, T., Yamada, S., Tsuboi, Y., Nakamura, Y., Sasaki, R., Kawai, H., Sato, T., Yamauchi, M., Hanyu, C., Hidaka, K., Yamaoka, K., and Shidatsu, M.: 2018, *The Astronomer's Telegram* **11399**, 1 133

Keek, L., Iwakiri, W., Serino, M., Ballantyne, D. R., in't Zand, J. J. M., and Strohmayer, T. E.: 2017, **836**, 111 88, 90, 91

King, A. R., Pringle, J. E., and Livio, M.: 2007, **376(4)**, 1740 31

King, A. R. and Wijnands, R.: 2006, **366**, L31 56, 77

Kolehmainen, M., Done, C., and Díaz Trigo, M.: 2011, **416**, 311 66

Körding, E., Rupen, M., Knigge, C., Fender, R., Dhawan, V., Templeton, M., and Muxlow, T.: 2008, *Science* **320(5881)**, 1318 98

Körding, E. G., Jester, S., and Fender, R.: 2006, **372(3)**, 1366 41, 98, 130

Kraft, R. P., Mathews, J., and Greenstein, J. L.: 1962, **136**, 312 29

Krimm, H. A., Barthelmy, S. D., Baumgartner, W., Cummings, J., Gehrels, N., Lien, A. Y., Markwardt, C. B., Palmer, D., Sakamoto, T., Stamatikos, M., and Ukwatta, T.: 2015a, *The Astronomer's Telegram* 6997 58

Krimm, H. A., Kennea, J. A., Siegel, M. H., and Sbarufatti, B.: 2015b, *The Astronomer's Telegram* 7039 58, 72

Krimm, H. A., Markwardt, C. B., Deloye, C. J., Romano, P., Chakrabarty, D., Campana, S., Cummings, J. R., Galloway, D. K., Gehrels, N., Hartman, J. M., Kaaret, P., Morgan, E. H., and Tueller, J.: 2007, **668**, L147 83, 90

Kubota, A. and Done, C.: 2004, **353(3)**, 980 37

Kubota, A., Makishima, K., and Ebisawa, K.: 2001, **560(2)**, L147 37

Kubota, A., Tanaka, Y., Makishima, K., Ueda, Y., Dotani, T., Inoue, H., and Yamaoka, K.: 1998, **50**, 667 63

Kuulkers, E., den Hartog, P. R., in't Zand, J. J. M., Verbunt, F. W. M., Harris, W. E., and Cocchi, M.: 2003, **399**, 663 27, 57, 74

Kuulkers, E., in't Zand, J. J. M., Atteia, J.-L., Levine, A. M., Brandt, S., Smith, D. A., Linares, M., Falanga, M., Sánchez-Fernández, C., Markwardt, C. B., Strohmayer, T. E., Cumming, A., and Suzuki, M.: 2010, **514**, A65 107

Lampe, N., Heger, A., and Galloway, D. K.: 2016, **819(1)**, 46 77

Landau, L. D. and Lifshitz, E. M.: 1975, *The classical theory of fields* 29

Lanzuisi, G., Perna, M., Comastri, A., Cappi, M., Dadina, M., Marinucci, A., Masini, A., Matt, G., Vagnetti, F., Vignali, C., Ballantyne, D. R., Bauer, F. E., Boggs, S. E., Brandt, W. N., Brusa, M., Christensen, F. E., Craig, W. W., Fabian, A. C., Farrah, D., Hailey, C. J., Harrison, F. A., Luo, B., Piconcelli, E., Puccetti, S., Ricci, C., Saez, C., Stern, D., Walton, D. J., and Zhang, W. W.: 2016, **590**, A77 54

Laor, A.: 1991, **376**, 90 137

Lasota, J.-P.: 2001, **45(7)**, 449 42

Leahy, D. A., Darbro, W., Elsner, R. F., Weisskopf, M. C., Sutherland, P. G., Kahn, S., and Grindlay, J. E.: 1983, **266**, 160 109

Lewin, W. H. G., van Paradijs, J., and Taam, R. E.: 1993, **62**, 223 58, 74

Lewis, F., Russell, D. M., Jonker, P. G., Linares, M., Tudose, V., Roche, P., Clark, J. S., Torres, M. A. P., Maitra, D., Bassa, C. G., Steeghs, D., Patruno, A., Migliari, S., Wijnands, R., Nelemans, G., Kewley, L. J., Stroud, V. E., Modjaz, M., Bloom, J. S., Blake, C. H., and Starr, D.: 2010, **517**, A72 114

Lin, D., Remillard, R. A., and Homan, J.: 2007, **667(2)**, 1073 37, 39

Lin, D., Strader, J., Carrasco, E. R., Page, D., Romanowsky, A. J., Homan, J., Irwin, J. A., Remillard, R. A., Godet, O., Webb, N. A., Baumgardt, H., Wijnands, R., Barret, D., Duc, P.-A., Brodie, J. P., and Gwyn, S. D. J.: 2018, *Nature Astronomy* **2**, 656 20

Linares, M., Altamirano, D., Watts, A., Strohmayer, T., Chakrabarty, D., Patruno, A., van der Klis, M., Wijnands, R., Casella, P., Armas-Padilla, M., Cavecchi, Y., Degenaar, N., Kalamkar, M., Kaur, R., Yang, Y., and Rea, N.: 2011, *The Astronomer's Telegram* 3568 91

Linares, M., Bahramian, A., Heinke, C., Wijnands, R., Patruno, A., Altamirano, D., Homan, J., Bogdanov, S., and Pooley, D.: 2014, **438**, 251 87

Linares, M., Wijnands, R., van der Klis, M., Krimm, H., Markwardt, C. B., and Chakrabarty, D.: 2008, **677(1)**, 515 90, 124

Liska, M., Hesp, C., Tchekhovskoy, A., Ingram, A., van der Klis, M., and Markoff, S.: 2018, **474(1)**, L81 127

Longair, M.: 2011, *High Energy Astrophysics*, Cambridge University Press 16, 17, 18, 19, 20, 100, 104

Ludlam, R. M., Miller, J. M., Bachetti, M., Barret, D., Bostrom, A. C., Cackett, E. M., Degenaar, N., Di Salvo, T., Natalucci, L., Tomsick, J. A., Paerels, F., and Parker, M. L.: 2017, **836**, 140 35

Ludlam, R. M., Miller, J. M., Barret, D., Cackett, E. M., Coughenour, B. M., Dauser, T., Degenaar, N., García, J. A., Harrison, F. A., and Paerels, F.: 2019, **873(1)**, 99 107, 124

Ludlam, R. M., Miller, J. M., Cackett, E. M., Fabian, A. C., Bachetti, M., Parker, M. L., Tomsick, J. A., Barret, D., Natalucci, L., Rana, V., and Harrison, F. A.: 2016, **824**, 37 58, 59, 60, 62, 63, 69, 71, 72

Lund, N., Budtz-Jørgensen, C., Westergaard, N. J., Brand t, S., Rasmussen, I. L., Hornstrup, A., Oxborrow, C. A., Chenevez, J., Jensen, P. A., Laursen, S., Andersen, K. H., Mogensen, P. B., Rasmussen, I., Omø, K., Pedersen, S. M., Polny, J., Andersson, H., Andersson, T., Kämäräinen, V., Vilhu, O., Huovelin, J., Maisala, S., Morawski, M., Juchnikowski, G., Costa, E., Feroci, M., Rubini, A., Rapisarda, M., Morelli, E., Carassiti, V., Frontera, F., Pelliciari, C., Loffredo, G., Martínez Núñez, S., Reglero, V., Velasco, T., Larsson, S., Svensson, R., Zdziarski, A. A., Castro-Tirado, A., Attina, P., Goria, M., Giulianelli, G., Cordero, F., Rezazad, M., Schmidt, M., Carli, R., Gomez, C., Jensen, P. L., Sarri, G., Tiemon, A., Orr, A., Much, R., Kretschmar, P., and Schnopper, H. W.: 2003, **411**, L231 49

Luo, Q. and Melrose, D. B.: 1992, **258(3)**, 616 18

Lyubarsky, Y.: 2010, **725(2)**, L234 105

Maccarone, T. J. and Patruno, A.: 2013, **428**, 1335 56

Madej, O. K., García, J., Jonker, P. G., Parker, M. L., Ross, R., Fabian, A. C., and Chenevez, J.: 2014, **442(2)**, 1157 107

Madsen, K. K., Grefenstette, B. W., Pike, S., Miyasaka, H., Brightman, M., Forster, K., and Harrison, F. A.: 2020, *arXiv e-prints* p. arXiv:2005.00569 134

Magdziarz, P. and Zdziarski, A. A.: 1995, **273**, 837 63

Malzac, J.: 2013, **429**, L20 12, 105, 106, 113, 123, 149

Malzac, J.: 2014, **443(1)**, 299 105, 106, 111

Malzac, J., Belmont, R., and Fabian, A. C.: 2009, **400(3)**, 1512 39

Malzac, J. and Celotti, A.: 2002, **335(1)**, 23 139

Malzac, J., Kalamkar, M., Vincentelli, F., Vue, A., Drappeau, S., Belmont, R., Casella, P., Clavel, M., Corbel, S., Coriat, M., Dornic, D., Ferreira, J., Henri, G., Maccarone, T. J., Marcowith, A., O'Brien, K., Péault, M., Petrucci, P.-O., Rodriguez, J., Russell, D. M., and Uttley, P.: 2018, **480(2)**, 2054 107

Malzac, J., Petrucci, P. O., Jourdain, E., Cadolle Bel, M., Sizun, P., Pooley, G., Cabanac, C., Chaty, S., Belloni, T., and Rodriguez, J.: 2006, **448(3)**, 1125 37

Marcel, G., Cangemi, F., Rodriguez, J., Neilsen, J., Ferreira, J., Petrucci, P. O., Malzac, J., Barnier, S., and Clavel, M.: 2020, *arXiv e-prints* p. arXiv:2005.10359 126, 131

Marcel, G., Ferreira, J., Clavel, M., Petrucci, P. O., Malzac, J., Corbel, S., Rodriguez, J., Belmont, R., Coriat, M., Henri, G., and Cangemi, F.: 2019, **626**, A115 126, 129, 131, 133, 147

Marcel, G., Ferreira, J., Petrucci, P. O., Belmont, R., Malzac, J., Clavel, M., Henri, G., Coriat, M., Corbel, S., Rodriguez, J., Loh, A., and Chakravorty, S.: 2018a, **617**, A46 126, 129, 132, 137

Marcel, G., Ferreira, J., Petrucci, P. O., Henri, G., Belmont, R., Clavel, M., Malzac, J., Coriat, M., Corbel, S., Rodriguez, J., Loh, A., Chakravorty, S., and Drappeau, S.: 2018b, **615**, A57 126, 127, 129, 130, 137, 149

Marino, A., Del Santo, M., Cocchi, M., D'Aı, A., Segreto, A., Ferrigno, C., Di Salvo, T., Malzac, J., Iaria, R., and Burderi, L.: 2019a, **490(2)**, 2300 59, 118

Marino, A., Di Salvo, T., Burderi, L., Sanna, A., Riggio, A., Papitto, A., Del Santo, M., Gambino, A. F., Iaria, R., and Mazzola, S. M.: 2019b, **627**, A125 84

Marino, A., Di Salvo, T., Gambino, A. F., Iaria, R., Burderi, L., Matranga, M., Sanna, A., and Riggio, A.: 2017, **603**, A137 84, 85, 88, 89, 93

Marino, A., Malzac, J., Del Santo, M., Migliari, S., Belmont, R., Di Salvo, T., Russell, D. M., Lopez Miralles, J., Perucho, M., D'Aì, A., Iaria, R., and Burderi, L.: 2020, **498(3)**, 3351 103, 104, 107, 110, 114

Markoff, S.: 2010, *From Multiwavelength to Mass Scaling: Accretion and Ejection in Microquasars and AGN*, Vol. 794, p. 143 102

Markwardt, C. B., Krimm, H., Wijnands, R., and Swank, J. H.: 2008, *The Astronomer's Telegram* **1709**, 1 90

Markwardt, C. B., Miller, J. M., and Wijnands, R.: 2002a, *The Astronomer's Telegram* 110 90

Markwardt, C. B., Strohmayer, T. E., and Swank, J. H.: 2003, *The Astronomer's Telegram* 164 83

Markwardt, C. B., Swank, J. H., Strohmayer, T. E., in 't Zand, J. J. M., and Marshall, F. E.: 2002b, **575**, L21 83

Marshall, D. J., Robin, A. C., Reylé, C., Schultheis, M., and Picaud, S.: 2006, **453**, 635 91, 92, 93

Martin, R. G., Nixon, C. J., Pringle, J. E., and Livio, M.: 2019, **70**, 7 31

Martinez, J. G., Stovall, K., Freire, P. C. C., Deneva, J. S., Jenet, F. A., McLaughlin, M. A., Bagchi, M., Bates, S. D., and Ridolfi, A.: 2015, **812**, 143 85, 93

Mas-Hesse, J. M., Giménez, A., Culhane, J. L., Jamar, C., McBreen, B., Torra, J., Hudec, R., Fabregat, J., Meurs, E., Swings, J. P., Alcacera, M. A., Balado, A., Beiztegui, R., Belenguer, T., Bradley, L., Caballero, M. D., Cabo, P., Defise, J. M., Díaz, E., Domingo, A., Figueras, F., Figueroa, I., Hanlon, L., Hroch, F., Hudcova, V., García, T., Jordan, B., Jordi, C., Kretschmar, P., Laviada, C., March, M., Martín, E., Mazy, E., Menéndez, M., Mi, J. M., de Miguel, E., Muñoz, T.,

Nolan, K., Olmedo, R., Plesseria, J. Y., Polcar, J., Reina, M., Renotte, E., Rochus, P., Sánchez, A., San Martín, J. C., Smith, A., Soldan, J., Thomas, P., Timón, V., and Walton, D.: 2003, **411**, L261 49

Mata Sánchez, D., Muñoz-Darias, T., Casares, J., and Jiménez-Ibarra, F.: 2017, **464**, L41 83

Matt, G., Perola, G. C., and Piro, L.: 1991, **247**, 25 40

Matthews, J., Bell, A., and Blundell, K.: 2020, *arXiv e-prints* p. arXiv:2003.06587 100

Mazzola, S. M., Iaria, R., Di Salvo, T., Del Santo, M., Sanna, A., Gambino, A. F., Riggio, A., Segreto, A., Burderi, L., Santangelo, A., and D'Amico, N.: 2019, **621**, A89 39, 63

McKinney, J. C. and Uzdensky, D. A.: 2012, **419(1)**, 573 101

Meier, D. L.: 2005, **300(1-3)**, 55 33

Meier, D. L.: 2011, in G. E. Romero, R. A. Sunyaev, and T. Belloni (eds.), *Jets at All Scales*, Vol. 275 of *IAU Symposium*, pp 13–23 100

Meier, D. L., Koide, S., and Uchida, Y.: 2001, *Science* **291(5501)**, 84 99

Melrose, D. B., Rafat, M. Z., and Mastrano, A.: 2020, *arXiv e-prints* p. arXiv:2006.15243 18

Méndez, M. and van der Klis, M.: 1997, **479**, 926 44

Merloni, A., Predehl, P., Becker, W., Böhringer, H., Boller, T., Brunner, H., Brusa, M., Dennerl, K., Freyberg, M., Friedrich, P., Georgakakis, A., Haberl, F., Hasinger, G., Meidinger, N., Mohr, J., Nandra, K., Rau, A., Reiprich, T. H., Robrade, J., Salvato, M., Santangelo, A., Sasaki, M., Schwope, A., Wilms, J., and German eROSITA Consortium, t.: 2012, *arXiv e-prints* p. arXiv:1209.3114 151

Mészáros, P. and Rees, M. J.: 1997, **482(1)**, L29 98

Meyer-Hofmeister, E., Liu, B. F., and Meyer, F.: 2005, **432(1)**, 181 126

Migliari, S. and Fender, R. P.: 2006, **366(1)**, 79 118

Migliari, S., Fender, R. P., Rupen, M., Jonker, P. G., Klein-Wolt, M., Hjellming, R. M., and van der Klis, M.: 2003, **342(4)**, L67 41, 98

Migliari, S., Fender, R. P., Rupen, M., Wachter, S., Jonker, P. G., Homan, J., and van der Klis, M.: 2004, **351(1)**, 186 41, 98

Migliari, S., Miller-Jones, J. C. A., and Russell, D. M.: 2011, **415(3)**, 2407 41, 99

Migliari, S., Tomsick, J. A., Miller-Jones, J. C. A., Heinz, S., Hynes, R. I., Fender, R. P., Gallo, E., Jonker, P. G., and Maccarone, T. J.: 2010, **710**, 117 107, 108, 109, 111, 114, 117, 118, 124

Miller, J. M., Homan, J., Steeghs, D., Rupen, M., Hunstead, R. W., Wijnands, R., Charles, P. A., and Fabian, A. C.: 2006, **653(1)**, 525 39

Miller-Jones, J. C. A., Moin, A., Tingay, S. J., Reynolds, C., Phillips, C. J., Tzioumis, A. K., Fender, R. P., McCallum, J. N., Nicolson, G. D., and Tudose, V.: 2012, **419(1)**, L49 98

Miniutti, G., Fabian, A. C., Goyder, R., and Lasenby, A. N.: 2003, **344(2)**, L22 139

Misner, C. W., Thorne, K. S., and Wheeler, J. A.: 1973, *Gravitation* 20

Mitsuda, K., Inoue, H., Koyama, K., Makishima, K., Matsuoka, M., Ogawara, Y., Suzuki, K., Tanaka, Y., Shibazaki, N., and Hirano, T.: 1984, **36**, 741 32, 63

Mitsuda, K., Inoue, H., Nakamura, N., and Tanaka, Y.: 1989, **41**, 97 39

Miyamoto, S., Kitamoto, S., Hayashida, K., and Egoshi, W.: 1995, **442**, L13 42

Morrison, P.: 1969, **157**, L73 100

Muñoz-Darias, T., Fender, R. P., Motta, S. E., and Belloni, T. M.: 2014, **443(4)**, 3270 40, 42, 43, 44, 72, 98, 107

Muñoz-Darias, T., Motta, S., and Belloni, T. M.: 2011, **410(1)**, 679 42

Mukherjee, D., Bult, P., van der Klis, M., and Bhattacharya, D.: 2015, **452(4)**, 3994 84

Muno, M. P., Pfahl, E., Baganoff, F. K., Brandt, W. N., Ghez, A., Lu, J., and Morris, M. R.: 2005, **622**, L113 56, 77

Narayan, R. and Yi, I.: 1995, **452**, 710 33

Nayakshin, S.: 2000, **534(2)**, 718 40

Negoro, H., Sugimoto, J., Mihara, T., Ueno, S., Tomida, H., Nakahira, S., Kimura, M., Ishikawa, M., Nakagawa, Y. E., Sugizaki, M., Serino, M., Morii, M., Takagi, T., Yoshikawa, A., Matsuoka, M., Kawai, N., Yoshii, T., Tachibana, Y., Yoshida, A., Sakamoto, T., Kawakubo, Y., Ohtsuki, H., Tsunemi, H., Uchida, D., Nakajima, M., Fukushima, K., Onodera, T., Suzuki, K., Namba, T., Fujita, M., Honda, F., Ueda, Y., Shidatsu, M., Kawamuro, T., Hori, T., Tsuboi, Y., Kawagoe, A., Yamauchi, M., Morooka, Y., Itoh, D., Yamaoka, K., and MAXI Team: 2015, *The Astronomer's Telegram* 7008 58

Nelemans, G., Jonker, P. G., Marsh, T. R., and van der Klis, M.: 2004, **348(1)**, L7 108

Nelson, L. A. and Rappaport, S.: 2003, **598**, 431 30, 86

Ng, M., Ray, P. S., Strohmayer, T. E., Bult, P. M., Chakrabarty, D., Altamirano, D., Jaisawal, G. K., Malacaria, C., Bogdanov, S., Gendreau, K. C., and Arzoumanian, Z.: 2020, *The Astronomer's Telegram* **14124**, 1 81

Nishiyama, S., Nagata, T., Tamura, M., Kand ori, R., Hatano, H., Sato, S., and Sugitani, K.: 2008, **680**, 1174 92

Nowak, M. A.: 1995, **107**, 1207 37

Oda, H., Machida, M., Nakamura, K. E., Matsumoto, R., and Narayan, R.: 2012, **64**, 15 126

Ootes, L. S., Watts, A. L., Galloway, D. K., and Wijnands, R.: 2017, **834(1)**, 21 57

Ootes, L. S., Wijnands, R., Page, D., and Degenaar, N.: 2018, **477**, 2900 88

Ortolani, S., Barbuy, B., and Bica, E.: 1994, **108**, 653 91

Ostriker, J. P. and Gunn, J. E.: 1969, **157**, 1395 19

Özel, F. and Freire, P.: 2016, **54**, 401 18, 57, 85, 93

Özel, F., Psaltis, D., Narayan, R., and Santos Villarreal, A.: 2012, **757**, 55 85, 111

Pacini, F.: 1967, **216(5115)**, 567 17

Paczyński, B.: 1971, **9**, 183 85

Paice, J. A., Gandhi, P., Shahbaz, T., Uttley, P., Arzoumanian, Z., Charles, P. A., Dhillon, V. S., Gendreau, K. C., Littlefair, S. P., Malzac, J., Markoff, S., Marsh, T. R., Misra, R., Russell, D. M., and Veledina, A.: 2019, **490(1)**, L62 133

Paizis, A., Farinelli, R., Titarchuk, L., Courvoisier, T. J. L., Bazzano, A., Beckmann, V., Frontera, F., Goldoni, P., Kuulkers, E., and Mereghetti, S.: 2006, **459(1)**, 187 37

Papitto, A., Ambrosino, F., Stella, L., Torres, D., Coti Zelati, F., Ghedina, A., Meddi, F., Sanna, A., Casella, P., Dallilar, Y., Eikenberry, S., Israel, G. L., Onori, F., Piranomonte, S., Bozzo, E., Burderi, L., Campana, S., de Martino, D., Di Salvo, T., Ferrigno, C., Rea, N., Riggio, A., Serrano, S., Veledina, A., and Zampieri, L.: 2019, **882(2)**, 104 82, 88

Papitto, A., Bozzo, E., Ferrigno, C., Belloni, T., Burderi, L., di Salvo, T., Riggio, A., D'Aì, A., and Iaria, R.: 2011a, **535**, L4 83

Papitto, A., Bozzo, E., Ferrigno, C., Burderi, L., di Salvo, T., and Riggio, A.: 2011b, *The Astronomer's Telegram* 3736 90

Papitto, A., Bozzo, E., Sanchez-Fernandez, C., Romano, P., Torres, D. F., Ferrigno, C., Kajava, J. J. E., and Kuulkers, E.: 2016, **596**, A71 90

Papitto, A., D'Aì, A., Di Salvo, T., Egron, E., Bozzo, E., Burderi, L., Iaria, R., Riggio, A., and Menna, M. T.: 2013a, **429**, 3411 90

Papitto, A., de Martino, D., Belloni, T. M., Burgay, M., Pellizzoni, A., Possenti, A., and Torres, D. F.: 2015, **449**, L26 82, 88

Papitto, A., di Salvo, T., Burderi, L., Menna, M. T., Lavagetto, G., and Riggio, A.: 2007, **375**, 971 90, 187, 189

Papitto, A., Ferrigno, C., Bozzo, E., Rea, N., Pavan, L., Burderi, L., Burgay, M., Campana, S., di Salvo, T., Falanga, M., Filipović, M. D., Freire, P. C. C., Hessels, J. W. T., Possenti, A., Ransom, S. M., Riggio, A., Romano, P., Sarkissian, J. M., Stairs, I. H., Stella, L., Torres, D. F., Wieringa, M. H., and Wong, G. F.: 2013b, **501**, 517 82, 83, 87, 92

Papitto, A., Menna, M. T., Burderi, L., di Salvo, T., and Riggio, A.: 2008, **383**, 411 91, 92

Papitto, A., Riggio, A., di Salvo, T., Burderi, L., D'Aì, A., Iaria, R., Bozzo, E., and Menna, M. T.: 2010, **407**, 2575 83, 90

Parfrey, K., Spitkovsky, A., and Beloborodov, A. M.: 2016, **822(1)**, 33 99, 123, 151

Parfrey, K. and Tchekhovskoy, A.: 2017, **851(2)**, L34 84

Parikh, A. S., Wijnands, R., Degenaar, N., Altamirano, D., Patruno, A., Gusinskaia, N. V., and Hessels, J. W. T.: 2017, **468**, 3979 39, 59, 70, 78

Parker, M. L., Tomsick, J. A., Miller, J. M., Yamaoka, K., Lohfink, A., Nowak, M., Fabian, A. C., Alston, W. N., Boggs, S. E., Christensen, F. E., Craig, W. W., Fürst, F., Gandhi, P., Grefenstette, B. W., Grinberg, V., Hailey, C. J., Harrison, F. A., Kara, E., King, A. L., Stern, D., Walton, D. J., Wilms, J., and Zhang, W. W.: 2015, **808(1)**, 9 39

Patruno, A.: 2012, **753(1)**, L12 82

Patruno, A., Altamirano, D., Hessels, J. W. T., Casella, P., Wijnands, R., and van der Klis, M.: 2009a, **690(2)**, 1856 82

Patruno, A., Altamirano, D., Watts, A., Armas Padilla, M., Cavecchi, Y., Degenaar, N., Kalamkar, M., Kaur, R., Soleri, P., Yang, Y. J., van der Klis, M., Wijnands, R., Casella, P., Linares, M., Rea, N., Heinke, C. O., and Pooley, D.: 2010, *The Astronomer's Telegram* 2407 90

Patruno, A., Archibald, A. M., Hessels, J. W. T., Bogdanov, S., Stappers, B. W., Bassa, C. G., Janssen, G. H., Kaspi, V. M., Tendulkar, S., and Lyne, A. G.: 2014, **781**, L3 87

Patruno, A. and D'Angelo, C.: 2013, **771**, 94 89, 90

Patruno, A., Markwardt, C. B., Strohmayer, T. E., Swank, J. H., Smith, S. E., and Pereira, D.: 2009b, *The Astronomer's Telegram* 2130 90

Patruno, A. and Watts, A. L.: 2012, *arXiv e-prints* p. arXiv:1206.2727 81

Patterson, J., Brincat, S., Stone, G., Hambsch, J., Richmond, M., Kemp, J., Monard, B., Lemay, D., Dvorak, S., Ulowetz, J., Vanmunster, T., Tordai, T., Myers, G., Campbell, T., Rock, J., Miller, I., Slauson, D., Cejudo, D., Lewin, P., Roberts, G., Epstein-Martin, M., and Smith, M.: 2018, *The Astronomer's Telegram* **11756**, 1 133

Paxton, B., Bildsten, L., Dotter, A., Herwig, F., Lesaffre, P., and Timmes, F.: 2010, *MESA: Modules for Experiments in Stellar Astrophysics* 150

Péault, M., Malzac, J., Coriat, M., Russell, T. D., Koljonen, K. I. I., Belmont, R., Corbel, S., Drappeau, S., Ferreira, J., Petrucci, P. O., Rodriguez, J., and Russell, D. M.: 2019, **482(2)**, 2447 106, 107, 110, 111, 114, 119, 123, 150

Pe'er, A.: 2014, **183(1-4)**, 371 98, 105, 114

Penrose, R.: 1969, *Nuovo Cimento Rivista Serie* **1**, 252 100

Pepe, C., Vila, G. S., and Romero, G. E.: 2015, **584**, A95 99

Petrucci, P. O., Ponti, G., Matt, G., Longinotti, A. L., Malzac, J., Mouchet, M., Boisson, C., Maraschi, L., Nandra, K., and Ferrando, P.: 2007, **470(3)**, 889 146

Pinto, C., Mehdipour, M., Walton, D. J., Middleton, M. J., Roberts, T. P., Fabian, A. C., Guainazzi, M., Soria, R., Kosec, P., and Ness, J. U.: 2020, **491(4)**, 5702 40

Pintore, F., Sanna, A., Di Salvo, T., Del Santo, M., Riggio, A., D'Aì, A., Burderi, L., Scarano, F., and Iaria, R.: 2016, **457**, 2988 82, 90

Pintore, F., Sanna, A., Riggio, A., Di Salvo, T., Mereghetti, S., Bozzo, E., Sánchez-Fernández, C., Burderi, L., and Iaria, R.: 2018, *Monthly Notices of the Royal Astronomical Society* **479(3)**, 4084 90

Piraino, S., Santangelo, A., Ford, E. C., and Kaaret, P.: 1999, **349**, L77 107, 117, 124

Ponti, G., Muñoz-Darias, T., and Fender, R. P.: 2014, **444(2)**, 1829 40

Pottschmidt, K., Wilms, J., Nowak, M. A., Pooley, G. G., Gleissner, T., Heindl, W. A., Smith, D. M., Remillard, R., and Staubert, R.: 2003, **407**, 1039 44

Poutanen, J. and Coppi, P. S.: 1998, *Physica Scripta Volume T* **77**, 57 37

Poutanen, J., Veledina, A., and Zdziarski, A. A.: 2018, **614**, A79 39

Press, W. H.: 1978, *Comments on Astrophysics* **7(4)**, 103 106

Proga, D.: 2003, **585(1)**, 406 40

Psaltis, D.: 2008, **688(2)**, 1282 82

Psaltis, D., Belloni, T., and van der Klis, M.: 1999, **520(1)**, 262 44

Pudritz, R. E., Hardcastle, M. J., and Gabuzda, D. C.: 2012, **169(1-4)**, 27 101

Pudritz, R. E., Rogers, C. S., and Ouyed, R.: 2006, **365(4)**, 1131 101

Radhakrishnan, V. and Cooke, D. J.: 1969, **3**, 225 18

Rees, M. J.: 1971, **229(5283)**, 312 100

Rees, M. J.: 1978, **184**, 61P 105

Rees, M. J. and Meszaros, P.: 1994, **430**, L93 105

Reig, P., van Straaten, S., and van der Klis, M.: 2004, **602(2)**, 918 44, 123, 124

Remillard, R. A. and McClintock, J. E.: 2006, **44(1)**, 49 42

Reynolds, C.: 1996, *Ph.D. thesis*, University of Cambridge 34

Reynolds, C. S. and Nowak, M. A.: 2003, **377(6)**, 389 35

Rezzolla, L., Pizzochero, P., Jones, D. I., Rea, N., and Vidaña, I.: 2018, *The Physics and Astrophysics of Neutron Stars*, Vol. 457 16

Riggio, A., Burderi, L., di Salvo, T., Papitto, A., D'Aì, A., Iaria, R., and Menna, M. T.: 2011, **531**, A140 88, 90

Riggio, A., Di Salvo, T., Burderi, L., Menna, M. T., Papitto, A., Iaria, R., and Lavagetto, G.: 2008, **678**, 1273 81

Roberts, M. S. E., Al Noori, H., Torres, R. A., McLaughlin, M. A., Gentile, P. A., Hessels, J. W. T., Ransom, S. M., Ray, P. S., Kerr, M., and Breton, R. P.: 2018, in P. Weltevrede, B. B. P. Perera, L. L. Preston, and S. Sanidas (eds.), *Pulsar Astrophysics the Next Fifty Years*, Vol. 337 of *IAU Symposium*, pp 43–46 81

Romano, P., Campana, S., Chincarini, G., Cummings, J., Cusumano, G., Holland, S. T., Mangano, V., Mineo, T., Page, K. L., Pal'Shin, V., Rol, E., Sakamoto, T., Zhang, B., Aptekar, R., Barbier, S., Barthelmy, S., Beardmore, A. P., Boyd, P., Burrows, D. N., Capalbi, M., Fenimore, E. E., Frederiks, D., Gehrels, N., Giommi, P., Goad, M. R., Godet, O., Golenetskii, S., Guetta, D., Kennea, J. A., La Parola, V., Malesani, D., Marshall, F., Moretti, A., Nousek, J. A., O'Brien, P. T., Osborne, J. P., Perri, M., and Tagliaferri, G.: 2006, **456**, 917 54

Romanova, M. M. and Lovelace, R. V. E.: 1992, **262**, 26 101

Romanova, M. M., Ustyugova, G. V., Koldoba, A. V., Chechetkin, V. M., and Lovelace, R. V. E.: 1998, **500(2)**, 703 127

Romanova, M. M., Ustyugova, G. V., Koldoba, A. V., and Lovelace, R. V. E.: 2005, **635(2)**, L165 80

Roming, P. W. A., Kennedy, T. E., Mason, K. O., Nousek, J. A., Ahr, L., Bingham, R. E., Broos, P. S., Carter, M. J., Hancock, B. K., Huckle, H. E., Hunsberger, S. D., Kawakami, H., Killough, R., Koch, T. S., McLelland, M. K., Smith, K., Smith, P. J., Soto, J. C., Boyd, P. T., Breeveld, A. A., Holland, S. T., Ivanushkina, M., Pryzby, M. S., Still, M. D., and Stock, J.: 2005, **120(3-4)**, 95 48

Roy, J., Ray, P. S., Bhattacharyya, B., Stappers, B., Chengalur, J. N., Deneva, J., Camilo, F., Johnson, T. J., Wolff, M., Hessels, J. W. T., Bassa, C. G., Keane, E. F., Ferrara, E. C., Harding, A. K., and Wood, K. S.: 2015, **800**, L12 83

Rupen, M. P., Mioduszewski, A. J., and Sokoloski, J. L.: 2008, **688(1)**, 559 98

Russell, D. M., Fender, R. P., Hynes, R. I., Brocksopp, C., Homan, J., Jonker, P. G., and Buxton, M. M.: 2006, **371(3)**, 1334 114, 119

Russell, D. M., Fender, R. P., and Jonker, P. G.: 2007, **379(3)**, 1108 114

Russell, T. D., Degenaar, N., Wijnands, R., van den Eijnden, J., Gusinskaia, N. V., Hessels, J. W. T., and Miller-Jones, J. C. A.: 2018, **869**, L16 93

Sanna, A., Bahramian, A., Bozzo, E., Heinke, C., Altamirano, D., Wijnands, R., Degenaar, N., Maccarone, T., Riggio, A., Di Salvo, T., Iaria, R., Burgay, M., Possenti, A., Ferrigno, C., Papitto, A., Sivakoff, G. R., D'Amico, N., and Burderi, L.: 2018a, **610**, L2 83, 90

Sanna, A., Bozzo, E., Papitto, A., Riggio, A., Ferrigno, C., Di Salvo, T., Iaria, R., Mazzola, S. M., D'Amico, N., and Burderi, L.: 2018b, **616**, L17 83, 84, 90

Sanna, A., Burderi, L., Riggio, A., Pintore, F., Di Salvo, T., Gambino, A. F., Iaria, R., Matranga, M., and Scarano, F.: 2016, **459**, 1340 82, 84, 90, 95

Sanna, A., Di Salvo, T., Burderi, L., Riggio, A., Pintore, F., Gambino, A. F., Iaria, R., Tailo, M., Scarano, F., and Papitto, A.: 2017a, **471**, 463 84, 95

Sanna, A., Di Salvo, T., Burderi, L., Riggio, A., Pintore, F., Gambino, A. F., Iaria, R., Tailo, M., Scarano, F., and Papitto, A.: 2017b, **471**, 463 95

Sanna, A., Ferrigno, C., Ray, P. S., Ducci, L., Jaisawal, G. K., Enoto, T., Bozzo, E., Altamirano, D., Di Salvo, T., Strohmayer, T. E., Papitto, A., Riggio, A., Burderi, L., Bult, P. M., Bogdanov, S., Gambino, A. F., Marino, A., Iaria, R., Arzoumanian, Z., Chakrabarty, D., Gendreau, K. C., Guillot, S., Markwardt, C., and Wolff, M. T.: 2018c, **617**, L8 83, 90, 93, 95

Sanna, A., Méndez, M., Altamirano, D., Belloni, T., Hiemstra, B., and Linares, M.: 2014, **440**, 3275 35

Sanna, A., Papitto, A., Burderi, L., Bozzo, E., Riggio, A., Di Salvo, T., Ferrigno, C., Rea, N., and Iaria, R.: 2017c, **598**, A34 82, 83, 90

Sanna, A., Pintore, F., Riggio, A., Mazzola, S. M., Bozzo, E., Di Salvo, T., Ferrigno, C., Gambino, A. F., Papitto, A., Iaria, R., and Burderi, L.: 2018d, **481**, 1658 83, 90

Sathyaprakash, R., Roberts, T. P., Walton, D. J., Fuerst, F., Bachetti, M., Pinto, C., Alston, W. N., Earnshaw, H. P., Fabian, A. C., Middleton, M. J., and Soria, R.: 2019, **488(1)**, L35 27

Seaton, M. J.: 1979a, **187**, 785 117

Seaton, M. J.: 1979b, **187**, 73 117

Segreto, A., Cusumano, G., Ferrigno, C., La Parola, V., Mangano, V., Mineo, T., and Romano, P.: 2010, **510**, A47 53

Shahbaz, T., Watson, C. A., Zurita, C., Villaver, E., and Hernandez-Peralta, H.: 2008, **120**, 848 107, 108

Shakura, N. I. and Sunyaev, R. A.: 1973, **500**, 33 31, 127

Shapiro, S. L., Lightman, A. P., and Eardley, D. M.: 1976, **204**, 187 33

Shappee, B., Prieto, J., Stanek, K. Z., Kochanek, C. S., Holoien, T., Jencson, J., Basu, U., Beacom, J. F., Szczygiel, D., Pojmanski, G., Brimacombe, J., Dubberley, M., Elphick, M., Foale, S., Hawkins, E., Mullins, D., Rosing, W., Ross, R., and Walker, Z.: 2014, in *American Astronomical Society Meeting Abstracts #223*, Vol. 223 of *American Astronomical Society Meeting Abstracts*, p. 236.03 133

Shidatsu, M., Nakahira, S., Yamada, S., Kawamuro, T., Ueda, Y., Negoro, H., Murata, K. L., Itoh, R., Tachibana, Y., Adachi, R., Yatsu, Y., Kawai, N., Hanayama, H., Horiuchi, T., Akitaya, H., Saito, T., Takayama, M., Ohshima, T., Katoh, N., Takahashi, J., Nagayama, T., Yamanaka, M., Kawabata, M., Nakaoka, T., Takagi, S., Morokuma, T., Morihana, K., Maehara, H., and Sekiguchi, K.: 2018, **868(1)**, 54 133

Sibgatullin, N. R. and Sunyaev, R. A.: 2000, *Astronomy Letters* **26**, 699 33

Skumanich, A.: 1972, **171**, 565 86

Smith, M. A.: 1979, **91**, 737 86

Sobacchi, E. and Lyubarsky, Y. E.: 2020, **491(3)**, 3900 105

Spada, M., Ghisellini, G., Lazzati, D., and Celotti, A.: 2001, **325(4)**, 1559 105

Spruit, H. C.: 2010, *Theory of Magnetically Powered Jets*, Vol. 794, p. 233 100, 101

Spruit, H. C., Foglizzo, T., and Stehle, R.: 1997, **288(2)**, 333 101

Stella, L. and Vietri, M.: 1998, **492(1)**, L59 114

Stirling, A. M., Spencer, R. E., de la Force, C. J., Garrett, M. A., Fender, R. P., and Ogley, R. N.: 2001, **327(4)**, 1273 40, 112

Strohmayer, T. E., Arzoumanian, Z., Bogdanov, S., Bult, P. M., Chakrabarty, D., Enoto, T., Gendreau, K. C., Guillot, S., Harding, A. K., Ho, W. C. G., Homan, J., Jaisawal, G. K., Keek, L., Kerr, M., Mahmoodifar, S., Markwardt, C. B., Ransom, S. M., Ray, P. S., Remillard, R., and Wolff, M. T.: 2018, **858**, L13 83, 88, 90

Strohmayer, T. E. and Markwardt, C. B.: 2002, **577(1)**, 337 57

Strohmayer, T. E., Markwardt, C. B., Swank, J. H., and in't Zand, J.: 2003, **596**, L67 91

Strohmayer, T. E., Zhang, W., Swank, J. H., Smale, A., Titarchuk, L., Day, C., and Lee, U.: 1996, **469**, L9 57

Sturner, S. J. and Dermer, C. D.: 1994, **281**, L101 18

Swank, J. H., Boldt, E. A., Holt, S. S., Serlemitsos, P. J., and Becker, R. H.: 1978, **182**, 349 107

Tailo, M., D'Antona, F., Burderi, L., Ventura, P., di Salvo, T., Sanna, A., Papitto, A., Riggio, A., and Maselli, A.: 2018, **479**, 817 30, 86, 150

Tarana, A., Belloni, T., Bazzano, A., Méndez, M., and Ubertini, P.: 2011, **416(2)**, 873 37

Tauris, T. M.: 2001, in P. Podsiadlowski, S. Rappaport, A. R. King, F. D'Antona, and L. Burderi (eds.), *Evolution of Binary and Multiple Star Systems*, Vol. 229 of *Astronomical Society of the Pacific Conference Series*, p. 145 86

Tetarenko, A. J., Bahramian, A., Sivakoff, G. R., Tremou, E., Linares, M., Tudor, V., Miller-Jones, J. C. A., Heinke, C. O., Chomiuk, L., Strader, J., Altamirano, D., Degenaar, N., Maccarone, T., Patruno, A., Sanna, A., and Wijnands, R.: 2016, **460(1)**, 345 41, 131

Titarchuk, L. and Lyubarskij, Y.: 1995, **450**, 876 62

Titarchuk, L. and Shaposhnikov, N.: 2005, **626**, 298 63

Tomsick, J. A., Kalemci, E., Kaaret, P., Markoff, S., Corbel, S., Migliari, S., Fender, R., Bailyn, C. D., and Buxton, M. M.: 2008, **680(1)**, 593 39

Torres, M. A. P., Casares, J., Jiménez-Ibarra, F., Álvarez-Hernández, A., Muñoz-Darias, T., Padilla, M. A., Jonker, P. G., and Heida, M.: 2020, **893(2)**, L37 133

Torres, M. A. P., Casares, J., Jiménez-Ibarra, F., Muñoz-Darias, T., Armas Padilla, M., Jonker, P. G., and Heida, M.: 2019, **882(2)**, L21 133

Trushkin, S. A., Nizhelskij, N. A., Tsybulev, P. G., and Erkenov, A.: 2018, *The Astronomer's Telegram* **11539**, 1 133, 147, 148

Tudor, V., Miller-Jones, J. C. A., Patruno, A., D'Angelo, C. R., Jonker, P. G., Russell, D. M., Russell, T. D., Bernardini, F., Lewis, F., Deller, A. T., Hessels, J. W. T., Migliari, S., Plotkin, R. M., Soria, R., and Wijnands, R.: 2017, **470(1)**, 324 41

Ubertini, P., Bazzano, A., Cocchi, M., Natalucci, L., Heise, J., Muller, J. M., and in 't Zand, J. J. M.: 1999, **514(1)**, L27 72

Ubertini, P., Lebrun, F., Di Cocco, G., Bazzano, A., Bird, A. J., Broenstad, K., Goldwurm, A., La Rosa, G., Labanti, C., Laurent, P., Mirabel, I. F., Quadrini, E. M., Ramsey, B., Reglero, V., Sabau, L., Sacco, B., Staubert, R., Vigroux, L., Weisskopf, M. C., and Zdziarski, A. A.: 2003, **411**, L131 49

Ueda, Y., Inoue, H., Tanaka, Y., Ebisawa, K., Nagase, F., Kotani, T., and Gehrels, N.: 1998, **492(2)**, 782 40

Šimon, V.: 2018, **477**, 67 81, 90

Valenti, E., Ferraro, F. R., and Origlia, L.: 2007, **133**, 1287 91

Van, K. X., Ivanova, N., and Heinke, C. O.: 2018, *arXiv e-prints* 84, 95

van den Eijnden, J., Degenaar, N., Pinto, C., Patruno, A., Wette, K., Messenger, C., Hernández Santisteban, J. V., Wijnands, R., Miller, J. M., Altamirano, D., Paerels, F., Chakrabarty, D., and Fabian, A. C.: 2018a, **475**, 2027 56

van den Eijnden, J., Degenaar, N., Russell, T. D., Wijnand s, R., Miller-Jones, J. C. A., Sivakoff, G. R., and Hernández Santisteban, J. V.: 2018b, **562(7726)**, 233 98

van der Klis, M.: 1989, **27**, 517 43, 44

van der Klis, M.: 2004, *arXiv e-prints* pp astro–ph/0410551 43

van der Klis, M.: 2006, *Advances in Space Research* **38(12)**, 2675 44

van Doesburgh, M. and van der Klis, M.: 2017, **465(3)**, 3581 123

van Paradijs, J., Dotani, T., Tanaka, Y., and Tsuru, T.: 1990, **42**, 633 58, 74

van Straaten, S., Ford, E. C., van der Klis, M., Méndez, M., and Kaaret, P.: 2000, **540**, 1049 107

van Straaten, S., van der Klis, M., di Salvo, T., and Belloni, T.: 2002, **568(2)**, 912 44, 123, 124

van Straaten, S., van der Klis, M., and Méndez, M.: 2003, **596(2)**, 1155 44, 123

van Straaten, S., van der Klis, M., and Wijnands, R.: 2005, **619(1)**, 455 44, 123

Vedrenne, G., Roques, J. P., Schönfelder, V., Mand rou, P., Lichti, G. G., von Kienlin, A., Cordier, B., Schanne, S., Knödlseder, J., Skinner, G., Jean, P., Sanchez, F., Caraveo, P., Teegarden, B., von Ballmoos, P., Bouchet, L., Paul, P., Matteson, J., Boggs, S., Wunderer, C., Leleux, P., Weidenspointner, G., Durouchoux, P., Diehl, R., Strong, A., Cassé, M., Clair, M. A., and André, Y.: 2003, **411**, L63 49

Verbunt, F., Belloni, T., Johnston, H., van der Klis, M., and Lewin, W.: 1994, **285**, 903 86

Verbunt, F. and van den Heuvel, E. P. J.: 1995, *X-ray Binaries* pp 457–494 84

Verbunt, F. and Zwaan, C.: 1981, **100**, L7 30, 86

Verner, D. A., Ferland, G. J., Korista, K. T., and Yakovlev, D. G.: 1996, **465**, 487 62, 137, 187

Vila, G. S. and Romero, G. E.: 2010, **403(3)**, 1457 99

Voges, W., Aschenbach, B., Boller, T., Bräuninger, H., Briel, U., Burkert, W., Dennerl, K., Englhauser, J., Gruber, R., Haberl, F., Hartner, G., Hasinger, G., Kürster, M., Pfeffermann, E., Pietsch, W., Predehl, P., Rosso, C., Schmitt, J. H. M. M., Trümper, J., and amfirimmermann, H. U.: 1999, **349**, 389 58

Volonteri, M.: 2010, **18(3)**, 279 20

Walker, M. A.: 1995, **453**, 37 20

Wang, J., Zhang, C. M., Zhao, Y. H., Kojima, Y., Yin, H. X., and Song, L. M.: 2011, **526**, A88 19

Wang, Z., Breton, R. P., Heinke, C. O., Deloye, C. J., and Zhong, J.: 2013, **765**, 151 30, 86

Watkins, L. L., van der Marel, R. P., Bellini, A., and Anderson, J.: 2015, **812**, 149 91

Weisskopf, M. C., Ramsey, B., O'Dell, S., Tennant, A., Elsner, R., Soffitta, P., Bellazzini, R., Costa, E., Kolodziejczak, J., Kaspi, V., Muleri, F., Marshall, H., Matt, G., and Romani, R.: 2016, in J.-W. A. den Herder, T. Takahashi, and M. Bautz (eds.), *Space Telescopes and Instrumentation 2016: Ultraviolet to Gamma Ray*, Vol. 9905 of *Society of Photo-Optical Instrumentation Engineers (SPIE) Conference Series*, p. 990517 151

Welsh, W. F., Robinson, E. L., and Young, P.: 2000, **120**, 943 81

Wheeler, J. A.: 1968, *American Scientist* **56(1)**, 1 20

White, N. E., Stella, L., and Parmar, A. N.: 1988, **324**, 363 39

Wijers, R. A. M. J., Rees, M. J., and Meszaros, P.: 1997, **288(4)**, L51 98

Wijnands, R.: 2001, *Advances in Space Research* **28(2-3)**, 469 25

Wijnands, R.: 2003, **588**, 425 90

Wijnands, R., Degenaar, N., Armas Padilla, M., Altamirano, D., Cavecchi, Y., Linares, M., Bahramian, A., and Heinke, C. O.: 2015, **454**, 1371 39, 70, 87

Wijnands, R., Degenaar, N., and Page, D.: 2017a, *Journal of Astrophysics and Astronomy* **38**, 49 124

Wijnands, R., in't Zand, J. J. M., Rupen, M., Maccarone, T., Homan, J., Cornelisse, R., Fender, R., Grindlay, J., van der Klis, M., Kuulkers, E., Markwardt, C. B., Miller-Jones, J. C. A., and Wang, Q. D.: 2006, **449**, 1117 13, 56, 77

Wijnands, R., Parikh, A. S., Altamirano, D., Homan, J., and Degenaar, N.: 2017b, **472**, 559 39, 45, 70

Wijnands, R., Rol, E., Cackett, E., Starling, R. L. C., and Remillard, R. A.: 2009, **393**, 126 91

Wijnands, R., Strohmayer, T., and Franco, L. M.: 2001, **549**, L71 57

Wijnands, R. and van der Klis, M.: 1998, **394**, 344 81, 83

Will, C. M.: 2006, *Living Reviews in Relativity* **9(1)**, 3 82

Wilms, J., Allen, A., and McCray, R.: 2000, **542**, 914 62, 137, 187

Winkler, C., Courvoisier, T. J. L., Di Cocco, G., Gehrels, N., Giménez, A., Grebenev, S., Hermsen, W., Mas-Hesse, J. M., Lebrun, F., Lund, N., Palumbo, G. G. C., Paul, J., Roques, J. P., Schnopper, H., Schönfelder, V., Sunyaev, R., Teegarden, B., Ubertini, P., Vedrenne, G., and Dean, A. J.: 2003, **411**, L1 49

Xie, F.-G. and Yuan, F.: 2012, **427(2)**, 1580 126

Xu, Y., Harrison, F. A., Tomsick, J. A., Hare, J., Fabian, A. C., and Walton, D. J.: 2020, **893(1)**, 42 133, 137, 147

Yuan, F.: 2001, **324(1)**, 119 33, 126

Zamfir, M., Cumming, A., and Galloway, D. K.: 2012, **749**, 69 74

Zdziarski, A. A. and De Marco, B.: 2020, **896(2)**, L36 34

Zdziarski, A. A., Gierliński, M., Mikołajewska, J., Wardziński, G., Smith, D. M., Harmon, B. A., and Kitamoto, S.: 2004, **351(3)**, 791 42

Zdziarski, A. A., Paul, D., Osborne, R., and Rao, A. R.: 2016, **463(2)**, 1153 103, 122

Zhang, S., Santangelo, A., Feroci, M., Xu, Y., Lu, F., Chen, Y., Feng, H., Zhang, S., Brandt, S., Hernanz, M., Baldini, L., Bozzo, E., Campana, R., De Rosa, A., Dong, Y., Evangelista, Y., Karas, V., Meidinger, N., Meuris, A., Nand ra, K., Pan, T., Pareschi, G., Orleanski, P., Huang, Q., Schanne, S., Sironi, G., Spiga, D., Svoboda, J., Tagliaferri, G., Tenzer, C., Vacchi, A., Zane, S., Walton, D., Wang, Z., Winter, B., Wu, X., in't Zand, J. J. M., Ahangarianabhari, M., Ambrosi, G., Ambrosino, F., Barbera, M., Basso, S., Bayer, J., Bellazzini, R., Bellutti, P., Bertucci, B., Bertuccio, G., Borghi, G., Cao, X., Cadoux, F., Campana, R., Ceraudo, F., Chen, T., Chen, Y., Chevenez, J., Civitani, M., Cui, W., Cui, W., Dauser, T., Del Monte, E., Di Cosimo, S., Diebold, S., Doroshenko, V., Dovciak, M., Du, Y., Ducci, L., Fan, Q., Favre, Y., Fuschino, F., Gálvez, J. L., Gao, M., Ge, M., Gevin, O., Grassi, M., Gu, Q., Gu, Y., Han, D., Hong, B., Hu, W., Ji, L., Jia,

S., Jiang, W., Kennedy, T., Kreykenbohm, I., Kuvvetli, I., Labanti, C., Latronico, L., Li, G., Li, M., Li, X., Li, W., Li, Z., Limousin, O., Liu, H., Liu, X., Lu, B., Luo, T., Macera, D., Malcovati, P., Martindale, A., Michalska, M., Meng, B., Minuti, M., Morbidini, A., Muleri, F., Paltani, S., Perinati, E., Picciotto, A., Piemonte, C., Qu, J., Rachevski, A., Rashevskaya, I., Rodriguez, J., Schanz, T., Shen, Z., Sheng, L., Song, J., Song, L., Sgro, C., Sun, L., Tan, Y., Uttley, P., Wang, B., Wang, D., Wang, G., Wang, J., Wang, L., Wang, Y., Watts, A. L., Wen, X., Wilms, J., Xiong, S., Yang, J., Yang, S., Yang, Y., Yu, N., Zhang, W., Zampa, G., Zampa, N., Zdziarski, A. A., Zhang, A., Zhang, C., Zhang, F., Zhang, L., Zhang, T., Zhang, Y., Zhang, X., Zhang, Z., Zhao, B., Zheng, S., Zhou, Y., Zorzi, N., and Zwart, J. F.: 2019, *Science China Physics, Mechanics, and Astronomy* **62(2)**, 29502 151

Zhang, S. N., Cui, W., and Chen, W.: 1997, **482**, L155 37

Zhang, W., Jahoda, K., Swank, J. H., Morgan, E. H., and Giles, A. B.: 1995, **449**, 930 109

Zhang, Z., Sakurai, S., Makishima, K., Nakazawa, K., Ono, K., Yamada, S., and Xu, H.: 2016, **823(2)**, 131 39

Ziółkowski, J. and Zdziarski, A. A.: 2018, **480**, 1580 84, 150

Appendices

A. Spectral Analysis of XTE J1814+338

Unlike any other source in the sample, spectral information about XTE J1814+338 during its one and only outburst in 2003 are not reported in literature. Furthermore the *RXTE*/PCA (Proportional Counter Array) light curve of the 53-days long outburst does not have a simple shape comparable to any geometrical figure (see Papitto et al. 2007, , figure 1): after a smooth rise lasting for $\sim$ 5 d, the emitted flux stabilized to an order of magnitude of 10^{-10} erg cm^{-2} s^{-1} (2.5-25 keV) for 33 d, with a peak flux of $5\times$ 10^{-10} erg cm^{-2} s^{-1} in the same energy range and fluctuations around 20%, until it decayed abruptly to one fourth of the peak flux. In order to calculate the fluence of the source we performed a simple spectral analysis of the system during the outburst.
In order to calculate the area subtended by the curve we described the light curve with a piecewise function, as shown in Figure A.1, and then we divided the whole area in 8 trapezes. The area of these trapezes is easy to calculate once we have the information about the flux at the beginning and at the end of the corresponding time segment. Therefore, I extracted the *RXTE* spectra from the *RXTE* standard products (in particular source and background spectra and the response file) of the source in 7 strategic points, in order to get the bolometric (0.1-300 keV) flux. It is important to notice that, according to the light curve shape, we considered the flux constant over two time windows, i.e. between points 2-3 and 8-9 in Figure A.1.
Standard data products are not meant to be used for a detailed analysis of the source, but they are suitable for our purpose to have rough information about the bolometric flux evolution from the source. The spectrum of each observation was analysed using the spectral package Heasarc XSPEC v. 12.9.1, and fitted to a simple power law, described by the POWERLAW model, multiplied by TBABS to take into account the interstellar absorption, with VERN cross-sections (Verner et al. 1996) and WILMS abundances (Wilms et al. 2000). Observations log and spectral fit results are reported in Table A.1.

TABLE A.1: **List of the observations used in this work and fits results**

	ObsID	**Date** (mm-dd-yyyy)	**Γ index**	**N_H** ($\times 10^{22}$ cm^{-2})	**F $_{bol}$ (0.1-300 keV)** ($\times 10^{-10}$ erg cm^{-2} s^{-1})	χ^2_ν (d.o.f.)
1	80145-02-01-01	06-07-2003	1.600±0.020	<0.48	6.80±0.68	1.45(47)
2	80418-01-02-06	06-15-2003	1.706±0.012	0.89±0.16	8.69±0.87	0.99(46)
3*						
4	80418-01-03-12	06-20-2003	1.659±0.015	0.40±0.20	8.27±0.83	0.90(46)
5	80418-01-03-08	06-24-2003	1.670±0.020	0.45±0.30	8.78±0.88	0.86(46)
6	80418-01-05-00	07-04-2003	1.700±0.030	0.50±0.40	6.85±0.69	0.71(46)
7	80418-01-05-09	07-09-2003	1.760±0.013	0.300†	6.96±0.70	0.93(48)
8	80418-01-06-02	07-13-2003	1.840±0.020	0.300†	2.16±0.22	0.97(47)
9*						

The data have been all analyzed using a simple TBABS×POWERLAW model. The quoted errors for Γ and N_H were calculated with the ERROR command for the resulting simulated posterior distribution and reflect 90% confidence intervals, while a standard uncertainty of 10% has been attributed to each of the bolometric flux values.
*: Under the assumption that the flux was almost the same between the previous data point and this one, an assumption based on the light curve shape over these time intervals, the bolometric flux at this time was considered equal to the flux reported in the preceding row;
†: the parameter was kept frozen to the reported value for the stability of the fit.

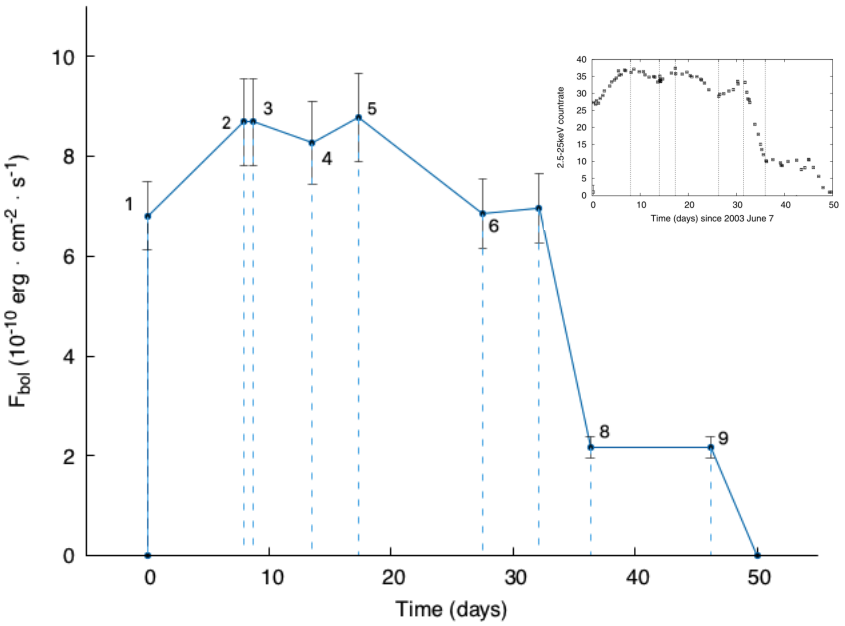

FIGURE A.1: Data points used to describe geometrically the light curve of the 2003 outburst of XTE J1814-338. In this representation, the light curve is described as the piecewise function connecting the data points and its area is obtained by dividing it in trapezes, whose vertical lines are the dashed lines in this figure, and summing their areas; the light curve is shown for comparison in the box above (Papitto et al. 2007).

B. List of refereed and non-refereed publications

B.1 List of refereed publications

- **A. Marino**, J. Malzac, M. Del Santo, S. Migliari, R. Belmont, T. Di Salvo, D. Russell, J. Lopez-Miralles, M. Perucho, A. D'Aì, R. Iaria, L. Burderi, 2020, MNRAS, 498, 3, pp. 3351-3367, *Testing jet geometries and disk-jet coupling in the neutron star LMXB 4U 0614+091 with internal shocks*. doi:10.1093/mnras/staa2570

- R. Iaria, S. M. Mazzola, T. Di Salvo, **A. Marino**, A. F. Gambino, A. Sanna, A. Riggio, L. Burderi, 2020, A&A, 635, id.A209, *Reflection component in the Bright Atoll Source GX 9+9*. doi:10.1051/0004-6361/202037491

- R. Iaria, T. Di Salvo, A. Sanna, S. M. Mazzola, A. F. Gambino, A. Riggio, **A. Marino**, G. Termini, L. Burderi, (in press, A&A), *Evidence of non-conservative mass-transfer in the ultra-compact X-ray source XB 1916-053*.

- **A. Marino**, T. Di Salvo, L. Burderi, A. Sanna, A. Riggio, M. Del Santo, A. Papitto, R. Iaria, A. F. Gambino, S. M. Mazzola, 2019, A&A, 627, id.A125, 11 pp., *Indications of non-conservative mass- transfer in AMXPs*. doi:10.1051/0004-6361/201834460.

- **A. Marino**, M. Del Santo, M. Cocchi, C. Ferrigno, A. Segreto, T. Di Salvo, R. Iaria, A. D'Ai, J. Malzac, L. Burderi, 2019, MNRAS, 490, 2, pp. 2300-2314, *New insights on the puzzling LMXB 1RXS J180408.9-342058: The intermediate state, the clocked bursts and much more.*, doi:10.1093/mnras/stz2726

- R. Amato, A. D'Ai. M. Del Santo, D. De Martino, **A. Marino**, T. Di Salvo, R. Iaria, T. Mineo, 2019, MNRAS, 486-3, p.3992-4000, *Search for multi-wavelength emission from the binary millisecond pulsar PSR J1836-2354A in the globular cluster M22*, doi:10.1093/mnras/stz1100

- A. F. Gambino, R. Iaria, T. Di Salvo, S. M. Mazzola, **A. Marino**, L. Burderi, A. Riggio, A. Sanna, N. D'Amico, 2019, A&A, 625, A92, *Spectral Analysis of the dipping LMXB system*

XB 1916-053, doi:10.1051/0004-6361/201832984

- S. M. Mazzola, R. Iaria, T. Di Salvo, A. F. Gambino, **A. Marino**, L. Burderi, A. Sanna, A. Riggio, F. D'Antona, 2019, A&A Volume 625, id.L12, 5 pp, *Updated orbital ephemeris of the ADC source X 1822-371: a stable orbital expansion over 40 years*, doi:10.1051/0004-6361/201935665

- R. Iaria, S. Mazzola, T. Bassi, A. F. Gambino, **A. Marino**, T. Di Salvo, A. Sanna, A. Riggio, L. Burderi, N. D'Amico, 2019, A&A, 630, A138, *Broadband spectral analysis of MXB 1659-298 in its soft and hard state*, doi:10.1051/0004-6361/201833982

- **A. Marino**, N. Degenaar, T. Di Salvo, R. Wijnands, L. Burderi, R. Iaria, 2018, MNRAS, 479, 3734, *On obtaining Neutron Star mass and radius constraints from quiescent Low Mass X-Ray Binaries in the Galactic Plane*, doi:10.1093/mnras/sty1585.

- A. Sanna, C. Ferrigno, P. S. Ray, L. Ducci, G. K. Jaisawal, T. Enoto, E. Bozzo, D. Altamirano, T. Di Salvo, T. E. Strohmayer, A. Papitto, A. Riggio, L. Burderi, P. M. Bult, S. Bogdanov, A. F. Gambino, **A. Marino**, R. Iaria, Z. Arzoumanian, D. Chakrabarty, K. C. Gendreau, S. Guillot, C. B. Markwardt, M. T. Wolff, 2018, A&A, 617, L8, *NuSTAR and NICER reveal IGR J17591-2342 as a new accreting millisecond X-ray pulsar*, doi:10.1051/0004-6361/201834160.

- **A. Marino**, T. Di Salvo, A. F. Gambino, R. Iaria, L. Burderi, M. Matranga, A. Sanna and A. Riggio, 2017, A&A, 603, A137, *Evidence of a non-conservative mass-transfer for the AMSP XTE J0929-314*, doi:10.1051/0004-6361/201730464

B.2 List of non-refereed publications

- T. Bassi, M. Del Santo, A. D'Ai, S. Motta, **A. Marino**, A. Segreto, 2019, The Astronomer's Telegram 12477, *Monitoring the transient MAXI J1348-630 with the Neil Gehrels Swift observatory*

- S. M. Mazzola, R. Iaria, A. F. Gambino, **A. Marino**, T. Di Salvo, T. Bassi, A. Sanna, A. Riggio, L. Burderi, 2019, arXiv: 1906.10960, *Broadband spectral analysis of MXB 1659-298*

B.3 List of publications in preparation

- **A. Marino**, P. O. Petrucci, S. Barnier, J. Malzac, M. Del Santo, A. Segreto, T. Di Salvo, T. D. Russell, J. Ferreira, G. Marcel, S. E. Motta, A. D'Aì, *A unified accretion-ejection paradigm: the evolving accretion flow in the hard state of MAXI J1820+070*.

- **A. Marino**, T. Di Salvo, M. Del Santo, T. Bassi, A. F. Gambino, R. Iaria, S. M. Mazzola, R. Iaria, L. Burderi, *A new Swift/Suzaku look to the LMXB 4U 0614+091*

- A. Anitra, et al., *Spectral analysis of the LMXB and X-ray Pulsar X1822-371*

- A. F. Gambino et al., *Probing the geometry of the accretion flow in the LMXB system 4U 1822-371 with eXTP*;

- T. D. Russell, M. Del Santo, A. Marino, et al., *A radio and X-ray analysis of the Galactic X-ray binary MAXI J1810−222 reveals a black hole candidate*;

- E. Ambrosi, A. Marino, et al., *TBD*